MACH-6 RECEPTIVITY MEASUREMENTS OF LASER-GENERATED PERTURBATIONS ON A FLARED CONE

A Dissertation

Submitted to the Faculty

of

Purdue University

by

Amanda Chou

In Partial Fulfillment of the

Requirements for the Degree

of

Doctor of Philosophy

August 2014

Purdue University

West Lafayette, Indiana

To Mom and Dad.

ACKNOWLEDGMENTS

The National Defense in Science and Engineering Graduate fellowship, a Zonta International Amelia Earhart fellowship, the NASA Pathways Intern Experience Program, and the Air Force Office of Scientific Research (Grant FA9550-12-1-0167) provided funding for this research.

A special thanks is also given here to Professor Schneider for providing guidance on the research presented here and to Professor Collicott, who provided much assistance with the legacy of the laser perturber system and designed the optical system to be used in the Mach-6 tunnel. I would also especially like to thank the machine shop at the Aerospace Sciences Lab. Without the hard work, patience, and expertise of John Phillips, Jim Younts, Robin Snodgrass, and Jerry Hahn, I would not have had the fine equipment that I had the pleasure of using for these experiments.

The advice and support from TU Braunschweig was also very helpful. A special thanks is given here to Professor Radespiel, who provided the suggestion to place the freestream disturbance off the centerline axis of the model. Dirk Heitmann at TU Braunschweig also provided much insight on their perturber apparatus. He also graciously allowed me to follow him around while we ran an experiment in HLB just so that I could learn how to run a similar apparatus at Purdue.

The support I received at NASA Langley Research Center is also deserving of recognition and gratitude. Without the guidance of the high-speed group in the Flow Physics and Control Branch, I would not have been able to make the most out of my data and my co-op. The guidance and support offered by Mike Kegerise was incredibly useful and much appreciated. The data presented in the NASA Langley chapters here would not be possible without the support of Ricky Clark and Rhonda Mills and their countless hours of patience in running the PCT. I would also like to thank Cathy McGinley in her unending support of and confidence in my work.

I'd like to also thank the members of my research group through the years for their friendship and help: Matt Borg, Tom Juliano, Katya Casper, Brad Wheaton, Peter Gilbert, Laura Steen, Chris Ward, Dennis Berridge, Laura Letterman, Ryan Luersen, Andrew Abney, Ryan Henderson, Brandon Chynoweth, Roger Greenwood, George Moraru, and Greg McKiernan. To my roommate at NASA Langley and former Team Schneider member, Shann Rufer, thank you for the guidance, the support, the living space, and of course, the wine and cheese! My fellow co-ops at NASA Langley, especially Jenna Eppink and Brett Bathel, are also deserving of credit for keeping me sane through food and hiking. Thank you also to Marcia, Angie, Anita, Kim, Jenette, Amber, Noah, Joe, Anna, Jillian, Bobbi, Lauren, Suzanne, Jessica, Sara, and Nico for helping me find peace and stillness in the chaos of grad school. And finally, a big thank you to my family for their boundless understanding and patience.

"Even when you think you have your life all mapped out, things happen that shape your destiny in ways you might never have imagined." — Deepak Chopra

TABLE OF CONTENTS

LIST OF TABLES

LIST OF FIGURES

SYMBOLS

a_0	speed of sound at stagnation conditions
a_∞	speed of sound in the freestream
D	cavity or perturbation diameter
D_{nose}	model nose diameter
E	voltage
f	frequency
$\tilde{J}$	estimated impulse magnitude of freestream laser perturbation
K	Gladstone-Dale constant
L	cavity depth
M	Mach number
N	growth factor
n	index of refraction
p	pressure
r	radius
R	radius of the nozzle
Re_L	freestream unit Reynolds number based on cavity depth
$Re_{\text{L,stop}}$	freestream unit Reynolds number based on cavity depth when resonance stops
Re/m	freestream unit Reynolds number
T	temperature
t	time after tunnel starts
t_p	time after laser pulse
u	speed
w	laser beam diameter or a subscript indicating a hot wire condition

x	horizontal location measured from the centerline of the Probe Calibration Tunnel, or axial distance from the nosetip of a model in the Boeing/AFOSR Mach-6 Quiet Tunnel
y	vertical location, measured from the centerline
z	axial location, measured from the throat in the BAM6QT and measured from the nozzle exit in the PCT
α	deflection angle
γ	ratio of specific heats
$\gamma/2$	damping constant
δ	bow shock standoff distance
Δ_y	vertical deflection
Δz	relative distance between perturbation and generation location
Δz_i	relative distance between probe and generation location
λ	wavelength
μ	dynamic viscosity, or Mach angle, depending on the context
ϕ	diameter of lens
ρ	density
ω	angular frequency
$'$	superscript indicating the fluctuation of the variable
0	subscript indicating stagnation condition
1	subscript indicating conditions upstream of a shock
2	subscript indicating conditions downstream of a shock
∞	subscript indicating freestream condition
base	subscript indicating condition at the base of a cavity
i	subscript indicating initial condition

ABBREVIATIONS

AFOSR	Air Force Office of Scientific Research
AO	acoustic origin
BAM6QT	Boeing/AFOSR Mach-6 Quiet Tunnel
CCA	constant current anemometer
CNC	computer numerical control
CTA	constant temperature anemometer
DNS	direct numerical simulation
FFT	fast Fourier transform
LaRC	NASA Langley Research Center
LDI	laser differential interferometer
NASA	National Aeronautics and Space Administration
Nd:YAG	Neodymium-doped Yttrium-Aluminum-Garnet crystal
n.e.	nozzle exit
PCB	PCB Piezotronics (pressure transducer manufacturer)
PCT	NASA LaRC Probe Calibration Tunnel
PDF	probability density function
PFI	Precision Filters, Inc.
PQFLT	Purdue Quiet Flow Ludwieg Tube (decommissioned Mach-4 quiet tunnel)
SNR	signal-to-noise ratio
TS	Tollmien-Schlichting
TTL	transistor-transistor logic

ABSTRACT

Chou, Amanda Ph.D., Purdue University, August 2014. Mach-6 Receptivity Measurements of Laser-Generated Perturbations on a Flared Cone. Major Professor: Steven P. Schneider.

A better understanding of receptivity can contribute to the development of an amplitude-based method of transition prediction. This type of prediction model would incorporate more physics than the widely-used semi-empirical methods. The experimental study of receptivity requires a characterization of the external disturbances and a study of their effect on the boundary-layer instabilities.

Characterization measurements for a laser-generated perturbation were made in two different wind tunnels. These measurements were made with hot-wire probes, optical techniques, and pressure transducer probes. Existing methods all have limitations, so better measurements will require the development of new instrumentation. Nevertheless, the freestream laser-generated perturbation has been shown to be about 8 mm in diameter at a freestream static density of about 0.040 kg/m^3. The amplitude of the perturbation is large, with a pitot pressure deficit at the center of the perturbation of about 65%. This amplitude may be too large for the study of linear growth.

The laser-generated perturbation was then placed in the freestream of the Boeing/AFOSR Mach-6 Quiet Tunnel (BAM6QT) upstream of a model. It was aligned to the centerline of a flared cone at zero angle of attack. The interaction of this laser-generated perturbation with the flared cone was measured with surface-mounted fast pressure transducers. A wave packet was generated by the perturbation and grew to nonlinear amplitudes along the length of the cone. Initial amplitudes of this wave packet were estimated to be very small compared to the freestream disturbance amplitude.

A marked difference was seen when different radii nosetips were used. On the flared cone with a blunt 1-mm nosetip, the generated wave packet only appeared near the aft end of the cone. On the flared cone with a nearly sharp nosetip, the generated wave packet appeared at all sensor locations. When the perturbation generated by the laser was placed off-axis of the cone centerline, the deliberate misalignment of the perturbation had a substantial effect for the blunt nosetip cone. Surprisingly, there was little to no effect of deliberate misalignment for the sharper nosetip. When the perturbation was aligned off-axis to the flared cone, the perturbation created a larger boundary layer disturbance on the side toward which the perturbation was aligned.

CHAPTER 1. INTRODUCTION

Laminar-turbulent transition in the hypersonic regime is not a well-understood process. To better understand this phenomenon, experimental data are needed. Flight tests cost orders of magnitude more than ground tests and generally return less data, so experiments conducted in wind tunnels are required. Receptivity, as termed by Morkovin in his 1969 review of transition [1], is the process by which freestream disturbances enter the boundary layer. When these disturbances enter the boundary layer, they can excite instabilities. These instabilities can affect the transition process by growing to create large fluctuations in the boundary layer, which can eventually break down into turbulence.

Current high-speed transition prediction methods are semi-empirical at best and incorporate only some physics. These methods estimate the transition process by examining the relative growth of instabilities. Choosing a transition criteria based only on the relative growth of instabilities does not take into consideration that the initial amplitude of the instability may be very large or very small. Receptivity studies can be used to help determine the initial amplitudes of the instabilities. If the receptivity process can be better understood, then an amplitude-based method of transition prediction can be developed.

Improvements on previous receptivity experiments are desired to contribute to an amplitude-based model for transition prediction. To do so, the freestream disturbance must be characterized quantitatively using measurements with probes or other techniques. Without an understanding of the freestream disturbances present, it is difficult to develop models of how these disturbances affect the instability growth and transition process. Ideally, both the amplitude and frequency content would be obtained from these measurements. The instabilities in the boundary layer created by these freestream disturbances can then be recorded. These characterization

measurements could eventually be used to predict the effect of the freestream disturbances on instabilities in the boundary layer. To develop an amplitude-based theory of transition requires the cooperation of theoretical, computational, and experimental efforts.

1.1 Receptivity and Transition

Freestream disturbances have the ability to excite instabilities within the boundary layer, which can grow and cause transition. High-speed boundary layer transition is of particular interest to several different aerospace applications, such as re-entry vehicles, reusable launch vehicles, and high-speed interceptor missiles. Transition affects the cost of high-speed vehicles, as many are over-designed to compensate for our lack of knowledge of the transition location. On the other hand, catastrophic failures are a concern if high-speed vehicles are under-designed [2, 3].

1.1.1 Transition Prediction

Transition prediction for a subsonic boundary layer is less complicated than for high-supersonic or hypersonic boundary layers. The disturbance spectrum of subsonic flow is comparatively simple. The Tollmien-Schlichting (T-S) wave is the dominant mechanism which causes transition on flat plates and axisymmetric bodies at zero angle of attack in subsonic flows. Using Mack's terminology, this T-S wave corresponds to the first mode [4]. Other modes of instability (Mack's second mode and higher) are also present in the boundary layer in higher-speed flows, complicating the disturbance spectra. These higher modes of instability correspond to inviscid instabilities and act like trapped acoustic waves [4].

Transition prediction is typically based on empirical and semi-empirical models. A popular semi-empirical model is the e^N method [5, 6], which considers the relative

linear growth of instability waves in the boundary layer. The growth factor N is defined as

$$N = \ln\left(\frac{A(x)}{A_0}\right) \tag{1.1}$$

where $A(x)$ is the amplitude of the disturbance at some location x and A_0 is the initial amplitude of the disturbance. The boundary layer is expected to transition when this growth factor exceeds some limit defined by a number N at transition, or N_{tr}. The value of N_{tr} may vary from tunnel to tunnel as well as model to model. The differences in the transition N-factor may be due to different freestream disturbance environments [2, 6–8], model surface finish [9], or model geometry [10].

The e^N model considers only linear growth and does not take into consideration the initial amplitude, nonlinear growth, or the total amplitude of the instability wave at breakdown. Smaller initial instability amplitudes result in disturbances which initially grow linearly. Eventually, these small instabilities can start to grow nonlinearly, which deviates from e^N-method predictions. Larger initial amplitudes may cause transient growth and bypass phenomena [11].

Freestream disturbance amplitudes affect initial disturbance amplitudes. These initial disturbance amplitudes affect the process of transition. Semi-empirical methods like e^N attempt to reconcile the differences between freestream disturbance amplitudes by choosing different N_{tr} for these environments. For example, high-speed environments with low acoustic noise, such as quiet tunnels and flight, often show an N-factor at transition to be about 8–11 [6–8]. In noisier environments, such as conventional tunnels, the N-factor at transition is typically about 4–5 [6, 12].

The receptivity of a model to the same level of freestream disturbance may also change, based on the shape of the leading edge and the surface roughness characteristics. The change in receptivity for different models may create different initial instability amplitudes for the same level of freestream disturbance. This may help to explain some of the differences in the value of N_{tr} for different models in similar environments.

An amplitude-based theory of transition prediction would consider receptivity, instability growth and some finite amplitude criteria for transition onset [13, 14]. This form of transition prediction requires the determination of initial amplitudes for instabilities in the boundary layer, which are nearly impossible to measure directly. Computational models of this problem are able to determine initial amplitudes of the boundary layer instabilities, given the spectral properties of the freestream disturbance and using receptivity theory. Experiments must be used to validate these models. However, few measurements of the evolution of the freestream disturbances into boundary layer instabilities exist due to the difficulty in making these measurements.

1.1.2 Receptivity

The purpose of studying receptivity is to find the source of instabilities in the boundary layer as they relate to unsteadiness in the freestream. Receptivity focuses on the generation and onset of the instabilities instead of simply recording the movement of the transition location due to changes in flow parameters. Receptivity analysis differs from stability analysis both physically and mathematically. Unlike the eigenvalue problems that stability analysis presents, the receptivity problem takes the form of a set of non-homogeneous equations and boundary conditions [15].

The predominant disturbance in subsonic flow is often vorticity, or velocity fluctuations. The time and length scales of the freestream disturbances differ from those of the dominant boundary layer disturbance, the T-S waves. Receptivity studies of the freestream and boundary-layer disturbances in this regime focus primarily on finding some form of transfer function or scale conversion mechanism that resolves this difference in scales [11]. The literature shows that the forcing length scale must be on the order of the T-S wavelength to generate these boundary-layer instabilities [16]. High-supersonic flow and hypersonic flow do not require this scale-conversion due to

the similarity in time and length scales between the acoustic waves and the boundary layer modes [17].

For supersonic flow, Mack developed a forcing theory [18] to apply to flat plate measurements taken at the Jet Propulsion Lab (JPL) in Pasadena, CA [13]. This theory uses empirical input derived from Kendall's measurements [13] and a forced response of the boundary layer, in which some applied forcing disturbances generate boundary-layer instabilities. These forcing disturbances were distinctly different from the freestream disturbances. Mack notes that the mechanism by which the freestream disturbances become forced disturbances was not described with this theory [18], but still provided good agreement with the measurements.

Schopper attempted to relate the freestream and forcing disturbances by modeling the effect of an acoustic field on a laminar boundary layer [19, 20]. This model was created to determine the effect of tunnel wall noise radiated onto a model in a tunnel. A transitional supersonic boundary layer was modeled using a Mach wave radiation field consisting of randomly-spaced pulses of varying amplitude and size. A weak shock wave emanated from each of these discrete entities, and created miniature sonic booms like shocklets in a supersonic boundary layer.

Schopper found that the shocklets focused in the outer region of a laminar boundary layer on a two-dimensional model. The forced response of the boundary layer to shocklets shows a possible matching between convection speeds and instability wave speeds and between disturbance profiles and eigenfunction shapes. This may indicate a mechanism for receptivity. Schopper also stated that the forced response to tunnel acoustic excitation seemed to be negatively correlated to the generation of TS waves. Positive changes in mass flux in the freestream acoustic disturbance generated a positive change in the mass flux of the forced response and a negative change in mass flux in the TS wave. Resolving the relation between freestream and forcing disturbances remains an ongoing problem, and measurements and computations need to be performed to reconcile this.

Three Sources of Freestream Disturbances

Several sources of freestream disturbances exist. Not all of these disturbances are easily measured. Three predominant types of disturbances are present in a uniform, steady compressible flow: vorticity (velocity fluctuations), entropy fluctuations (temperature spottiness), and acoustic noise [21]. These three types of disturbances are not necessarily the only types of disturbances that cause instability waves and, ultimately, transition. For example, freestream particulates are rarely studied, but can have a significant impact on transition. Fedorov has used a combination of receptivity and amplitude-based theory to show that particles can cause transition on a flat plate at an equivalent condition of $N \approx 11$ [22]. Particulates are capable of not only altering flow characteristics, but of altering model characteristics by changing the surface roughness through the deposition or the removal of material.

Large freestream disturbances can interact with each other. In shear flows, vorticity and entropy waves dominate the flow and their interaction is large. In an environment such as in low supersonic flight or a quiet tunnel, all three modes can be considered as separate quantities that do not interact [21]. Kovasznay indicates that if the disturbance wavelength is on the order of a millimeter and the domain is on the order of a few centimeters, then the diffusion/interaction terms in the governing equations become negligible [21]. This means that the diffusion of the acoustic, vortical, and entropic fluctuations happens relatively slowly in a wind tunnel environment. This assumption also suggests that the vorticity and entropy fluctuations are essentially flow-fixed [21]. The acoustic wave acts like a pure wave, traveling at the sound speed relative to the fluid.

A freestream disturbance must first pass through a bow shock before it affects a high-speed boundary layer. Disturbances typically interact with a shock in one of four ways:

- As an incident acoustic wave from upstream of the shock
- As an incident entropy wave from upstream of the shock

- As an incident vorticity wave from upstream of the shock
- As an incident acoustic wave propagating from downstream of the shock

Entropy waves and vorticity waves are flow-fixed, meaning that they can only travel with the flow. Thus, they can never impinge on an oblique shock wave from downstream when the flow downstream is supersonic. Acoustic waves, on the other hand, propagate in the flow at the speed of sound in the fluid in all directions. This means that the slowest wavefront of an acoustic disturbance can travel slower than the flow and appear to be moving "backwards" from a flow-fixed reference frame. This disturbance, however, travels "forward" in an inertial reference frame since the flow is moving faster than the sound speed. The acoustic disturbance also does not need to travel along the streamlines. Acoustic disturbances that impinge on the shock from downstream of the shock cannot create disturbances upstream of the shock, due to the nature of supersonic flow.

The Interaction of Disturbances and Shock Waves

When a disturbance interacts with a shock wave, several things may happen:

- The shock distorts as a result of the interaction
- The disturbance is transmitted
- The disturbance is reflected

The distortion of the shock wave is typically very small and very fast. The bow shock may oscillate as it processes the disturbance [23–25]. When a disturbance (vorticity, entropy, sound) is processed by the shock, it can be transmitted as any of the three types of disturbances discussed previously. When entropy waves and pressure waves of equivalent amplitudes pass through a shock, they "transmit" sound waves with similar amplitude [26].

The directions of the transmission and the reflection of the disturbance waves are governed by Snell's Law. This law states that the wave vector perpendicular to the

plane of the shock must be preserved for small plane waves interacting with a shock wave. McKenzie and Westphal provide formulations for the angles of transmission and reflection for the three types of disturbance waves discussed previously [26]. Entropy and vorticity waves will essentially have the same transmission angle. Acoustic plane waves will have two different transmission or reflection angles, corresponding to slow or fast acoustic waves. These angles of transmission and reflection are given relative to the normal to an unperturbed shock. The angle at which the disturbance is incident upon the shock is also of great importance. At some angle, the disturbance cannot be reflected. This angle, called the critical angle or the Brewster angle, is the angle at which the transmission of the disturbance is largest.

The shock through which these disturbances pass amplifies the incident disturbance. For a strong shock, the transmission coefficient of an acoustic disturbance is proportional to the square of the incident Mach number, M_{1n}^2. The transmission coefficient at the critical angle is proportional to the third power of the incident Mach number M_{1n}^3. The acoustic disturbance is typically the strongest disturbance transmitted through the shock [26].

For a blunt hypersonic body, the shock wave is detached. In addition to the generation of the three aforementioned disturbances, the blunt body may generate many other types of disturbances which affect the shock. Reflections and re-reflections may affect the disturbances. Since vorticity and entropy waves are convected with the flow, no body-reflected vorticity and entropy waves are possible. Only acoustic disturbances are reflected from the body. These reflections could attenuate any transmitted disturbances or enhance the transmitted disturbance. If these reflections were between an infinitely flat body and an infinite normal shock, resonance would likely occur. However, this is not the case at the nose of a blunt body. The curvature at the nose of a blunt body is more likely to scatter these sound waves and the curvature of the shock is more likely to focus the waves. Also, the phases of the shock oscillation and of the incoming and outgoing disturbances are such that resonance of the acoustic waves is unlikely to build up [23]. This seems to suggest that blunt

nosetips are less receptive than sharp nosetips. Kara [27] and Balakumar [28] reached a similar conclusion when computing receptivity of hypersonic bodies to incoming acoustic plane waves.

Disturbances Generating Boundary Layer Instabilities

Freestream disturbances passing through the shock and entropy layer become forcing disturbances in the boundary layer through the process of receptivity. These forcing disturbances can excite different modes of oscillation (stable or unstable waves) in the boundary layer. F and S modes are two types of normal modes of oscillation, which are related to the boundary layer instabilities. The normal modes of oscillation are found through an analysis of the linearized Navier-Stokes equations. These modes are referred to as modes 1 and 2 in older literature. The terminology was later changed due to confusion with Mack's first and second modes [29]. As the Reynolds number and angle of attack tend toward 0 (e.g., at the leading edge of a flat plate at zero angle of attack) these modes synchronize with acoustic waves. The acoustic waves and modes are synchronized when their frequencies and wavenumbers match. The F mode is synchronized with the fast acoustic waves and the S mode is synchronized with the slow acoustic waves [29].

The phase speed of mode S increases and approaches, but never matches, the speed of the fluid as the Reynolds number increases. Mode F slows down with increasing Reynolds number. At some point, mode F travels at the same speed as the fluid. Here, the F mode is synchronized with vorticity and entropy waves, making the boundary layer more receptive to freestream turbulence (vorticity) and temperature spottiness (entropy). This type of receptivity can be the dominant mechanism in environments where the freestream acoustic field is very small, as in flight and quiet tunnels [17].

Instabilities in the boundary layer can be excited in several different ways. Depending on the flow conditions, both F and S modes may be unstable or only mode S may be unstable. When only mode S is unstable, two maxima in the growth rate

of this mode occur. The low-frequency maximum of mode S corresponds to Mack's first mode. The high-frequency maximum of mode S corresponds to Mack's second mode [29]. Mack's second mode is the instability most likely to cause transition in hypersonic flow for axisymmetric bodies at zero angle of attack [4].

An example of how these methods of excitation cause the unstable mode S to grow is given in Figure 1.1. This example considers a flat plate at zero angle of attack with an adiabatic wall. In this case, mode S is the unstable mode. The different ways in which the unstable mode S can be excited are:

- Option A
    1. The fast acoustic waves excite mode F, the stable mode, at the leading edge.
    2. Intermodal exchange occurs (modes F and S synchronize so that energy transfer can occur between the two modes) and mode S, the unstable mode, is excited.
- Option B
    1. Vorticity and/or entropy waves in the freestream excite stable mode F.
    2. Mode F quickly synchronizes with mode S and intermodal energy exchange occurs.
- Option C
    1. Slow acoustic waves excite unstable mode S at the leading edge.

The unstable mode S can be identified with the Mack modes at sufficient downstream distances. Thus, this mode grows linearly for some distance. Nonlinear growth can occur, depending on the initial amplitude, and transition ensues [17].

Option B is of particular interest in experiments using a laser perturber because it involves the receptivity of entropy waves. Computations of the receptivity coefficient can show the location where an impinging entropy wave may have the largest effect. For example, on a sharp flat plate at Mach 5.9, two local maxima appear for the

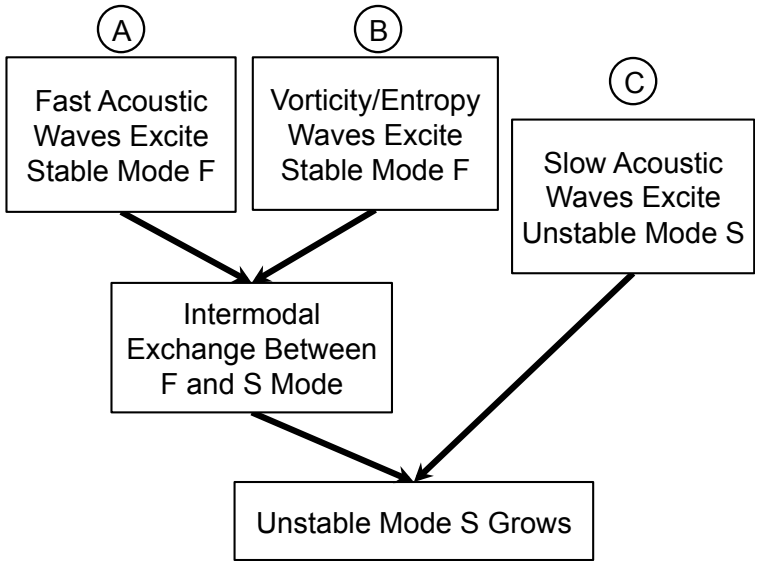

Figure 1.1. Diagram showing different ways instabilities can be excited.

highest receptivity of such a disturbance [17]. One of these maxima occurs outside the boundary layer and one is inside the boundary layer. The maximum that occurs outside the boundary layer can show where entropy waves must intersect the flow to change the excitation of the instabilities.

Several computations exist for the receptivity of acoustic waves in high speed flows. For the purposes of this review, only those involving smooth models are listed. Balakumar has computed the receptivity of plane acoustic waves on a blunted flat plate and a blunted 5-degree cone at Mach-3.5 [30], on flared and straight cones [28], and on a 7-degree sharp cone and wedge at Mach 6 [31]. In these computations, the initial disturbances are generated at the nosetip. The boundary layer also appears to be more receptive to slow acoustic waves than to fast acoustic waves or vortical disturbances [31]. Balakumar shows that the bluntness of a model can affect the initial amplitude of the instability waves. Blunter nosetips will yield smaller initial disturbance amplitudes, while sharper nosetips yield larger initial disturbance amplitudes [28].

1.1.3 Methods of Generating Freestream Disturbances

One of the largest problems in receptivity studies lies in the ability to create well-defined, well-controlled disturbances [15]. First, the disturbance must be repeatable and its amplitude well-controlled. Second, the disturbance must not be so large that the freestream disturbance causes bypass transition. Lastly, the equipment used to generate the upstream disturbance must not alter the overall freestream conditions (e.g., mean background noise level, Mach number, etc.).

Kendall introduced freestream turbulence in a low-turbulence subsonic wind tunnel using an array of jets [32]. This allowed for a variation of freestream turbulence intensity by adjusting the strength of the jets. Another method Kendall employed was an array of metal rods upstream of the test section to introduce turbulence. These methods work well for subsonic tunnels, but may not be applicable to high-speed tunnels. Shock waves and Mach waves are generated by such components in supersonic tunnels.

Kendall also used a two-dimensional perturber, which consisted of two long parallel electrodes, for earlier compressible flow studies [13]. Maslov's flat plate studies at Mach 5.92 used a model upstream of the test model with electrode perturbers mounted to the surface of the upstream model [33]. Two perturber models were used: a two-dimensional perturber similar to that used in Kendall's compressible flow experiments and a localized glow perturber. While this method can be useful, it is not ideal for a facility such as the Boeing/AFOSR Mach-6 Quiet Tunnel (BAM6QT). The space requirements of this apparatus limit the testable Reynolds numbers. Furthermore, the upstream model generates additional unwanted disturbances, which could interfere with the noise studies conducted in the BAM6QT. The geometry of these perturbations is also complex and difficult to characterize, making this perturbation difficult to compare to a computation.

Wiegel and Wlezien did a subsonic study using an acoustic freestream disturbance to investigate non-localized acoustic-roughness receptivity. An acoustic freestream

disturbance was introduced upstream via a speaker system mounted in the walls of their wind tunnel [34]. Similarly, a perturber could be mounted on the nozzle wall of the BAM6QT as in Reference [35]. However, the disturbance propagates differently and produces the same problems with characterization as in Maslov et al.'s flat-plate perturber [33].

Previous experiments at Purdue University performed by Schmisseur [36] and Salyer [37] used a laser-generated freestream perturbation. However, the perturbation did not produce instability waves on a model in the Purdue Quiet Flow Ludwieg Tube (PQFLT), a Mach-4 quiet tunnel that is now decommissioned. Laser perturbations have also been used for studies at TU Braunschweig [38]. Computations by Huang et al. at UCLA have shown the effect of a very small laser-generated thermal disturbance on the boundary layer of a flared cone [39–41].

The concept of using a laser-generated freestream perturbation as a controlled fluid-dynamic disturbance was first tested by McGuire in the early 1990s [42]. These perturbations were created using a high-powered laser and a single lens, which was used to focus the laser beam in a Mach-2.5 tunnel at Purdue University. The focused laser beam photoionizes a small region of air, from which a weak shock wave is emitted. After a short amount of time, this shock wave dissipates and a hot thermal core is left behind. Studies of the characteristics of this perturbation were performed, but it was not until Schmisseur implemented this apparatus for use in studies of a 4:1 elliptic cone that the laser perturber was used for receptivity studies [43]. The laser perturbation was deposited upstream of the test model in the PQFLT, as shown in Figure 1.2.

Creating a Laser-Based Freestream Perturber

Typically, high-speed wind tunnel environments have very low-density air in the freestream. The laser-induced breakdown process is difficult in a low-density environment, because the breakdown threshold of the air is relatively high. The use of

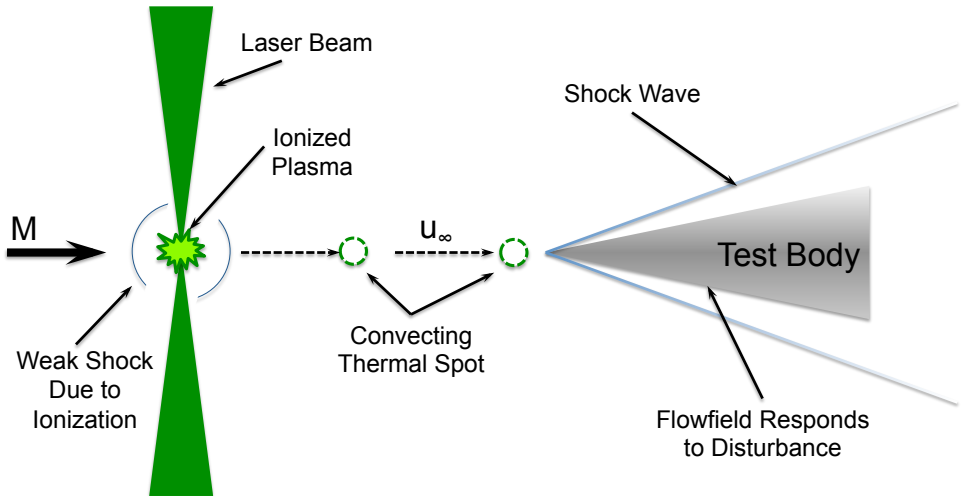

Figure 1.2. Diagram of laser perturbation and elliptic cone model.

the laser-induced perturbation as a controlled freestream disturbance relies on the repeatability of this process. To increase the repeatability, the energy density in the focal region of this laser should be well above the threshold energy density required to cause breakdown. A desirable laser-perturber apparatus has the following characteristics:

- as large an energy density as possible: high energy, smaller focal region, etc.
- as low a cost as possible
- as safe as possible

The concept of using a laser-induced breakdown plasma as a controllable fluid-dynamic disturbance is a relatively recent development, starting in the early 1990s at Purdue University [42]. Laser-induced breakdown plasmas are typically used in spectroscopy, and more recently, as an ignition source for combustible flows. However, these flows are typically at higher pressure than the static pressure seen in a hypersonic wind tunnel environment. These experiments thus provide little insight for the problem of plasma creation in low-pressure and low-density air.

A frequency-doubled (532-nm-wavelength) Nd:YAG laser outputs photons with an energy of 2.33 eV (3.73×10^{-19} J) each. The typical ionization energy of a molecule,

however, is an order of magnitude larger, as detailed in Table 1.1. Thus, one quantum of visible light (a photon) cannot break down air molecules. The high beam intensities and large photon fluxes provided by Q-switched (high-power) lasers allows the deposition of multiple quanta of light to a small region. This allows a molecule within that small region to incur ionization through the absorption of multiple photons.

Table 1.1 Comparison of ionization energies for molecules present in air [44].

Molecule/Atom	**Symbol**	**Ionization Energy (eV)**
Diatomic Nitrogen	N_2	15.581
Diatomic Oxygen	O_2	12.0697
Carbon Dioxide	CO_2	13.777
Water	H_2O	12.621
Argon	Ar	15.759

Gaussian Optics

The ideal optical beam generated by a laser typically has a Gaussian irradiance distribution and propagates like a plane or spherical wave [45]. The propagation of a laser beam may appear as shown in Fig. 1.3. Here, the beam appears to diverge from some point. This divergence angle is small for most laser beams, on the order of tenths of milliradians. The cross-sectional irradiance at a location x along the propagation axis of the beam should represent a two-dimensional Gaussian distribution with a maximum irradiance at the center ($r = 0$). The radius at which the irradiance decays to a value of $1/e^2$ is referred to as the "spot size" ($w(x)$) of the beam. The beam waist is the smallest spot size of a propagating Gaussian beam. The wavefront of the beam is planar at the beam waist. This waist is typically located somewhere within the laser cavity. A second beam waist may be formed if this laser beam is focused.

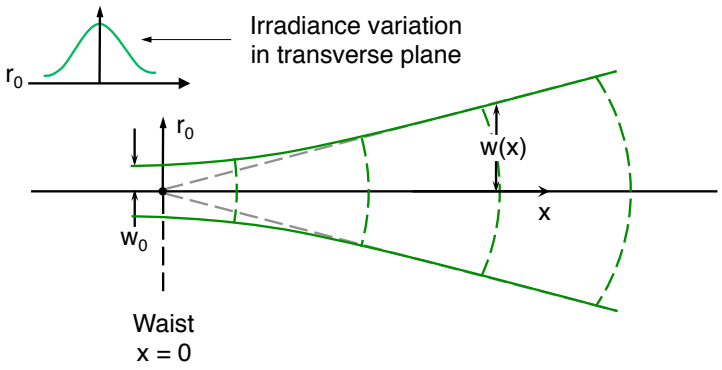

Figure 1.3. Gaussian beam propagating in x direction. Redrawn from Reference [45].

A beam with waist w_{01} located at a distance $\hat{x}_1$ before a focusing lens is shown in Fig. 1.4. The focus radius w_{02} and focus distance from the lens $\hat{x}_2$ can be found. For a beam with $w_{01} \gg w_{02}$, such as in the case where a beam is first expanded before being focused to a small point, w_{02} is approximated as:

$$w_{02} \approxeq \frac{f\lambda}{\pi w_{01}} = \frac{2\lambda}{\pi}\left(\frac{f}{\phi}\right) \tag{1.2}$$

where $\phi = 2w_{01}$ is the diameter of the beam on the lens and f/ϕ is the f-number of the focusing lens.

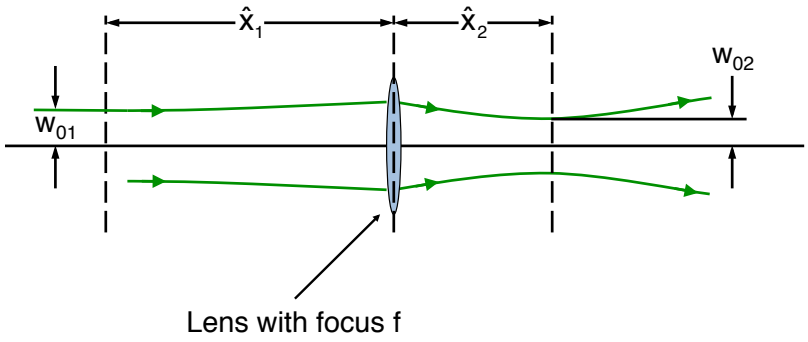

Figure 1.4. Diagram of a focused Gaussian beam. Redrawn from Reference [45].

The fundamental Gaussian mode is the ideal and simplest mode that the beam profile can take. Typically a laser will be made up of multiple modes, which can be Hermite-Gaussian or other higher-order modes. These modes create a beam profile with a pattern of "hot spots" which deviate from the structure of a simple Gaussian distribution. Calculations of beam propagation also become much more difficult as more modes are added. The ideal single-mode case requires the laser to have a Gaussian distribution in irradiance across the beam profile.

The effect of the mode structure of a laser beam on photoionization was investigated and is detailed in Reference [46]. The time-averaged intensity of a focused single-mode (Gaussian) laser reaches a maximum value at the center of the spot. This maximum is about 1.4 times larger than the space-averaged value of the beam. Theoretically, the Gaussian beam profile is the ideal shape for obtaining the tightest focus (smallest w_{02}). However, the cost of having an "enhanced spatial mode" laser, or one that has a beam with a high percentage Gaussian fit, is on the order of $5300 and can reduce pulse energy by about 30% [47]. Multi-mode lasers, on the other hand, can produce interference structures at the focus of a lens system. The intensity of these structures can be as high as two orders of magnitude above the mean intensity of the focus. Theoretically, the high-intensity interference structures have the possibility of aiding multiphoton ionization. However, experiments have shown that the breakdown threshold using a multi-mode laser is not significantly lower than for a single-mode laser [48]. These interference structures can also be time-varying, which can reduce the repeatability of a laser perturber apparatus [43]. It is important to note that no beam will ever be perfectly Gaussian, so these high-intensity interference structures are still possible in near-Gaussian beams. The use of a laser with a near-Gaussian beam profile is still beneficial, despite the added cost. The beam shape is closer to the theoretical beam shape, and thus, more likely to match the beam propagation calculations and to provide more repeatable breakdown.

Ionization

When a high-powered laser is focused in a gas, the following steps occur [49]:

1. Multi-photon absorption occurs to ionize a small number of molecules. Ionization releases a small number of electrons.
2. Nearby molecules in the focal region also ionize due to the cascade ionization process, from the initial release of electrons. This is a less likely process when the density of the medium is low.
3. Laser energy is absorbed and reflected by the plasma created in the gas.
4. The plasma region begins to cool and a shock wave is formed around the plasma. The shock wave propagates out into the surrounding gas and a thermal core is left in the plasma region.

The first three steps in this process usually occur on the order of tens of nanoseconds after a laser pulse is fired. The fourth step is the process of importance to this study of receptivity.

Multiphoton absorption is one method by which atoms can be ionized. This is the mechanism that tends to dominate in low-pressure, low-density environments such as wind tunnels. As an atom absorbs a photon, the atom exists in an excited state for an undetermined amount of time. This time is less than $1/\nu$, where ν is the frequency of light. This time limit is fixed by the Heisenberg uncertainty principle. This process occurs on the order of less than 10^{-14} s for visible and infrared light. If this excited atom absorbs another quanta of light before it decays back to its rest state, the atom moves into an even higher excited state. This second higher state has a lifetime on the order of $1/(2\nu)$. The absorption of more photons can occur in succession until, ultimately, the atom is ionized. A photon flux on the order of about 10^{30} photons/(cm$^2\cdot$ s) causes multiphoton ionization in most common gases [50].

Multiphoton ionization can occur due to the application of a high intensity laser beam. This high-intensity light is also associated with a high-intensity electromagnetic field. If the laser's electric field is strong enough, this can shift and broaden the

allowed atomic energy levels. This effect can cause a smearing of the upper energy levels in an atom to create a quasi-continuum. Intermediate energy levels may also be shifted so they are in resonance with an integer number of light quanta. Thus, fewer quanta of light may cause ionization [50].

Multiphoton ionization is the process that dominates when $p\,\Delta t_{\text{pulse}} \lesssim 10^{-7}$ torr·s, where p denotes the pressure at which ionization is to occur. Theoretically, the dependence of this process on pressure is weak, following a power-law of the form $p^{-1/k}$, where k is an integer greater than 1. This is unlike the pressure dependence of cascade ionization, which follows a stronger p^{-1} law [46,50]. Experiments have shown that the break between absorption-dominated and collision-dominated ionization may occur at different places for different types of lasers. Armstrong et al. were unable to observe the same $p^{-1/k}$ for a nanosecond laser and in fact saw more of a similarity to the p^{-1} law observed in cascade ionization [51].

The photon flux needs to be large to increase the likelihood of multiphoton absorption. The photon flux (F) is given by

$$F = \frac{I_{\text{peak}}}{h\nu} \tag{1.3}$$

where I_{peak} is the peak irradiance of the laser and $h = 6.626068 \times 10^{-34}$ J·s is Planck's constant. An approximation of I_{peak} is given by:

$$I_{\text{peak}} = \frac{E_{\text{pulse}}}{\pi\, w_0^2\, \Delta t_{\text{pulse}}} \tag{1.4}$$

where E_{pulse} is the pulse energy of the laser, w_0 is the radius of the laser beam, and Δt_{pulse} is the pulse width (duration of the laser pulse). From Equations 1.3 and 1.4, it appears that the photon flux can be increased by:

- decreasing the focal radius w_0
- increasing the pulse energy E_{pulse}
- decreasing the pulse width (duration) Δt_{pulse}
- decreasing the frequency of light ν.

The focal radius can be decreased fairly inexpensively using lens systems. Many experiments use this method of increasing photon flux to photoionize air because no modifications need to be made to the laser. Due to the lower freestream static density of the PQFLT, a three-lens optimized system was used to create perturbations in the freestream with a high-powered laser for Schmisseur's experiments [43]. The three lenses allowed for the beam diameter to be expanded before being focused. This decreased the f-number of the system, which in turn decreased the focal volume of the system (Equation 1.2). This decreased focal volume allowed the laser to impart a much larger photon flux and facilitated photoionization in the low-density facility. Schmisseur also found that the merit function for optimization of the perturbation-forming lens system should be based on the RMS radius at the focus. The diffraction-limited, or Airy, radius had little effect on the ability of the optics to form perturbations [43].

It is expensive to increase the pulse energy or to decrease the pulse width to create a higher photon flux. For example, increasing the maximum pulse energy for a Spectra-Physics nanosecond laser by 200 mJ (from 450 mJ to 650 mJ) costs on the order of $4,000 [47]. This is a small cost compared to the price of the laser itself at around $83,000. However, this increase in price is associated with the selection of different models of lasers. Large modifications to the pulse energy are typically not a feasible option for equipment that has already been obtained. Decreasing the pulse width of a nanosecond laser from 7 ns to 2.5 ns can cost on the order of $4800, but also reduces the energy of the pulse by 10% [47]. The hardware associated with this decrease in pulse width is also incompatible with a laser injection seeder. An injection seeder is desired to be able to increase the shot-to-shot repeatability of the laser pulses [42, 43], so this is not a desirable method of increasing the photon flux.

From Equation 1.3, it also appears that the photon flux can be increased by decreasing the frequency of light. However, the breakdown threshold of gases is not a monotonic function with respect to frequency. This is likely due to the characteristics of molecules in different vibrational and rotational energies. The breakdown threshold

of a gas is typically at a maximum somewhere between the visible and ultraviolet portion of the electromagnetic spectrum [46, 52]. There is no simple relationship between the frequency of the photons used and the photon flux, but there are other reasons for changing the frequency of the laser used to induce photoionization. Light in the visible portion of the spectrum is often desired to reduce the number of eye safety hazards. The fundamental wavelength for a Nd:YAG laser is 1064 nm. A harmonic generator crystal and associated electronics need to be added to the laser system to make the beam output light in the visible spectrum. The addition of a harmonic generator is about $10,000, making an increase in frequency fairly costly [47]. This is often considered to be an acceptable cost because this addition increases the safety of the apparatus.

Plasma Development after Ionization

After the air has been broken down via photoionization, a plasma forms near the focus. A nearly-spherical shock wave is generated due to rapid expansion soon after this plasma has formed. This shock wave moves at a much higher speed than that of the plasma front. The shock wave also typically dissipates faster than the high-temperature core of the plasma, especially in a cold wind tunnel environment.

Several experimental studies have noted the formation of an elliptic plasma. This could occur for two major reasons: as part of an inverse Bremsstrahlung process (particles gain kinetic energy by absorbing photons) or due to spherical aberration of the plasma-forming optics [53]. Furthermore, the temporal evolution of the plasma seems to suggest that the plasma shape distorts in the laser direction [46]. These spatial distortions cause the shock wave emitted from the plasma to be more elliptical or pear-like in shape, as observed by Mori [54]. Research by Adelgren et al. also shows the same pear-like shape in the flow up to at least 40 μs after the pulse is deposited in the freestream of a Mach-3.45 flow [49].

Measurements of the characteristics of this plasma in still, quiescent air have been attempted in the past using hot-wire and cold-wire probes [42,43], Rayleigh scattering techniques [49,55], and filtered Rayleigh scattering techniques [55–57]. The large magnitude of the disturbance invalidated the assumptions needed to interpret the probe measurements as quantitative physical properties. Rayleigh scattering and filtered Rayleigh scattering techniques have shown pretty good agreement with Sedov-Taylor theory [58,59] and normal shock relations. A majority of the historical measurements made with optical techniques occur at atmospheric conditions or soon after the production of the plasma. This is probably done to take advantage of the larger signal available in these conditions.

Schmisseur made several measurements of the spanwise and streamwise profile of the laser perturbation in quiet flow at Mach 4 [43]. The streamwise profile of the laser perturbation could not be fully resolved with a constant temperature anemometer (CTA) due to bandwidth limitations. The passage of the thermal core of the laser perturbation was too fast to be accurately measured by the CTA used. The spanwise profile of the perturbation was found to be about 2 mm in width. The amplitudes of the CTA measurements could not be quantified in terms of the physical properties because the thermal disturbance was large.

Filtered Rayleigh scattering measurements of the laser-induced disturbance at Mach 3.45 were primarily used to measure the blast wave radius and to provide a visualization of the development of the laser-induced discharge in air [49]. The technique was used mostly to monitor the shock structure interaction as a complement to schlieren images. The measurements showed that the freestream disturbance may start out ellipsoidal with a weak spherical shock, but the thermal core of the disturbance becomes more spherical starting about 25 μs after formation. A toroidal structure appears between 20–900 μs after the laser disturbance is fired. This corresponds to a vortex ring, which results from the initial asymmetric plasma formation. At about 100 μs, the weak shock wave around the disturbance essentially dissipates.

Glumac et al. studied the effect of pressure on this laser-induced breakdown plasma with a filtered Rayleigh scattering technique in a test chamber [57]. This experiment was used to measure the temperature of the plasma as well as the electron number density of the plasma up to a time of about 1000 ns after the creation of the plasma. They found that at pressures lower than 0.5 atm (50.7 kPa), the plasma propagates both away from and toward the direction of incoming laser light, creating a shape that looks more like a barbell than an ellipse or pear. The size of the plasma decreased as the pressure decreased. The temperature of the plasma across pressures of 0.2–1.0 atm (20.3–101.3 kPa) were within 10% of each other at about 18000 K after 1000 ns. At 400 ns after the plasma was formed, the temperature of the plasma at 0.1 atm (10.1 kPa) was more than 7000 K below the other plasmas. After 400 ns, the lowest tested pressure did not produce a high enough signal to determine a temperature from the spectral lines.

Assuming an ambient temperature of 300 K in their test cell, the density at this lowest condition is about 0.12 kg/m^3, almost three times the freestream density of the Boeing/AFOSR Mach-6 Quiet Tunnel at the maximum quiet condition. This suggests that Glumac's measurement method may not be viable in a hypersonic wind tunnel. Thus, these measurements are helpful but do not directly apply to the lower-density conditions necessary for hypersonic receptivity experiments.

1.1.4 Experiments with Laser-Generated Perturbations

The thermal core was used as a controlled freestream perturbation in quiet Mach-4 flow for Schmisseur's studies with the 4:1 elliptic cone [43]. Measurements with the CTA within the boundary layer showed that the thermal disturbance in the boundary layer has a different shape than that of the freestream disturbance. The duration of the thermal disturbance was also an order of magnitude larger than in the freestream. A small disturbance between the shock and boundary layer was also observed. This

disturbance is thought to have been a wave or shocklet, which may be a result of the freestream disturbance interacting with the model's shock wave.

No clear instability waves were observed with a CTA on the centerline of the elliptic cone. This was suspected to be due to the low Reynolds numbers available in the PQFLT. The freestream unit Reynolds number range through which these measurements were made spanned 3.52– 5.12×10^6/m. The length of the elliptic cone was 127 mm long. Furthermore, the shape of the disturbance in the boundary layer of the elliptic cone appeared to change as the tunnel run progressed. This change was attributed to the changing boundary layer thickness caused by the changing tunnel conditions in the PQFLT. The effect of this perturbation on the crossflow instability, which occurs off-centerline on an elliptic cone, was not tested.

Salyer continued using the laser perturber with experiments on hemispheres in the PQFLT [25]. These measurements were conducted with Kulite pressure transducers and a laser-differential interferometer (LDI). Characteristics of the thermal disturbance such as amplitudes, spatial characteristics, and repeatability were measured with the LDI for varying flow conditions [37]. The thermal disturbance caused oscillations in the subsonic region behind a bow shock, but these oscillations were not self-sustained and quickly decayed. These oscillations persisted longer than the passing of the thermal disturbance. Some evidence of the onset of instabilities may also have been seen in these studies but the data were inconclusive. The induction of a vortex ring caused by the impingement of the thermal disturbance on the hemispherical nose was observed with high-speed schlieren images.

TU Braunschweig created a laser perturber for use with their hypersonic Ludwieg tube (HLB). The HLB is a conventional-noise tunnel, which operates at Mach 6 and has a test section with a 0.5-m diameter, about 5 times the width of the PQFLT. Unlike the Purdue University laser perturber, which mounts the perturbation-forming optics outside the wind tunnel, the TU Braunschweig laser perturber had optics mounted within the tunnel. A single converging lens is used to form perturbations in the HLB and this lens is mounted inside the tunnel within a wedge structure.

Some disturbances are created by the oblique shock from the lens-holder wedge. This can affect the measurements on the model and also requires the placement of the perturbation farther aft, with respect to a model.

Mounting the perturbation-forming optics outside of a tunnel the size of the HLB can be expensive. The test section width requires the beam to be focused over a long distance. Thus, to achieve the same f-number as for a smaller tunnel requires the beam to be expanded proportionally. A larger beam diameter requires a proportionally larger-diameter focusing lens. The diameter of the focusing lens would then be on the order of 200 mm when typical focusing lenses have a diameter of 50.8 mm or less. Such a lens may have to be custom-ground, which would be more expensive.

For experiments in the HLB, the shock wave that emanates from the thermal core is used for a controlled disturbance. The laser-generated perturbation is also placed behind the bow shock from the model. The pressure disturbance spreads faster than the influence of the thermal disturbance. A wave packet was induced by each laser pulse when a laser perturbation was generated close to the surface of the cone [60]. Pressure measurements with a PCB sensor showed axial growth of an instability wave packet of the same frequency as Mack's second mode. The Navier-Stokes computation showed that the frequency and amplitude of the wave packet should have characteristics similar to the naturally-occurring instability. These measurements agreed with the computation [60].

1.1.5 Computations on the Receptivity of Thermal Disturbances

A group from the Moscow Institute of Physics and Technology computed the receptivity of temperature spottiness on a flat plate with a sharp leading edge at Mach 6 [61]. A theory of how these temperature spots excite the F mode in the boundary layer is presented, using a bi-orthogonal eigenfunction decomposition method. Temperature spots generated behind the shock propagate toward the upper boundary layer edge on the flat plate. As these spots propagate into the boundary layer, they

generate the F mode, which eventually synchronizes with the S mode to generate the second mode. A DNS study of the temperature spots behind the shock was also conducted and found to agree well with this theory. When the thermal spots propagate from the freestream and through the bow shock into the boundary layer, the mechanism through which the boundary layer instabilities are generated is different. The passage of the thermal spot through the shock perturbs the shock and excites acoustic waves. These waves generate the S mode within the boundary layer. DNS simulations of this process of propagation yield instability amplitudes almost an order of magnitude higher than when the temperature spots are generated behind the shock.

Computations by Huang et al. involve a circular-arc flared cone at Mach 6, similar to the model used at Purdue University [40,41]. The thermal perturbation placed upstream of this flow has a peak amplitude of 0.01%. This perturbation is several orders of magnitude smaller than the perturbation previously measured by Schmisseur [43]. Huang et al. use a DNS code with a shock-fitting method to compute the receptivity of this thermal perturbation and its effect on the generation of the second-mode disturbance [40]. Computations show that the freestream perturbation generates a first mode instability which quickly decays and then creates a second-mode wave packet in the boundary layer of the flared cone model. The DNS simulation only provides information on the receptivity to very small freestream perturbations, but may still provide some insight to the mechanisms which create boundary layer instabilities.

1.1.6 Nonlinear Growth and Breakdown

The process of transition is not simple and many paths to transition can be taken. Figure 1.5 shows a schematic of some of the different paths to transition that are possible. Variations on this schematic have been adopted since, but the premise is the same. Transition can occur through following any of these paths, depending on the freestream disturbance field.

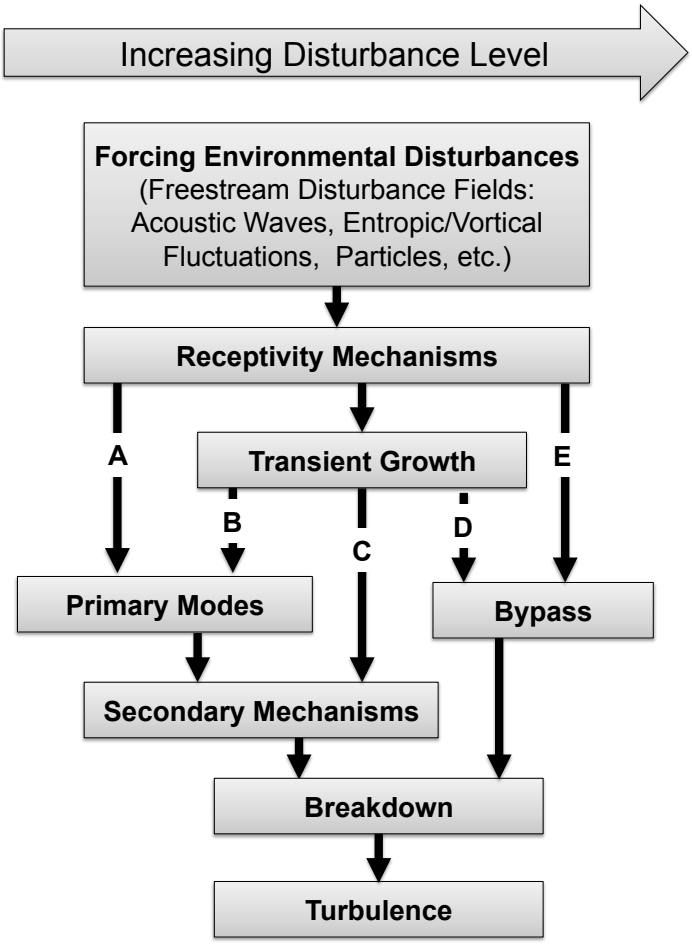

Figure 1.5. Paths to transition, redrawn from Reference [62].

The path most likely for small freestream disturbances is labeled as path A in Figure 1.5. Path A indicates that after the receptivity mechanisms have taken place, the primary modes of instability in the boundary layer are excited. Then, the secondary mechanisms in the boundary layer eventually cause the boundary layer to break down to turbulence. These secondary mechanisms imply the interaction of secondary instabilities and nonlinear transition mechanisms.

Nonlinear growth has been studied extensively in the subsonic regime. Klebanoff studied the generation of three-dimensional instabilities on a flat plate at incompressible speeds [63]. A vibrating ribbon was used to introduce the three-dimensional

disturbances in the flat plate boundary layer, which naturally has a two-dimensional Tollmien-Schlichting instability. The transitional mechanisms prior to breakdown that Klebanoff observed have since been coined K-type breakdown mechanisms [64]. This type of mechanism results from the interaction of a primary and secondary wave pair. The primary wave consists of a high-amplitude two-dimensional wave, like a TS wave. The secondary waves are a pair of lower-amplitude oblique waves with the same frequency as the primary waves. These secondary waves have opposite wave angles. Fundamental breakdown, the K-type breakdown, is characterized by a primary wave that is phase-locked to the oblique waves. This phase-locking allows for energy transfer between these two modes, which causes an amplification of the secondary waves. This mechanism creates lambda-vortices aligned in the streamwise direction on the flat plate boundary layer. When the secondary oblique waves have half the frequency of the primary wave, a subharmonic resonance occurs. The breakdown resulting from this combination of waves is typically referred to as an H-type or N-type breakdown.

The oblique breakdown process was first discovered numerically for a supersonic boundary layer at Mach 1.6 by Fasel et al. [65]. This mechanism uses a wave-vortex triad consisting of a pair of oblique waves and a streamwise vortex to cause breakdown. The oblique waves grow linearly and interact if they have sufficient amplitude. The interaction generates a nonlinear streamwise vortex. The nonlinearity of the vortex causes it to grow rapidly. The oblique waves are always initially generated linearly, but the vortex and higher modes can be generated nonlinearly. Chang and Malik also investigated the oblique breakdown mechanism using modal analysis [66]. The oblique mode breakdown was found to be characterized initially by a checkerboard pattern created by vortices with even azimuthal modes and oblique waves with odd azimuthal modes. These instabilities then reach a large enough amplitude that large waves can be generated by nonlinear interaction. Higher modes are generated by this triad of instabilities through nonlinear interaction and eventually these interactions lead to breakdown and turbulence.

Terwilliger computed the fundamental resonance and oblique breakdown mechanisms for a nearly sharp flared cone using a DNS code [67]. This cone is the same flared cone used at Purdue University. The effects of linear and nonlinear wave packets in the boundary layer for this model were also computed. The DNS uses suction and blowing through an artificial hole to generate different amplitudes of wave packets. Terwilliger observed that the forced response of the flared cone was dominated by the second mode, an axisymmetric wave. As a result, the seeded amplitude of this mode in the simulation was much higher than the amplitudes of the oblique waves.

The linear wave packet remained fairly two dimensional, but the nonlinear wave packet exhibited three-dimensionality in the center at later stages of development. Terwilliger's computations also noted that the nonlinear wave packet experienced saturation in the second mode at around $x = 0.35$ m. Some problems were seen with the domain of the computation for the nonlinear wave packet. Due to its large amplitude, the wave packet spread to the edges of the domain and caused large reflections of the wave packet back into the domain. This issue with the domain affected the computations, so the three-dimensionality observed may only be a product of numerical error.

Sivasubramanian [68] used direct numerical simulations to study the effect of three-dimensional wave packets generated in the boundary layer of a 7-degree cone at Mach 6. Three types of wave packets were studied: a linear wave packet, a weakly nonlinear wave packet, and a strongly nonlinear wave packet. The linear wave packet was dominated by a two-dimensional second mode. An oblique first mode was also observed, but this mode was weak compared to the second mode. The nonlinear wave packets produced a fundamental resonance mechanism to cause breakdown to turbulence. This fundamental resonance mechanism is characterized by the presence of subharmonics. Oblique breakdown mechanisms may have also been present and likely contribute to the breakdown process. The fundamental resonance and oblique breakdown of these large-amplitude wave packets lead to turbulent spots. The fun-

damental breakdown process under these conditions for this particular cone model has a longer transition region than an oblique breakdown process.

1.2 Research Objectives

This research allows for the fundamental study of receptivity: how disturbances enter the boundary layer and cause transition. Data from these experiments can contribute to an amplitude-based model for transition prediction. The development of the amplitude-based model can contribute to the development of design models and computational models. The approach is to create a controlled disturbance in the freestream of a wind tunnel facility with a high-powered laser and then to study the effect of that disturbance on the boundary-layer instabilities.

The objectives of this research project are as follows:

1. Create a well-controlled freestream perturbation with a solid-state laser in the freestream of a wind tunnel facility.
2. Define the amplitude, shape, and velocity of the freestream perturbation.
3. Measure the amplitude, shape, and velocity of the perturbation after it has passed through a shock.
4. Measure the instability amplitudes and frequency content that are induced by the perturbation on a flared cone.
5. Prove that this method of generating perturbations can work for models in the Boeing/AFOSR Mach-6 Quiet Tunnel (BAM6QT) by using the apparatus with a forward-facing cavity model. Compare the cavity response to the perturbations with previous work done at Mach 4.
6. Measure the instability amplitudes that are induced on the flared cone using nosetips of different radii.

CHAPTER 2. FACILITIES AND APPARATUS

2.1 The Boeing/AFOSR Mach-6 Quiet Tunnel (BAM6QT)

The Boeing/AFOSR Mach-6 Quiet Tunnel (BAM6QT) is a unique facility in which it is possible to create a highly-controlled freestream environment (Figure 2.1). It is currently one of three known quiet hypersonic tunnels in the world. The others are the old NASA Langley Mach-6 Quiet Tunnel (M6QT), which is now at Texas A&M University [69], and a Mach-6 quiet tunnel at Peking University [70]. Conventional hypersonic tunnels typically have turbulent boundary layers on the nozzle wall, which radiate acoustic noise into the freestream. This noise can have a significant effect on transition [7, 8]. Quiet-flow facilities are unique in that the freestream pressure fluctuations are less than 0.1 percent. This is achieved by maintaining laminar boundary layers on the nozzle wall.

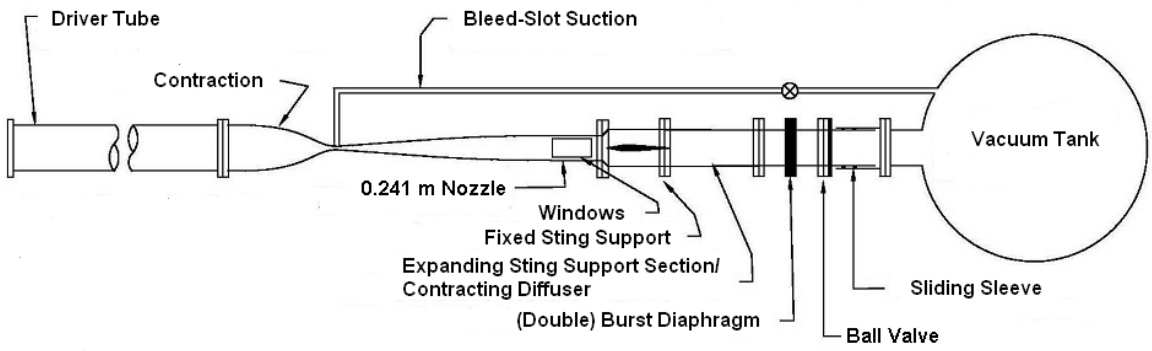

Figure 2.1. Schematic drawing of the Boeing/AFOSR Mach-6 Quiet Tunnel at Purdue University.

The BAM6QT maintains laminar nozzle-wall boundary layers in a number of different ways. An air dryer is used with a Sullair variable-speed compressor to

maintain a low humidity. Typical dewpoint values are on the order of -20 to -10°C. The surface of the nozzle is polished to a mirror finish in order to reduce the likelihood of roughness-induced transition. A series of 1-μm filters is also used to reduce the number of particles in the tunnel. The third and last filter in the series is a 0.01-μm filter. Particles can scratch the throat and cause roughness-induced transition in the nozzle-wall boundary layer. The nozzle length is longer than most in order to suppress the growth of the Görtler instability, a boundary layer instability which develops on concave walls. Finally, a bleed-slot valve is used to suction off the air at the throat. A new boundary layer is formed after this suction valve. To run this tunnel in a "noisy" configuration, for comparison to conventional tunnels, this suction valve can be closed off.

The BAM6QT is a Ludwieg tube facility, where the burst diaphragms are positioned downstream of the test section. Test articles and any optical access must thus be capable of withstanding the full stagnation pressure of the tunnel, with some factor of safety. A pair of burst diaphragms separates the pressurized volume of the driver tube from the vacuum. To run the tunnel, the diaphragms are broken by evacuating the air between the two diaphragms. A shock wave is created by this process, which travels downstream into the vacuum tank. An expansion wave travels upstream and reflects between the end of the driver tube and the entrance to the contraction. The wave reflects about every 0.2 seconds and each reflection creates a stair-step decrease in the initial stagnation conditions.

An example of the decreasing tunnel conditions is shown in Figure 2.2. This figure shows the stagnation pressure in the driver tube ($p_{0,1}$), as measured by a Kulite XTEL-190-500A transducer mounted flush to the driver tube wall near the entrance of the contraction. An isentropic flow assumption is used to determine the stagnation temperature of the flow. The stagnation temperature of the flow at a given point in time is inferred using

$$\frac{p_{0,1i}}{p_{0,1}} = \left(\frac{T_{0,i}}{T_0}\right)^{\frac{\gamma}{\gamma-1}} \tag{2.1}$$

where $T_{0,i}$ is the initial stagnation temperature, $p_{0,1i}$ is the initial stagnation pressure, $p_{0,1}$ is the stagnation pressure at the corresponding moment in time, and γ is the ratio of specific heats. The initial stagnation temperature is measured at the beginning of each run, but the stagnation temperature during the run was never measured independently for the data presented in this dissertation. Previous measurements by Borg validated the use of Equation 2.1 to approximate the stagnation pressure during the run [71].

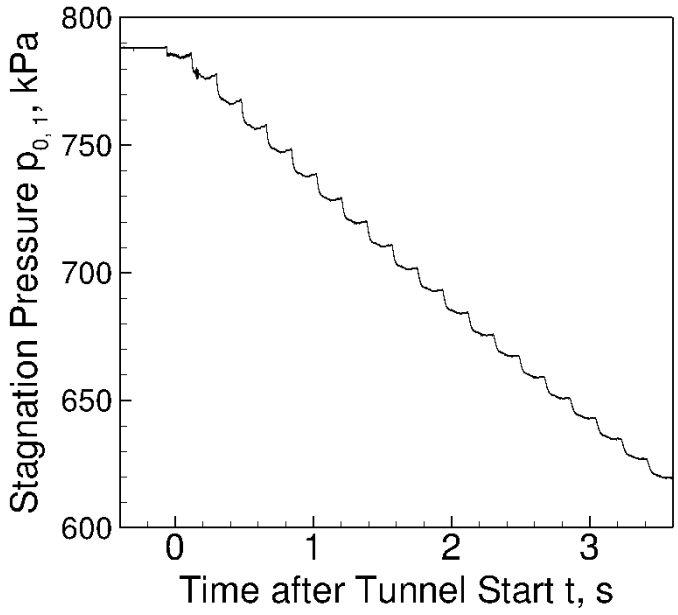

Figure 2.2. Example time trace showing change in stagnation pressure during a run.

Nozzle-wall hot films are used to monitor whether the nozzle-wall boundary layer is quiet. These sensors provide qualitative data on fluctuations in the boundary layer. An array of over 40 different elements was created by Senflex and pasted near the end of the nozzle wall [72]. Typically, one or two of these elements is monitored with a custom Bruhn constant temperature anemometer. These hot films are particularly useful in determining the presence of turbulent spots at high stagnation pressures and boundary layer separation at low stagnation pressures.

The coordinate system used in the tunnel is positioned as shown in Figure 2.3. The $+z$-direction increases with axial distance downstream from the nozzle throat, where $z = 0$. The $+y$-direction increases with vertical distance from the tunnel centerline, where $y = 0$. The horizontal direction is not used for measurements in the BAM6QT. The x-coordinate is used for the model axial coordinate in the context of BAM6QT measurements.

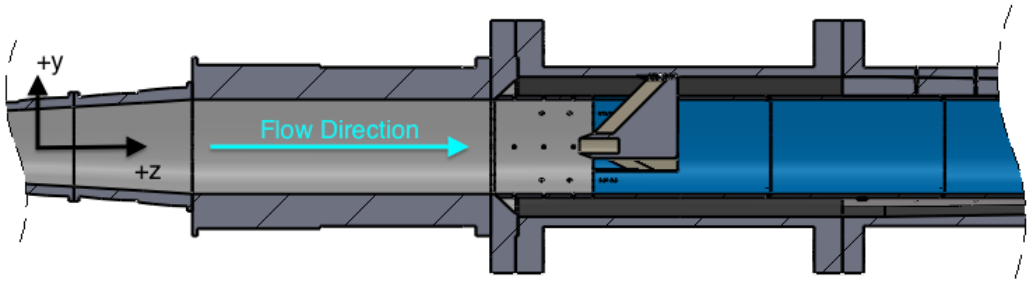

Figure 2.3. Schematic drawing of the Boeing/AFOSR Mach-6 Quiet Tunnel at Purdue University with coordinate system.

2.1.1 Laser Window Inserts

The axisymmetric nozzle for the BAM6QT is more aerodynamically desirable than a two-dimensional nozzle. However, this nozzle shape presents an optical challenge for beam focusing. The BAM6QT was designed with interchangeable tunnel wall inserts with an inside contour matching the nozzle wall geometry. The farthest upstream inserts are referred to as the 3×10-inch windows and four of these are installed in the BAM6QT at all times, positioned 90° apart. One of these inserts contains the Senflex hot-film array, discussed further in Chapter 3. Three of these inserts contain

a separate 63.3-mm-diameter insert centered at $z = 1.924$ m. A laser window can be mounted in this position, as shown in Figure 2.4.

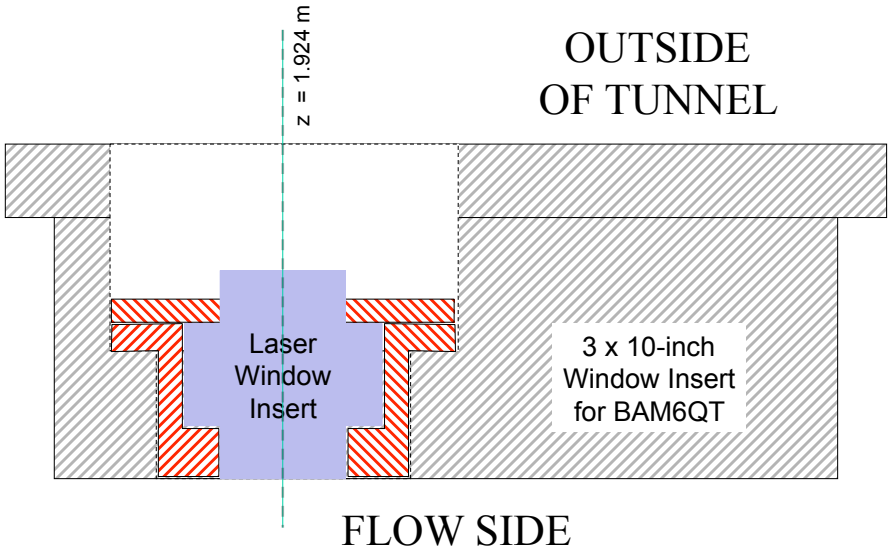

Figure 2.4. Schematic of laser window insert inside 3 × 10-inch BAM6QT insert.

The 17-4PH stainless steel sleeve and clamp sandwich a piece of anti-reflection coated glass, as shown in Figure 2.5. The laser window glass has a shoulder which allows it to be clamped in place by the stainless steel pieces. A small gap between the glass window and stainless steel sleeve exists to allow for some thermal expansion. The window is mounted using Cerrotru, a low-melting point tin-bismuth alloy, and a Dow Corning 734 Flowable RTV silicone. The window mounts into the side of the BAM6QT nozzle, so that the stainless steel sleeve is flush with the inside nozzle contour. The axisymmetric nozzle is still expanding at this location, so the inside surface has two directions of curvature. The windows and window inserts were fabricated by MetroLaser in 2002 as part of a Phase III SBIR project for AEDC and eventually shipped to Purdue as government-furnished equipment. The stainless steel portions of the insert were manufactured by TriModels, Inc. and the glass was ground by B-Con Engineering, Inc. in Ontario, Canada. Later, a back-up window was ground by Optimax Systems, Inc. in Ontario, New York.

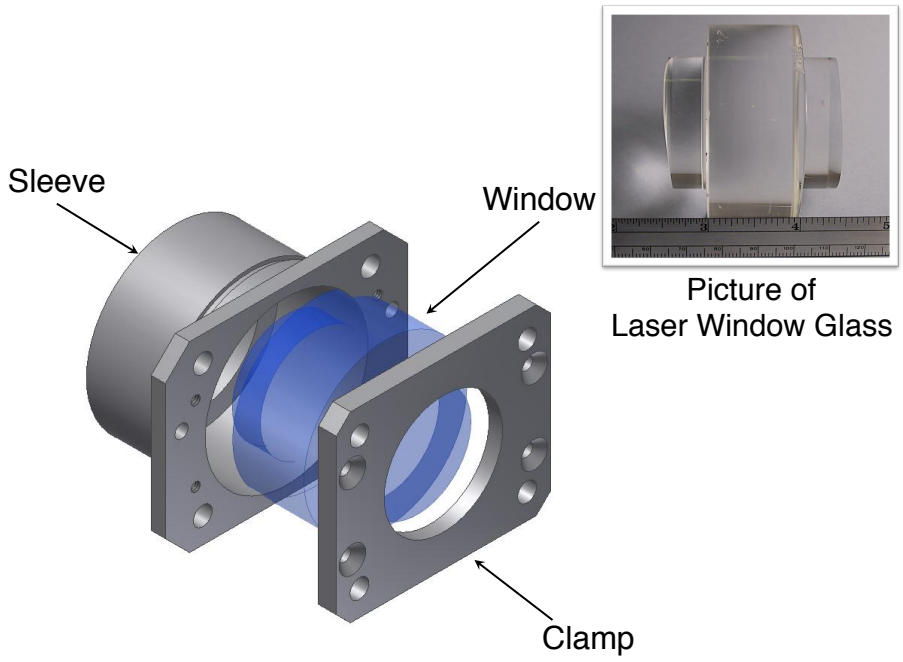

Figure 2.5. CAD model of the laser window inserts used in the BAM6QT. Picture of contoured window glass in inset.

The first of these laser windows is flat. This window is set within the stainless steel insert so that the flat surface lies tangent to the curvature of the nozzle. A slight step exists between the edge of the stainless steel sleeve and the window glass. The schematic in Figure 2.6 shows an example of what this step might look like. The laser window is mounted within the stainless steel sleeve and secured in place with dental plaster. A silicone sealant is then applied to the gap between the laser window glass and the stainless steel sleeve. The use of the silicone sealant between the window glass and sleeve may help to reduce this step, but the main purpose of the silicone is to help pressure-seal the window. A close-up of the flow side of the flat window is shown in Figure 2.7 with different components of the window labeled.

The second window is a contoured window, pictured in Figure 2.8. This close-up picture of the flow side of the contoured window shows how the glass more closely matches the contour of the flow side surface of the nozzle. This window had to

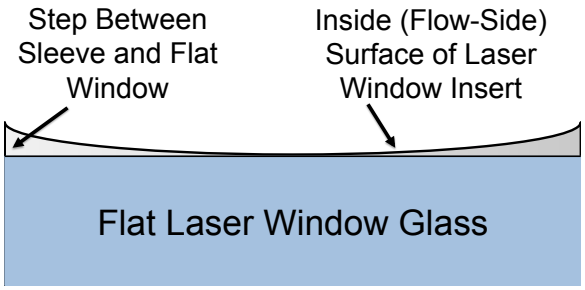

Figure 2.6. Schematic of flat window placement with respect to stainless steel sleeve.

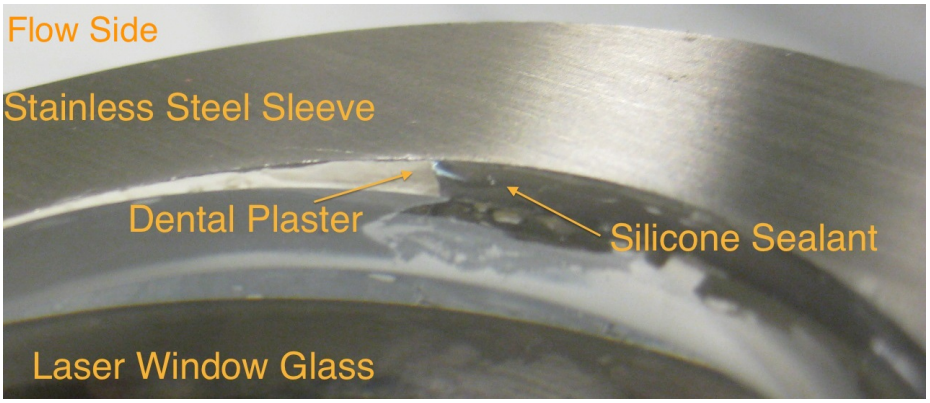

Figure 2.7. Close-up picture of flow-side surface of flat laser window.

be custom ground due to the two surfaces of curvature, which increased the cost. Focusing the laser light through this window is more difficult due to the different surfaces of curvature. This issue is discussed in more detail in Chapter 2.4.

2.1.2 Tektronix Oscilloscopes

All sensor data from the BAM6QT are acquired with Tektronix oscilloscopes. Four of these oscilloscopes are used in the following experiments with the BAM6QT: two DPO7054, one DPO7104, and one TDS7104. The analog bandwidth on the 7104 oscilloscopes is 1 GHz and the analog bandwidth on the 7054 oscilloscopes is 500 MHz. The TDS7104 oscilloscope has a maximum record length of 2 million

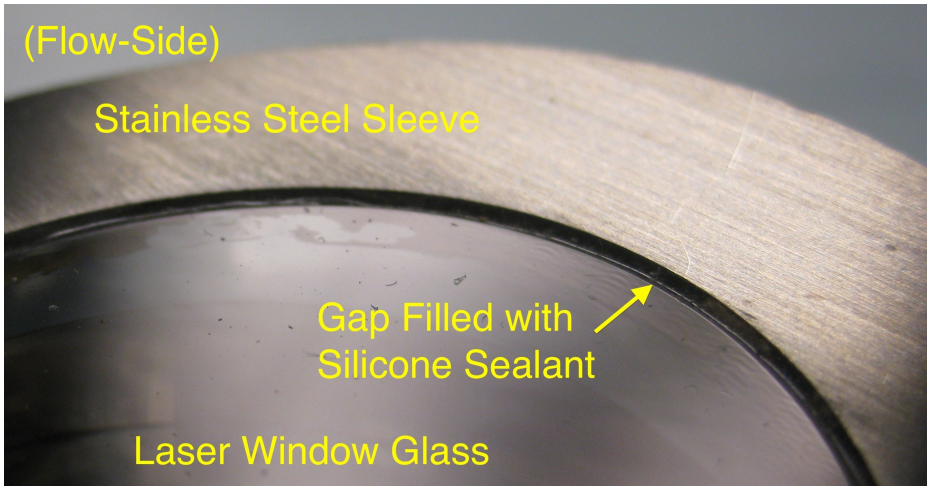

Figure 2.8. Close-up picture of flow-side surface of contoured laser window.

points, so it is typically used to acquire data that can be sampled at lower frequencies. This oscilloscope is typically used to monitor Kulite sensors, linear encoder signals, traverse signals, hot film sensors, or laser sync signals. The DPO oscilloscopes have a maximum 25-million-point record length per channel and can be used to sample signals at a higher rate [73]. These oscilloscopes are used to acquire data for high-bandwidth sensors with up to 1 MHz frequency response. All four oscilloscopes have an 8-bit vertical resolution, but can provide 12-bit resolution using the "Hi-Res" mode. This mode on the oscilloscope samples the data at the maximum rate possible for the model, averages in real time, then saves data at the user-specified sampling rate.

2.1.3 Traverse and Linear Encoder

An Aerotech BMS280-AH-MS-E100H brushless rotary motor and NDriveHL 10-80-A-IO controller is used with the BAM6QT to move probes during a tunnel run. A linear DC power supply (Agilent E3631A-0EM triple-output power supply) is used to power this motor and to reduce electromagnetic noise. A Renishaw RGH22X30F00 series linear encoder is used to determine the position of the traverse during a tun-

nel run. The linear encoder is set to have a calibration of 0.4 mm/V and a zero on the tunnel centerline. More information on the traverse system is available in Reference [74].

2.1.4 Kulite Pressure Transducers

Kulite reports that the frequency response of their XCQ and XCE model sensors is only about 20 kHz [75], but tests by Rotea et al. [76] and later by Beresh et al. [77] indicate that the frequency response may be as much as 20% of the resonant frequency of the sensor diaphragm. This benchmark implies a flat frequency response of up to 50–60 kHz for the sensors used in these experiments. The screens available for these pressure transducers also have some effect on the sensor frequency response. All of the experiments in this dissertation use only B-screen transducers, which further reduces the frequency response of the sensor. This trade-off is considered acceptable because a B-screen helps to protect the sensor from particle impact in a forward-facing configuration. Although there are few particles in the BAM6QT, there may still be some small particles that could destroy the sensor.

The diameter of the XCE-062 and XCQ-062 sensor is about 1.59 mm. These two models of sensor are essentially the same, but the XCE model sensor is capable of withstanding higher operating temperatures. Several Kulite XCQ model transducers are mounted in a number of different pitot-style probes. A Kulite XCE model transducer is mounted in a forward-facing cavity model, which is discussed in Chapter 7.

Two types of probes are used to measure freestream disturbances in the BAM6QT: a long pitot-style probe to measure farther upstream (where a model nosetip might be located) and a short pitot-style probe to measure farther downstream (where a model base may be located). The probes are constructed from seamless, type 304 stainless steel tubing. The tubing has a straightness tolerance of about 0.9 mm per meter. An example of a long pitot-style Kulite probe is shown in Figure 2.9. Two types of protective caps are also shown in this figure. The first is simply used in order

to protect the Kulite sensor while the probe is being stored. The second protective cap has a toothpick mounted in the end. This toothpick is used to align the center of the probe head with a laser perturbation. The probe head is positioned on the tunnel centerline by traversing the probe up and down and measuring its position with a precision scale.

Figure 2.9. Picture of long pitot-style Kulite probe with protective caps.

Signals from the Kulite sensors are passed to custom-made signal conditioners. The transducer output is amplified by a gain of 100, using an INA103 instrumentation amplifier chip. This signal is used to determine a DC voltage. The signal is then passed to a high-pass filter with a cutoff frequency of 840 Hz and amplified again by a gain of 100 using another INA103 chip. This portion of the signal is used to measure small AC fluctuations. The pressure transducers are statically calibrated using a Paroscientific Series 740-30A Laboratory Standard with a range of 0–30 psia.

2.1.5 PCB Fast Pressure Transducers

One PCB 132A31 fast pressure transducer is mounted in a short pitot-style probe. This pressure transducer is used to make freestream measurements. The PCB 132A31 sensors can also be mounted in models so that the sensor face is nearly flush with the model surface. These sensors are piezoelectric sensors, which were originally

manufactured as time-of-arrival sensors. However, these sensors have also shown an ability to measure high-frequency pressure fluctuations in hypersonic wind tunnels [12, 78–80]. The sensing element on this sensor is a 0.762-mm square placed arbitrarily on the 3.18-mm-diameter sensor head and covered with a conductive epoxy. The arbitrary placement of the sensing element makes the active sensing area uncertain. The conductive epoxy on the sensor head also aids in the measurement of pressure, according to PCB. The contribution of the response of the epoxy to the signal makes the extent of spatial averaging on this sensor unknown.

The PCB132A31 sensors have a reported frequency response of over 1 MHz. Two types of signal conditioners are used with these sensors: a PCB 482A22 and a PCB 483A02. The sensor output is high-pass filtered through the signal conditioners with a 3-dB cutoff at 11 kHz. These cutoff values mean that the PCB sensor only measures the pressure fluctuations. Thus, the mean pitot pressure must be inferred from the freestream stagnation pressure using the relation for the pressure across a normal shock wave:

$$\frac{p_{0,2}}{p_{0,1}} = \left[\frac{(\gamma+1)M^2}{(\gamma-1)M^2+2}\right]^{\frac{\gamma}{\gamma-1}} \left[\frac{\gamma+1}{2\gamma M^2-\gamma+1}\right] \tag{2.2}$$

where $p_{0,2}$ is the pitot pressure, $p_{0,1}$ is the freestream stagnation condition, $\gamma = 1.4$ is the ratio of specific heats, and M is the freestream Mach number. Calibration of these sensors is not straightforward and work is underway to devise methods of dynamic calibration [77, 81]. Due to the lack of a mean voltage output from these sensors, a static calibration cannot be performed. Thus, the factory-provided calibration is used for these pressure transducers.

2.2 The Probe Calibration Tunnel (PCT)

The Probe Calibration Tunnel (PCT) at the National Aeronautics and Space Administration (NASA) Langley Research Center (LARC) is a conventional blow-down tunnel that is capable of being run continuously. The tunnel can be outfitted with a nominally Mach-3.5 nozzle with an exit diameter of 80 mm. The pressure and temper-

ature of this facility can be varied independently, but the stagnation temperature of the flow was held fixed at 310.5 ± 1.5 K for these experiments. The flow quality of this facility is less well-known than the flow quality of the BAM6QT, because the PCT is typically used for small-scale projects and probe calibrations. Thus, some baseline measurements were made with a hot-wire probe to determine the flow quality of the facility and are reported in Chapter 3.

The long-duration runs of this tunnel allow for very detailed measurements of the freestream laser-generated perturbation. Hot-wire probe measurements and deflectometry measurements can be made easily in this facility. Furthermore, the open-jet configuration of the tunnel allows the hot wires to be shielded from the flow during the start-up and shut-down processes, which is when many wires break. A similar shielding procedure would be difficult to perform during the short run time in the BAM6QT. A probe can be mounted to a probe holder strut, which can traverse in the $\pm x$-direction (horizontally) across the nozzle exit of the PCT (Figure 2.10). Note that unlike the BAM6QT coordinate system, the x-coordinate corresponds to a horizontal spanwise location in the PCT.

2.2.1 National Instruments PXIe-6366 Data Acquisition Card

A LabView program was written to acquire data in the PCT with a PXIe-6366 card. This card is capable of sampling 8 simultaneous analog inputs at up to 2 MHz per channel with 16-bit resolution. Data acquisition can be triggered externally with a digital transistor-transistor logic (TTL) signal. When a pulsed laser is present in the flow, the data acquisition can be synchronized with the firing of the laser. The hot-wire measurements are sampled at 1 MHz in 10,000-sample blocks after each laser pulse. Deflectometry measurements are sampled at 2 MHz for 150 blocks of 10,000 samples. When no laser is used, the data acquisition can be performed in a continuous sampling mode. The baseline flow quality measurements are sampled at 500 kHz for 2 seconds at each survey location.

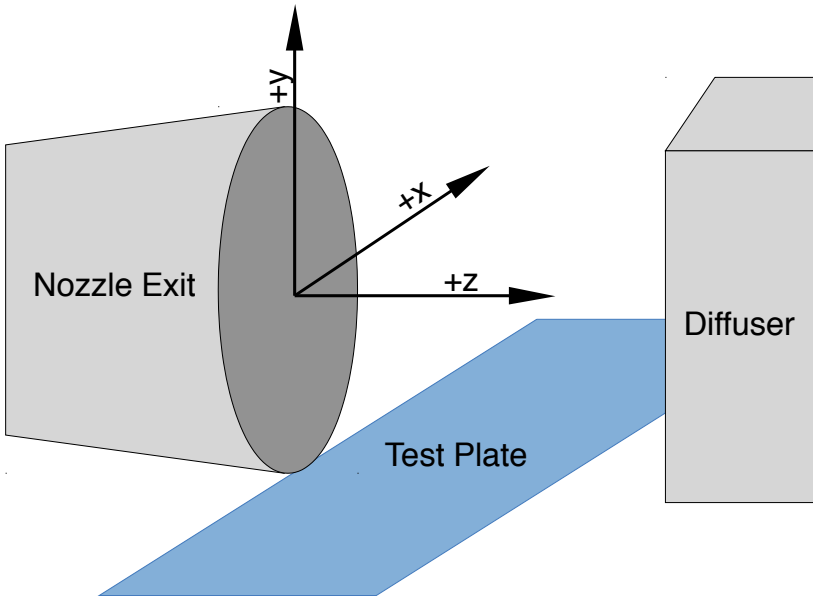

Figure 2.10. Schematic of test section of PCT, showing coordinate system. Flow is in the $+z$-direction.

2.2.2 Signal Conditioners

For the hot-wire measurements, a Precision Filters, Inc. (PFI) 28000 signal conditioning system is used to filter and amplify the output voltage from the CTA. A PFI 28608B Octal Programmable Filter/Amplifier card is used to low-pass filter the CTA signal to provide a mean voltage measurement of the DC-coupled signal. A "LP8F" 8-pole low-pass filter with a 20 Hz cutoff frequency is applied to the DC-coupled signal with this card. The filtered signal is then passed to an Agilent 34401A 6.5-Digit Digital Multimeter, which provides a mean voltage reading. The AC-coupled signal from the CTA is band-pass filtered. A "HP4F" 4-pole high-pass filter with a 100 Hz cutoff frequency is applied to the signal to high-pass the AC-coupled signal. This signal is then low-pass filtered with a "LP8F" 8-pole filter at 200 kHz.

Deflectometry measurements require the use of high-bandwidth photosensors. These sensors have a bandwidth which greatly exceeds the maximum cutoff frequency for the PFI 28000 signal conditioning system. Instead, the deflectometry measure-

ments are passed through a PFI 6611B-B-LPI-6ACDG anti-aliasing filter. This is a 6-pole/6-zero elliptic low-pass filter with a 900 kHz cutoff. The roll-off on this filter is 80 dB per octave.

The acquisition of both types of measurements is handled in the same way. The mean voltage provided by an HP 34401A digital multimeter is sent to the data acquisition system and recorded with the AC signal in a binary file. The mean voltage recorded by the data acquisition system is added back to the recorded AC signal to get a total voltage trace.

2.2.3 Linear Stage

A Newport UTS150CC Mid-Range Travel Linear Stage, controlled by a Newport EPS300 traverse system, is used for measurements in the PCT. This linear stage traverses hot wire probes across the PCT test section in the $\pm x$-direction. In this case, the hot wire probe remains at a constant height, or y-location. Two UTS150CC linear stages are used for deflectometry measurements to probe a two-dimensional image plane aft of the PCT nozzle. In this case, both z- and y-coordinates can change but the x-location is fixed at the conjugate physical plane of the schlieren image plane.

The traverse uses a DC servo motor with a screw-mounted rotary encoder. Electronic noise from the motor can affect measurements made in the PCT, despite running on DC power. To reduce the electronic noise from the motor, the traverse is turned off during data acquisition. The rotary encoder can be used to provide a position readout, which is converted to a length scale by the Labview data acquisition program.

2.2.4 Hot Wire Anemometry

A TSI IFA-100 constant temperature anemometer (CTA) is used with a 5-μm-diameter platinum-plated tungsten wire for hot-wire measurements. The wire aspect

ratio was at least 250 to minimize end-conduction effects. The hot wire is tuned via square-wave injection to a frequency response of about 260 kHz, and the signal is sampled at 1 MHz. A 1:1 bridge is used for these measurements. The overheat ratio, τ, is defined as:

$$\tau = \frac{T_w - \eta T_0}{T_0} \tag{2.3}$$

where T_w is the wire temperature and $\eta = 0.94$ is the wire recovery factor found from previous tests by Kegerise et al. [82]. The overheat ratio used for these tests is between 0.75 and 0.80, to bias the hot wire toward a higher sensitivity to mass flux variation [83].

The coordinate system for the hot-wire measurements is the same as shown in Figure 2.10. The z-coordinate is the streamwise distance from the nozzle exit and x is the horizontal distance from the centerline. The positive-x direction corresponds to a direction toward the laser head and the negative-x direction corresponds to a direction away from the laser head.

A calibration of the wire is performed by holding the probe on the nozzle centerline while varying the stagnation pressure between 48.2–241 kPa. The stagnation temperature is held constant at 310 ± 1.5 K during the calibration to match the run temperature. The hot-wire voltage is sampled at each run condition and an intermediate condition for the calibration. A calibration curve of the form:

$$E_0^2 \left(\frac{T_0}{T_c} \right) = L + M(\rho u)^n \tag{2.4}$$

was assumed as in Reference 82. Here, E_0 is the mean voltage output, $T_c = 310$ K is the nominal calibration temperature, and ρu is the mass flux. This form of King's Law assumes that the temperature fluctuations are fairly small. In addition, this calibration is only applicable at high overheat ratios. The constants L, M, and n are found using a Gauss-Newton nonlinear least-squares method. This algorithm is slow and fairly susceptible to divergence. To reduce the possibility of divergence, the initial guess for the nonlinear least-squares method was as close as possible to the

best fit. The initial guess for this algorithm uses a power-law fit to the data using the form:

$$E_0^2\left(\frac{T_0}{T_c}\right) = M(\rho u)^n \tag{2.5}$$

Calibrations taken for both wires used in this experiment needed at most 5 iterations of the fitting algorithm before the percent difference in the residual changed less than 0.01%.

The hot-wire calibration is used only for freestream mass-flux measurements. The large temperature change across the laser-generated thermal perturbation invalidates the assumptions of the calibration. Thus, measurements of the thermal perturbation with this technique are only qualitative in nature. The lack of calibrated measurements for the thermal perturbation are discussed further in Chapter 4.1.

The hot wire was calibrated in the jet freestream when there was no perturbation in the freestream. Example calibration points and the best fit curve through these points are shown in Figure 2.11. The first hot wire used a calibration curve of

$$E_0^2\left(\frac{T_0}{T_c}\right) = 0.1052 + 0.3236(\rho u)^{0.6069} \tag{2.6}$$

When the probe was accidentally traversed into the beam path, the wire broke and had to be replaced. The second wire was also calibrated in the freestream of the PCT when there were no laser-generated disturbances. The calibration of this second hot wire was

$$E_0^2\left(\frac{T_0}{T_c}\right) = 0.2758 + 0.3073(\rho u)^{0.6254} \tag{2.7}$$

Since the data were taken in an open jet, the inferred mass flux was then normalized by the nominal mass flux, or mass flux at the nozzle exit. The nominal mass flux ($\rho u_{n.e.}$) is then calculated using the isentropic flow relations for a perfect gas to give the equation

$$\rho u_{n.e.} = \frac{p_0}{\sqrt{T_0}}\sqrt{\frac{\gamma}{R}}M\left(1+\frac{\gamma-1}{2}M^2\right)^{-\frac{\gamma+1}{2(\gamma-1)}} \tag{2.8}$$

where p_0 is the stagnation pressure, γ is the ratio of specific heats and assumed to be 1.4, and R is the gas constant $287\,\mathrm{J/(kg\cdot K)}$.

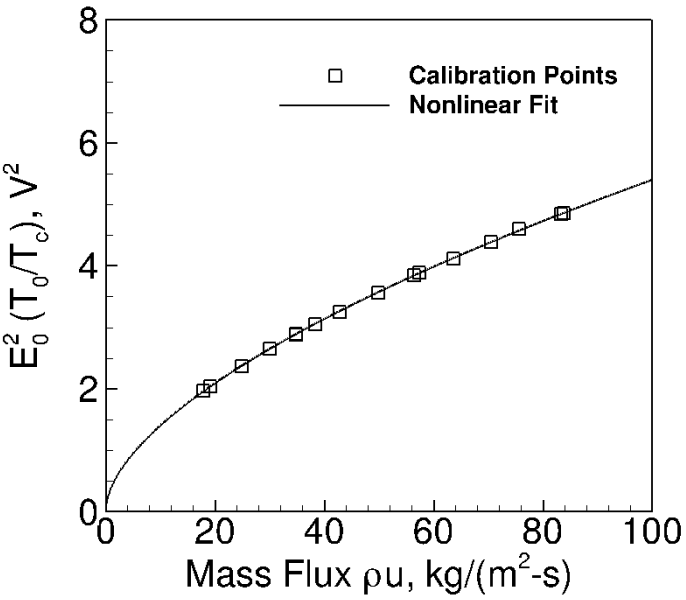

Figure 2.11. Example hot-wire calibration: $E_0^2\,(T_0/T_c) = 0.1052 + 0.3236(\rho u)^{0.6069}$.

2.2.5 Deflectometry

Optical methods typically have a higher frequency response than hot wires. A deflectometry method was used to characterize the laser-generated perturbation in the PCT freestream. The deflectometry method used in this experiment is similar to a method was first proposed by Davis [84] and later implemented by McIntyre et al. [85]. The method used by McIntyre et al. involves the use of a schlieren system with a continuous light source. In this case, the light source used was a xenon arc lamp. Variations in the light intensity and in the room temperature are accounted for by referencing measurements taken within the flow field to one taken outside of the flow field. Fiber optic cables can be made to traverse the schlieren image. These fiber optic cables can be connected to photomultiplier tubes in order to convert the illumination levels at a point on the schlieren image to an analog signal.

The schlieren system used in the present experiment uses a Toepler Z-type setup, as shown in Figure 2.12. The continuous light source used is a xenon arc lamp (1 in Figure 2.12). This light source is placed at the focus of a parabolic mirror with a

50-inch focus (2), which collimates the light and directs it toward a flat mirror (3). The light then is reflected off of the flat mirror through the test section. On the other side of the test section, the light beams are reflected off of another flat mirror (4) to another parabolic mirror (5), which refocuses the image of the light source. Due to spatial constraints on the available optical benches in the facility, the light path had to be folded once more, using a flat mirror (6) before being passed to the knife edge (7). The knife edge is oriented horizontally to make the measurements sensitive to flow-normal density gradients. The image was then split with a 50/50 beamsplitter (8) immediately after the knife edge to allow for simultaneous measurements at two different locations on the schlieren image. The two images are referred to as a "reference" image (11) and a "probe" image (9) to indicate the types of measurements made in each image. Two separate 200-μm fiber optic cables and photosensors were used to probe the reference image and the probe image.

The probe photosensor used was a Hamamatsu HC124-01 photomultiplier tube with a frequency response of 8 MHz. This high frequency response was expected to provide the necessary resolution to show the streamwise extent of the perturbation. The probe fiber optic was traversed across the schlieren image projected onto the traversing image plane. The reference photosensor used was a Hammamatsu H5784-20 photosensor module with a frequency response of 20 kHz. A higher frequency response was not required for this sensor because it was used only to measure mean values of light intensity.

Calibration of the Photosensors to Measure Deflection

A calibration of the photosensors requires the matching of the deflection of a light beam across the knife edge (light intensity fluctuations) to the voltage output of the photosensor. Light rays are not refracted without the presence of a density gradient. Light rays are refracted by some angle α_y when they pass through a density gradient, which translates to a vertical deflection Δ_y at some image plane. The image of a light

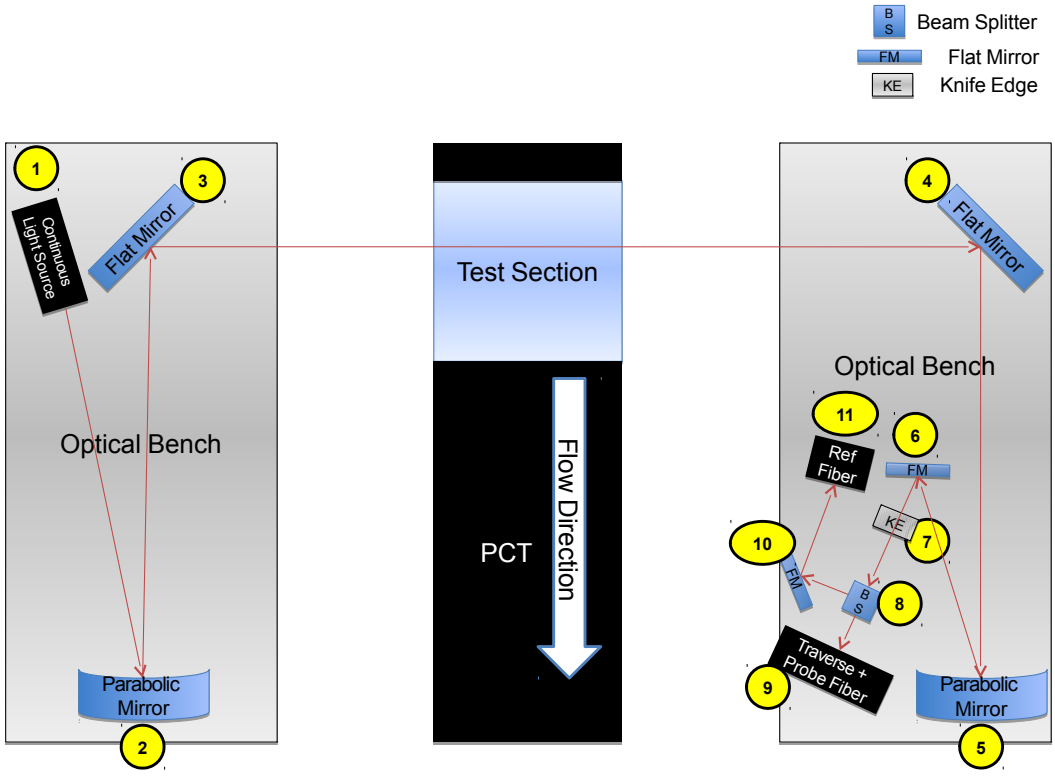

Figure 2.12. Diagram of optical deflectometer used for PCT measurements.

source associated with a single point in the test section theoretically is not deflected when there is no flow in the tunnel. The image of this same light source will deflect vertically by an amount Δ_y related to the density gradient when there is flow. The amount of deflection at the knife edge can be simulated by simply traversing the knife edge across the image of the light source without any flow in the tunnel. The light through the test section is theoretically parallel, so the relation between α_y and Δ_y is given by geometric optics:

$$\tan \alpha_y = \Delta_y / f \tag{2.9}$$

where f is the focal length of the parabolic mirrors [86]. If α_y is small, then $\alpha_y = \Delta_y / f$.

An idealized schematic of the calibration that can be obtained is given in Figure 2.13. This calibration shows typical saturation characteristics. At two knife edge positions, the photosensor detects little or no change in the light intensity. In the lower limit, the light-source image experiences full cutoff and is deflected to a location where the knife edge completely covers the source. In the upper saturation limit, the light-source image experiences no cutoff and is deflected to a location where the knife edge does not cover any portion of the source. A real calibration will show a rounding of the corners near the saturation limits due to diffraction from the fiber optics used.

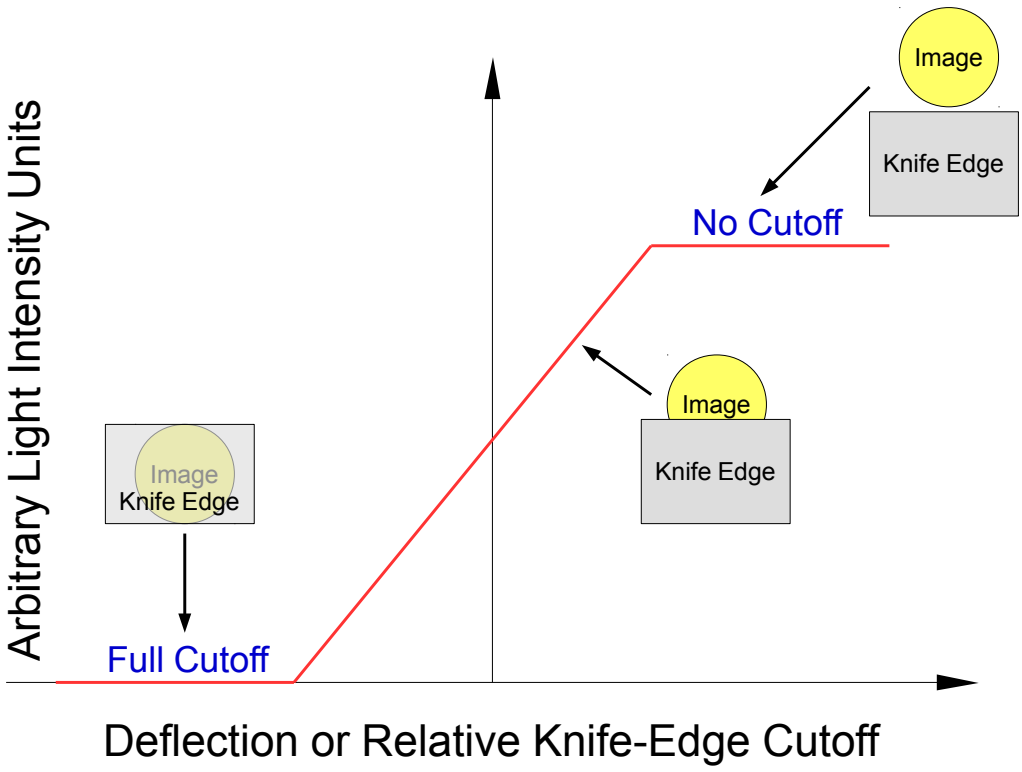

Figure 2.13. Schematic of an ideal calibration for a photosensor.

Non-Uniformity in the Schlieren Image Plane

Non-uniform illumination on the schlieren image plane can affect density-gradient measurements. The sources of these non-uniformities can come from the flow-induced changes to light intensity, which is what this technique tries to measure. The non-uniformities that are caused by the setup are of greater concern, because they may introduce unnecessary uncertainty into the deflectometry measurements. The light source may not be spatially or temporally uniform, which may cause measurement bias depending on the measurement time and location. The ambient room temperature may also change significantly throughout the course of a run or throughout the course of a day. The ambient room temperature changes have a tendency to produce thermal shift in the schlieren optics and could cause drift in the cutoff position of the knife edge.

Reference measurements are taken on the reference image with a stationary fiber to account for small fluctuations in light intensity and ambient temperature. The reference sensor has a frequency response of 20 kHz and a peak in sensitivity at 630 nm. Only the mean voltage was used from this sensor. The reference sensor (a Hammamatsu H5784-20) is placed so that it monitors a region of the schlieren image where there is no flow. This positioning helps to track gross fluctuations in the intensity of the light source as well as fluctuations due to changes in the ambient conditions without being affected by density gradients in the flow field. This positioning does not necessarily account for the spatial non-uniformity of the light source.

To account for spatial non-uniformity, a calibration of the probe sensor can be performed for each of the measurement locations. Example calibrations at various (z, y) stations in the PCT are shown in Figure 2.14. The calibration process is time consuming, however, and can take up to 20 minutes for each measurement location. A closer look at Figure 2.14 shows that the shape of the calibration curve for each of the measurement stations is similar in shape. The maximum voltage appears to

decrease with the z-location of the calibration, but the decrease is not systematic. A position of (50, 0) mm is very close to the center of the test section image while (130, 0) mm corresponds to the edge of the image plane, near the diffuser. This variation in maximum voltage is likely related to the variation in light intensity at the light source, which may be brighter in the center than at the edges of the image plane.

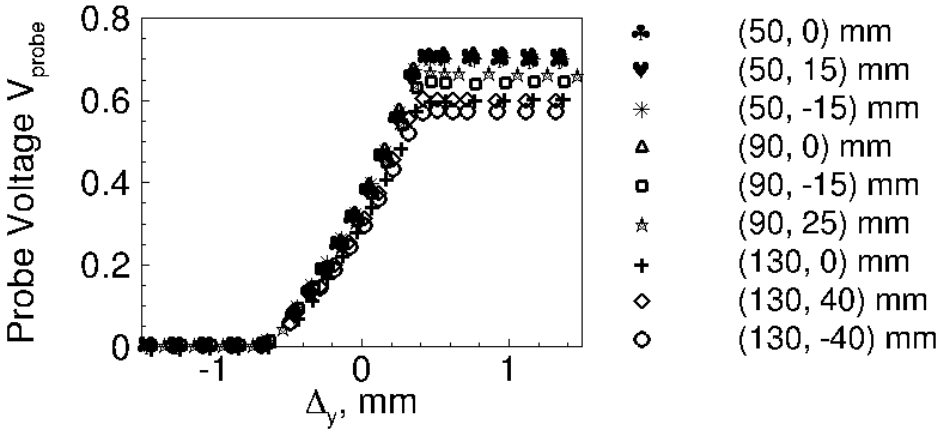

Figure 2.14. Example calibrations for the raw probe sensor voltage at various stations.

Figure 2.15 shows that the calibrations take on the same shape when they are normalized by the no-cutoff voltage (the voltage when the knife edge is traversed out of the schlieren beam path). This similarity in the calibrations allows for a simplification of the spatial calibration process. First, the spatial non-uniformity is taken into account by first taking a survey of the yz-plane with no flow and with the knife edge in a no-cutoff position. This action essentially maps out the spatial non-uniformity of the light source for each of the survey points. Then, the calibration of the probe and reference sensors is performed at a single location with no flow and the knife edge traversing across the image of the light source. The calibration can then be normalized to produce a calibration similar to Figure 2.15.

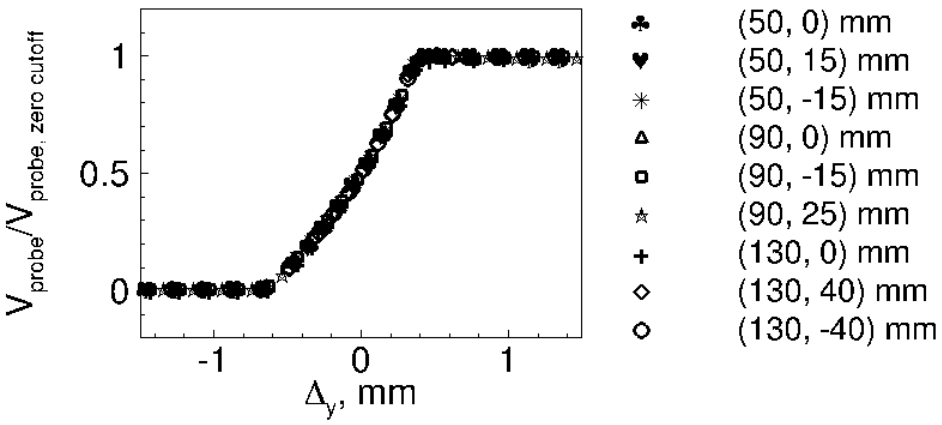

Figure 2.15. Example calibrations for the normalized probe sensor voltage at various stations.

Derivation of Index of Refraction from Deflection Measurements

The deflection measured by the photosensors at a given point is the result of an integration across the perturbation. A derivation of the exact equations to obtain the index of refraction from deflection measurements was formed by Kogelschatz et al. [87]. Variables used in the derivation are shown in the diagram in Figure 2.16. This figure shows a medium or object with radius R, looking down the axis of symmetry. The light beam passes from left to right through the medium or object at a height y above the centerline. The light beam path is denoted by a vector r. On the other side of the medium or object, the light beam is deflected by an angle α. The index of refraction of the medium is given by $n(r)$ and the index of refraction outside the medium is given by n_0.

The only assumptions used in the derivation of the inverse Abel transform include:

1. The medium being measured has cylindrical symmetry (is axisymmetric).
2. The index of refraction n is continuous and its derivative $\frac{dn}{dr}$ is a piecewise continuous function.
3. The index of refraction is constant outside of some radius R.
4. The derivative of the quantity $r \cdot n$ is positive within the radius R.

The first assumption of axisymmetry works for a perturbation in the freestream. Previous measurements [37, 43] show that this assumption is likely true. However, for laser-generated perturbations that are similar in shape to those seen by Mori et al. [54], this assumption would not hold. The second assumption that the index of refraction is continuous and that its derivative is piecewise continuous requires that the region of interest does not include any shocks. The third assumption that the index of refraction is constant (n_0) outside of R is true in that the freestream index of refraction should not change far away from the perturbation. The last assumption is not particularly straightforward. This assumption requires that the quantity $r \cdot n$ be a monotonically increasing function as r increases from 0 to R, which is true for most plasmas.

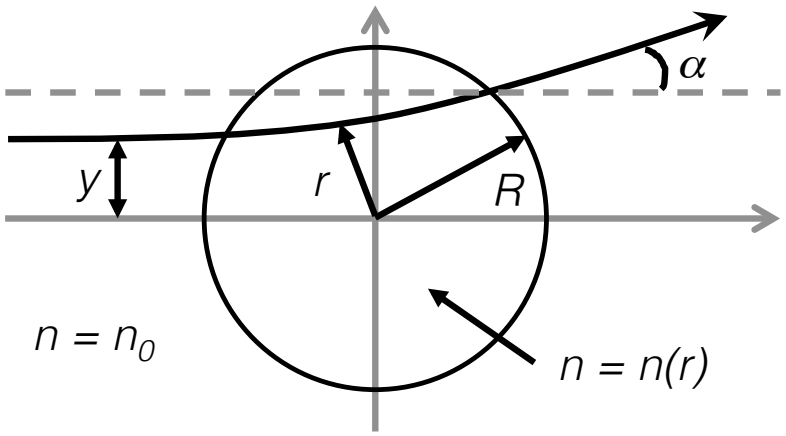

Figure 2.16. Diagram of variables used in Kogelschatz et al. derivation of Abel transform for a medium with cylindrical symmetry. [87]

The derived equations for the inverse Abel transform can be parameterized by a value s. This parameter s is related to the quantities of distance from the centerline r, the index of refraction n, and the freestream index of refraction n_0 using:

$$s = \frac{r \cdot n(r)}{n_0}. \tag{2.10}$$

The inverse Abel transform is then written as:

$$\phi(s) = \frac{1}{\pi}\int_s^R \frac{\alpha(y)}{\sqrt{y^2 - s^2}} dy \tag{2.11}$$

$$n(s) = n_0 \exp[-\phi(s)] \tag{2.12}$$

$$r(s) = s \exp[\phi(s)] \tag{2.13}$$

where $\alpha(y)$ is the measured angular deflection at each vertical (spanwise) location. When the small-angle assumption is also made, Equations 2.12 and 2.13 simplify to:

$$r(s) \approx s \tag{2.14}$$

$$n(s) \approx n(r) \approx n_0 \exp[-\phi(r)] \approx n_0[1 - \phi(r)] \tag{2.15}$$

Conversion of Index of Refraction to Density

The index of refraction can be converted to a density via the Gladstone-Dale relation if the number of free electrons and ions in the perturbation is also assumed to be negligible. The Gladstone-Dale relation is:

$$n - 1 = K\rho \tag{2.16}$$

where n is the index of refraction, $K = 2.259 \times 10^{-4}$ m^3/kg for air, and ρ is the density. The assumption of negligible free electrons and ions may be a poor assumption for a freestream laser-generated perturbation, considering that the lifetime of a laser-generated plasma can be up to several microseconds. The presence of the free electrons and molecular ions can also last for several tens of microseconds. In the PCT, this time scale translates to a distance on the order of about 50 mm downstream of the perturbation generation location.

If instead we assume that the perturbation is a fully-ionized plasma, the index of refraction is a function of the electron density:

$$n - 1 = -4.46 \times 10^{-14} N_e \lambda^2 \tag{2.17}$$

where N_e is the electron density and λ is the wavelength the photodetector measures [87]. As equation 2.17 shows, the electron density provides a negative contribution to the index of refraction. Depending on the time and distance downstream of the perturbation generation location, the presence of electrons may provide an index of refraction with a value of less than 1.0. Upon inspection of equation 2.16, this could cause the calculation of density to be negative, which is non-physical.

2.3 Comparison of Conditions in Both Facilities

Table 2.1 provides a comparison of the conditions in the different tunnels. If the disturbance is estimated to be about 2 mm in diameter (D) [43], then the frequency response required to resolve this perturbation in the BAM6QT is on the order of 1 MHz. Few types of instrumentation can achieve this frequency response. Optical measurement techniques are the primary candidate. Characterization measurements in a facility with a lower freestream velocity require less bandwidth. Thus, it may be desirable first to attempt to characterize the perturbation at a lower velocity, where the required bandwidth is lower. Another advantage of using a facility such as the LaRC PCT is the benefit of longer run times. A long run time allows for detailed measurements that would be difficult to make in a facility such as the BAM6QT.

Table 2.1 A comparison of conditions and disturbance speeds in three tunnels.

	BAM6QT	**PCT**
Nominal Mach Number	6.0	3.5
Stagnation Temperature T_0, K	433	311
Freestream Speed u_∞, m/s (Speed of Thermal Disturbance)	874	660
Frequency Response Required $2u_\infty/D$, kHz	874	660

The perturbation created in different facilities with different equipment may not be the same. Comparisons of the measurements made in the BAM6QT and PCT are required. To compare the measurements in these different facilities, the freestream static density in each facility is matched. The mechanism of generating perturbations in the freestream involves laser-induced breakdown of air. This process is driven by the energy density of the volume of air to be ionized. In this case, it seems best to assume the density drives the generation and development of the freestream perturbation rather than other flow characteristics. The corresponding stagnation pressure and temperature for both tunnels at each of the desired densities is provided in Table 2.2.

Table 2.2 BAM6QT and PCT conditions corresponding to densities where a laser perturbation was created and measured.

Case	**Density**	**BAM6QT** ($M_\infty = 6.0$)		**PCT** ($M_\infty = 3.5$)	
	ρ_∞, **kg/m^3**	p_0, **kPa**	T_0, **K**	p_0, **kPa**	T_0, **K**
BAM6QT Maximum Quiet Pressure	0.049	1170	433	96.7	311
Transitional Boundary Layer in Quiet Flow on a Flared Cone [10]	0.043	1030	433	85.3	311
Intermediate Condition	0.035	827	433	68.2	311
Laminar Boundary Layer in Quiet Flow on a Flared Cone [10]	0.026	621	433	51.2	311

2.4 The Laser Perturber

The laser perturber apparatus is similar to the system developed in the 1990s by Schmisseur [43] and Salyer [25]. It consists of a high-powered Nd:YAG laser, which is focused down to a small focal volume. The increased energy density in the focal region causes photoionization of the air. The plasma that is created during photoionization quickly cools and a weak shock wave propagates from this thermal core. This process is detailed in several references, including References [50, 52, 88]. The weak shock wave dissipates and the thermal perturbation persists to interact with downstream models or probes. A schematic of the structure of this perturbation is provided in Figure 2.17. The thermal core and shock wave should ideally be spherical.

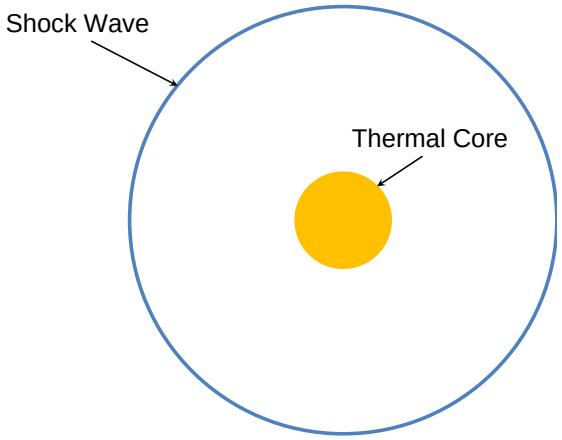

Figure 2.17. Schematic of the composition of the ideal laser-generated perturbation.

Nd:YAG Laser

The laser available for use with the BAM6QT is a Spectra-Physics GCR-190 with a 4-mm beam diameter. The average pulse energy of this laser is about 270 mJ/pulse. The Spectra-Physics GCR-190 used with the BAM6QT is the same laser used by Schmisseur [43] and Salyer [25]. The laser available for use with the PCT is a Spectra-Physics PIV-400 laser with a 9-mm beam diameter, which is reduced to a 4-mm beam

diameter by an aperture. Although the PIV-400 is a double-pulse laser, only the first pulse is used to generate perturbations in the freestream of the flow. The average pulse energy of this laser is about 250 mJ/pulse. Both lasers are frequency-doubled Nd:YAG lasers, emitting light at 532 nm. These lasers are also both seeded, pulse at 10 Hz, and have a pulse width of about 7 ns.

Forming Optics

The laser-generated perturbation is created by focusing a high-powered laser down to a small volume. The previous optics system designed by Schmisseur [43] for the PQFLT did not have a long enough focal length to be used in the BAM6QT. Thus, a new set of perturbation-forming optics were designed by Collicott using Zemax, an optical design program [89]. The optical system was optimized by minimizing the spot size at the focus. The design used for most of the experiments in this dissertation used three lenses (Figure 2.18):

1. a CVI/Melles-Griot YAN-50.0-10.0 lens to expand the beam diameter
2. a CVI/Melles-Griot YAP-200.0-40.0 lens to approximately collimate the beam
3. a CVI/Melles-Griot YAP-200.0-40.0 lens to focus the beam

The three-lens system decreases the f-number of the optics, which ensures as small a focal volume as possible. A smaller focal volume increases the energy density of the system and allows for perturbations to be made more easily in low-density environments, such as a wind tunnel. The spacing of the lenses is provided in Table 2.3.

The RMS and geometric radius of the focal region was determined using Zemax. The RMS radius was calculated as being 1.25 μm and the geometric radius was calculated as being 2.20 μm. The Airy radius, a diffraction-limited radius, was also calculated in Zemax as being 3.98 μm [90]. This value can also be computed for a Gaussian beam using equation 1.2. Previous studies by Schmisseur indicate that the ideal system has a minimized RMS radius as well as a minimized Airy radius [43].

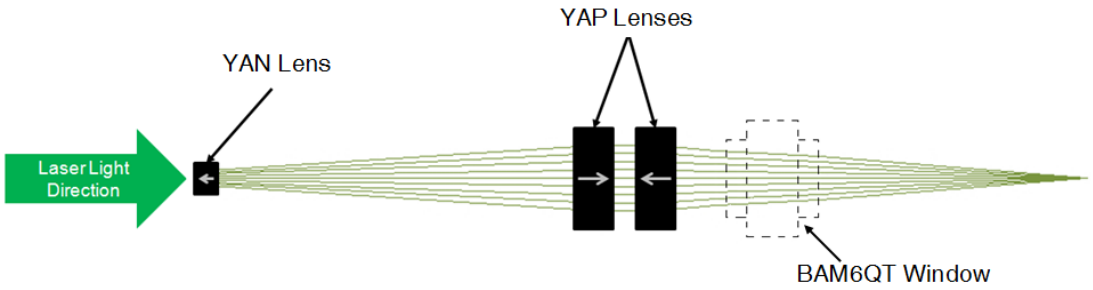

Figure 2.18. Schematic of the optical setup. Laser light propagates from left to right.

Table 2.3 Spacing of focusing optics for laser perturber apparatus.

Optical Element	**Distance to Next Optical Element, mm**
YAN-50.0-10.0	162.9
YAP-200.0-40.0	10.0
YAP-200.0-40.0	20.0
BAM6QT Window (Optional)	118.5
Perturbation	—

Other Forming Optics Designs

The initial design of the optical system included the addition of a tilted cylindrical lens. The purpose of this lens was to attempt to compensate for the change in curvature across the contoured window. The original spacing of these optical elements is provided in Table 2.4. This system created an Airy radius of 9.17 μm and an RMS radius of 0.917 μm. Preliminary bench-top tests at atmospheric pressures with this optical system and contoured window did not produce laser-induced breakdown.

One of the assumptions made to optimize the optical system design is that the beam is a perfect Gaussian shape. Although the laser used for the perturber apparatus has 90-95% fit to Gaussian, this does not preclude the existence of transverse modes.

Table 2.4 Spacing of preliminary focusing optics design for laser perturber apparatus. [89]

Optical Element	**Distance to Next Optical Element, mm**
YAN-50.0-10.0	127.0
SCX-50.8-1000.0-C (tilted 1.33° away from yz-plane of tunnel)	11.7
YAP-200.0-40.0	10.0
YAP-200.0-40.0	20.0
BAM6QT Window (Optional)	118.5
Perturbation	—

The optical elements can also create optical distortion. Chromatic aberration cannot exist, since the laser used in the perturber apparatus is essentially monochromatic. Furthermore, the lenses used are achromats, air-spaced triplets meant to be used for 532- and 1064-nm-wavelength beams. These specialty lenses can also be used to reduce spherical aberration, which may occur due to the shaping of the lenses. Astigmatism, on the other hand, is a significant problem when using the contoured window. Distortion is created along the different surfaces of curvature of this window. The presence of the tilted cylindrical lens can help to reduce this. Unfortunately, the cylindrical lens is not able to reduce the astigmatism enough to create laser-induced breakdown.

Other perturber optics were used for the purposes of bench-top testing and understanding different measurement techniques. The optimized optics used by Schmisseur [43] and Salyer [25] in the PQFLT (the now-decommissioned Mach-4 quiet tunnel) were used briefly for learning purposes and bench-top tests. The RMS radius of the PQFLT optics was 19.22 μm and the f-number was 19.37.

The BAM6QT perturbation-forming optics were also slightly modified for the PCT tests. Hot-wire measurements in the PCT are conducted with only the last YAP-200.0-40.0 lens in the system. This modified PCT system is used because a method of fitting the BAM6QT optics in the PCT had not yet been devised at the time of the tests. The effect of using the modified PCT system is that the beam diameter is reduced and the f-number is decreased. This effectively reduces the converging angle of the focused light and causes the focal region to become elongated and more elliptical. This could cause the breakdown process to require higher energy in order to achieve breakdown and could possibly distort the initial shape of the perturbation. Measurements are typically taken farther downstream, allowing the plasma and thermal perturbation time to equilibrate, so this optical modification may have little effect. Deflectometry tests in the PCT use the BAM6QT optics, so that both tunnels use the same perturbation-forming optics. The only difference between the setup of the BAM6QT optics in the PCT and the BAM6QT optics in the BAM6QT is that the laser window is not used in the PCT. The lack of a thick window at the end of the optics changes the focal length of the system slightly.

General Procedure for Aligning the Laser-Generated Perturbation to the Probes or Models

This section discusses the general procedure by which the laser perturbation is aligned to the probes or the models. Details or modifications of this alignment procedure are discussed further in Chapters 4, 5, 7, 8. Most of these separate experiments did not need to modify this procedure.

A toothpick is used to align the laser-generated perturbation to the probes or models. This method was first used by Schmisseur in the 1990s, when the apparatus was used with hot wires and a 4:1 elliptic cone. The toothpick is typically mounted in either a modified nosetip or a modified probe. A small hole, about 1.5 mm in

diameter and 3 mm in depth, is drilled into the center of this modified nosetip or probe. The toothpick is then press-fit into the end of the modified nosetip or probe.

The laser perturber is then aligned on low power (long pulse mode) so that the focus of the beam lies near the end of the toothpick, as shown in Figure 2.19. The side-to-side alignment is checked by monitoring the focus with respect to the toothpick end in a window located 90° from the laser beam axis. The vertical location of the focus is checked by looking at an angle slightly off of the laser beam axis. After this alignment is completed, the laser is then turned on to a high-powered or Q-switched mode. This change in power creates a laser-generated perturbation. Typically, the first alignment will produce such a perturbation slightly offset from the toothpick end. The alignment is adjusted using translational and rotational stages mounted on an optical bench. Several iterations are made between adjusting the focal region on low power to high power. When the perturbation finally appears to be located at the toothpick end, a loud snap is heard, indicating that the end of the toothpick has been burned or ablated away. The end of the toothpick is checked after the alignment process is finished. The burned or ablated region should be at the center of the toothpick.

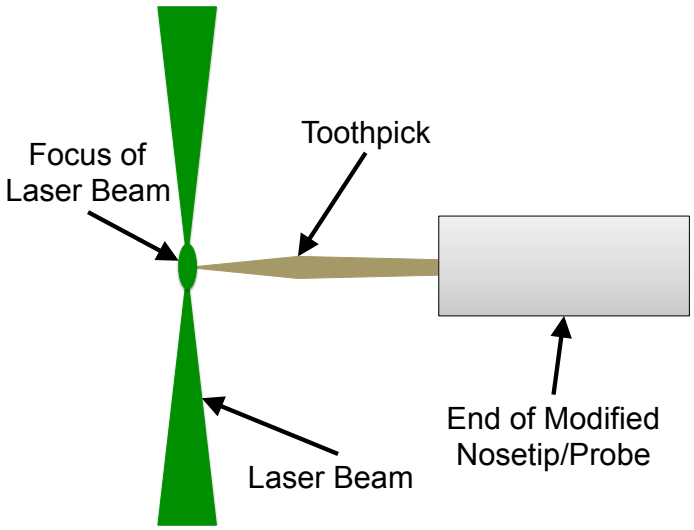

Figure 2.19. Diagram showing the alignment of the laser beam to the modified nosetip or probe.

The forward-facing cavity was the first model on which this alignment method was used and its large nose diameter could interfere with the focusing of the laser light. Thus, initial toothpick lengths used were on the order of about 25 mm to ensure that no laser light would impinge on the model nose. The straightness of the toothpicks had an effect on the alignment of the perturbation to the model. To measure the straightness of the toothpicks, they were mounted on a lathe and the change in displacement of the tip was measured with a dial indicator. Some error in the dial indicator measurements may exist because the dial indicator spring was stiffer than the toothpick. The maximum change in displacement was used to determine a straightness variation. Some of the toothpicks had as much as 2.5 mm variation in straightness for the longer lengths of toothpick. Better selection criteria of toothpicks reduced this variation down to 0.76 mm. Later, toothpick lengths were reduced to as little as 8 mm in total length for the probes and flared cone model. The shorter length of toothpick reduced the variation in straightness down to 0.20 mm.

CHAPTER 3. BASELINE FLOW QUALITY MEASUREMENTS

The freestream disturbances in the facilities are important to measure, as they are part of the disturbance input. This freestream disturbance content provides a necessary component of the amplitude-based method of transition prediction. The premise of this research also requires the generation of a controlled disturbance in a controlled environment. The background freestream disturbances must be small compared to the controlled freestream disturbance.

3.1 Flow Quality of the BAM6QT at Purdue University

The freestream flow quality of the BAM6QT is of particular interest because it is a quiet tunnel. Extensive freestream measurements of the fluctuations in the BAM6QT have been done in the past by Juliano [91] and Steen [92] with pitot-style pressure probes, described in the previous chapter. The maximum quiet stagnation pressure was around $p_{0,i} = 660$ kPa for Juliano's measurements. The maximum quiet stagnation pressure was around $p_{0,i} = 1010$ kPa for Steen's measurements.

Steen observed an increase in the freestream acoustic disturbance level after about 2 seconds of run time under quiet flow [92]. The exact time at which this increase occurred differed depending on the initial stagnation pressure and varied slightly from run to run. This effect was observed in measurements made by Juliano, but was not studied in detail [91]. An increase in noise caused by free convection is also seen in the contraction at around the same time [71]. Whether these two phenomenon are related has yet to be shown.

The nozzle was accidentally scratched in 2010, which temporarily lowered the maximum quiet pressure. The nozzle was eventually repolished, but this setback forced Steen to make many of her quiet flow measurements at lower stagnation pressures.

Since then, the maximum quiet pressure for the BAM6QT has slowly increased over a period of two years to a maximum quiet pressure of about $p_{0,i} = 1170$ kPa. The increase in maximum quiet pressure is suspected to be caused by more researchers running the tunnel at higher pressures to clear the dust out of the nozzle.

Steen calculates the RMS pitot pressure fluctuation using the power spectra, integrating to 50 kHz, then taking the square root. This method differs slightly from the methods used by Juliano and Borg in their determination of RMS fluctuation, which used the full frequency response of the sensor. Juliano and Borg found that the RMS pitot fluctuation in the tunnel was less than 0.05% of the mean. Steen's measurements showed that the acoustic noise in the tunnel is about 0.02% of the mean.

The flow quality of the BAM6QT is also partially monitored for every run by using the Senflex hot-film array discussed in the previous chapter. The hot-film array on the nozzle wall does not provide a quantitative measurement of the freestream noise level. Instead, the array provides a qualitative measurement of the turbulence levels in the nozzle-wall boundary layer.

Small fluctuations measured by this array indicate laminar boundary layers, and thus, less freestream acoustic noise. An example of a hot film measuring a laminar boundary layer on the nozzle wall is shown in Figure 3.1. Turbulent spots are present at $t = 1.5$, 3.6, and 4.0 s. There also appears to be a slight increase in noise in the trace starting at about $t = 3.1$ s. This increase in noise is similar to Steen's observations in her flow quality measurements [92].

Large fluctuations measured by this array indicate turbulent boundary layers, and thus, more freestream acoustic noise. An example of a hot film measuring a turbulent boundary layer on the nozzle wall is shown in Figure 3.2. Although the hot films are uncalibrated, they show a relative increase in noise and no turbulent spots.

Turbulent spots appear on the nozzle wall for a large pressure range. These appear as large spikes, as shown in Figure 3.1. An increase in the freestream stagnation pressure will produce more turbulent spots. Figure 3.3 shows a hot film measuring

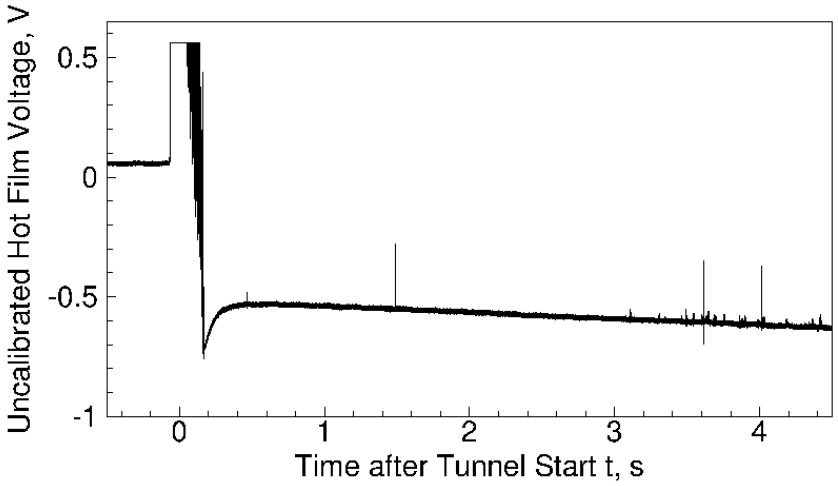

Figure 3.1. Uncalibrated nozzle-wall hot film at $z = 1.880$ m showing a laminar boundary layer. $p_{0,i} = 786.0$ kPa, $T_{0,i} = 433.5$ K, forward-facing cavity model in tunnel, bleed valves open.

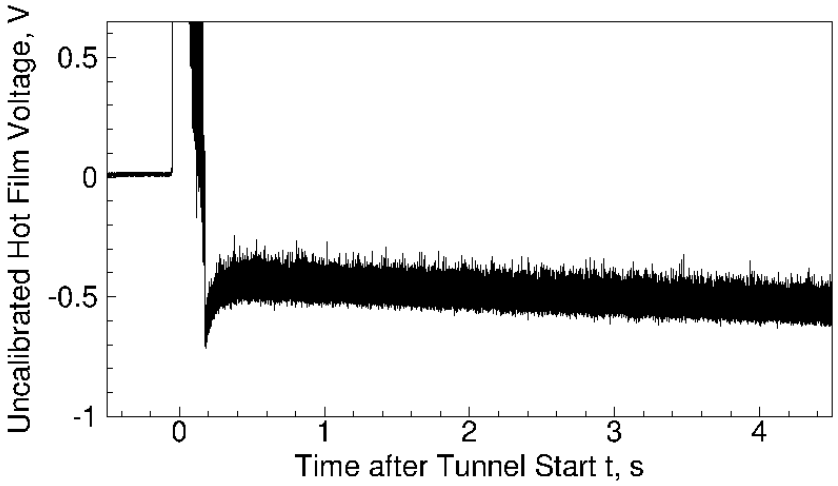

Figure 3.2. Uncalibrated nozzle-wall hot film at $z = 1.892$ m showing a turbulent boundary layer. $p_{0,i} = 634.3$ kPa, $T_{0,i} = 430.2$ K, nearly sharp flared cone model in tunnel, bleed valves closed.

the nozzle-wall boundary layer near the maximum quiet condition at the time of the test (February 9, 2012). The flow takes about 0.2 s to establish in the BAM6QT and the nozzle-wall boundary layer starts out turbulent between 0.2–0.4 s. After 0.4 s, the boundary layer quickly laminarizes, due to a drop in freestream stagnation pressure.

The slight increase in noise at the end of the run appears to start sooner than the laminar boundary layer case shown in Figure 3.1. The change in the relative magnitude of the noise increase is typical for the change in conditions between Figure 3.1 and Figure 3.3 and was seen by Steen [92, Figure 4.13].

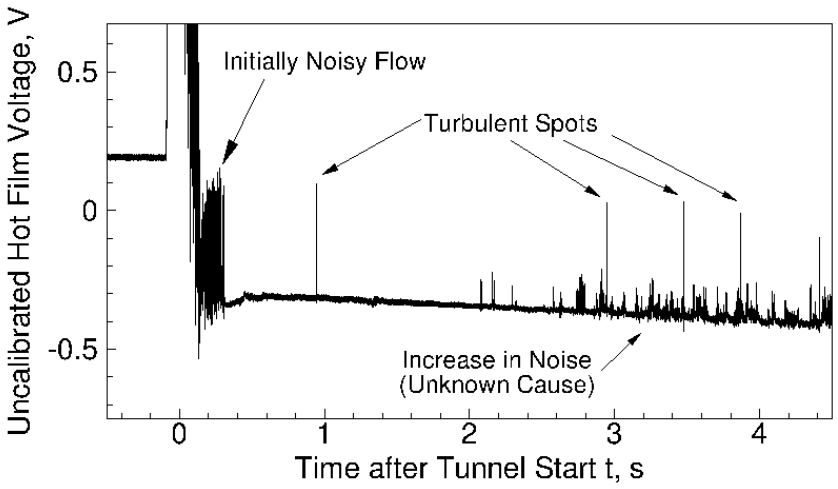

Figure 3.3. Uncalibrated nozzle-wall hot film at $z = 1.880$ m showing a laminar boundary layer with several turbulent spots. Tunnel is near maximum quiet pressure on February 9, 2012. $p_{0,i} = 1181$ kPa, $T_{0,i} = 435.8$ K, forward-facing cavity model in tunnel, bleed valves open.

The hot-film array can also show whether the nozzle-wall boundary layer is separated. Separation of the nozzle-wall boundary layer only occurs for some models, such as the flared cone model. More discussion of the effects of this nozzle-wall separation is given in Chapter 8. Figure 3.4 shows the measurement of a separated nozzle-wall boundary layer for the model used in Chapter 8. The run starts out with laminar flow on the nozzle wall. The nozzle-wall boundary layer separates at about $t = 1.0$ s, and then starts to reattach between $t = 2.4$–3.1 s. At the end of the run, the boundary layer is attached and laminar. This interpretation is supported by measurements on the model. When this effect is observed, the model is typically moved upstream or downstream, or the suction slots in the diffuser section might be adjusted [93].

However, typical efforts were unable to reduce the separation effect on the flared cone model.

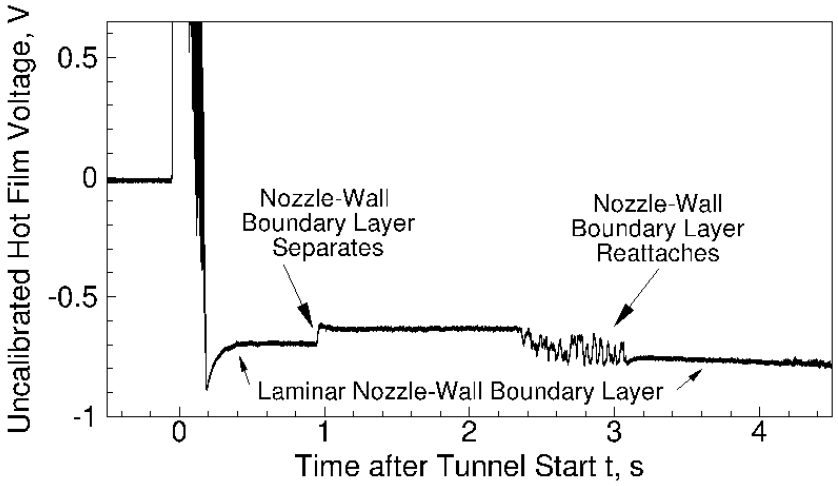

Figure 3.4. Uncalibrated nozzle-wall hot film showing a laminar separated boundary layer. $p_{0,i} = 631.6$ kPa, $T_{0,i} = 436.1$ K, hot film at $z = 1.892$ m, nearly sharp flared cone model in tunnel, bleed valves open.

3.1.1 Effects of the Laser Window Insert

The laser window mounted in the nozzle wall might create disturbances that could propagate into the freestream. Common thermal conductivity values for fused silica are around 1.3 W/(m-K) while stainless steel has a thermal conductivity of about 17 W/(m-K). The difference in the thermal conductivity of the materials can create a temperature gradient after several runs on the nozzle wall when the nozzle begins to heat up. Furthermore, the glass-to-steel joint produces some roughness, which could affect transition characteristics on the nozzle wall or send compression waves into the freestream.

The laser windows discussed in Chapter 2.1.1 were mounted in the 3×10-inch insert located on the top of the tunnel to measure the effect of the laser window on the BAM6QT flow quality. No laser perturbations were created during these

measurements of the baseline flow quality. The configuration of the window with respect to the traverse is shown in Figure 3.5. This configuration allowed the probe to traverse across the path of any Mach waves along the centerplane of the window. The coordinate system used for these noise measurements is also shown in Figure 3.5.

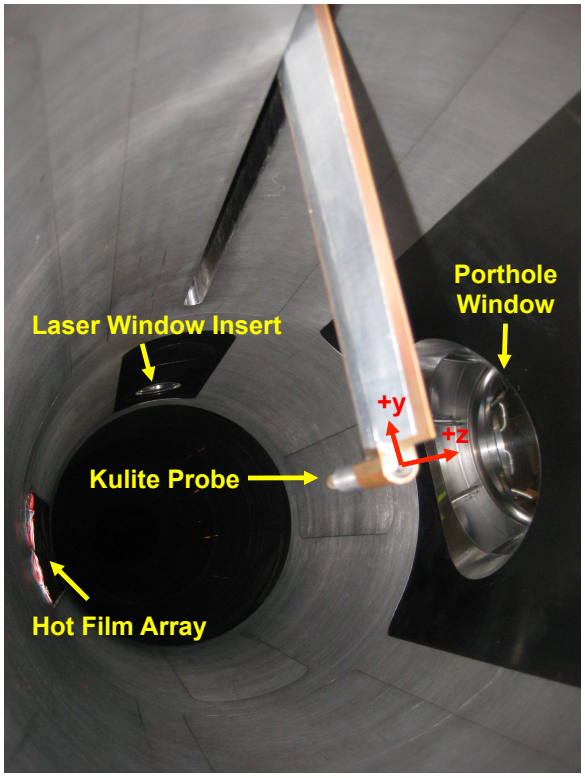

Figure 3.5. Tunnel set-up for freestream disturbance measurements.

Initially, the linear encoder system on the traverse was not functioning. Thus, surveys of the flow were conducted by holding the probe steady at a single location for the entirety of the run. After the linear encoder was fixed, the probe was held steady at each location for a total of 0.2–0.3 seconds before moving to the next location.

The acoustic origin (AO) is the location on the nozzle wall from which noise is radiated to a measurement location. It is estimated by tracing a Mach line from the measurement location to the closest wall. The nozzle flow field is assumed to be inviscid and of constant diameter in order to correlate the acoustic origin of the

noise to the vertical measurement position. This assumption is necessary to make an estimate of the acoustic origin, but is not necessarily accurate. The BAM6QT nozzle has a thick boundary layer on the nozzle wall (a laminar boundary layer has an edge thickness of about 25 mm at $p_0 \approx 620$ kPa [94]) and the radius changes along the nozzle length up to $z = 2.590$ m. The axial location of the acoustic origin is approximated as

$$z_{AO} = z_{\text{probe}} - \frac{R - y}{\tan \mu} \tag{3.1}$$

where z_{probe} is the axial location of the probe with respect to the throat, R is the assumed-constant radius of the tunnel, y is the probe's distance from the tunnel centerline, and μ is the Mach angle.

Figure 3.6 shows the Mach number inferred from Kulite measurements of the stagnation pressure across the test section. The Mach number is calculated from the Rayleigh pitot formula:

$$\frac{p_{0,2}}{p_{0,1}} = \left[\frac{(\gamma+1)\,M_1^2}{(\gamma-1)\,M_1^2+2}\right]^{\frac{\gamma}{\gamma-1}} \left[\frac{\gamma+1}{2\gamma M_1^2-\gamma+1}\right]^{\frac{1}{\gamma-1}} \tag{3.2}$$

This equation is solved numerically using a Newton-Raphson method with the measured pitot pressure ($p_{0,2}$) and the measured stagnation pressure of the driver tube ($p_{0,1}$). The gray shaded area shows the z_{probe} measurement location that has a calculated z_{AO} near the laser window insert. The gray measurement area corresponds to Mach waves propagating from the edges of the contoured stainless steel blank. The blue measurement area corresponds to Mach waves propagating from the window glass. Measurements with the stainless-steel blank in the nozzle wall (filled black circles) and the contoured window (blue open circles) both show a fairly constant Mach number across the test section. These measurements were made with the probes held steady at a single y-location for less than 0.3 s. Fewer measurements were made for the stainless-steel blank due to time limitations. The amount of time each tunnel run takes is up to 1 hour and previous research by Juliano [91] and [92] contain more measurements with the stainless-steel blank. Thus, more measurements were made

with the laser windows because previous measurements with these inserts did not exist.

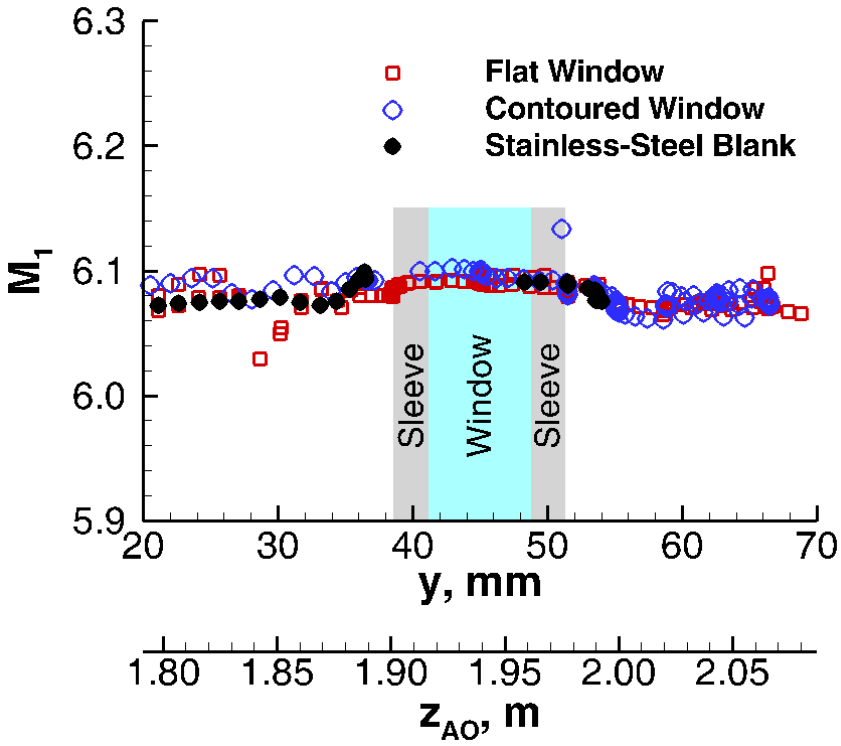

Figure 3.6. Measured Mach number across the test section for different windows and blanks. $z_{\text{probe}} = 2.374$ m.

Measurements taken with the flat window mounted in the nozzle wall (red squares in Figure 3.6) show a slight dip in Mach number at a measurement position of about 30 mm above the centerline of the tunnel. The open red squares show two separate surveys across this region, with the traverse moving in opposite directions. These separate surveys agree with each other, confirming the dip in Mach number. These measurements were taken with $z_{\text{probe}} = 2.374$ m, which corresponds to the aft end of most models in the BAM6QT. Thus, it seems likely that the Mach wave may intersect with the aft end of most models in the BAM6QT.

Using the inviscid acoustic origin estimation (Equation 3.1), this dip does not appear to correspond with the window edges or sleeves. The dip may still be related

to the position of the laser window. The acoustic origin estimate assumes a one-dimensional, inviscid flow and may not capture the real effects of the laser window. Furthermore, the changing nozzle radius is not taken into account in the acoustic origin estimate. Measurements at this location are given by a fairly coarse survey. Further tests need to be conducted to better measure the location of the Mach wave that results from the junction of the flat window and the tunnel wall.

The noise level across the test section was also measured to determine the effect of this Mach wave. The noise levels measured at different vertical positions at $z_{\text{probe}} = 2.374$ m and an initial stagnation pressure of $p_{0,i} \approx 1100$ kPa are shown in Figure 3.7. The probe was held in place for at least 0.3 s for many of these points due to problems with the linear encoder, so there are fewer data points than in Figure 3.6. As expected, the stainless-steel blank shows a low, nearly-constant noise level, regardless of measurement location. For both windows, the noise level is higher for a measurement location that corresponds to an acoustic origin downstream of the window location. This increase in noise was expected for the flat window, but not for the contoured window. Fortunately, this increase in noise does not exceed the quiet flow limit of 0.06% [92] for either window.

Sources of this noise increase were considered. It is possible that there was a bad seal around the contoured window which creates a jet on the nozzle wall during a run. This possibility was checked by putting soapy water around the window while the tunnel was pressurized. Since these windows were subjected to the full stagnation pressure prior to a run, bubbles would form in the soapy water if there was a leak around the window. No bubbles were observed in the soapy water, so it was unlikely that the increase in noise was caused by a bad seal. It is also possible that this increase in noise was due to a shimmering Mach wave. A shimmering Mach wave can be caused by the interaction of disturbances generated by nozzle wall roughness and boundary layer fluctuations [95]. As stated previously, there may also be a difference in temperature between the stainless steel sleeve and the window glass. The cause of this noise increase is unknown and requires further investigation. More efforts were

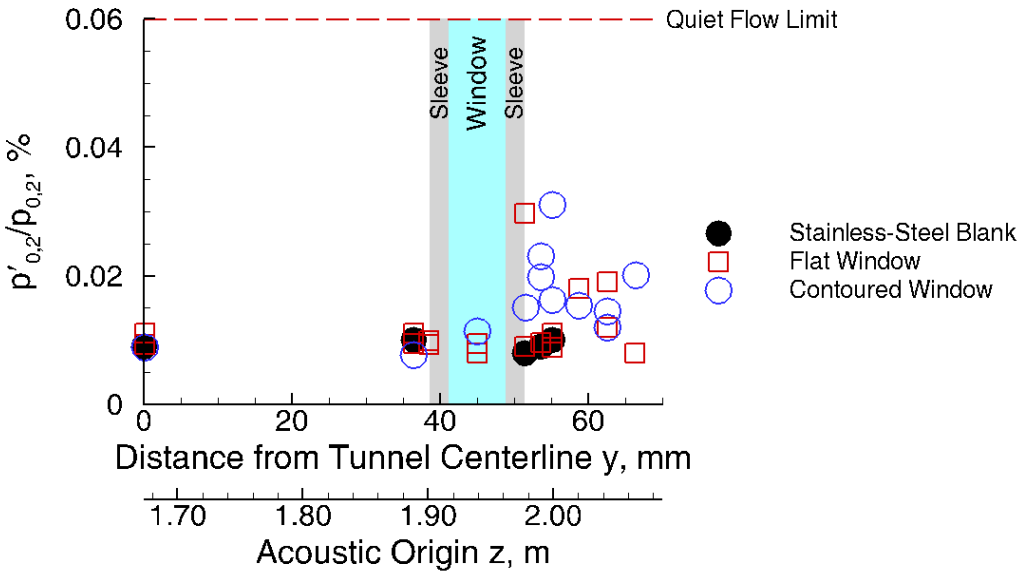

Figure 3.7. Noise measurements showing effects of different window inserts. Probe located at $z_{\text{probe}} = 2.374$ m.

not focused on finding the source because the increase was still less than the quiet flow limit.

3.2 Flow Quality in the NASA LaRC PCT

Hot-wire (mass flux) measurements were made in the PCT to determine the uniformity of the flow. Again, no laser perturbations were created in the freestream for these tests. The hot-wire calibration used is the same as in Figure 2.11. Spanwise surveys ranging from $x = \pm 35$ mm were taken at four different streamwise locations: $z = 0.635$ mm, 31.4 mm, 46.9 mm, and 54.5 mm. Typical operation of the PCT only uses probes placed near the farthest upstream location in the tunnel, with the diffuser placed as close to the nozzle as the probe will allow. The positioning of this diffuser is significant due to the open-jet configuration of the tunnel. For these measurements, the diffuser in the PCT had to be moved farther downstream to accommodate the streamwise positioning of the traverse. As a result, an unsteadiness in the jet was

observed between pressures of about 68 kPa to 207 kPa. The unsteadiness does not exist when the probe is removed from the flow, so this effect is likely due to a shock interaction between the probe and diffuser.

The measured mass flux is normalized by a nominal mass flux, which is the expected mass flux at the nozzle exit, $\rho u_{n.e.}$. The mean mass flux changes with the distance from the nozzle exit due to the open-jet configuration. This value of mass flux is calculated using isentropic flow relations (Equation 2.8). The Mach number in the open jet is slightly lower than the nominal value, at around $M = 3.42$, for locations farther downstream. Plots of the normalized mean mass flux for four survey locations are provided in Figure 3.8. Repeated surveys are marked using dashed lines.

The mean mass flux across the measurement region is fairly uniform at locations spanning from about $x = \pm 20$ mm. The mean mass flux is about the same as the expected nozzle-exit mass flux at all streamwise (z) measurement locations in this region. Between $x = \pm 20$ mm the mean mass flux varies only about 5% from the nominal (nozzle-exit) value. At the two most upstream streamwise surveys ($z = 0.635$ and 31.4 mm), the mass flux varies no more than 2% from the nominal value. At $z = 46.9$ mm, the mean mass flux is consistently higher than the nominal value, varying from 2% to 3% higher than the theoretical mass flux at the nozzle exit for higher stagnation pressures and up to 7% for the lowest tested stagnation pressure. This increase in mass flux may be due to some small entrainment of fluid into the shear layer at the edge of the jet increasing the mass flux. At $z = 54.5$ mm, the higher stagnation pressures again show mass fluxes higher than the nominal value, from about 2–5% higher. However, the lowest stagnation pressure tested shows mass fluxes up to 4% lower than the nominal value. At all but the farthest forward location, the mass flux decreases towards the spanwise edges of the measurement region. The jet is under-expanded, so this decrease likely indicates the effect of the expansion fan. Figure 3.9 shows the same data as in Figure 3.8, but the plots group the spanwise measurements by stagnation pressure instead.

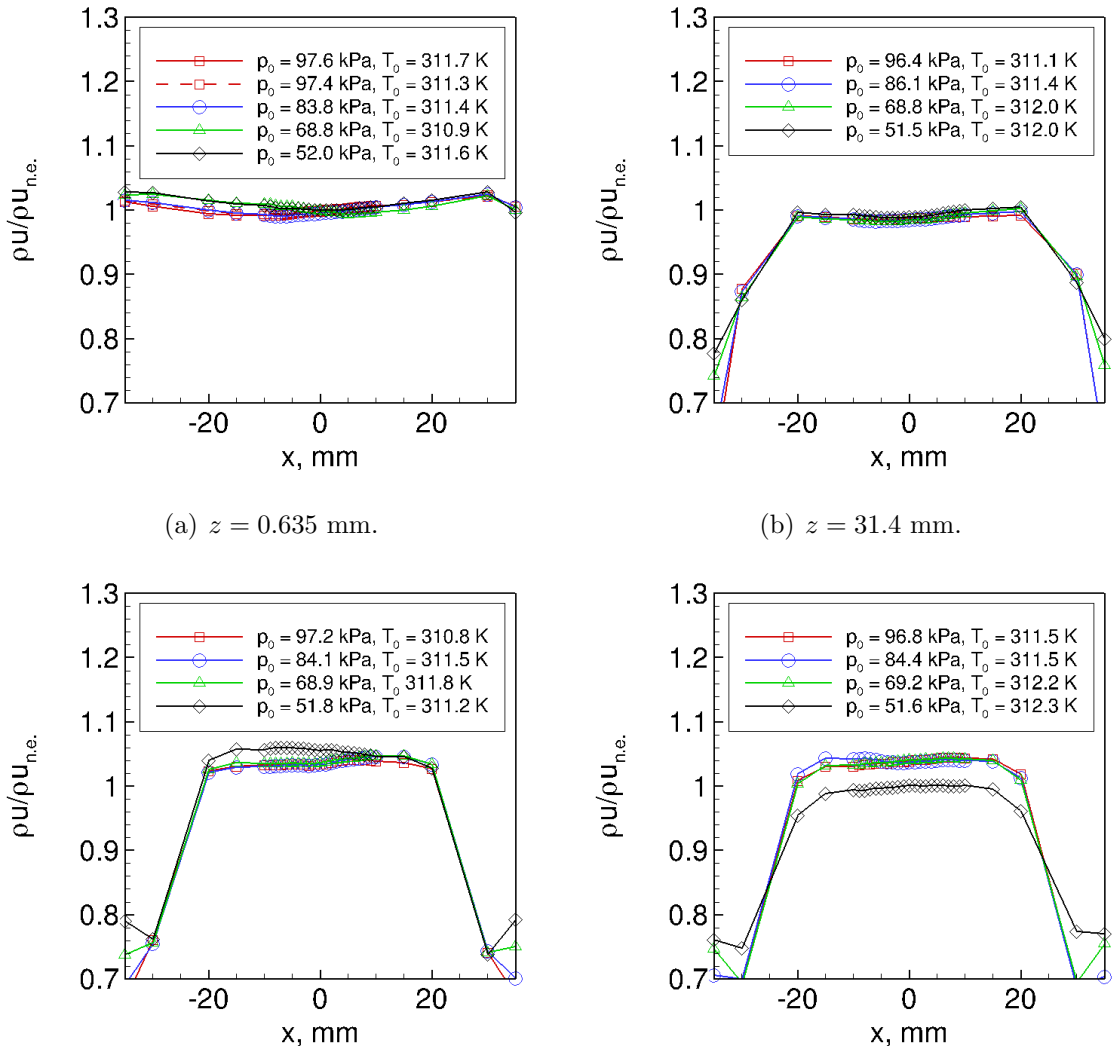

(a) $z = 0.635$ mm.

(b) $z = 31.4$ mm.

(c) $z = 46.9$ mm.

(d) $z = 54.5$ mm.

Figure 3.8. Mean mass flux measurements across the PCT nozzle at four different streamwise stations.

The spectra of the mass flux measurements were computed using a Welch spectrum estimation method. Blackman windows were applied to 50 different 5000-point blocks, which were allowed to have up to a 50% overlap. The spectra along the centerline of the tunnel at different stagnation pressures are given in Figure 3.10. The spectra along the centerline of the tunnel at different streamwise stations is given in Figure 3.11. These spectra show that the measurements along the centerline appear

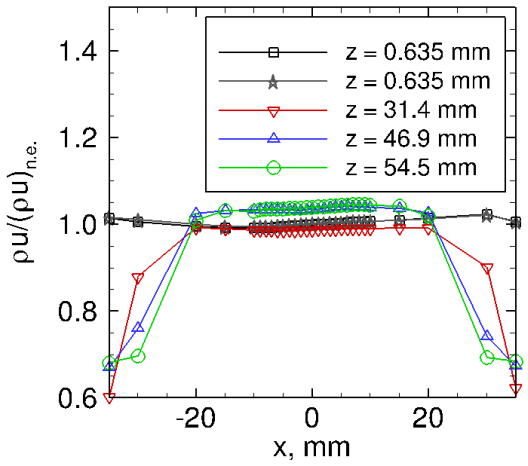

(a) p_0 = 97.1 kPa, T_0 = 311.3 K, ρ_∞ = 0.052 kg/m^3.

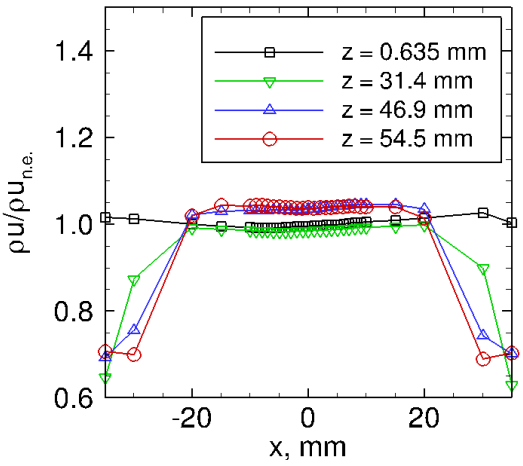

(b) p_0 = 84.6 kPa, T_0 = 311.4 K, ρ_∞ = 0.046 kg/m^3.

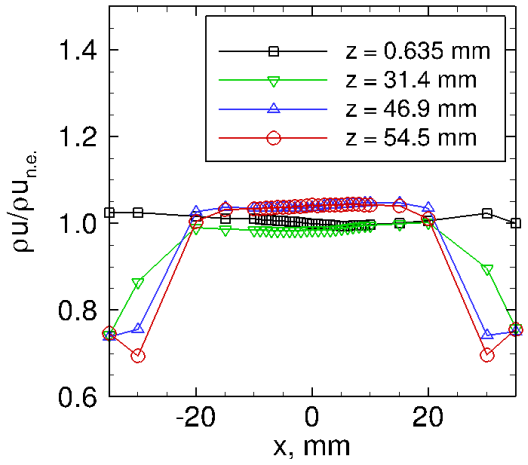

(c) p_0 = 68.9 kPa, T_0 = 311.8 K, ρ_∞ = 0.037 kg/m^3.

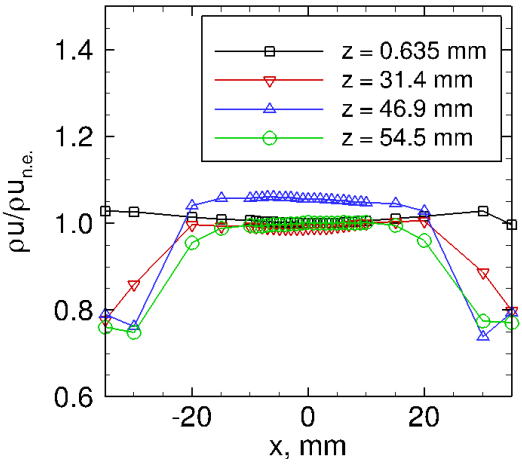

(d) p_0 = 51.7 kPa, T_0 = 311.8 K, ρ_∞ = 0.029 kg/m^3.

Figure 3.9. Mean mass flux measurements of PCT with Mach 3.5 nozzle and no forced perturbations at different stagnation pressures.

to be dominated by the electronic noise at these conditions. From about 2 kHz to the cutoff frequency of 250 kHz, the spectra match the electronic noise spectra.

The spanwise variation of the frequency content for the stagnation pressures and streamwise stations in this experiment are summarized using Figures 3.12 and 3.13.

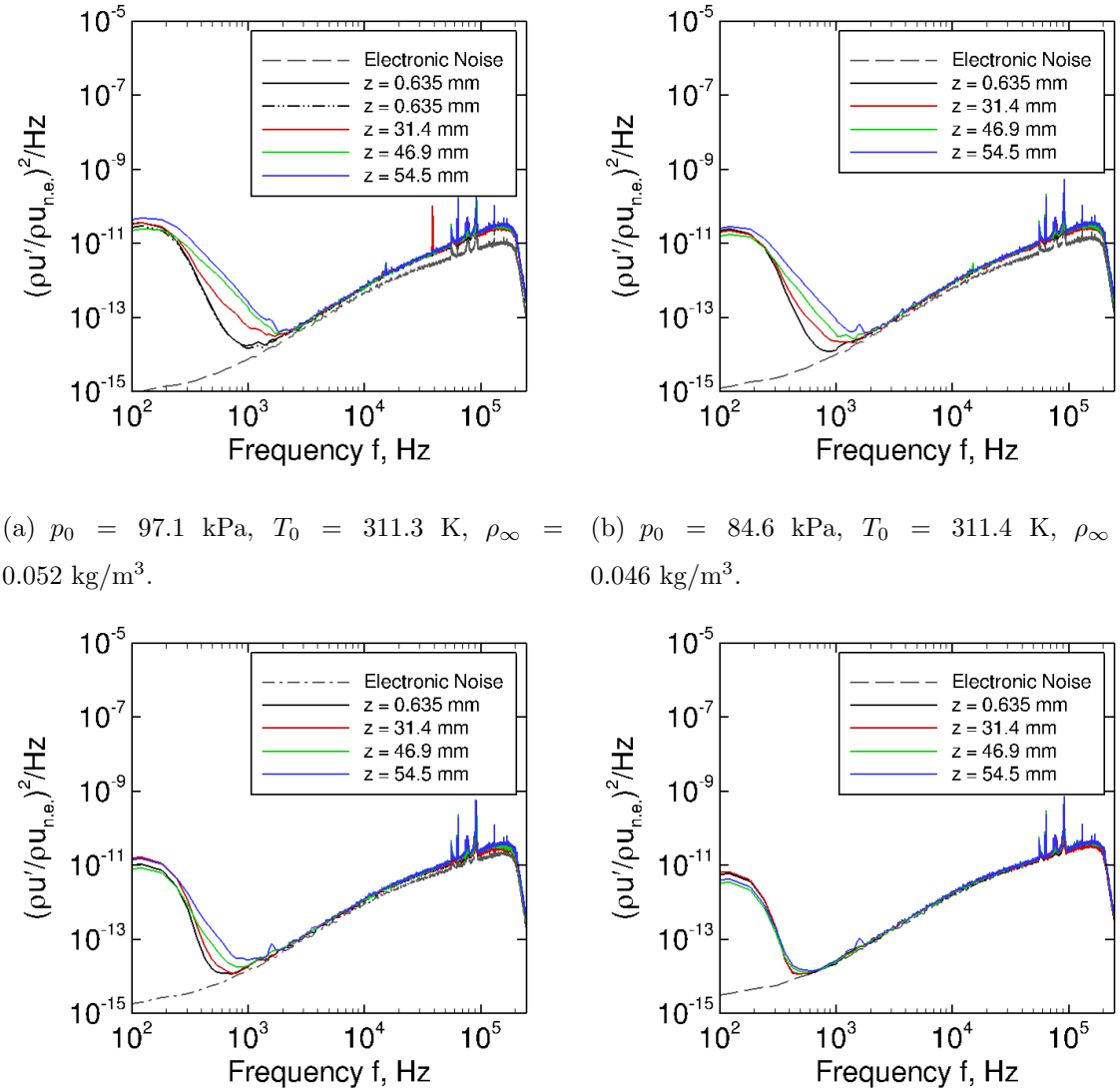

(a) p_0 = 97.1 kPa, T_0 = 311.3 K, ρ_∞ = 0.052 kg/m^3.

(b) p_0 = 84.6 kPa, T_0 = 311.4 K, ρ_∞ = 0.046 kg/m^3.

(c) p_0 = 68.9 kPa, T_0 = 311.8 K, ρ_∞ = 0.037 kg/m^3.

(d) p_0 = 51.7 kPa, T_0 = 311.8 K, ρ_∞ = 0.029 kg/m^3.

Figure 3.10. Power spectra of mass flux measurements at four different stagnation pressures on the PCT nozzle centerline.

The spanwise variation of frequency content appears to be very similar up to a location of ±20 mm from the nozzle centerline except at the highest stagnation pressures. In this central region of the nozzle, a majority of the frequency content is between 100 Hz–2 kHz. The two outermost spanwise stations show a broadening of the spec-

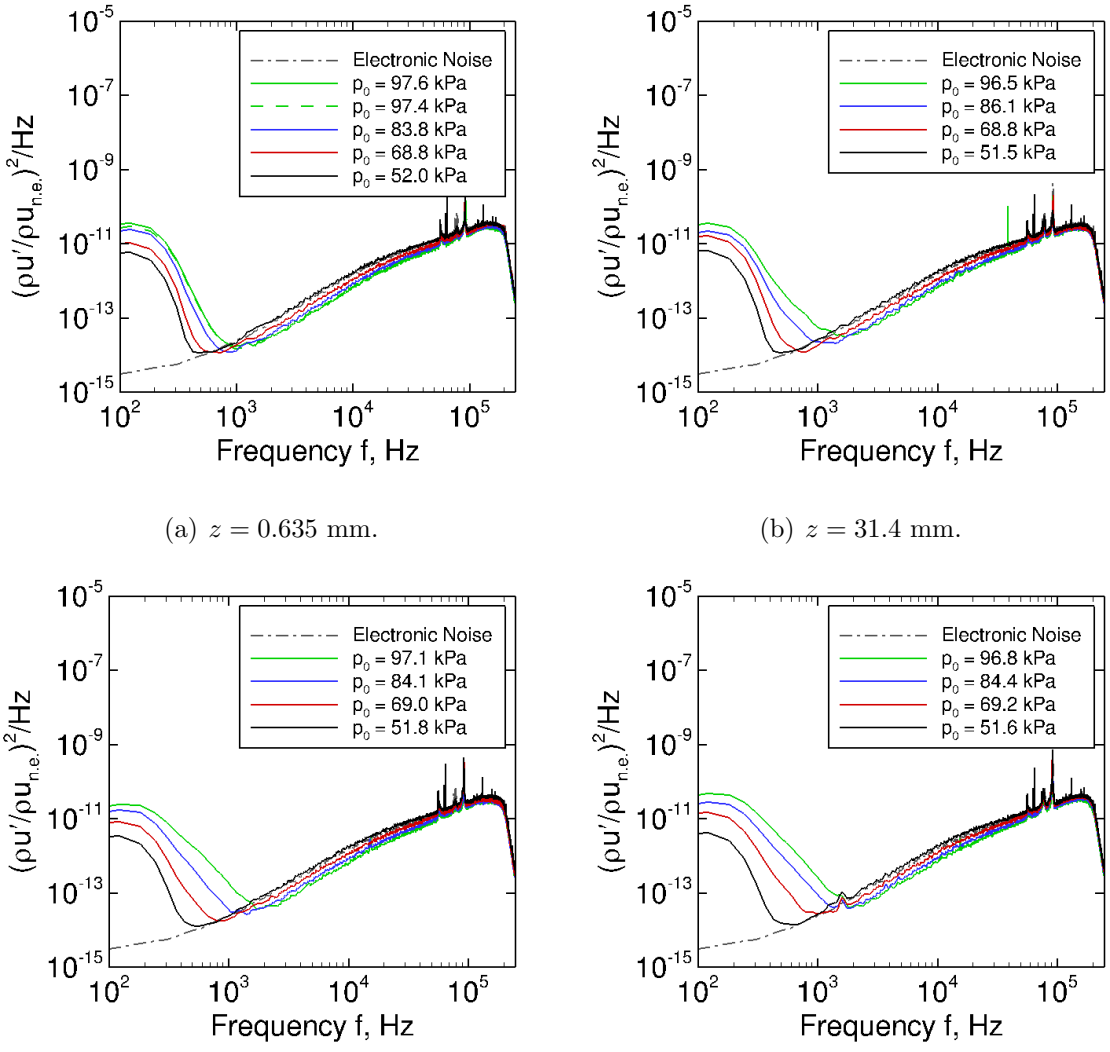

(a) $z = 0.635$ mm.

(b) $z = 31.4$ mm.

(c) $z = 46.9$ mm.

(d) $z = 54.5$ mm.

Figure 3.11. Power spectra of mass flux measurements at four different streamwise stations on the PCT nozzle centerline.

trum, especially at far-downstream stations. This increase in broadband frequencies is indicative of turbulence and likely indicates the position of the shear layer of the jet.

The RMS mass flux was computed by first integrating the spectra from 100 Hz–2 kHz, and then taking the square root. The RMS was only integrated up to this frequency because the spectra show that the signal is dominated by electronic noise

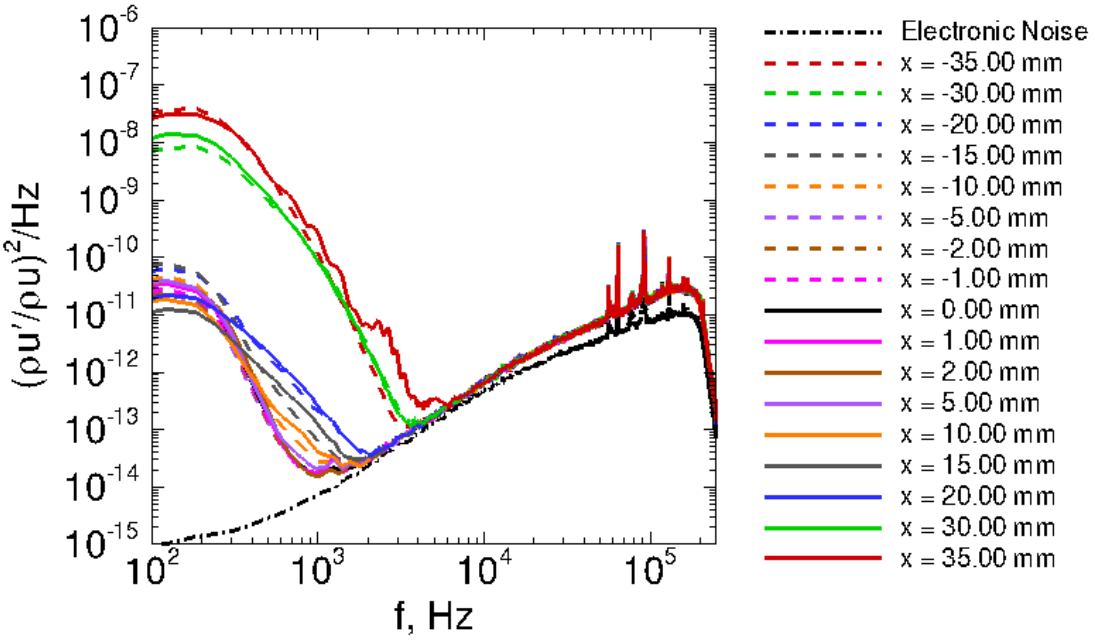

(a) $p_0 = 97.6$ kPa, $T_0 = 311.7$ K, $\rho_\infty = 0.052$ kg/m^3, $z = 0.635$ mm

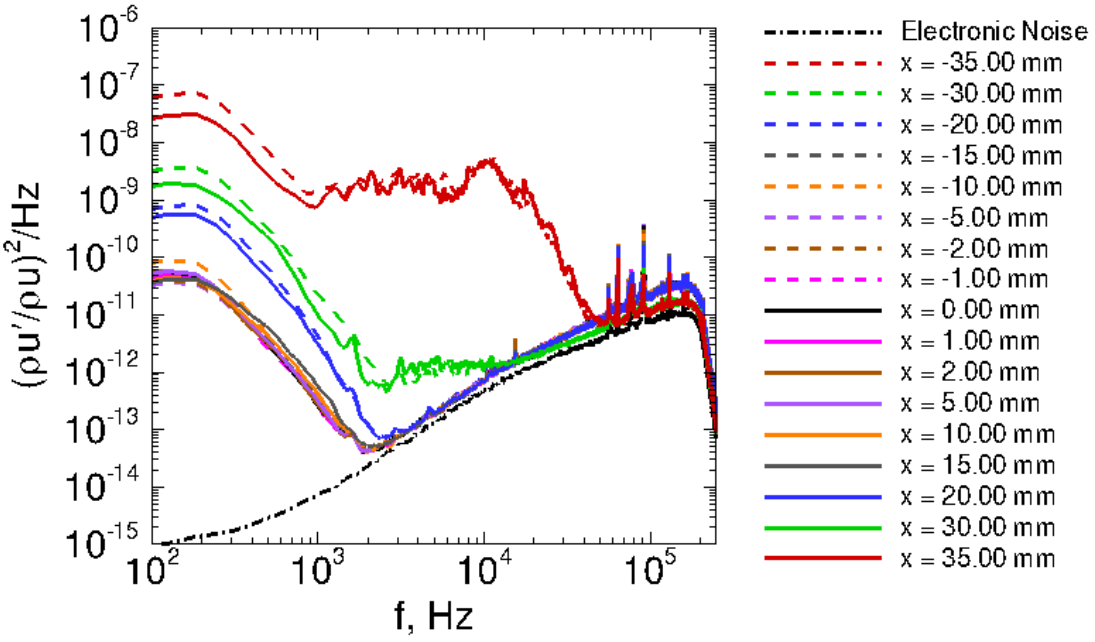

(b) $p_0 = 96.8$ kPa, $T_0 = 311.5$ K, $\rho_\infty = 0.052$ kg/m^3, $z = 54.5$ mm

Figure 3.12. Spanwise variation in power spectra for $\rho_\infty = 0.052$ kg/m^3.

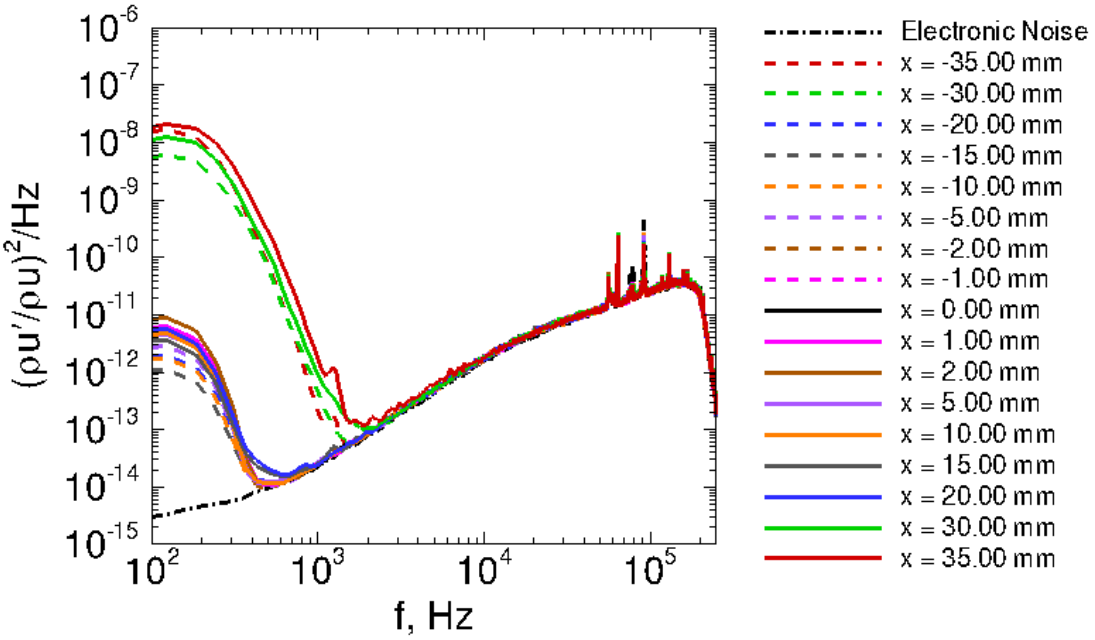

(a) $p_0 = 52.0$ kPa, $T_0 = 311.6$ K, $\rho_\infty = 0.028$ kg/m^3, $z = 0.635$ mm

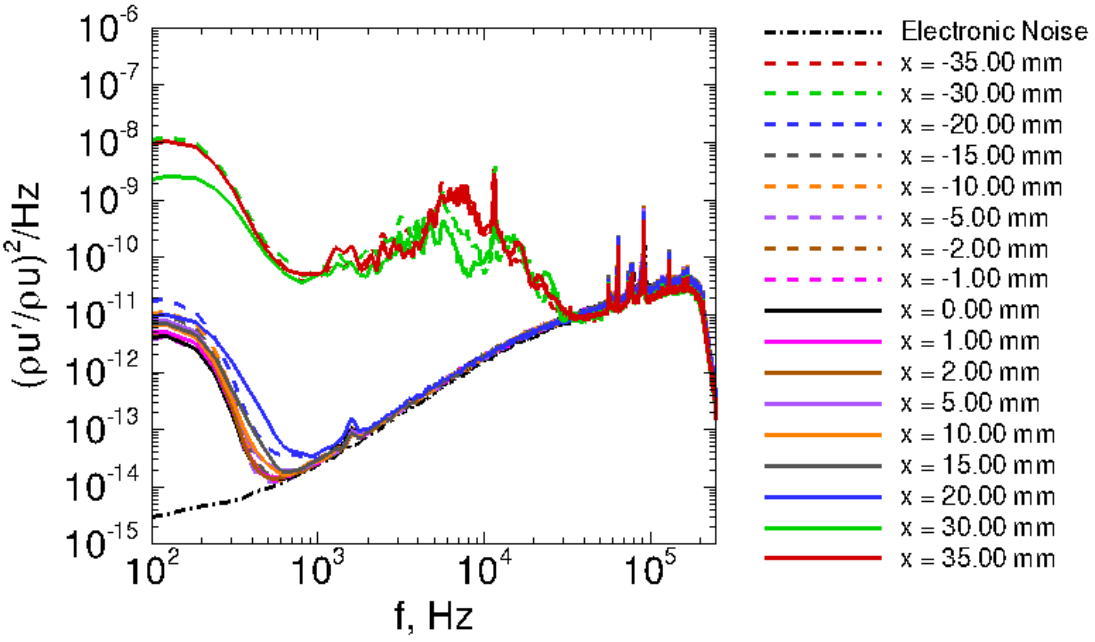

(b) $p_0 = 51.6$ kPa, $T_0 = 312.4$ K, $\rho_\infty = 0.028$ kg/m^3, $z = 54.5$ mm

Figure 3.13. Spanwise variation in power spectra for $\rho_\infty = 0.028$ kg/m^3.

at higher frequencies. The RMS is normalized by the measured mean mass flux at each spanwise station and plotted in Figure 3.14. These plots show that the RMS mass flux is very low at the centerline of the PCT, on the order of 0.001–0.005% of the mean. This RMS mass flux is similar to typical values seen in the NASA Langley Supersonic Low Disturbance Tunnel (SLDT), a Mach-3.5 quiet tunnel. The SLDT has a RMS mass flux of 0.002% across the same frequency band (100 Hz–2 kHz) at a unit Reynolds number $Re/m = 9.8 \times 10^6$/m [96].

The PCT nozzle-wall boundary layer may still be laminar at these low Reynolds numbers. The range of unit Reynolds numbers tested in PCT was $Re/m = 2.77$–5.25×10^6/m. Beckwith reported a laminar nozzle-wall boundary layer on the JPL 20-inch tunnel (now the 20-inch Supersonic Wind Tunnel at NASA Langley) up to a unit Reynolds number of about 2×10^6/m at Mach 4.5 [97]. However, Beckwith also stated that the unit Reynolds number is not necessarily the best value to use in comparing laminar nozzle-wall boundary layers because many factors contribute to this quality. Amick [98] used a throat Reynolds number to compare laminar nozzle walls:

$$Re^* = \frac{\rho^* u^* d^*}{\mu^*} \tag{3.3}$$

where ρ^*, u^*, and μ^* are the sonic values of density, velocity, and viscosity corresponding to the nozzle transition location. The nozzle throat diameter is d^*. The tested PCT stagnation pressures correspond to throat Reynolds numbers of 0.271–0.522×10^6. Amick saw transition in a range of throat Reynolds numbers from 0.6–0.85×10^6 in a conical Mach-8 nozzle, depending on the throat curvature. Amick's transitional throat Reynolds numbers are slightly higher than the range tested in PCT.

A further investigation of the freestream conditions in the PCT was conducted by performing these surveys at higher stagnation pressures. If the flow is laminar on the nozzle wall at these low stagnation pressures, then the boundary layer on the nozzle wall must become transitional and eventually turbulent at higher stagnation pressures. Transitional nozzle-wall boundary layers develop turbulent spots that can

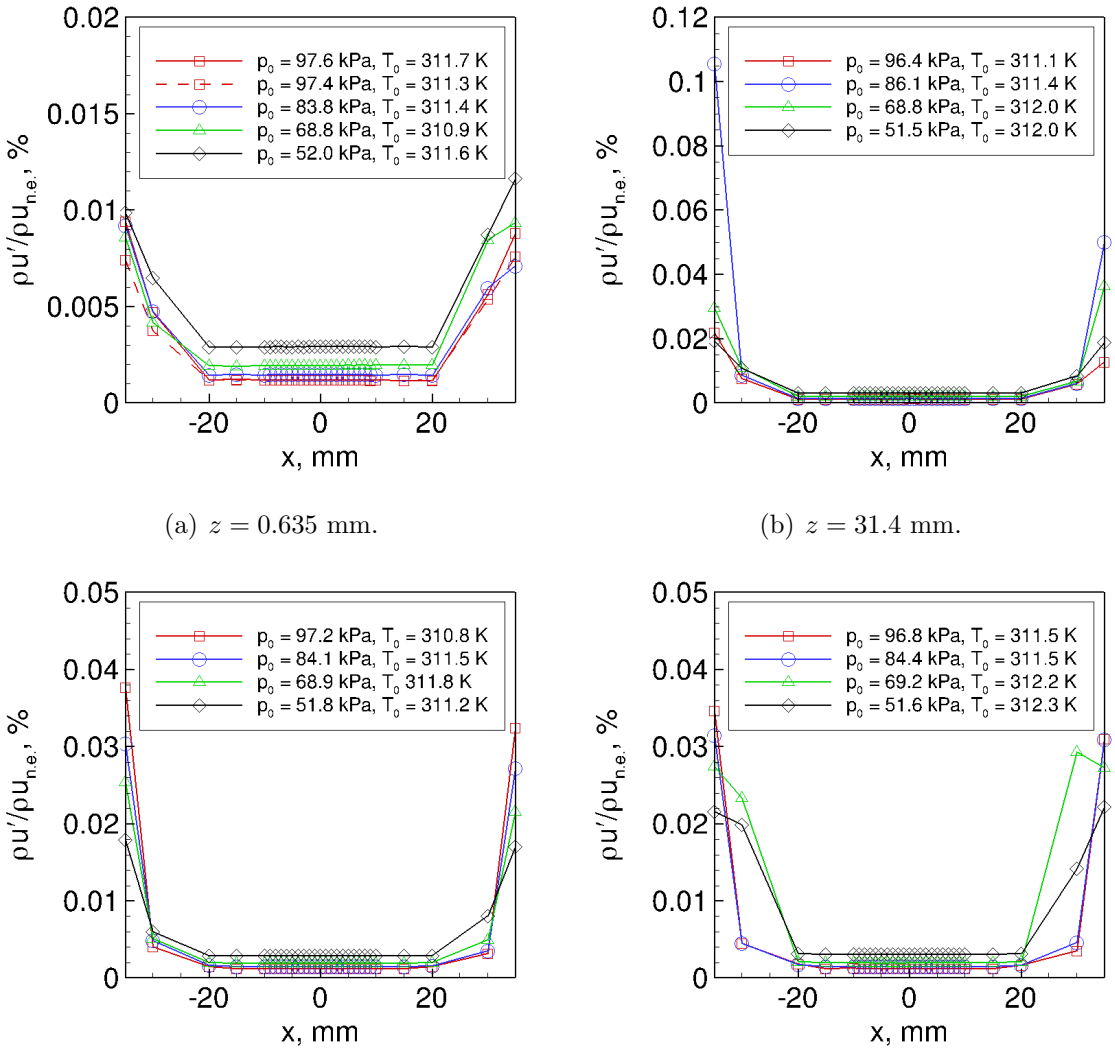

(a) $z = 0.635$ mm.

(b) $z = 31.4$ mm.

(c) $z = 46.9$ mm.

(d) $z = 54.5$ mm.

Figure 3.14. RMS mass flux measurements across the PCT nozzle at four different streamwise stations.

radiate acoustic noise into the freestream. Probes in the flow can measure the effects of the passing turbulent spots. An example trace of such a measurement with a hot wire is shown in Figure 3.15. The boundary layer on the nozzle wall is likely laminar in this example, up to about $t = 0.9985$ s, since the hot wire shows little fluctuation. Turbulent spots appear to develop just afterward, showing up in the hot wire trace

as five large spikes in mass flux in Figure 3.15. After the passage of these turbulent spots, the flow returns to the low fluctuation levels seen previously.

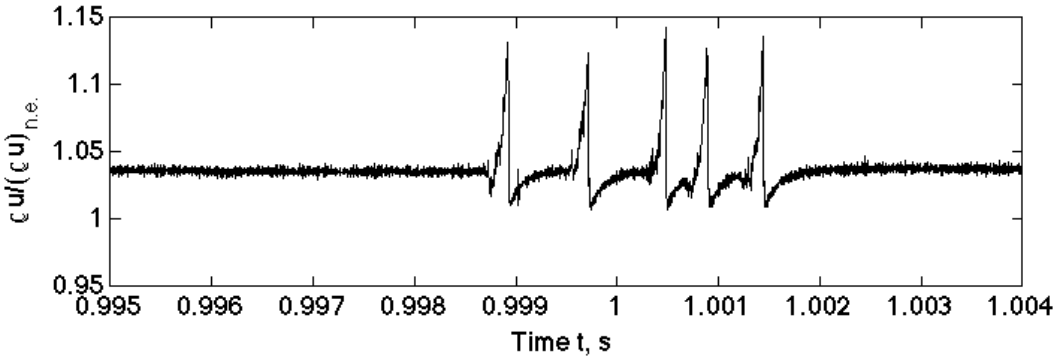

Figure 3.15. Example trace from hot wire of measurements of turbulent spots in the PCT. $p_0 = 201.9$ kPa, $T_0 = 310.5$ K, $Re/m = 11.41 \times 10^6$/m, $z = 54.5$ mm, $M = 3.42$.

Figure 3.16 shows time traces from four different surveys taken at similar stagnation pressures. Each time trace is from a measurement taken on the centerline at each of the specified distances from the nozzle exit. The intermittent spikes seem to be caused by acoustic noise radiated from turbulent spots on the nozzle wall. Small variations in temperature and pressure appear to change the number of turbulent spots that are measured by the hot wire. This indicates that the boundary layer on the nozzle wall is likely transitional at this particular condition. Similar phenomena occur in quiet tunnels nearing their maximum quiet Reynolds number [92, 99]. The RMS mass flux between 100–2000 Hz is about 0.2–0.3% for the conditions shown in Figure 3.16. Since this stagnation pressure is much higher than that used for the subsequent experiments, it is likely that the nozzle-wall boundary layer at the tested stagnation pressures is laminar.

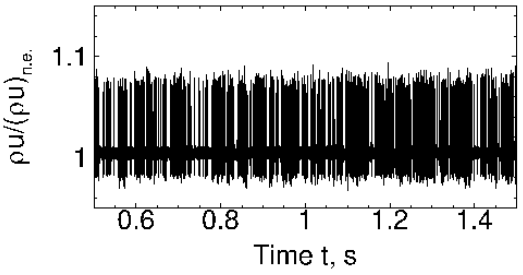

(a) $p_0 = 201.5$ kPa, $T_0 = 310.7$ K, $Re/m = 11.37 \times 10^6$/m, $z = 0.635$ mm.

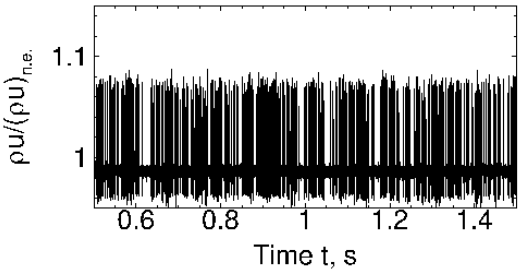

(b) $p_0 = 200.4$ kPa, $T_0 = 310.6$ K, $Re/m = 11.32 \times 10^6$/m, $z = 31.4$ mm.

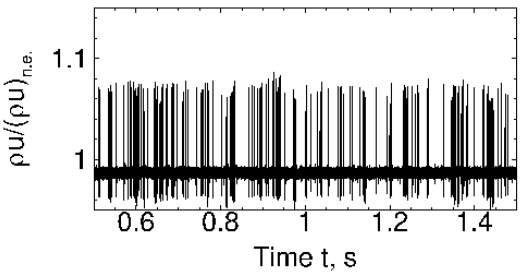

(c) $p_0 = 199.0$ kPa, $T_0 = 310.5$ K, $Re/m = 11.24 \times 10^6$/m, $z = 31.4$ mm.

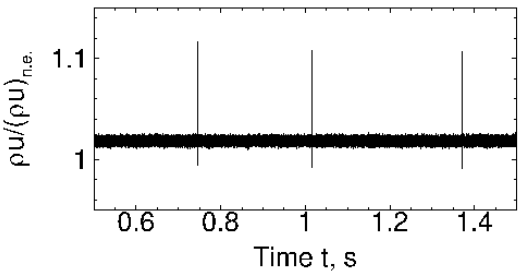

(d) $p_0 = 199.3$ kPa, $T_0 = 311.5$ K, $Re/m = 11.21 \times 10^6$/m, $z = 46.9$ mm.

Figure 3.16. Single point measurements with a hot wire on the centerline of the tunnel, organized by decreasing unit Reynolds number.

CHAPTER 4. MEASUREMENTS OF THE FREESTREAM DISTURBANCE IN MACH-3.42 FLOW

Measurements of the laser-generated disturbance in the freestream were performed in Mach-3.42 flow at the NASA LaRC PCT. Two types of measurements were made in this facility: hot wire and schlieren deflectometry. The goal of the experiments at the NASA LaRC PCT was to characterize the laser-generated perturbation in a facility with a slower speed and longer run time than possible in the BAM6QT. More detailed measurements were to be made in this type of environment. If these measurements could be shown to match similar characterization measurements in the BAM6QT, the measurements in the less-forgiving environment need not be carried out to the same depth.

An attempt was made to match as many of the conditions in the BAM6QT as possible for measurements in the PCT. This involved the matching of not only the fluid-dynamic properties, but also of the properties of the perturbation-forming optics. Not every condition in the PCT could be matched to conditions in the BAM6QT. For example, the stagnation temperature of the BAM6QT is 433 ± 6 K. This means that the freestream static temperature is about 52.8 K. To match this static temperature in the PCT, the stagnation temperature would have had to be set at about 180 K. This temperature was not in the possible range of temperatures for the PCT. Instead, the stagnation temperature of the PCT was set to a value that was easier to maintain: 311 K (100°F).

As stated in Chapter 2.3, the density is assumed to be the driving factor in the creation of the freestream disturbance. Thus, instead of matching Reynolds numbers, the freestream density conditions of the PCT and BAM6QT were matched. The densities of the following cases were used to determine the stagnation pressure conditions for the PCT:

1. The density at the maximum quiet stagnation pressure in the BAM6QT
2. The density at which transition under quiet flow is observed on a flared cone model in the BAM6QT
3. The density at which no transition is observed on a flared cone model (completely laminar boundary layer) in the BAM6QT
4. The lowest density at which laser-generated perturbations can be made in the BAM6QT
5. An intermediate density

The PCT stagnation pressures that provide these densities are in Table 2.2. The stagnation pressures range from about 51–100 kPa for densities of about 0.02–0.05 kg/m^3. The stagnation pressure in the PCT corresponding to the lowest density at which laser-generated perturbations could be made in the BAM6QT was outside the range of feasible pressures. That condition was not attempted, but all of the other conditions were used in this experiment.

4.1 Measurements with a Hot Wire

The dimensions of the PCT test section were too wide to use the BAM6QT perturbation-forming optics outside the test section while still forming a perturbation within the flow. Placing the perturbation-forming optics inside the test section also did not work due to the presence of back reflections from the first lens in the optical system. Focused back-reflections are undesirable when using a high-powered laser, as they can destroy or ablate the medium in which they are focused. Therefore, while methods of accommodating the full optical system were being designed, a modified optical system was used for the hot-wire measurements.

This modified optical system used only the last lens of the BAM6QT optical system: a single CVI/Melles-Griot YAP-200.0-40.0 lens. This optical element was placed in the PCT test section as shown in Figure 4.1. Figure 4.1 also shows that the traversing direction is nearly along the same axis as the laser-beam path. Surveys

taken very close to the laser focal region had the possibility that the hot wire would traverse into the beam path. The change in the focusing optics greatly alters the laser perturber system by changing the f/D of the system, which in turn changes the focal volume of the perturber. The modified optical system has the possibility of creating a perturbation that is not similar to that made with the BAM6QT optical system. Measurements closer to the area where the perturbation is initially formed may show the effect of how this disturbance is formed.

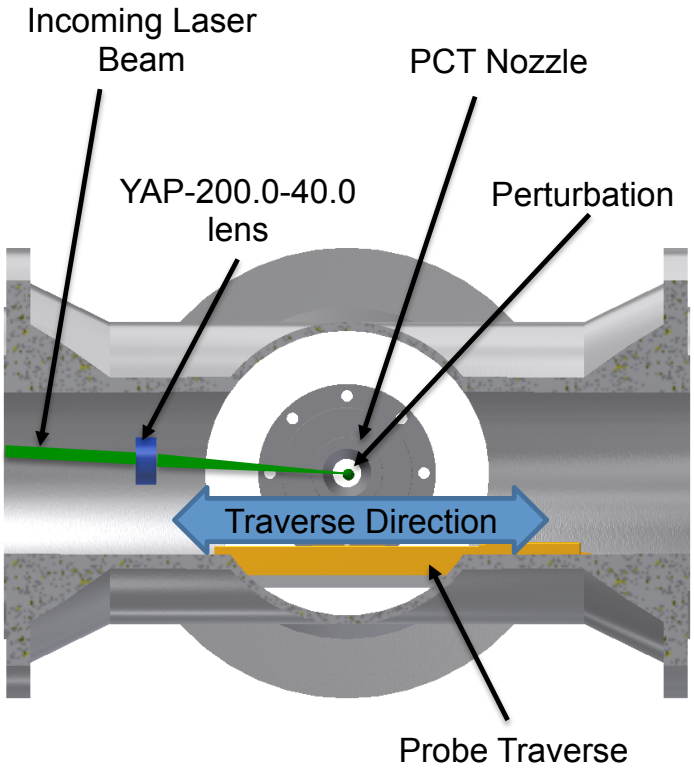

Figure 4.1. Schematic of modified perturbation optics for hot-wire measurements, looking upstream in PCT.

Only uncalibrated hot-wire measurements are shown in this chapter. The hot-wire calibrations (Equations 2.6 and 2.7) assume a high overheat ratio and small temperature fluctuations to make the measurements sensitive to mass-flow fluctuations [83].

However, Schmisseur approximated that the temperature of the freestream perturbation was about 100 K above the freestream temperature [43]. This large-temperature perturbation invalidates the assumption of a small temperature fluctuation. Thus, for a very hot thermal perturbation, the wire is no longer sensitive to mass flux. The presence of free electrons produced by the laser-induced breakdown process may also affect the hot-wire measurements. These factors can cause the hot-wire calibrations to give non-physical results such as imaginary mass flux.

4.1.1 Example Data

The raw hot-wire measurements were passed through a band-pass filter with cutoff frequencies at 100 Hz and 200 kHz. These data were then sampled by the data acquisition system at 1 MHz. A total of 100 different laser pulses were used for each survey location and 10,000 data points were taken after each of the different laser pulses. The time data was converted to an equivalent distance from the generation location by assuming that the perturbation was flow-fixed and that the flow was isentropic and calorically perfect. The generation location was the z-coordinate of the focal region of the perturber apparatus. The relative distance between the perturbation and generation location is

$$\Delta z = u_\infty \cdot t_p = M_\infty \sqrt{\gamma R T_\infty} \cdot t_p \tag{4.1}$$

where u_∞ is the freestream speed, M_∞ is the freestream Mach number, and t_p is the time after a laser pulse is fired. The location of the wire is given in the following sections as z_w and the initial distance between the wire and perturbation is Δz_i.

The freestream disturbance is expected to convect at the freestream velocity because it consists mainly of a thermal perturbation. Thermal disturbances are expected to convect with the freestream [21]. The time of arrival of the disturbance at $\Delta z_i = 29.9$ mm was used to determine the speed of the freestream disturbance. Due to the lower frequency response of the hot wire (about 250 kHz), the 10% rise (or fall) time of the hot-wire measurement is used to determine the time of arrival

of the perturbation. The 10% rise time is taken to be the time at which the voltage measured drops to 10% of the minimum voltage measured. The mean time of arrival measured over 400 different laser shots is 44.7 μs. This measurement has about a 2.7 μs standard deviation. The speed inferred from the time of arrival is then 678.9 m/s, which is about 3.9% different from the speed inferred from the freestream temperature. This discrepancy may be due to measurement errors or to the Mach number that was assumed.

To check that the hot-wire response to the laser perturbation was repeatable, 10 different time traces from a single run were compared. An example of these 10 different time traces is shown in Figure 4.2. The individual traces showed a maximum variation in voltage of about 2%. The shape of the perturbation appeared skewed, which was likely due to the limited frequency response of the hot wire. The required frequency response to measure the speed of the passing perturbation is on the order of 600 kHz, but the hot wires used are only capable of reaching a frequency response of about 250–270 kHz. The limited frequency response caused some averaging of the amplitude of the perturbation, as well as a "smearing out" of the perturbation over time.

To remove some of the effects of stochastic noise, all 100 measurements after each laser pulse were ensemble-averaged for each survey location. An example of this trace is shown in Figure 4.3. Each streamwise (z) survey station contains 32 spanwise ($\pm x$) points. The ensemble-averaged time traces at each survey station can be plotted as lines on a single graph. Figure 4.4 shows some of the survey points plotted on top of each other. This type of plot makes the spanwise symmetry of the perturbation easier to see, however, it does not show the measurements from all survey points. The traces from all of the survey points are better visualized as a contour plot, as in Figure 4.5.

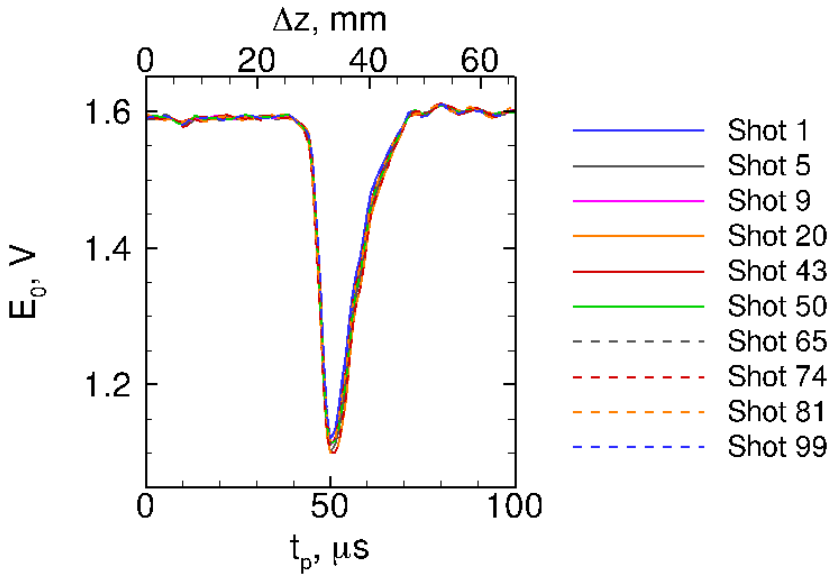

Figure 4.2. Sample hot-wire data showing the repeatability of the perturbation in the PCT. $p_0 = 68.9$ kPa, $T_0 = 311.1$ K, $\rho_\infty = 0.039$ kg/m^3, $\Delta z_i = 29.9$ mm.

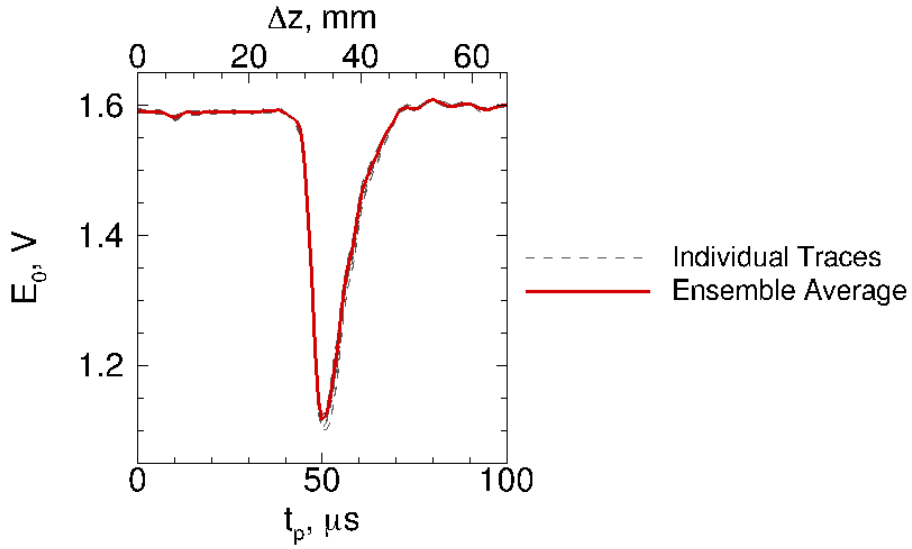

Figure 4.3. Sample ensemble average of hot-wire data in the PCT. $p_0 = 68.9$ kPa, $T_0 = 311.1$ K, $\rho_\infty = 0.039$ kg/m^3, $\Delta z_i = 29.9$ mm.

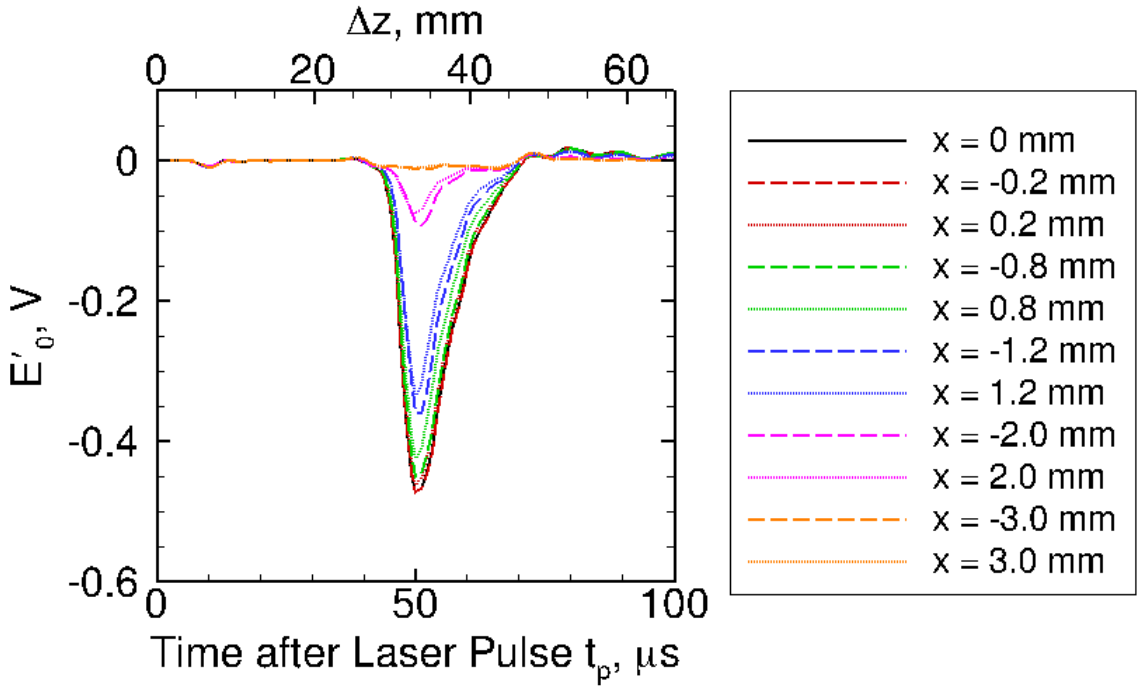

Figure 4.4. Line plots of hot-wire traces across a laser-generated perturbation. $p_0 = 68.9$ kPa, $T_0 = 311.1$ K, $\rho_\infty = 0.039$ kg/m^3, $\Delta z_i = 29.9$ mm.

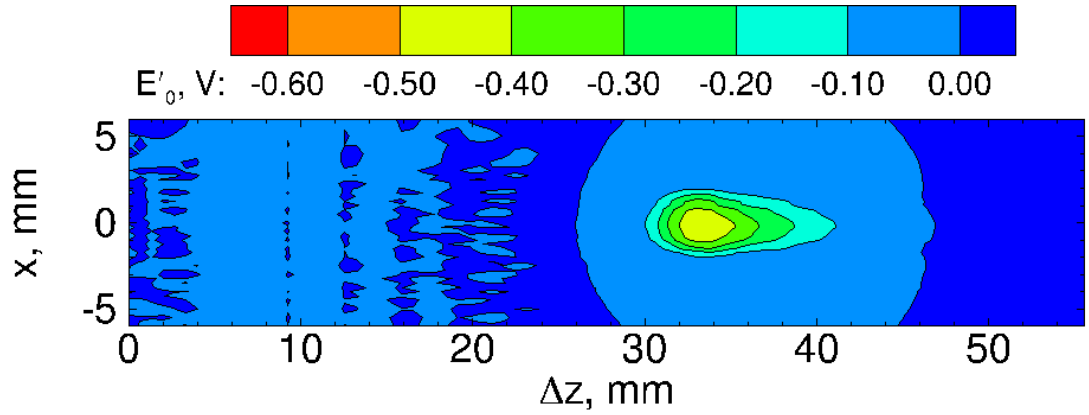

Figure 4.5. Contour plot of hot-wire traces across a laser-generated perturbation. $p_0 = 68.9$ kPa, $T_0 = 311.1$ K, $\rho_\infty = 0.039$ kg/m^3, $\Delta z_i = 29.9$ mm.

4.1.2 Hot-Wire Measurements in the PCT Close to the Generation Location

Initial hot-wire measurements of the freestream laser-generated disturbance were made in the PCT with the probe traversing in the $\pm x$-direction at a location $\Delta z_i = 2.78$ mm downstream of the generation location. An example of a hot-wire survey of the perturbation in the freestream at this nearby location is given in Figure 4.6. This contour plot shows the raw voltage of the hot wire at different points in the survey region.

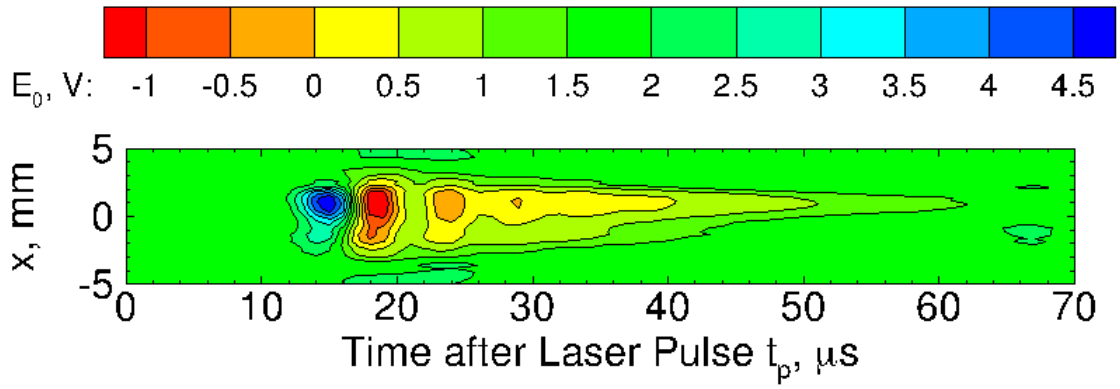

Figure 4.6. Example of hot-wire voltage measurements of the freestream perturbation when probe is placed close to the perturbation.

A similar contour plot showing the hot-wire voltage fluctuations is in Figure 4.7. This plot shows features that are not visible in the contour plot of the total measured voltage. Some fluctuations are visible on the outer edges of the survey region ($x = \pm 5$ mm). A time trace of the hot-wire measurement at a survey location of $x = -4.5$ mm is shown in Figure 4.8. A large downward spike is followed by a large upward spike at the beginning of this time trace. Small fluctuations began about 30 μs after the laser pulse is fired.

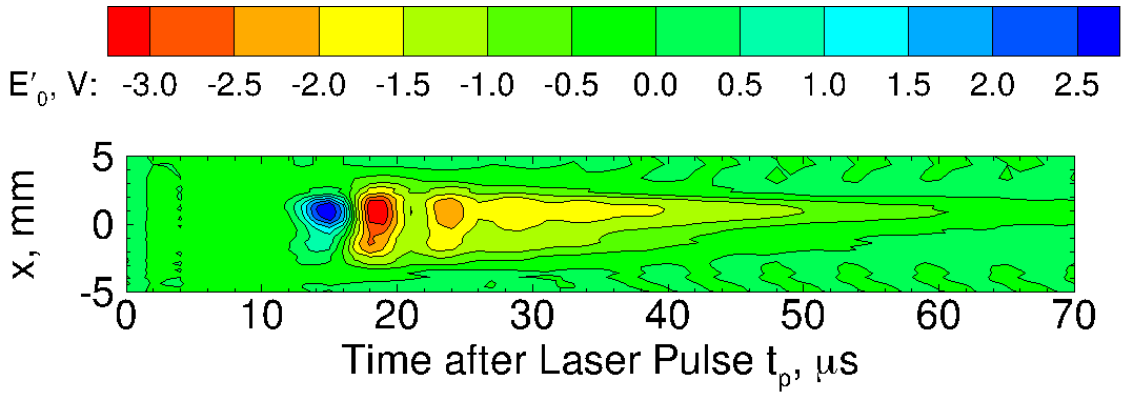

Figure 4.7. Example of measurements of hot-wire voltage fluctuation when probe is placed close to the perturbation generation location.

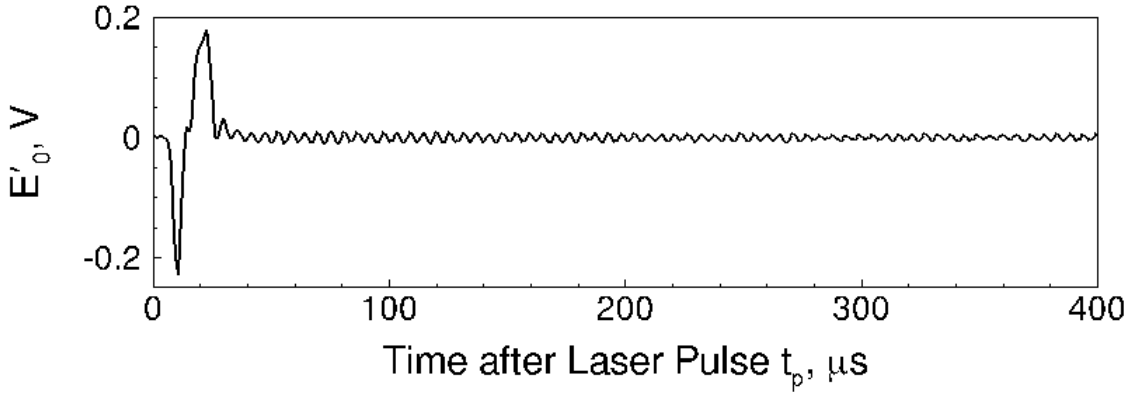

Figure 4.8. Example time trace of hot-wire voltage fluctuation measurement, showing nonlinear effect from anemometer. $x = -4.5$ mm.

The large downward and upward spike is likely from the passage of the thermal perturbation. However, this characteristic does not compare well with measurements made by Schmisseur in the PQFLT [43]. Schmisseur's hot-wire measurements in the PQFLT showed a distorted spherical shape with a central thermal disturbance. Measurements close to perturbation in the PCT showed a strange and elongated shape. No clear central thermal disturbance is visible, and there appear to be four

distinct regions in the perturbation shape. It is difficult to interpret these regions as a measurement of some physical characteristic of the perturbation. The fluctuations starting at $t \approx 30$ μs are assumed to be an electrical response in the CTA excited by the large-amplitude, short-duration perturbation. Schmisseur notes a similar effect in some of his measurements [43].

This measurement location in the PCT is much closer to the perturbation generation location than Schmisseur's measurements, which may explain some of the differences. The perturbation is likely still in the early stages of formation at the nearby measurement location, so free electrons and ions from the laser-induced breakdown process are likely present. The temperature may also still be very high because the perturbation has not had time to cool before being measured by the hot wire. Glumac et al. reported that the temperature of a laser-induced breakdown plasma after about 400 ns is still near 10,000 K [56]. These properties require the CTA to operate outside the range of parameters where it is most effective.

4.1.3 Hot-Wire Measurements in the PCT Farther Downstream of the Generation Location

Measurements were made farther downstream at a location of $\Delta z_i = 29.9$ mm. This produced data more similar to the existing historical data. Measurements along the centerline of the perturbation for four different freestream densities are shown in Figure 4.9. The freestream densities are inferred using isentropic and perfect-gas assumptions. The freestream density is varied by decreasing the total pressure while maintaining a nearly constant total temperature of about 310 K. As the freestream stagnation pressure decreases, the magnitude of the perturbation also appears to decrease. The time after a laser pulse is fired t_p is shown on the lower horizontal axis, and the corresponding distance calculated using Equation 4.1 is shown on the upper horizontal axis.

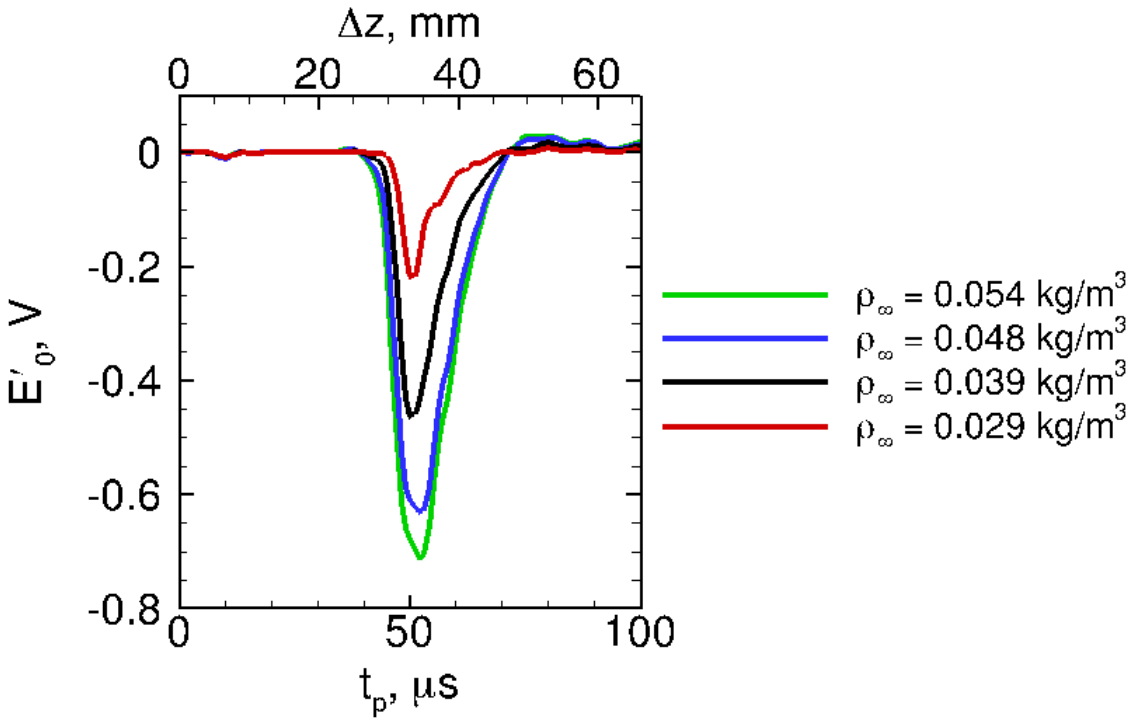

Figure 4.9. Uncalibrated hot-wire measurements of a laser-generated disturbance in the freestream, 29.9 mm downstream of the generation location.

Information can still be garnered from these data despite the lack of a valid calibration. The spanwise width and the perturbation's spanwise symmetry in the direction of the laser beam path can be determined. Contour plots of the uncalibrated measurements of the perturbation for freestream densities of 0.054, 0.048, 0.039, and 0.029 kg/m^3 are shown in Figures 4.10, 4.11, 4.5, and 4.12 respectively. These contour plots show information that is similar to the line plots: the amplitude and spanwise width of the perturbation decreases with decreasing freestream density.

Determination of the maximum width of the perturbation was limited by the resolution of the spacing in the survey points. The spacing of the survey points was 0.25 mm at the center of the contour plots. The edges of the perturbation were considered to be the spanwise location x at which the voltage fluctuation dropped

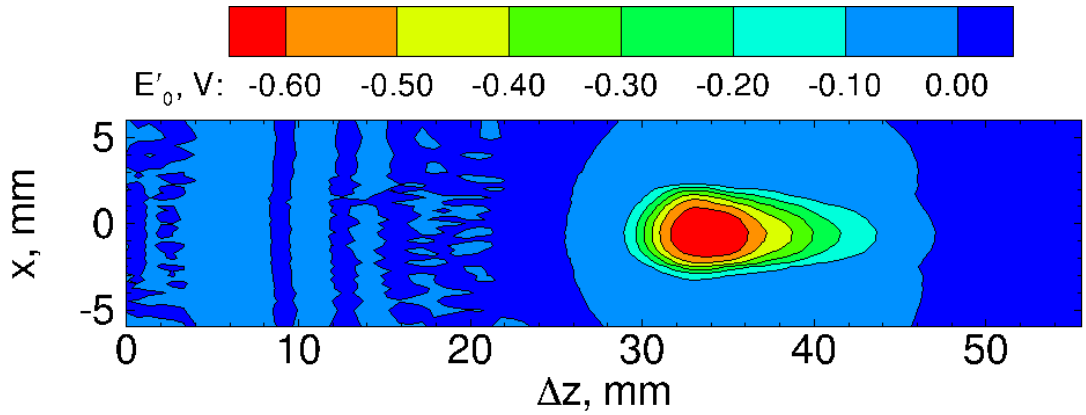

Figure 4.10. Contour plot of uncalibrated hot-wire measurements of a freestream laser-generated perturbation. $M = 3.42$, $\Delta z_i = 29.9$ mm, $\rho_\infty = 0.054$ kg/m^3.

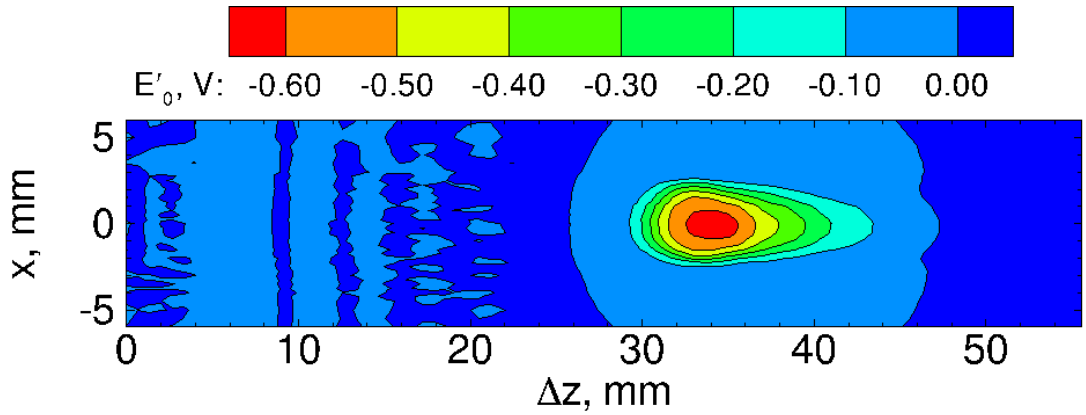

Figure 4.11. Contour plot of uncalibrated hot-wire measurements of a freestream laser-generated perturbation. $M = 3.42$, $\Delta z_i = 29.9$ mm, $\rho_\infty = 0.048$ kg/m^3.

below -0.15 V. The spanwise width in the x-direction for each of the perturbations was computed by finding the difference in the x-location of the edges. The thresholding method of finding the edges provides an uncertainty of ± 0.25 mm in the calculation

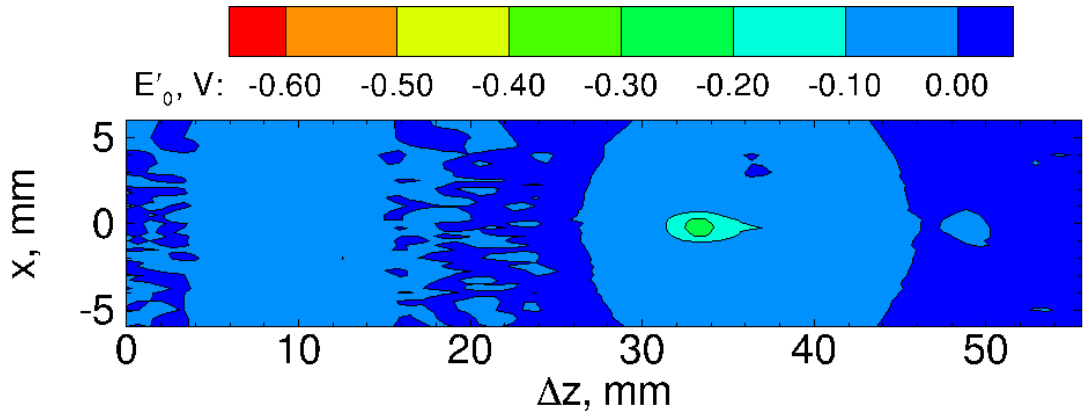

Figure 4.12. Contour plot of uncalibrated hot-wire measurements of a freestream laser-generated perturbation. $M = 3.42$, $\Delta z_i = 29.9$ mm, $\rho_\infty = 0.029$ kg/m^3.

of the width of the perturbation. The spanwise width (Δx) for each of the tested conditions is given in Table 4.1.

Table 4.1 Spanwise width of the perturbation in the x-direction, found with uncalibrated hot wires in the PCT

Stagnation Pressure p_0, **kPa**	**Stagnation Temperature** T_0, **K**	**Freestream Density** ρ_∞, **kg/m^3**	**Perturbation Width** Δx, **mm**
95.8	311.1	0.054	5.70
86.2	310.9	0.048	5.18
68.9	311.1	0.039	4.00
51.6	311.6	0.029	2.00

The symmetry of the perturbation was also determined by looking at the time traces from individual survey points, as in Figure 4.4. Similar plots for the other freestream densities are given in Figures 4.13, 4.14, and 4.15. Often, the perturbation is not quite symmetric and is slightly smaller in amplitude at the $+x$ stations. Mea-

surements at the same spanwise distance from the perturbation centerline differed as much as 34%. The largest differences in the time traces occurred closer to the edges of the perturbation and at lower freestream densities.

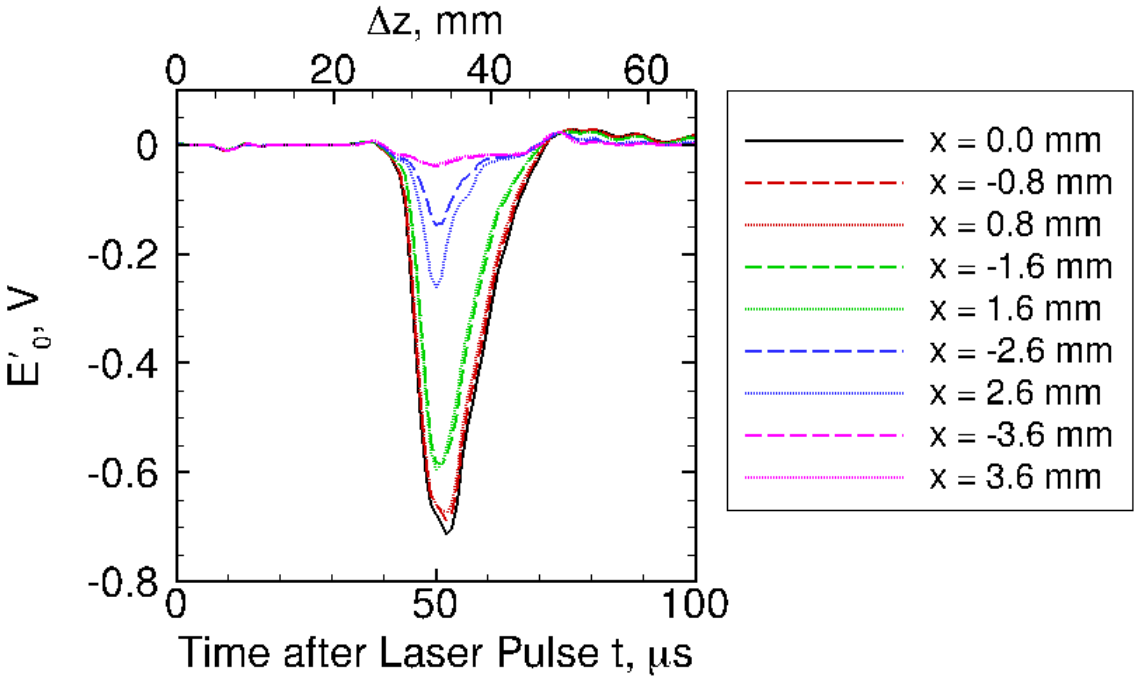

Figure 4.13. Line plots of hot-wire traces across a laser-generated perturbation. $p_0 = 95.8$ kPa, $T_0 = 311.1$ K, $\rho_\infty = 0.054$ kg/m^3.

The laser beam was set up to run from the $-x$ to $+x$-direction, so the $-x$-direction is closer to the laser head. It is possible that the measured asymmetry is due to the initial formation of the laser-generated disturbance. In Reference [54] and [53], the laser-induced breakdown process occasionally creates a pear-shaped disturbance, with the larger lobe created toward the laser head. This initial asymmetry can create an asymmetric perturbation downstream. It is unlikely that this asymmetry was caused by the probe, since the probe was mounted to protrude into the flow from the y-direction. Thus, the same amount of the flow impinged on the probe in both the $-x$ and $+x$-stations.

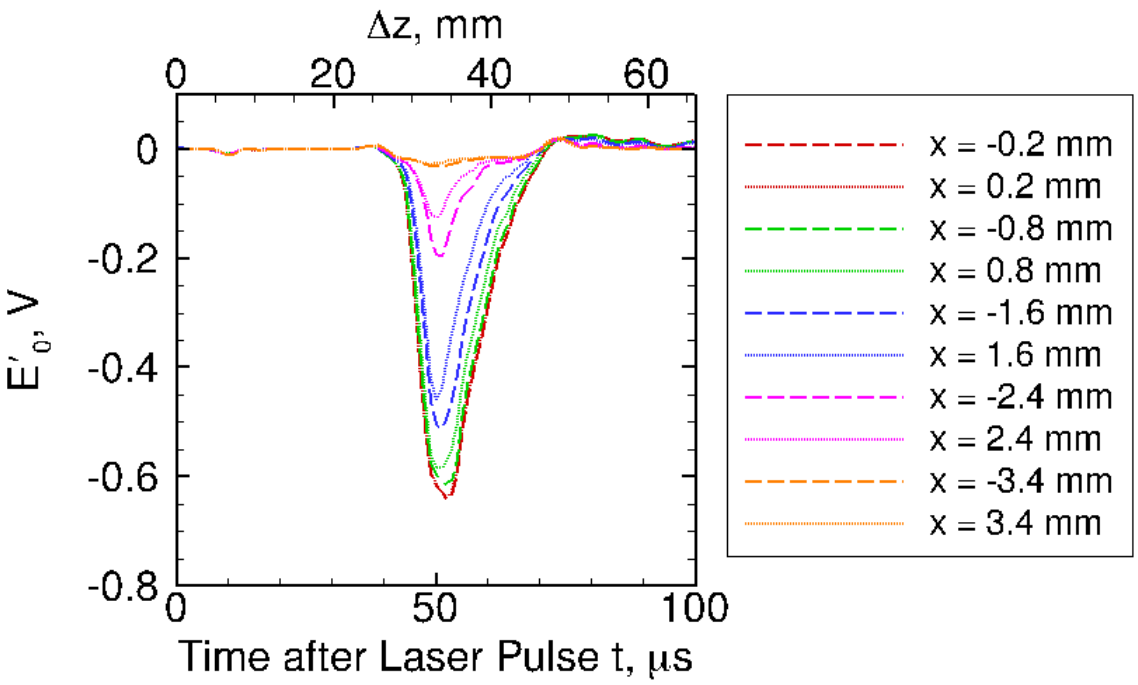

Figure 4.14. Line plots of hot-wire traces across a laser-generated perturbation. $p_0 = 86.2$ kPa, $T_0 = 310.9$ K, $\rho_\infty = 0.048$ kg/m^3.

Information about the frequency content of these traces was determined by looking at the power spectra. The power spectra were determined by taking a FFT of the data segments from each of 100 laser pulses and then averaging together the FFTs. The FFT used Welch's spectrum estimation method and Blackman windows for the 10,000-point data segments after each laser pulse. Then, the fast Fourier transforms were ensemble-averaged together to form the power spectra. Anemometer noise appears to dominate the spectra above about 20 kHz. Four electronic noise peaks also appear in the spectra at these higher frequencies between 30–100 kHz. The spectral analysis showed that a majority of the measurable content was at lower frequencies. The spectra are plotted on log-log plots to display the lower frequency content more clearly.

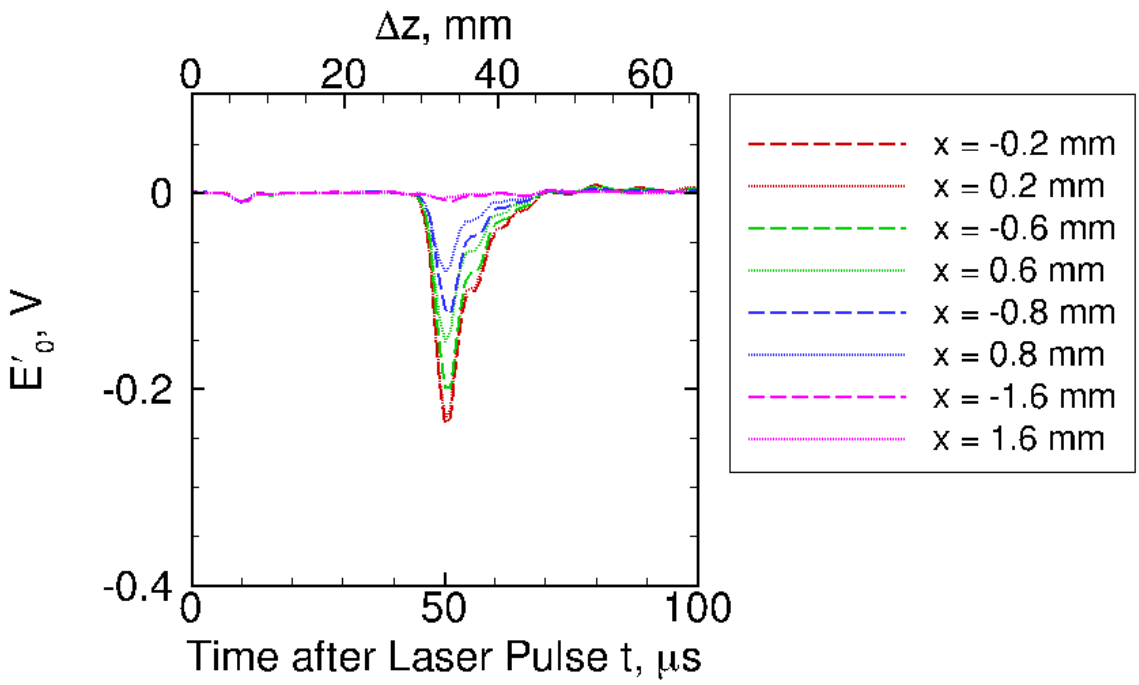

Figure 4.15. Line plots of hot-wire traces across a laser-generated perturbation. $p_0 = 51.6$ kPa, $T_0 = 311.6$ K, $\rho_\infty = 0.029$ kg/m^3.

Data acquired in these measurements required an adjustment of the gain applied by the in-line signal conditioners. A gain of 128 was applied to the measurement of the electronic noise. The baseline freestream measurements with no laser-generated perturbation also used this gain, so they do not see an effect of the change in gain. However, measurements that included a laser perturbation typically did not use any gain. The magnitude of the thermal disturbance was large enough that any gain on the signal would have caused the analog-to-digital converter to clip the signal.

A reduction of gain will reduce the signal-to-noise ratio (SNR) of the measurements. An example of how the spectra change with the amount of gain applied to the signal is given in Figure 4.16. The spectra shown here are from measurements with a different hot wire than used for the measurements of the freestream perturbation. Similar data for the same hot-wire probe is not available because the wire

broke. However, the setup for the signal conditioners remains the same. The spectra in Figure 4.16 are of the electronic noise with no flow and no laser perturbations. Some convection currents are probably present. A peak at 890 kHz appears when the gain is reduced to about 16. The source of this peak is unknown and the peak could not be eliminated. As the gain is reduced, the noise floor in the spectra increases. The content up to about 300 Hz is likely due to the convection currents present. The content from between 300–7000 Hz shows the increase in the noise floor as the gain is reduced.

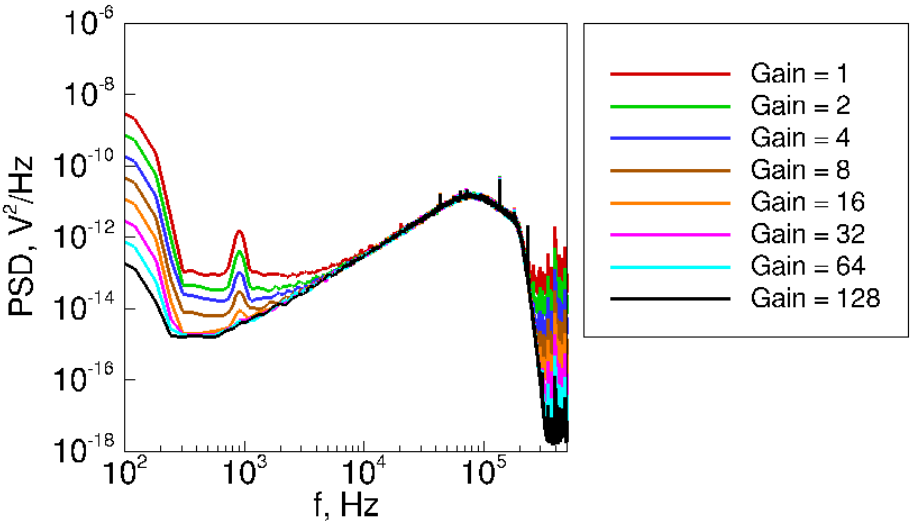

Figure 4.16. Power spectra of electronic noise with a hot wire showing the effect of gain.

Figure 4.17 shows power spectra of the data from the centerline survey point of the perturbation for multiple stagnation pressures. The high-frequency data between 1–200 kHz appear to be dominated by the anemometer or filter noise. The centerline measurements are nearly the same as the electronic noise signal in the 10–200 kHz bandwidth. At 200 kHz, the anti-aliasing filter took effect, so the data above this frequency were essentially a measurement of the noise created by the in-line filter. Between 1–10 kHz, the spectra may also still be affected by filter noise, as the amplitude of the measurements in this range appeared to be similar to the measurements at

frequencies greater than 200 kHz. The data between 100 Hz–1 kHz appeared to be a true physical measurement of the signal above the noise in the flow. This bandwidth is a very narrow band at which useful data can be obtained. However, the amplitude of the measurements in this frequency range increased with the freestream stagnation pressures.

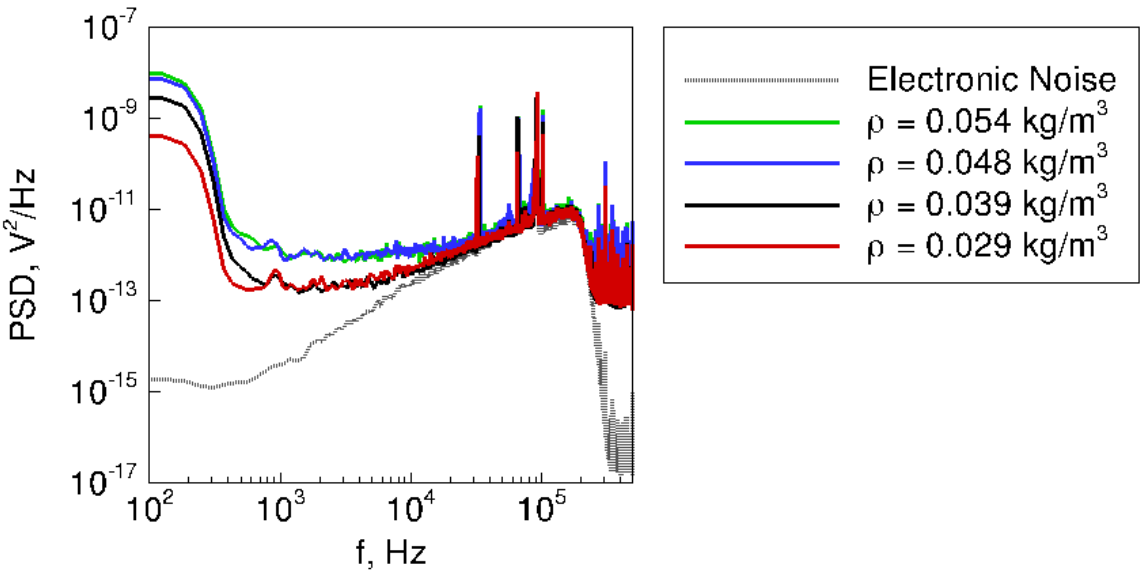

Figure 4.17. Power spectra of hot-wire measurements on the centerline of a laser-generated perturbation, taken at 30 mm downstream of the generation location.

Plots of the symmetry in the frequency content across the perturbation are given in Figures 4.18–4.21. The spectra showed fairly good symmetry in the relevant frequency band of 100 Hz–1 kHz. The frequency content closer to the centerline showed an increase in power while the frequency content at the edges of the perturbation show decreased power. There was a slight increase in the power in some of the measurements on the negative side of the perturbation, similar to what was seen in the time traces.

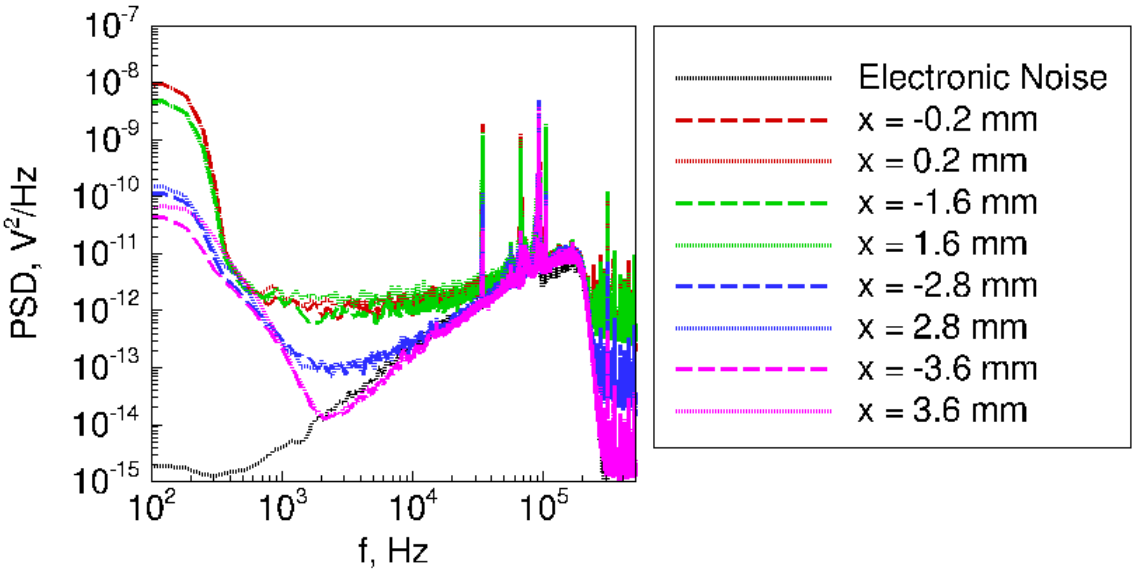

Figure 4.18. Power spectra of hot-wire measurements across a laser-generated perturbation. $p_0 = 95.8$ kPa, $T_0 = 311.1$ K, $\rho_\infty = 0.054$ kg/m^3.

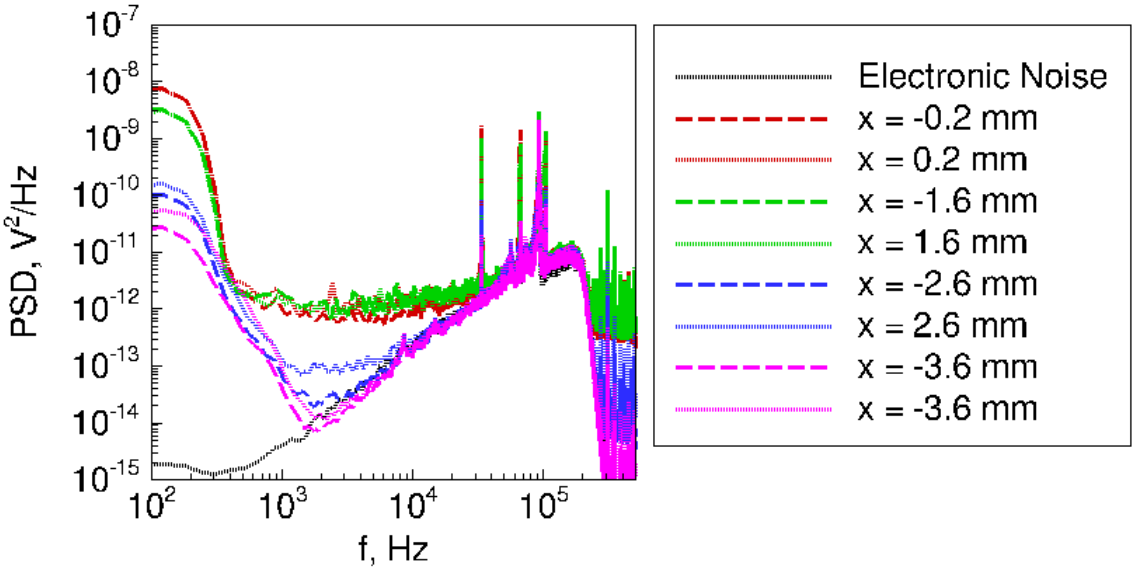

Figure 4.19. Power spectra of hot-wire measurements across a laser-generated perturbation. $p_0 = 86.2$ kPa, $T_0 = 310.9$ K, $\rho_\infty = 0.048$ kg/m^3.

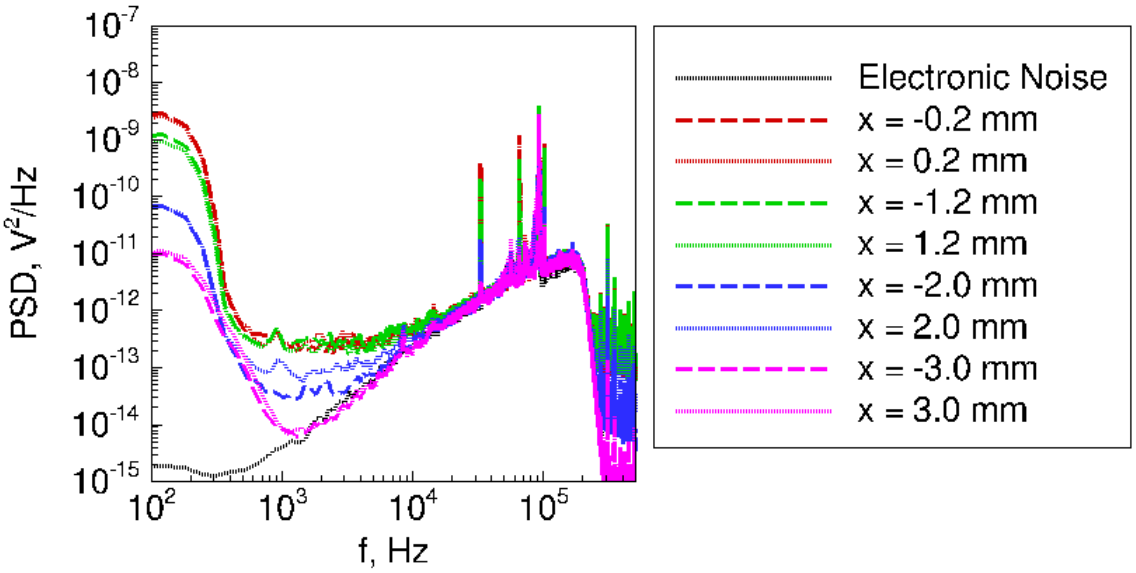

Figure 4.20. Power spectra of hot-wire measurements across a laser-generated perturbation. p_0 = 68.9 kPa, T_0 = 311.1 K, ρ_∞ = 0.039 kg/m^3.

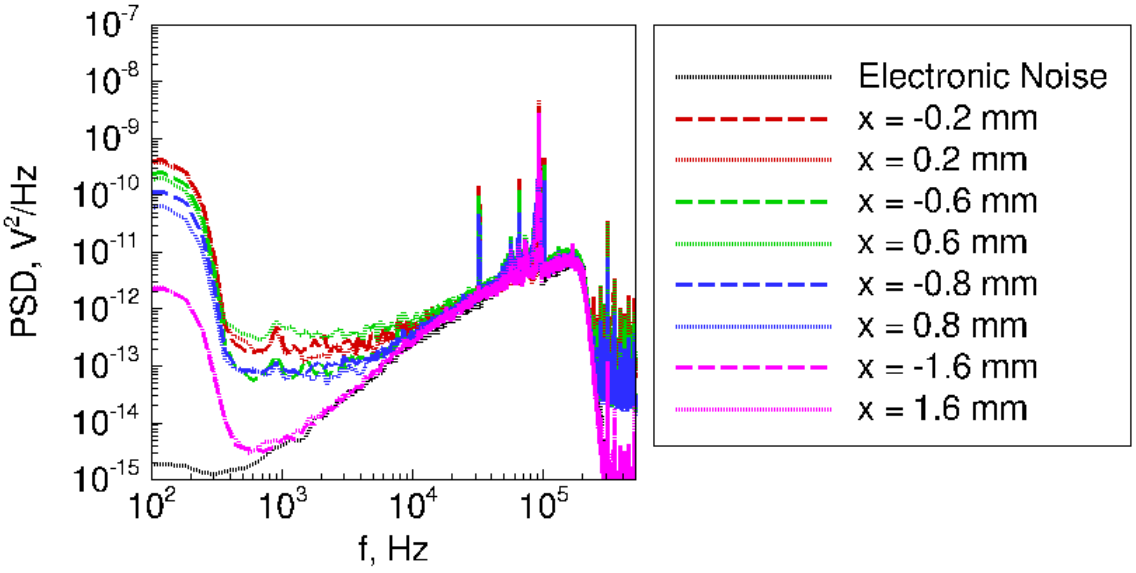

Figure 4.21. Power spectra of hot-wire measurements across a laser-generated perturbation. p_0 = 51.6 kPa, T_0 = 311.6 K, ρ_∞ = 0.029 kg/m^3.

4.2 Measurements with Deflectometry

The deflectometry technique used by McIntyre et al. [85] was used to make measurements in the PCT to resolve higher frequencies. The frequency of photosensors is typically on the order of a few megahertz, which was more than adequate to measure the passage of a 2–6 mm perturbation moving 675 m/s. The deflectometry measurements were used to provide a density-fluctuation measurement. The setup of this technique implemented the use of the existing schlieren system, with the modifications discussed in Chapter 2.2.5.

For these measurements, the BAM6QT perturbation-forming optics were used. A set of mirrors were mounted to the nozzle to reflect the focusing beam, as illustrated in Figure 4.22. This setup allowed for all elements of the BAM6QT perturbation-forming optics to be placed within the PCT test section. Only one set of windows provided optical access into the PCT. Thus, the laser beam axis and the schlieren optical system lay along the same axis. The Nd:YAG laser beam was terminated in a beam block to avoid damaging the schlieren camera. The presence of the perturbation-forming optics in the test section caused portions of the schlieren image to be blocked. The fully-saturated schlieren image (no knife-edge cutoff) is shown in Figure 4.23. The measurement survey region is marked in this figure with red text and was only about 60 mm long in the streamwise direction.

A vertical profile of the perturbation was taken at four different axial locations. The probe sensor was traversed in the $\pm y$-direction at $z = 90$, 110, 130, and 150 mm. These deflectometry profiles were taken 90° from the hot-wire profiles. The deflectometry technique only allowed a probing of the yz-plane. In comparison, the hot-wire setup only allowed for measurements to be made in the $\pm x$-direction. For all of the data shown here, the perturbation was created on the nozzle centerline at a location of $z = 35.9$ mm. Thus, $z = 90$, 110, 130, and 150 mm corresponds to $\Delta z_i = 54.1$, 74.1, 94.1, and 114 mm.

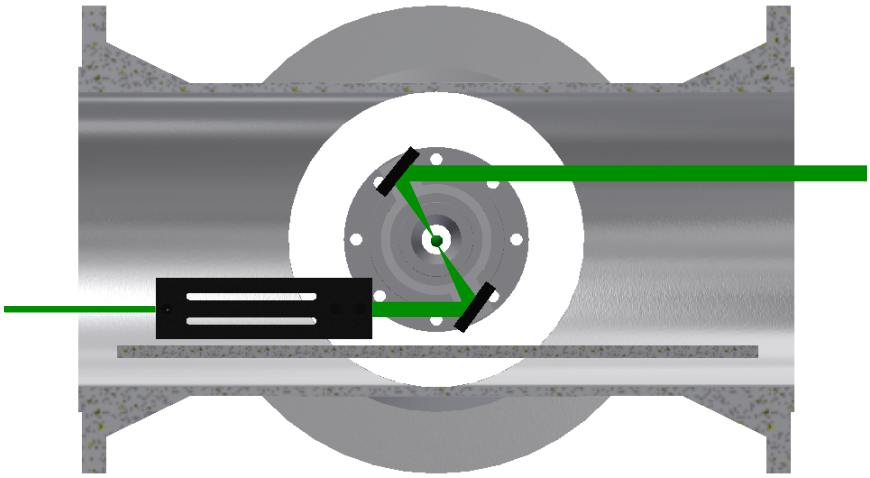

Figure 4.22. Perturbation-forming optics in PCT used to make deflectometry measurements. Laser beam runs from left to right. Looking upstream in PCT, flow out of page.

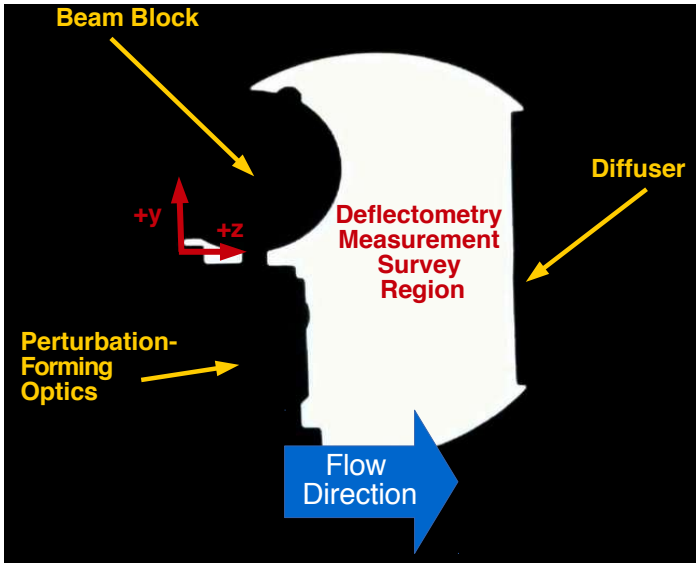

Figure 4.23. Schlieren image of PCT test section with shadows of important elements of the experiment.

A photosensor calibration was taken at the location of (z, y) = (110, 0) mm. The no-cutoff values were taken at each of the survey location points prior to each tunnel run. This value was used to scale the normalized photosensor calibrations discussed in Chapter 2.2.5. The no-cutoff values were recorded again after the run and averaged with the pre-run no-cutoff values. Typically there was a 2% change in values at most. The data analysis code used the averaged values to adjust the calibration for each survey point in case there was a larger deviation.

The knife edge in the schlieren system is oriented to provide horizontal cutoff of the schlieren source. This orientation of the knife edge relates the deflection measurements Δ_y to the density gradient in the vertical direction, $\partial\rho/\partial y$. The flowfield in the PCT with no forced perturbations should show a nonzero deflection Δ_y, and the deflection fluctuations Δ'_y should be nearly zero. In fact, the measurement of Δ'_y with no freestream laser perturbations should give an estimate of the measurement noise generated by flow through the jet. When no flow is present, the measurement of Δ'_y will give only the electronic noise.

Measurements were made in the test section with no freestream laser perturbations to obtain measurements of the noise created by the flow. These measurements were done at the same conditions as for measurements with laser perturbations. An example of the deflection fluctuation (Δ'_y) measured at the same three locations is given in Figure 4.24. The RMS fluctuations of the deflection over time is about 4 μm.

4.2.1 Raw Deflection Measurements of the Laser-Generated Perturbation

The signal-to-noise ratio was a concern for many of the deflectometry measurements made in the PCT. A low signal-to-noise ratio may create large numerical errors in integration. The measured effect of 150 different laser perturbations were averaged together to provide a larger signal-to-noise ratio. Due to the number of perturbations that had to be used, at least 15 seconds were required for each survey station. Furthermore, traversing the probe fiber across the schlieren image and writing the data

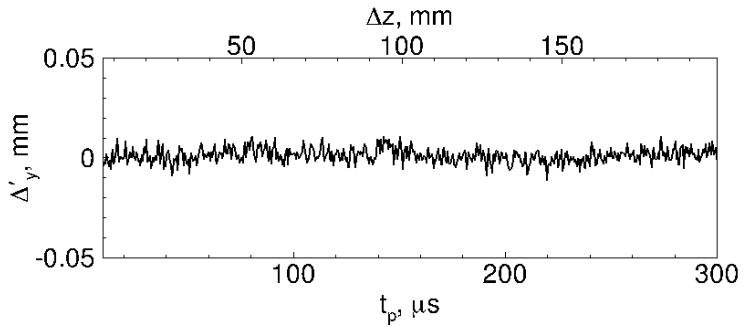

(a) $y = -1.5$ mm.

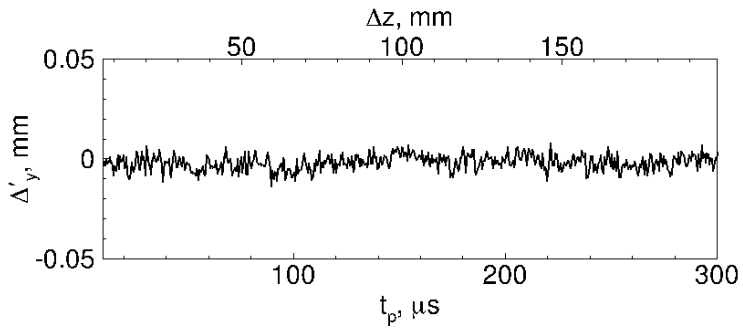

(b) $y = 0$ mm.

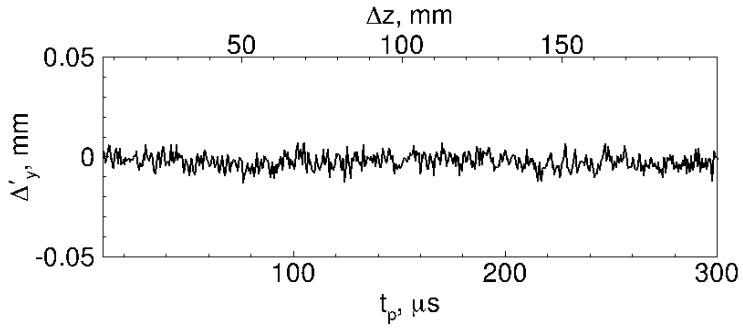

(c) $y = +1.5$ mm.

Figure 4.24. Example deflection fluctuation (Δ'_y) measurements at $z = 90$ mm. $p_0 = 97.4$ kPa, $T_0 = 310.9$ K, $\rho_\infty = 0.053$ kg/m^3, $M = 3.42$.

to a file requires time. The data were sampled at 2 MHz, so 5×10^7 data points were written for each measurement station. Thus, profiles at each z-station took up to 5 minutes.

Time traces using the deflectometry method provide a streamwise history of the deflection of the perturbation. Like the hot-wire measurements, these time traces can be converted to a distance using Equation 4.1. The deflection fluctuation measurements made at a single axial measurement station can be compiled into contour plots, as shown in Figure 4.25. This contour plot shows the deflection fluctuation (Δ'_y) measurements at $z = 90$ mm at $\rho_\infty = 0.053$ kg/m^3. This density corresponds to the maximum stagnation pressure tested. Two distinct lobes are seen in this contour plot. The upper lobe consists of positive Δ'_y values, which correspond to a positive $\frac{\partial \rho}{\partial y}$. The lower lobe consists of negative Δ'_y values, which correspond to a negative $\frac{\partial \rho}{\partial y}$. The lobes are separated by a region where there is hardly any deflection fluctuation, indicating that $\frac{\partial \rho}{\partial y} = 0$. The combination of these features suggests an axisymmetric shape.

An example of the deflection fluctuation values at various z-stations is shown in Figure 4.26. These line cuts of the deflection fluctuation Δ'_y are taken at the t_p associated with the center of the perturbation. The center of the perturbation is located by finding the maximum Δ'_y in each of the time traces. The t_p associated with the center of the perturbation increases with the z measurement station. This is expected because the perturbation convects with the freestream velocity. A compilation of the inverse Abel transforms were used to determine the velocity of the perturbation. The time of arrival of the perturbation was a mean of 663.7 m/s for the four different surveys shown in this chapter. Equation 4.1 shows that as the separation between the perturbation location and the measurement station increases, the t_p should also increase.

At the farthest downstream z-location, the deflection fluctuation measurements were only slightly larger than the deflection measurements without the laser perturbation. This low signal-to-noise ratio indicates that the perturbation may not be

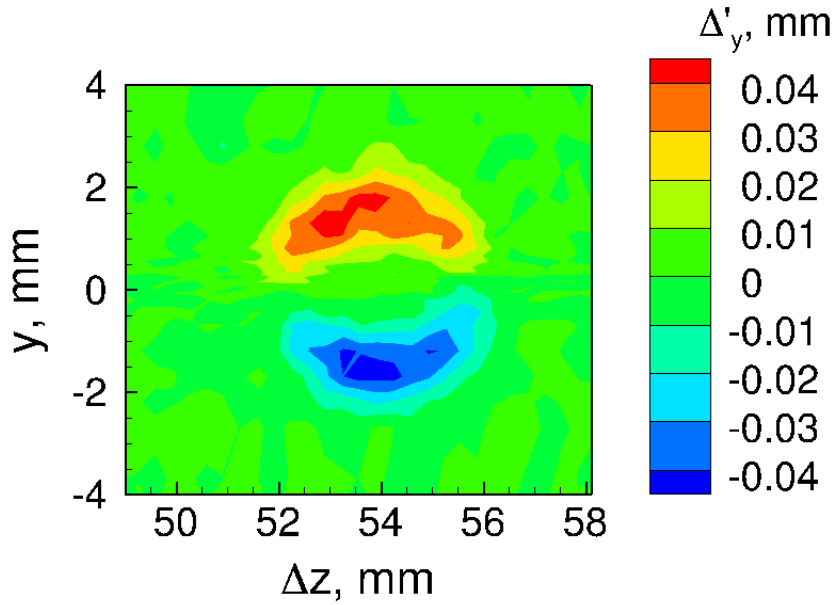

Figure 4.25. Example contour plot of deflection fluctation measurements. $p_0 = 96.6$ kPa, $T_0 = 310.8$ K, $\rho_\infty = 0.053$ kg/m^3, $M = 3.42$, $z = 90$ mm.

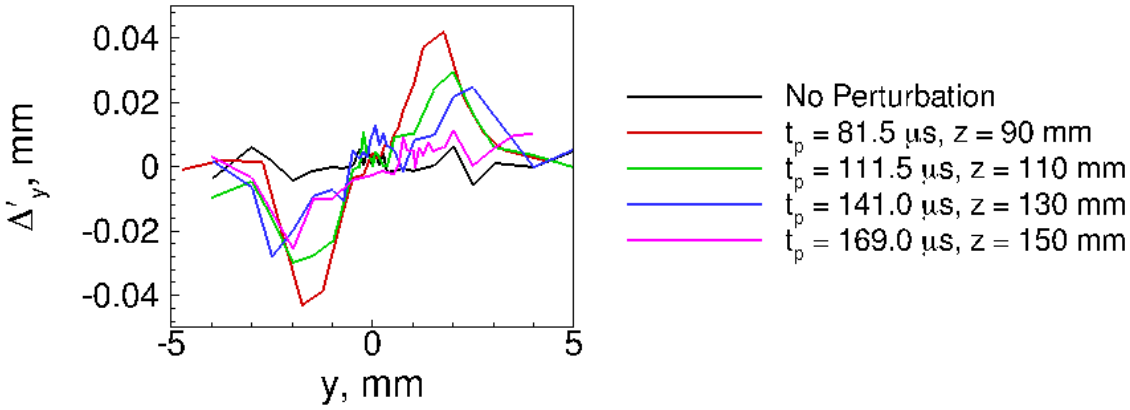

Figure 4.26. Example of deflection measurements at various z measurement stations. $p_0 = 96.6$ kPa, $T_0 = 310.8$ K, $\rho_\infty = 0.053$ kg/m^3, $M = 3.42$.

measurable at this z-station. The decrease in signal with increasing z-station indicates a decay in the perturbation amplitude over time. A qualitative comparison to the rough 1-D computations in Appendix A shows that this decay over time is expected.

The perturbation amplitude also appears to decrease with the freestream density. Figure 4.27 shows the deflection fluctuation y-profile at $t_p = 81.5$ μs after the laser pulse is fired. This time roughly corresponds to the time of arrival of the laser-generated disturbance when the probe is traversing in the y-direction at $z = 90$ mm—the axial station where these y-profiles were taken. The different lines represent the different freestream densities. The signal decreases as the freestream density decrease, so the perturbation is barely detectable at the lowest freestream density. The signal-to-noise ratio for this measurement technique is too low at the lowest density tested, and thus, yields very little information at this density.

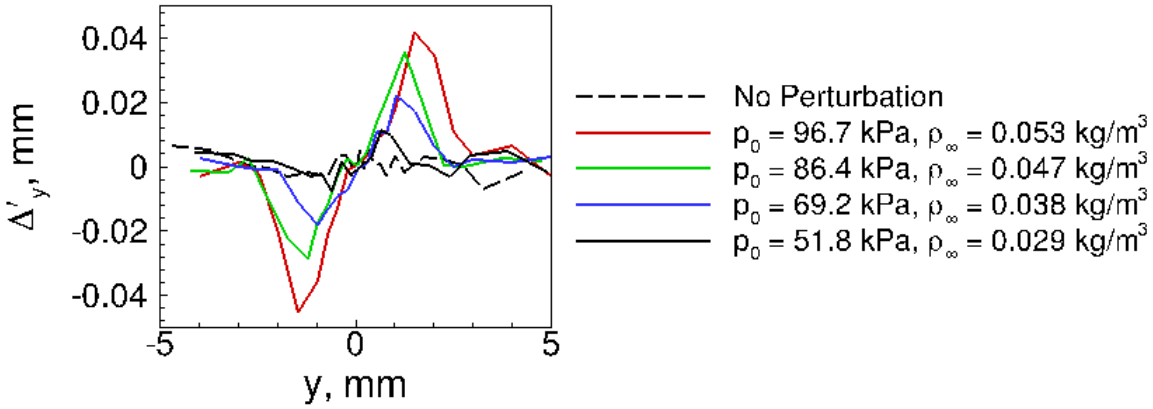

Figure 4.27. Example deflection measurements at various freestream densities. $z = 90$ mm, $t_p = 81.5$ μs, $M = 3.42$.

4.2.2 Use of the Inverse Abel Transform to Find Index of Refraction

Equations 2.11-2.13 define the inverse Abel transform. The value of α, or the angular deflection, is calculated using trigonometry. The ensemble-averaged time traces at each y survey point were used in the inverse Abel transform of the deflectometry measurements. The inverse Abel transform requires an integration in the vertical direction to provide a radial index of refraction profile. This is a result of the orientation of the knife edge in the schlieren. The vertical points used in the inverse Abel transform correspond to the same time after the laser pulse was fired, t_p. Simpson's rule is used to integrate across these spanwise points at t_p after the laser pulse is fired.

The integration across these points yields an index of refraction profile in the y-direction. The time after the laser pulse is fired can be converted to a distance to yield a contour plot of the perturbation. An example of the index of refraction profile for the highest-density case at $t_p = 81.5$ μs is shown in Figure 4.28. Here, the profile is of $(n-1) \times 10^6$. The inverse Abel transform calculates the value $(n-1)$, and the variation about this value is very small.

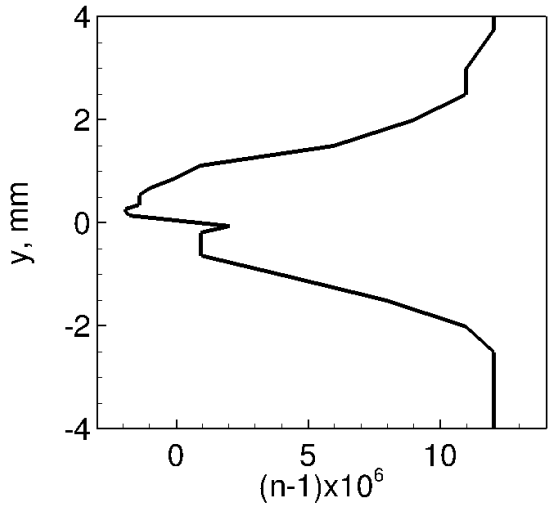

Figure 4.28. Index of refraction profile for $p_0 = 96.6$ kPa, $T_0 = 310.8$ K, $\rho_\infty = 0.053$ kg/m^3, $M = 3.42$ at $t_p = 81.5$ μs, $z = 90$ mm.

Figure 4.28 shows a problem with the data taken at the most upstream survey station. At 81.5 μs after the laser pulse occurs, the index of refraction is computed to be less than 1. An index of refraction less than 1 does not make physical sense when discussing neutral atoms and molecules.

This $n < 1$ phenomenon can be related to the physical properties of the disturbance. Ions and free electrons have a negative contribution to the index of refraction (Equation 2.17). Deflectometry measurements of the perturbation showed an increase in minimum index of refraction if the freestream density decreased or if the z measurement station increased. Hot-wire measurements show that decreased freestream densities create weaker perturbations, so fewer molecules are probably ionized in the creation of these perturbations. As the z-station increases, the ions have more time to recombine. At the most upstream survey location of $z = 90$ mm, about 80 μs have passed since the laser perturbation was created. At the most downstream survey location of $z = 150$ mm, about 170 μs have passed since the laser perturbation was created. Thus, the $n < 1$ phenomenon may be related to the presence of ions and electrons in the perturbation.

Profiles such as the one shown in Figure 4.28 were compiled to produce multiple profiles. These were plotted in Figure 4.29, offset from each other by an amount of time proportional to the time after the laser pulse is fired. The lines shown here are y-profiles ranging from 74.5–88.5 μs after the laser pulse has been fired.

Figure 4.30 shows the data in Figure 4.29 plotted as a contour plot. The scaling of the horizontal axis is 0.6616 times the scaling of the vertical axis. This scaling factor gives the contour plot the same relative divisions, as if the time scale had been converted to a distance using the freestream velocity. Figure 4.31 is a contour plot with the horizontal axis in units of distance, for comparison. These plots show a perturbation that is about 4 mm in diameter. Some peaks are seen in the perturbation around $t_p = 80$ μs ($\Delta z = 53$ mm) and $t_p = 83.5$ μs ($\Delta z = 55$ mm), but these are likely artifacts created by integrating the noisy measurements.

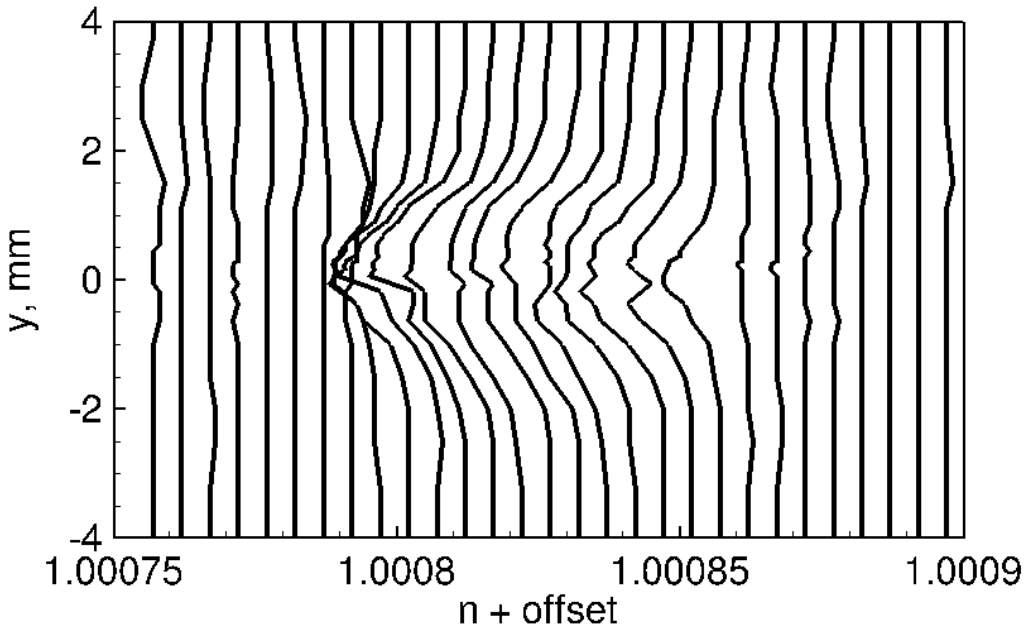

Figure 4.29. Multiple index of refraction profiles for $p_0 = 96.6$ kPa, $T_0 = 310.8$ K, $\rho_\infty = 0.053$ kg/m^3, $M = 3.42$, $z = 90$ mm at different times after the laser pulse is fired.

Figures 4.32 and 4.33 show perturbations at two lower freestream densities than that of Figure 4.30. Figure 4.32 shows a perturbation with fewer regions where the index of refraction is less than 1. Figure 4.33 shows a perturbation with regions where the index of refraction is always greater than 1. The signal-to-noise ratio at $p_0 = 69.0$ kPa was fairly poor and integration of these measurements produced a distorted shape in the contour plots. The lowest tested stagnation pressure is depicted in Figure 4.34, which shows that the disturbance is no longer discernible from the background noise.

The contour plots all show a perturbation with a roughly elliptical or circular shape. The frequency response of the measurement technique is on the order of 8 MHz, which should be fast enough to resolve the short duration of the laser perturbation. Thus, this perturbation is probably ellipsoidal or spherical, as previous measurements

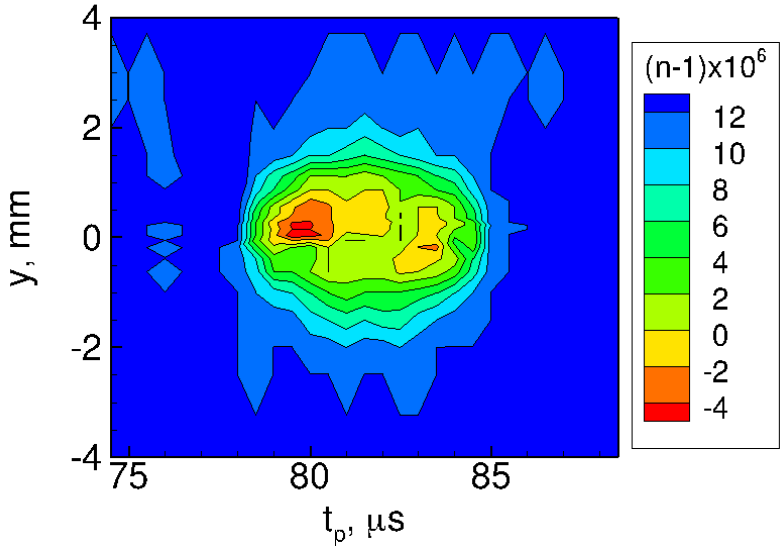

Figure 4.30. Contour plot of index of refraction for $p_0 = 96.6$ kPa, $T_0 = 310.8$ K, $\rho_\infty = 0.053$ kg/m^3, $M = 3.42$, $z = 90$ mm.

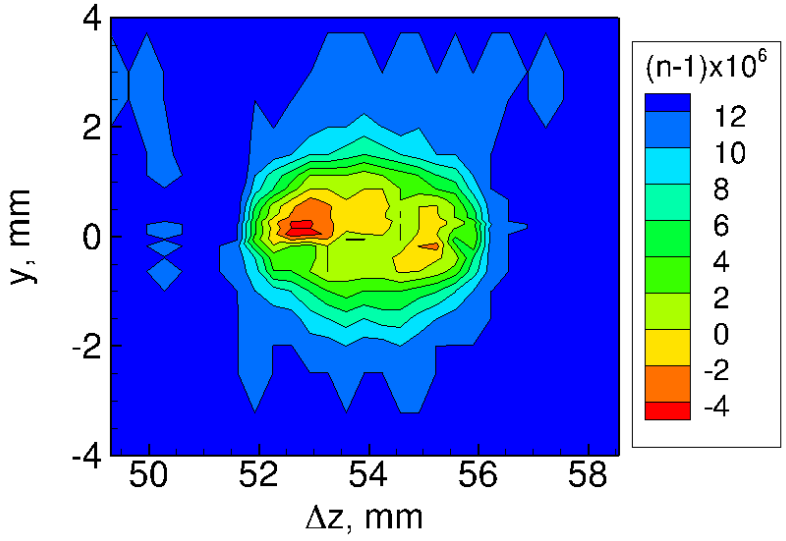

Figure 4.31. Contour plot of index of refraction for $p_0 = 96.6$ kPa, $T_0 = 310.8$ K, $\rho_\infty = 0.053$ kg/m^3, $M = 3.42$, $z = 90$ mm. Axes are in units of distance.

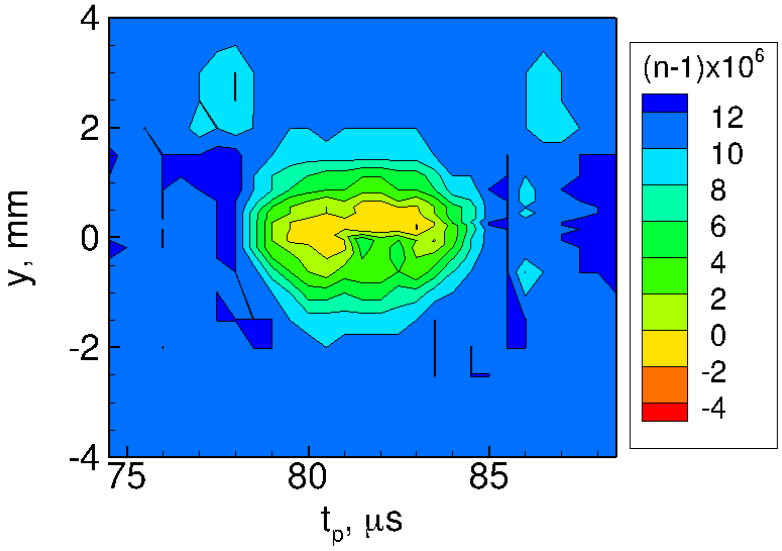

Figure 4.32. Contour plot of index of refraction for $p_0 = 86.4$ kPa, $T_0 = 311.1$ K, $\rho_\infty = 0.047$ kg/m^3, $M = 3.42$.

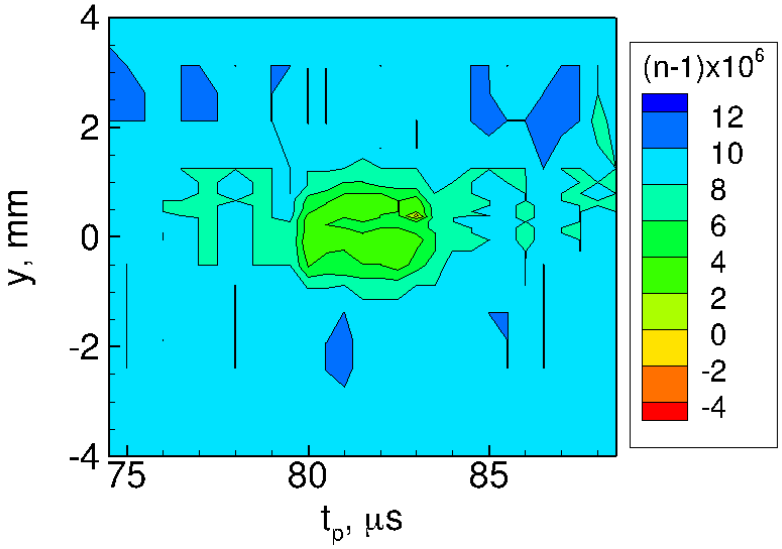

Figure 4.33. Contour plot of index of refraction for $p_0 = 69.0$ kPa, $T_0 = 311.1$ K, $\rho_\infty = 0.038$ kg/m^3, $M = 3.42$.

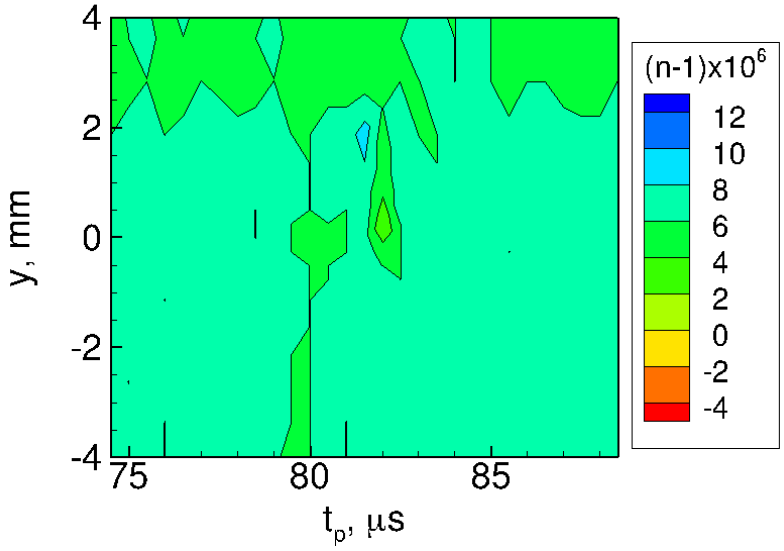

Figure 4.34. Example contour plot of index of refraction for $p_0 = 51.8$ kPa, $T_0 = 311.1$ K, $\rho_\infty = 0.028$ kg/m^3, $M = 3.42$.

by Salyer have suggested [37]. However, this measurement technique is limited by the signal-to-noise ratio and the need to assume an axisymmetric perturbation.

4.2.3 Use of the Gladstone-Dale Relation to Obtain Density Measurements

Density contours of the laser-generated perturbation that correspond to Figures 4.30–4.33 are shown in Figures 4.35–4.37, respectively. These contours were created by applying the Gladstone-Dale relation to the index of refraction. The Gladstone-Dale assumption assumes that there are no ions or electrons present in the measurement region. This assumption may not be true, as discussed in the previous section. However, the Gladstone-Dale relation can provide some insight into the density fluctuation created by the thermal disturbance. This relation essentially assumes that the density is proportional to $(n - 1)$.

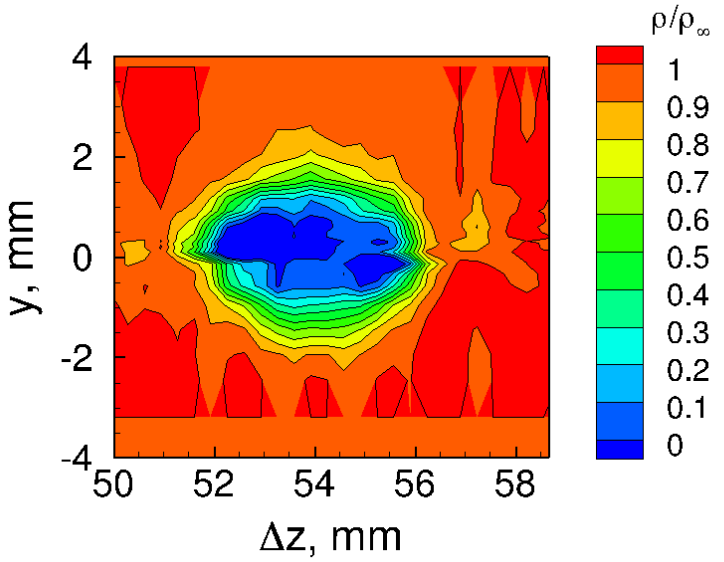

Figure 4.35. Density contour plot of freestream laser perturbation. $p_0 = 96.6$ kPa, $T_0 = 310.8$ K, $\rho_\infty = 0.053$ kg/m^3, $M = 3.42$, $z = 90$ mm.

Line cuts from these contour plots can also be taken to yield density profiles as shown in Figure 4.38. Figure 4.38(a) shows the variation in density profiles when surveys are taken at different axial stations. Figure 4.38(b) shows the variation in density profiles when the freestream stagnation pressure is varied. There was a large amount of noise in the measurements at the greatest Δz in Figure 4.38(a) and at the lowest stagnation pressure in Figure 4.38(b). Deflection measurements of the weaker perturbation have a poorer signal-to-noise ratio. The measured noise is then carried through the inverse Abel transform to produce the large noise at the center of the perturbation's index of refraction profile. This noise is carried through to the density profile because the Gladstone-Dale relation is only a scaling of the index of refraction.

Measurements taken closer to the perturbation at $z = 90$ mm at the highest stagnation pressures yield density profiles across the perturbation that do not seem physical. For example, Figure 4.38(b) shows the different stagnation pressures tested in the PCT at the survey location of $z = 90$ mm. At the highest stagnation pressure

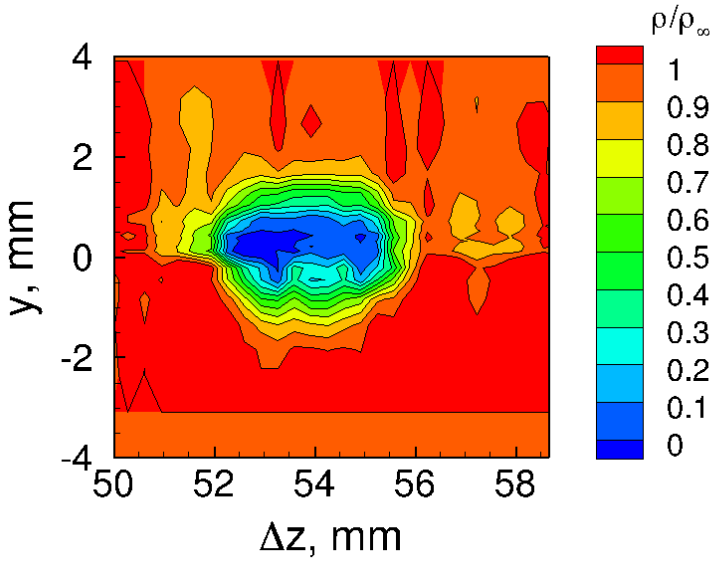

Figure 4.36. Density contour plot of freestream laser perturbation. $p_0 = 86.4$ kPa, $T_0 = 311.1$ K, $\rho_\infty = 0.047$ kg/m^3, $M = 3.42$, $z = 90$ mm.

shown ($p_0 = 96.6$ kPa), the density profile yields a negative density close to the perturbation centerline. At these next highest stagnation pressure shown ($p_0 = 86.4$ kPa), the density profile yields a near-zero density at the perturbation centerline. A negative density is non-physical, which indicates that the Gladstone-Dale relation is not applicable to the perturbation. However, the index of refraction inferred from the inverse Abel transform is still valid.

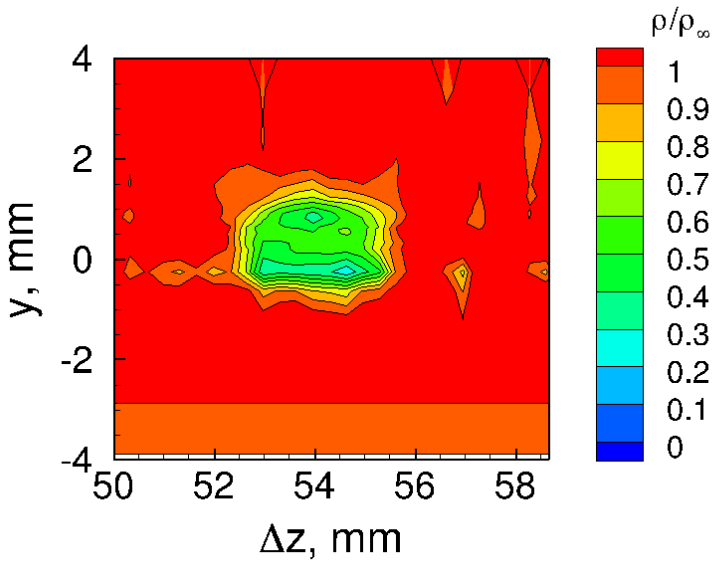

Figure 4.37. Density contour for $p_0 = 69.0$ kPa, $T_0 = 311.1$ K, $\rho_\infty = 0.038$ kg/m^3, $M = 3.42$, $z = 90$ mm.

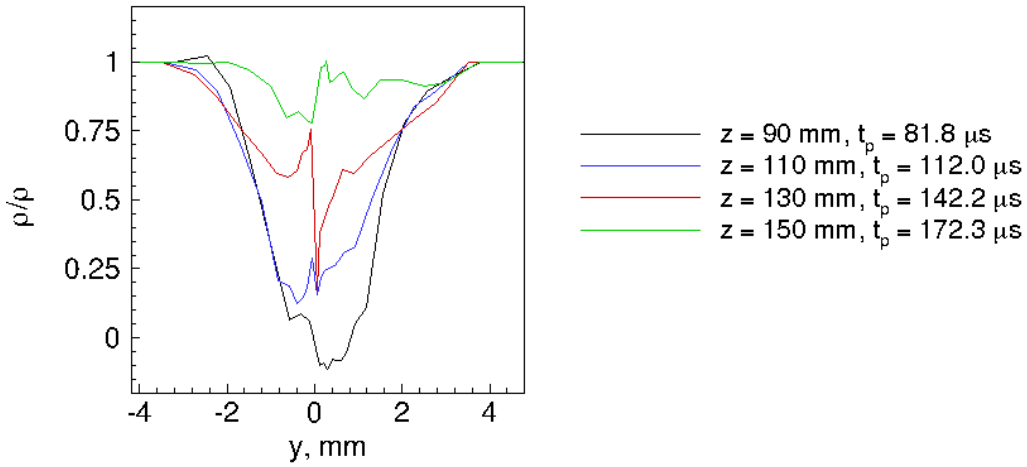

(a) $p_0 \approx 97$ kPa, $T_0 \approx 311$ K, $\rho_\infty \approx 0.05$ kg/m^3, different measurement positions.

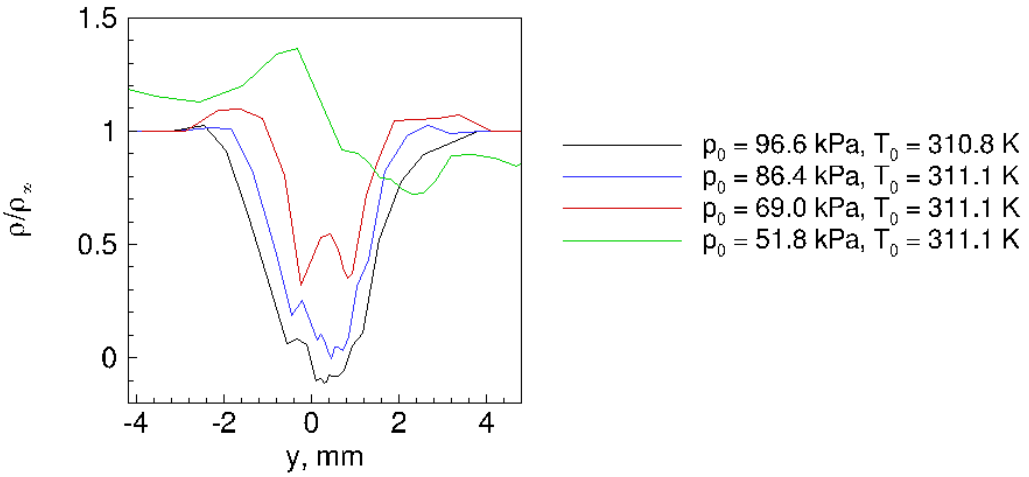

(b) Density distribution at $z = 90$ mm for different freestream stagnation pressures.

Figure 4.38. A comparison of density contour plots for the laser-generated perturbation, created from deflectometry measurements made in the PCT ($M_\infty \approx 3.42$). 150 shots averaged.

CHAPTER 5. MEASUREMENTS OF THE FREESTREAM DISTURBANCE IN MACH-6 FLOW

The BAM6QT traverse system only allows for movement in the y-direction along the vertical centerplane. The short run times in the BAM6QT required an entire run of the BAM6QT to be dedicated to a single y-station in the profile. The run-to-run variation in the freestream conditions needed to be reduced as much as possible. Previous experiments have shown that the nozzle wall temperature increases during the day [94]. Wheaton found that the top of the nozzle tended to have a higher temperature than the bottom of nozzle. The temperature of the nozzle wall can affect the boundary layer thickness. A difference in boundary layer thickness around the azimuth of the nozzle can create flow angularity. To limit the run-to-run variation, the BAM6QT was allowed to cool after each run. Typical operational procedures allow the next run to be set up almost immediately after a run. Anywhere from 30 minutes to a couple of hours were allowed to elapse between the end of a run and the setup of the next run.

Each run takes about 1 hour to set up, especially when filling to higher stagnation pressures or when allowing for the tunnel to cool between runs. For a typical high-pressure run, the run becomes subsonic after about 4–5 seconds, but an increase in freestream noise begins around 1.7 seconds after the run starts. This increase in noise was seen previously by Steen [92], but occurred around 2 s for lower stagnation pressures. Turbulent bursts, which may interfere with the experiment, are also more prevalent at higher stagnation pressures. After removing laser pulses affected by turbulent bursts or increased noise, only 10–15 freestream perturbations can be used for analysis for each run in the tunnel.

Each spanwise profile of the perturbation requires multiple tunnel runs, so the measurement technique must be robust. The violent startup and shut down processes

in the BAM6QT do not allow delicate hot-wire probes to be used for measurements of the laser perturbation. Deflectometry measurements could not be made in in the BAM6QT either, because a schlieren system does not exist. Thus, the measurements made in the PCT could not be duplicated in the BAM6QT. Rather, the measurements in the two facilities had to complement each other, so Kulite and PCB pressure transducer probes were used to characterize the perturbation in the BAM6QT.

The flat laser window insert was used in the BAM6QT wall with the perturbation-generating optics to create the laser-generated perturbations. Some disturbances were generated in the freestream by the Mach wave from the window, as previously discussed in Chapter 3. Measurements of the freestream laser-generated perturbation were made upstream of the Mach wave disturbance measured in Chapter 3. Thus, these disturbances did not cause a detectable interference with the profile measurements.

5.1 Example Time Traces of the Perturbation

5.1.1 Example Kulite Probe Measurements

Profiles of the freestream perturbation were made with a Kulite XCQ-062-15A B-screen sensor. The Kulite sensor that was used has a resonant frequency of about 325 kHz. To reduce the effect of this resonance in the data analysis, an 8-pole Butterworth low-pass filter with a 200-kHz cutoff frequency was applied to the data in post-processing. Each y-station in the profile consists of an average of 10 different laser pulses. An example of the measured response of a single laser-generated disturbance is shown in Figure 5.1. In this trace, the probe was positioned on the centerline of the perturbation at $z = 1.965$ m for a $\Delta z_i = 50.0$ mm. At about $t_p = 46.0$ μs, the weak shock wave is measured by the Kulite probe. At about $t_p = 60.0$ μs, the thermal disturbance is measured by the Kulite probe. The other side of the weak spherical shock wave may be present at $t_p = 74.0$ μs, but this could also be due to ringing in the Kulite sensor. due to the large thermal disturbance.

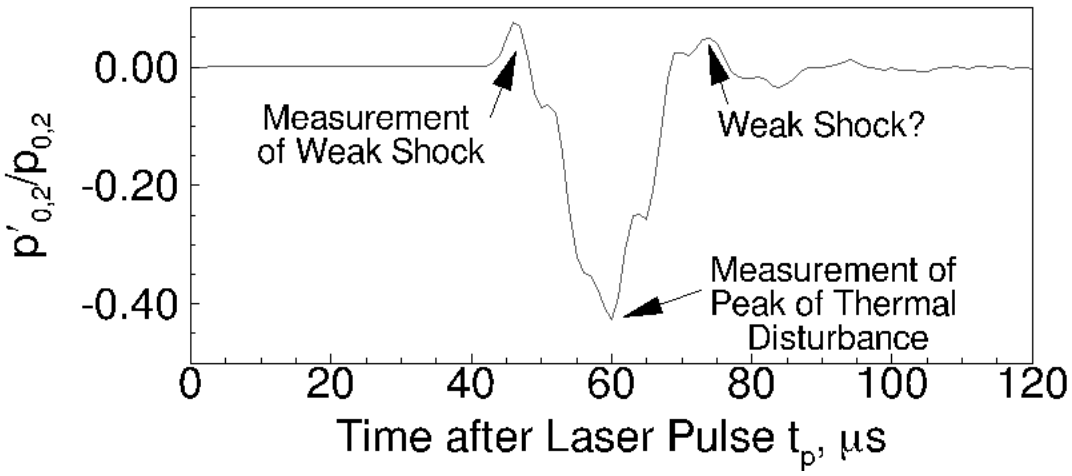

Figure 5.1. Example of a Kulite pitot-probe measurement of a laser-generated disturbance. Laser shot number 7, run number 14-09: $p_0 = 1103$ kPa, $T_0 = 429.3$ K, $\rho_\infty = 0.040$ kg/m^3, $y = 0$ mm, $t = 0.7259$ s, $z = 1.965$ m.

The BAM6QT experiences a stair-step decrease in Reynolds number due to an expansion wave reflecting between the end of the driver tube and the contraction, as discussed in Chapter 2.1. Thus, the first usable laser perturbation and the last usable laser perturbation occur at two different Reynolds numbers, which may differ by as much as 10%. Tests in the PCT showed that a change in freestream density can have an effect on the amplitude and dimensions of the perturbation. Therefore, an ensemble-average of the measurements of the freestream perturbation by the Kulite probe may not be representative of each individual trace.

The individual Kulite probe measurements after each laser shot in a single run are shown in Figure 5.2. Each pressure trace is offset by an amount proportional to t, the time at which the laser pulse occurs after the tunnel starts. The traces only vary in amplitude by as much as 2.5% in the example shown. Laser pulses at $t = 0.9259$ s and 1.5259 s occurred shortly after turbulent bursts on the nozzle wall occurred, and thus, were removed by the data analysis code. The time of arrival of the thermal disturbance never varied more than 1–2 μs from shot to shot. This time

of arrival variation was similar to the time of arrival variation seen by Schmisseur [43] and Salyer [25].

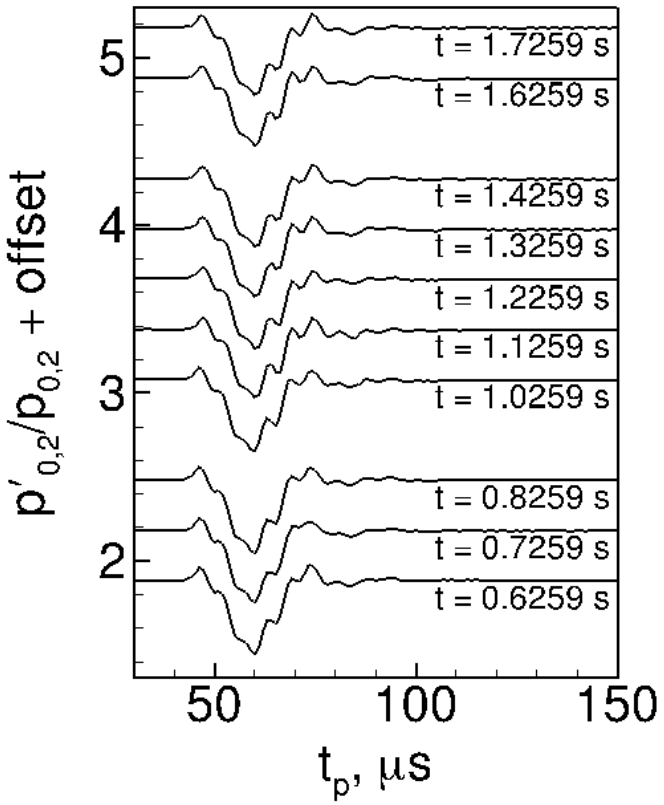

Figure 5.2. An example of the variation from shot-to-shot of the time traces. Laser shot numbers 6–8, 10–14, 16, 17. Run number 14-09: $p_0 = 1070$ kPa, $T_0 = 425.6$ K, $\rho_\infty = 0.040$ kg/m^3, $z = 1.965$ m.

An ensemble average of the 10 available traces shown in Figure 5.2 is given in Figure 5.3. The ensemble average is plotted over each of the individual traces from each laser shot. The ensemble average is a good representation of each of the individual traces, as it is difficult to distinguish between the average and each of the individual traces. Thus, ensemble averages of the perturbation can be useful representations, at least for some cases, despite the changing freestream conditions.

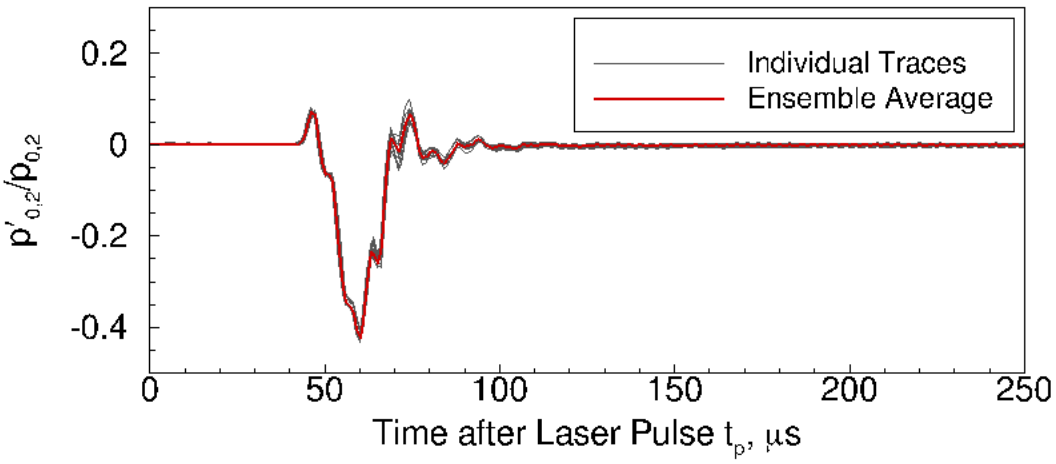

Figure 5.3. Ensemble average of the available shots in Figure 5.2 for run number 14-09: $p_0 = 1070$ kPa, $T_0 = 425.6$ K, $\rho_\infty = 0.040$ kg/m^3, $z = 1.965$ m. Laser shot numbers 6–8, 10–14, 16, 17.

5.1.2 Example PCB Probe Measurements

Only one profile of the freestream perturbation was made with a PCB 132A31 probe. The probe was positioned on the centerline of the perturbation at $z = 2.145$ mm for a $\Delta z_i = 219$ mm. Only one PCB probe exists, so only farther aft measurements could be made with this probe. The measurements were sampled at 5 MHz for 5 s. An in-line PCB 482A22 signal conditioner was used with the PCB sensor. The signal conditioners have built-in high-pass filters, with a cutoff frequency at 11 kHz.

An example of the centerline measurements of the disturbance is shown in Figure 5.4. This plot shows the measured PCB response to 10 different laser shots made in the BAM6QT. The arrival time of the perturbation appears to increase as the tunnel run time t increases. Again, this is probably due to the stagnation temperature decreasing with each reflection of the expansion wave. More on this effect is discussed in the next section.

The ensemble average of the traces shown in Figure 5.4 is shown in Figure 5.5. This plot shows that the ensemble average of the PCB traces removes some of the

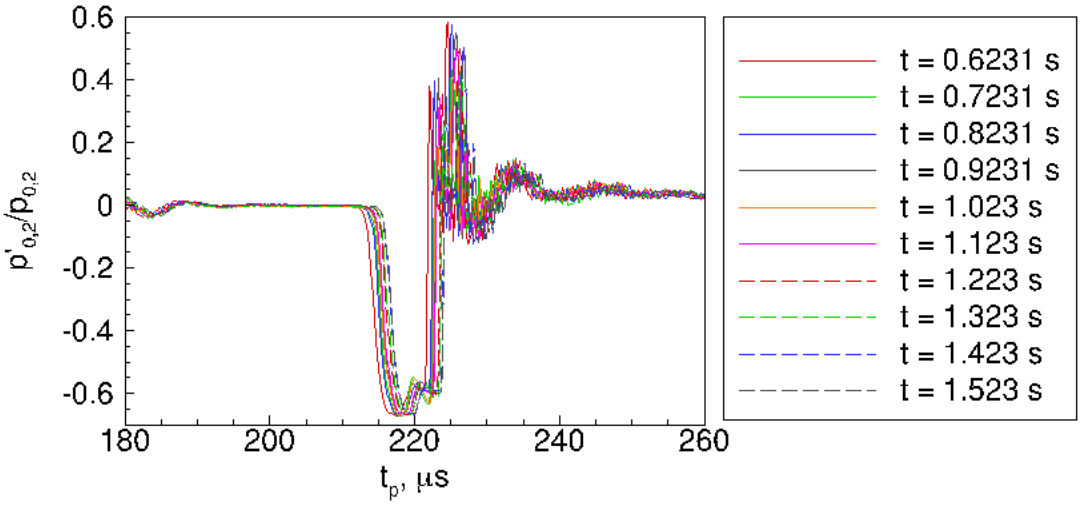

Figure 5.4. A plot of laser perturbations made during a single run. Laser shot numbers 6–15. Run number 16-36: $p_{0,i} = 1118$ kPa, $T_{0,i} = 429.8$ K, $\rho_{\infty,i} = 0.047$ kg/m^3, $z = 2.145$ m, $y = 0$.

effects of sensor resonance around 225 μs after the laser pulse has been fired. The ensemble averaging also averages out the changes in the arrival time of the freestream perturbation.

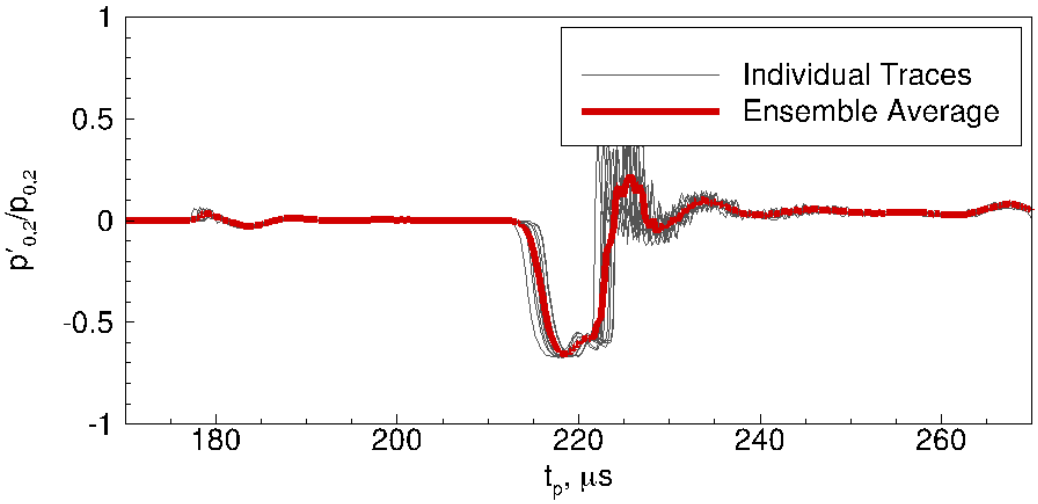

Figure 5.5. Ensemble average of 10 laser perturbations made during a single run. Laser shot numbers 6–15. Run number 16-36: $p_{0,i} = 1118$ kPa, $T_{0,i} = 429.8$ K, $\rho_{\infty,i} = 0.047$ kg/m^3, $z = 2.145$ m, $y = 0$.

5.2 Time of Arrival of the Laser Perturbation in Probe Measurements in the BAM6QT

5.2.1 Speed of the Perturbation

Centerline measurements of the perturbation were made at $z = 1.965$ m and 2.019 m with the Kulite probe and at $z = 219.0$ mm with the PCB probe. These correspond to distances of $\Delta z_i = 50.0$ mm, 103.5 mm, and 219.0 mm between the probe head and the location where the perturbation is generated. One repeat run was made at $\Delta z_i = 103.5$ with the Kulite probe. The centerline measurements taken at these three streamwise stations in the tunnel can provide information on the speed of the disturbance and the change in amplitude of the disturbance.

The time of arrival of the perturbation can be used to calculate the speed of the freestream perturbation. The time of arrival of the shock front can be defined as the maximum of the first portion of the perturbation ($t_{p,s}$) or as the 10% rise time of the peak ($t_{r,s}$). The 10% rise time is the time at which the pressure measurement reaches 10% of the maximum amplitude. A similar process can be used to find the time of arrival of the thermal disturbance. However, the 10% rise time of the thermal disturbance ($t_{r,t}$) is not always easily distinguishable due to resonance in the sensor, so it will not be considered here. The times for the 10% rise time of the weak shock ($t_{r,s}$), the maximum of the weak shock ($t_{p,s}$), and the minimum of the thermal disturbance ($t_{p,t}$) are illustrated in a representative trace in Figure 5.6. Perturbations unaffected by turbulent bursts created between $t = 0.4$–1.7 s were used to determine these values. The average values and the standard deviation of these parameters are recorded with the corresponding measurement distance Δz_i in Table 5.1 for each measurement made on the perturbation centerline.

The speed of the freestream perturbation can be found in two ways: by assuming a constant speed or by finding a linear least-squares fit through the data. When a constant speed is assumed, the speed of a disturbance can be found by dividing

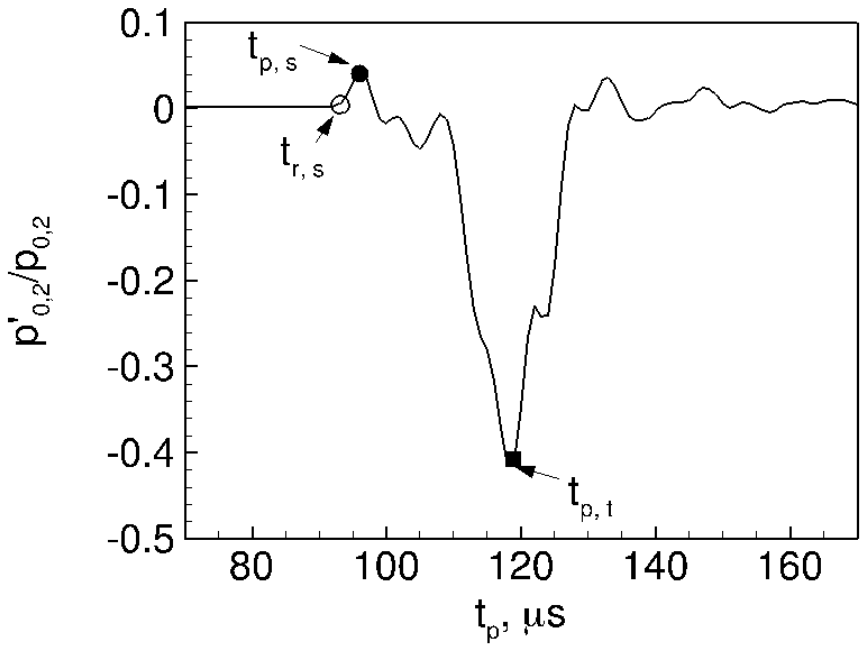

Figure 5.6. Schematic of time of arrival parameters for an example centerline trace at $z = 2.019$ m. $p_{0,1} = 1071$ kPa, $T_0 = 421.3$ K, $\rho_\infty = 0.039$ kg/m^3.

Table 5.1 Table of average arrival times for different portions of the freestream perturbation in the BAM6QT.

Probe Distance Δz_i, **mm**	**Mean Shock Rise Time** $\overline{t_{r,s}}$, μ**s**	**Standard Deviation** $\sigma\,(t_{r,s})$, μ**s**	**Mean Shock Peak Time** $\overline{t_{p,s}}$, μ**s**	**Standard Deviation** $\sigma\,(t_{p,s})$, μ**s**	**Mean Thermal Peak Time** $\overline{t_{p,t}}$, μ**s**	**Standard Deviation** $\sigma\,(t_{p,t})$, μ**s**
50.0	42.0	0.77	46.4	0.49	59.9	0.30
103.5	92.8	0.56	96.5	0.50	118.7	0.45
103.5	92.6	0.48	95.9	0.64	117.9	0.80
219.0	210.5	0.83	211.1	0.86	251.3	1.04

Δz_i by the times of arrival summarized in Table 5.1. The speed of the weak shock disturbance is approximated by using the 10% rise time

$$u_{r,s} = \frac{\Delta z_i}{t_{r,s}} \tag{5.1}$$

or by using the peak time

$$u_{p,s} = \frac{\Delta z_i}{t_{p,s}} \tag{5.2}$$

where the subscript s denotes a quantity corresponding to the shock, r denotes the rise time, and p denotes the peak time. The speed of the thermal disturbance is approximated by

$$u_{p,t} = \frac{\Delta z_i}{t_{p,t}} \tag{5.3}$$

where the subscript t denotes a quantity corresponding to the thermal disturbance. These equations were used to determine the speed for each laser shot during a run at each Δz_i. The table of the mean and standard deviation of the calculated speeds is given in Table 5.2. The overall mean and standard deviation values are given in the last row.

Table 5.2 Table of average speeds found by dividing Δz_i by the arrival time of the freestream perturbation in the BAM6QT.

Probe Distance Δz_i, mm	**Mean Shock Rise Speed $\overline{u_{r,s}}$, μs**	**Standard Deviation $\sigma(u_{r,s})$, μs**	**Mean Shock Peak Speed $\overline{u_{p,s}}$, μs**	**Standard Deviation $\sigma(u_{p,s})$, μs**	**Mean Thermal Peak Speed $\overline{u_{p,t}}$, μs**	**Standard Deviation $\sigma(u_{p,t})$, μs**
50.0	1191	22.5	1078	11.3	834.8	4.23
103.5	1116	6.96	1073	5.77	871.9	3.46
103.5	1117	6.02	1080	7.46	877.7	6.16
219.0	1040	4.12	1038	4.37	871.6	3.74
Overall	1108	52.7	1065	19.3	866.4	15.9

The constant-speed method yields a shock speed of $u_{r,s} = 1108$ m/s or $u_{p,t} = 1065$ m/s. The nominal stagnation temperature of the nominally Mach-6 tunnel is 433 K, which yields a freestream speed of sound of 145.7 m/s. The nominal freestream sound speed was used to calculate the inferred Mach number of the weak shock disturbance. The inferred Mach number of the weak shock disturbance for these speeds is about $M_{r,s} = 7.6$ and $M_{p,s} = 7.3$, respectively. These inferred Mach numbers are 8.6% and 4.4% higher than the nominal value of $M = 7$ for a weak shock wave. The inferred Mach number may be higher for a number of reasons. The stagnation pressure and temperature at which the measurements were made are near the condensation limit of air, so the accuracy of the isentropic and perfect gas relations used may be in question. A 1% error in the pitot measurements can also create a 1.0–6.5% error in the calculation of Mach number [92]. Furthermore, the weak shock wave may start out supersonic before decaying to an acoustic wave, so the speed may not be constant over time. Thus, the assumption of a constant speed yields large errors. The thermal perturbation speed is 866.4 m/s and has a standard deviation of about 5.95 m/s. This speed corresponds to $M = 5.95$ using the nominal BAM6QT temperature. This is 0.9% lower than the nominal Mach number of 6, which is a small difference.

The speed of the freestream perturbation can also be found using a linear least-squares fit comparing the relative probe position Δz_i and the arrival times given in Table 5.1. The least-squares fit used the time of arrival of each laser shot, not just the average time of arrival at each location. The speeds found through the linear least-squares fit are given in Table 5.3. Using the 10% rise time of the shock yields a shock speed of 994.1 m/s. This corresponds to an inferred Mach number of 6.82, which is 2.5% different from $M = 7$. Using the peak time of the shock yields a shock speed of 1018 m/s. This corresponds to an inferred Mach number of 6.99, which is 0.2% different from $M = 7$. These shock speeds are reasonable speeds for an acoustic disturbance in Mach-6 flow. Using the peak time of the thermal disturbance yields a thermal disturbance speed of 877.4 m/s. This corresponds to an inferred Mach number of 6.02, which is 0.3% different from the nominal Mach number.

The disturbance speeds found with the linear least-squares fit to the data agree better to the design conditions than when the constant-speed method was used. This is expected because the least-squares fit does not consider data very close to where the perturbation is generated. At distances farther from the location where the perturbation is generated, the shock wave has time to decay into an acoustic wave.

Table 5.3 Parameters for least-squares fit through data points summarized in Table 5.1.

Parameter	**Speed of Perturbation (Slope) u, m/s**	**Offset, mm**	**Coefficient of Determination R^2**
10% rise of shock response $t_{r,s}$	994.1	0.010	1.00
Maximum shock response $t_{p,s}$	1018	0.005	1.00
Minimum thermal response $t_{p,t}$	877.4	0.001	1.00

The least-squares fit provides freestream velocities of the weak shock and thermal disturbance that agree best with the nominal values. The peak time of arrival provided the closest fit to the nominal values. The velocity of the thermal disturbance is probably very close to the nominal freestream speed. Theory suggests that the thermal disturbance should convect with the freestream, and both methods used here to find the disturbance speed were close to the nominal freestream speed, with less than 1% difference.

5.2.2 Shot-to-Shot Changes in the Freestream Perturbation

The freestream perturbation showed some variation in its time of arrival and amplitude. The shot-to-shot changes in the time of arrival of the perturbation were examined for probe measurements in the BAM6QT. These analyses are for measurements made at a single location in a single run. Several factors can affect the measurement of these freestream disturbances. The decreasing freestream conditions

have the ability to cause an increase in the time of arrival of the disturbance at the probe head. Slight vibrations in the probe may cause small misalignments to the freestream perturbation, which affects the time of arrival of the disturbance detected by the probe. The location at which the perturbation is formed may also vary slightly from shot to shot. Problems with timing in the electronics are also possible.

Measurements of the response to the first usable laser shot are cross-correlated to the response to subsequent laser shots in the run. The delay time found in the cross-correlation algorithm is used to determine changes in the shot-to-shot time of arrival. Thus, all of the changes in time of arrival are given with respect to the time of arrival of the first usable laser perturbation within a run.

The use of the cross-correlation method in the Kulite probe measurements shows at most a 2 μs variation in the perturbation arrival time. This change in arrival time over the course of the run is plotted in Figure 5.7. This change in perturbation arrival time is similar to what both Schmisseur and Salyer saw in the PQFLT. In the BAM6QT, the freestream temperature decreases as the run time increases. Thus, the freestream velocity also decreases during the run. The Kulite sensors do not appear to capture the effect of the changing conditions, probably due to the limited frequency response of the sensor. However, the amount of change in time of arrival appears to increase over the run time.

Changes in the shot-to-shot time of arrival were also seen in the PCB probe measurements of the freestream laser perturbation. Figure 5.8 shows the change in shot-to-shot arrival time as the run increases. The maximum difference in the time of arrival of the perturbation is about 4.2 μs, about twice as much as what was observed in the Kulite measurements. Furthermore, this change in the perturbation arrival time appears to increase fairly linearly with the time after the tunnel starts. The linear increase in time of arrival suggests a relation with the decrease in the freestream velocity.

The speed of the disturbances are calculated using Equations 5.1 and 5.3 to determine if the amount of change in the time of arrival is related to the drop in freestream

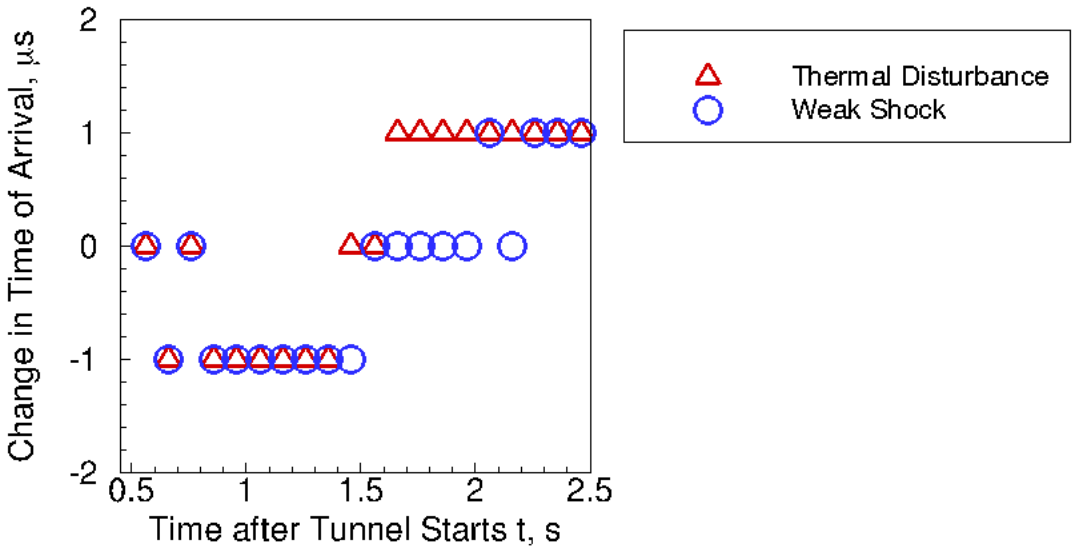

Figure 5.7. Shot-to-shot changes in arrival time of perturbation measured with a Kulite probe. Laser shot numbers 5–24, run number 14-42: $p_{0,i} = 1134.2$ kPa, $T_{0,i} = 435.6$ K, $\rho_{\infty,i} = 0.047$ kg/m^3, $M = 6.0$, $\Delta z_i = 103.5$ mm, $y = 0$ mm.

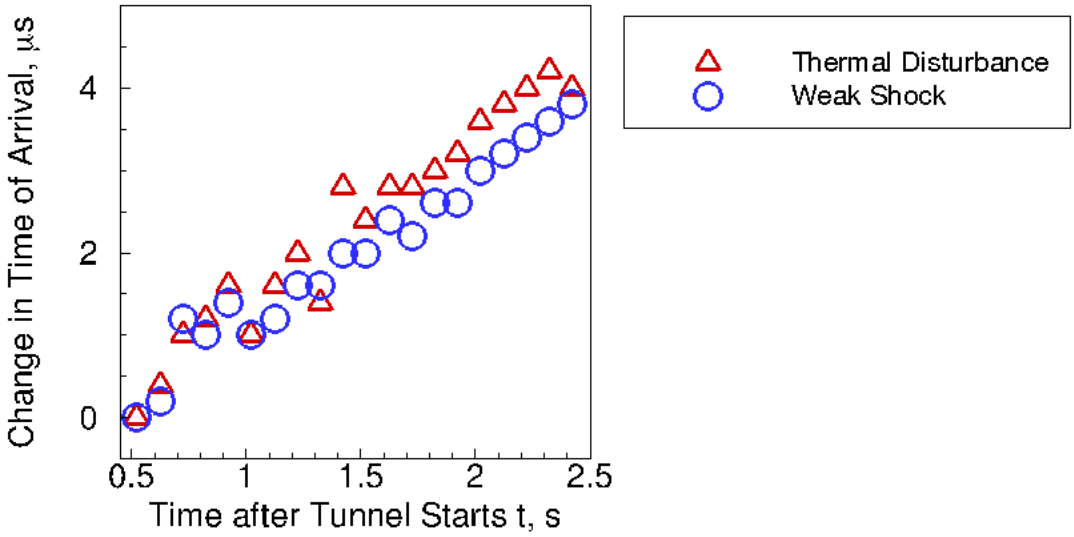

Figure 5.8. Changes in shot-to-shot time of arrival for PCB probe measurements as a function of time. Laser shot numbers 5–24, run number 16-36: $p_{0,i} = 1118$ kPa, $T_{0,i} = 429.8$ K, $\rho_{\infty,i} = 0.047$ kg/m^3, $z = 2.145$ m, $y = 0$.

velocity during the run. A linear least-squares fit is made to the data and plotted over the inferred disturbance speeds in Figure 5.9. The inferred speed of each laser shot is given by the open symbols. Red triangles represent the speed of the thermal perturbation and blue circles represent the speed of the weak shock wave emanating from the perturbation. A least-squares fit to the data is given by the dashed lines. The solid lines represent the nominal freestream velocity of the tunnel and the nominal velocity of a fast acoustic wave traveling at $M = 1$ relative to the freestream. The nominal freestream velocity is calculated using the measured freestream total pressure $p_{0,1}$, the initial stagnation temperature $T_{0,i}$, the isentropic relations, and the perfect gas equation. The overall trend of the data shows the decrease in the speed of the disturbance over time is about the same as the decrease of the nominal freestream speed in the tunnel. The 4.2 μs increase in disturbance arrival time is likely caused by decreasing temperature in the tunnel.

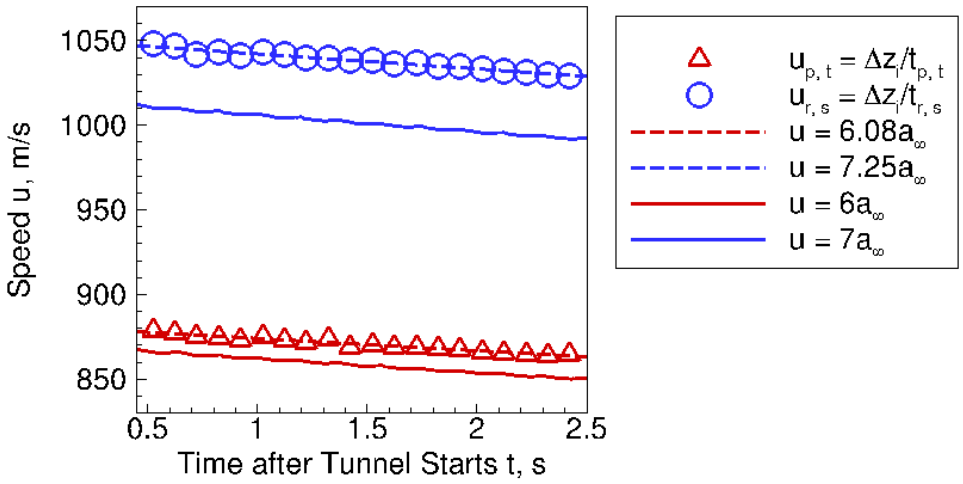

Figure 5.9. Speed of laser-generated disturbances measured by PCB probe compared to the nominal freestream speed.

The least-squares fit to the thermal disturbance data shows that the disturbance appears to travel at about $M = 6.09$. This is a 1.3% deviation when comparing the speed of the thermal disturbance to the nominal freestream Mach number of 6. A least-squares fit to the shock disturbance data shows that the weak acoustic

disturbance travels at $M = 7.25$. This is a 3.7% deviation when compared to the nominal speed of a fast acoustic wave in the freestream ($M = 7$).

Measurements in the PCT also showed that the perturbation diameter and amplitude appears to change with the freestream conditions. The BAM6QT stagnation pressure drops during the run, which causes the freestream Reynolds number and density to also drop during the run. The changing freestream density in the BAM6QT during a run has the possibility of affecting the perturbation amplitude.

The decrease of the perturbation amplitude during the run was analyzed by looking at only the centerline traces. The amplitude of the perturbation was determined by estimating the impulse magnitude of the minimum pressure deficit across the perturbation. The magnitude of the impulse can be found by integrating across the deficit in the pressure deficit in time trace. A simplified estimate of the impulse is

$$\tilde{J} = -\int_{t_1}^{t_2} \left(\frac{p'_{0,2}}{p_{0,2}} \right) \, dt \tag{5.4}$$

where $p'_{0,2}/p_{0,2}$ is the normalized pressure fluctuation, t_1 corresponds to the 10% rise (fall) time caused by the passage of the thermal perturbation, and t_2 corresponds to when the normalized pressure fluctuation recovers back to 10% of the minimum after the thermal perturbation has passed. Figure 5.10 shows an example time trace with the times used for t_1 and t_2. The integration of the recorded time traces uses the trapezoid rule.

The estimated impulse for the Kulite measurements are plotted against the time after the tunnel starts, t, in Figure 5.11. Each point represents a laser pulse fired during the run. Laser pulses affected by turbulent bursts are not shown. A large amount of scatter in the measurements appears to occur at the beginning of the run. The estimated impulse appears fairly constant for the farther aft measurement, but decreases for the farther forward measurement. In the farther forward measurement, the estimated impulse of the perturbation dropped by about 11% during the run.

The separation between the probe measurement location and the location where the perturbation was generated determines the amount of time elapsed before the perturbation is measured. A simple one-dimensional heat transfer calculation of the

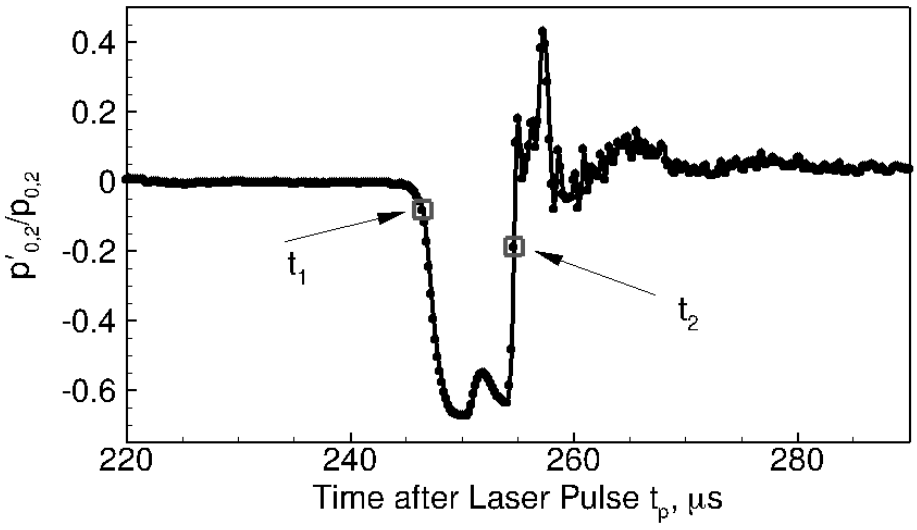

Figure 5.10. Example PCB time trace showing t_1 and t_2 for impulse estimate integration. Run 16-36, laser shot 8.

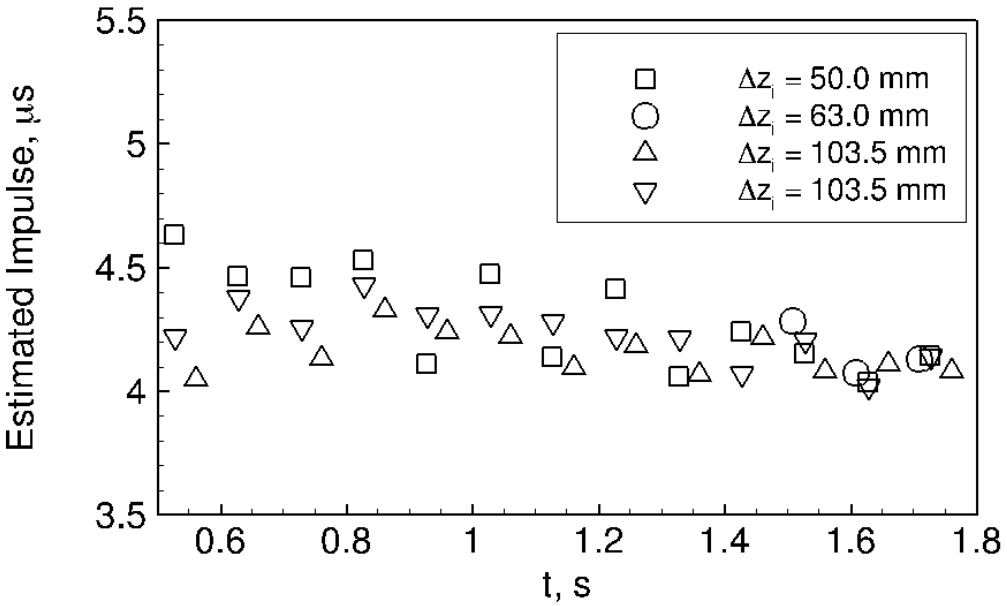

Figure 5.11. Estimated impulse amplitude measured by the Kulite for different axial stations within the tunnel. Laser shots 6–19. Runs 14-09, 14-27, 14-42.

thermal perturbation amplitude (Appendix A) indicated that the perturbation probably cools slightly over time. The temperature of the thermal perturbation should also asymptote near some value.

A similar plot with the PCB probe measurements on the centerline of the perturbation is shown in Figure 5.12. The magnitude of the estimated impulse is about the same as the Kulite. Although the pressure deficit measured by the PCB is of a shorter duration, it has a larger magnitude. As the run time increases, the freestream disturbance impulse amplitude decreases 7%. As in the Kulite measurements, there is more scatter at the beginning of the run than at the end of the run.

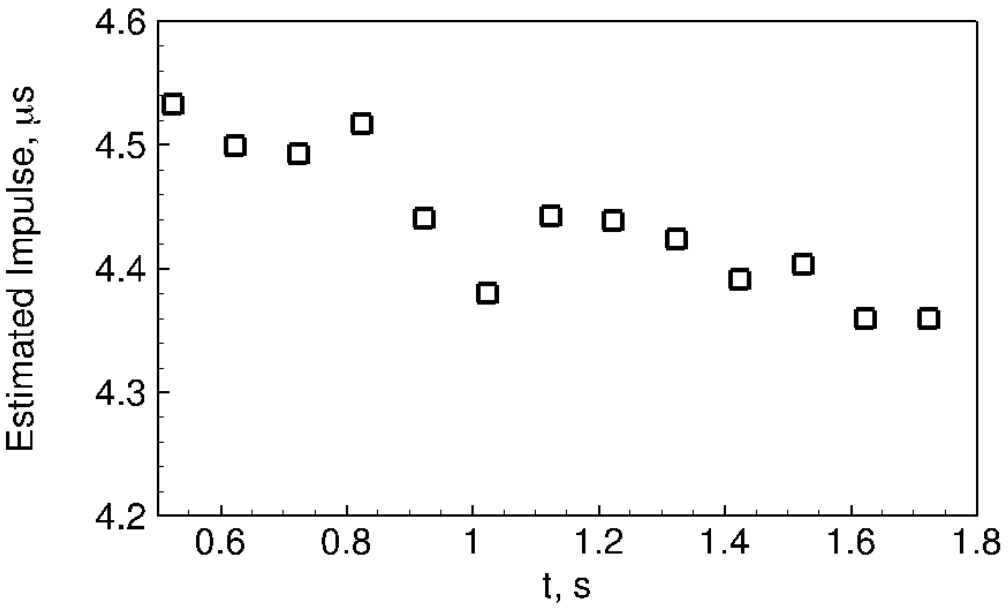

Figure 5.12. Estimated impulse amplitude measured by PCB probe. Laser shots 6–17. Run 16-36.

5.3 Measurements of the Freestream Laser-Generated Perturbation with a Kulite Probe

Profiles of the freestream perturbation were made at locations of $z = 1.965$ and 2.019 m. These locations correspond to $\Delta z_i = 50.0$ and 103.5 mm, respectively.

Profiles were measured at only one stagnation pressure because multiple runs had to be made to create a single profile. This process was time-consuming and more stagnation pressures could not be tested in the allotted time. The tested condition had a stagnation pressure around $p_0 = 1070$ kPa and a stagnation temperature around $T_0 = 425$ K, which corresponds to a freestream density of about 0.039 kg/m^3. The farthest-forward profile consists of 9 y-stations. The farthest-aft profile consists of 11 y-stations.

The ensemble-averaged traces from the 9 different y-stations at $z = 50.0$ mm are shown in Figure 5.13. These traces are offset by the y-position of the time trace. These traces can then be compiled to form a contour plot, as shown in Figure 5.14. The time after a laser pulse t_p was converted to an equivalent distance using the freestream velocity (Equation 4.1). The contour plot shows the thermal perturbation is about 8 mm wide in the y-direction. It has an elongated shape, which is likely a result of the limited frequency response of the Kulite sensor. A dark blue annular region corresponding to pressure fluctuations greater than 5% of the mean pitot pressure surrounds the thermal perturbation. This ring may correspond to the weak shock wave formed in the perturbation-generation process.

A contour plot of the farther aft measurements is given in Figure 5.15. Again, the thermal perturbation appears to have an elongated shape, similar to that seen in Figure 5.14. The amplitude of the perturbation also appears to have decreased slightly at the farther aft measurement station. However, the width of the perturbation in the y-direction remains the same at about 8 mm.

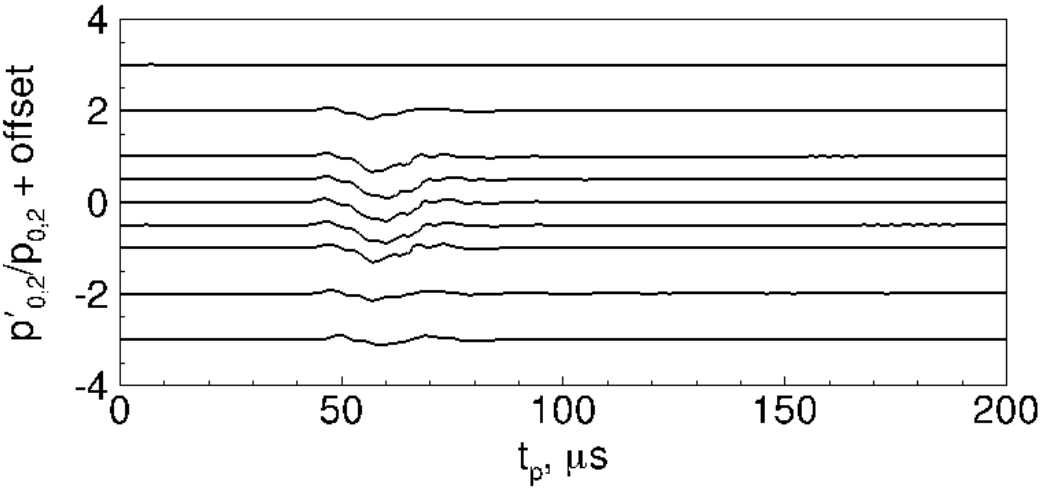

Figure 5.13. Ensemble-averaged time traces from each y measurement station at $z = 1.965$ m ($\Delta z_i = 50.0$ mm). Run numbers 14-05–14-13: $p_{0,1} = 1047$ kPa, $T_0 = 426.9$ K, $\rho_\infty = 0.039$ kg/m^3.

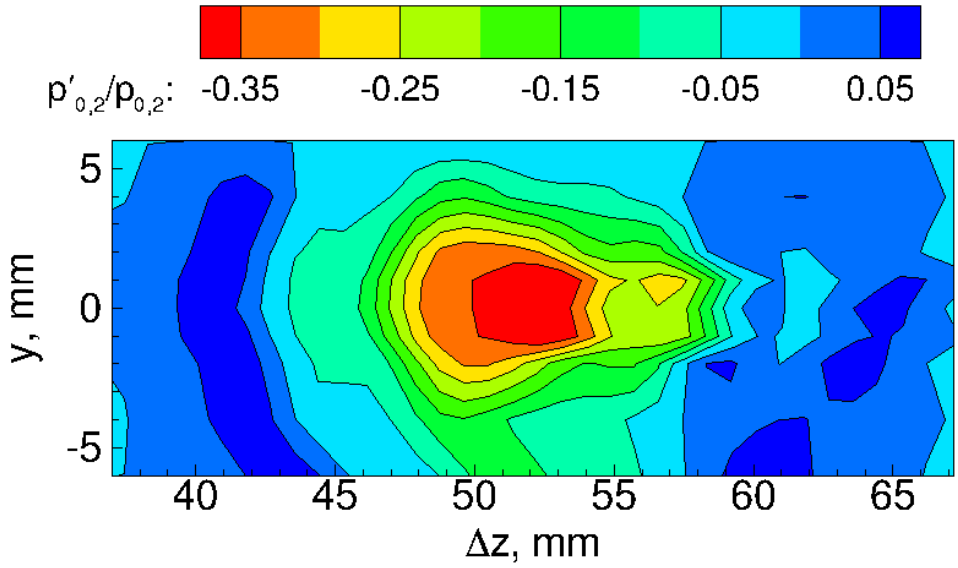

Figure 5.14. Contour plot of ensemble-averaged time traces from each y measurement station at $\Delta z_i = 50.0$ mm. Run numbers 14-05–14-13: $p_{0,1} = 1047$ kPa, $T_0 = 426.9$ K, $\rho_\infty = 0.039$ kg/m^3.

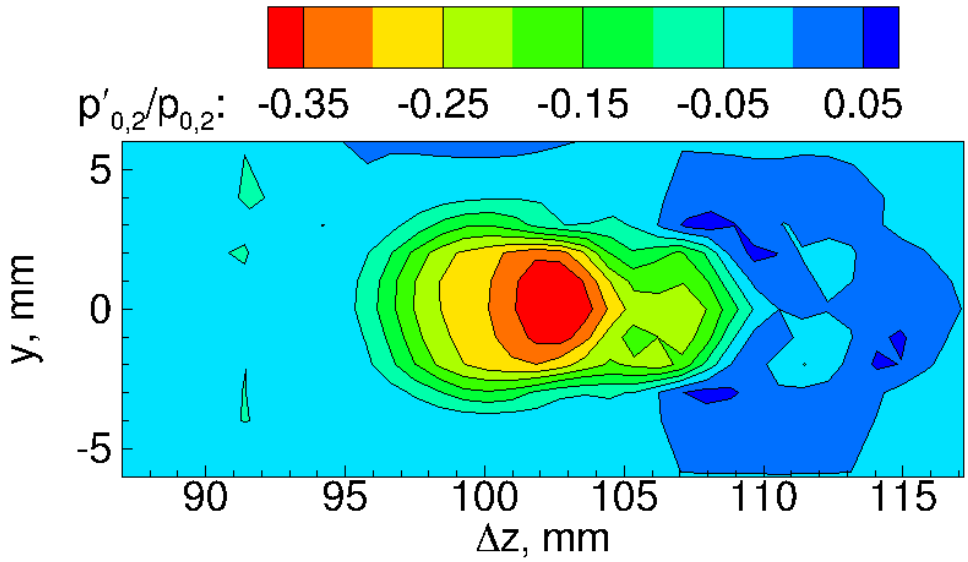

Figure 5.15. Contour plot of ensemble-averaged time traces from each y measurement station at $\Delta z_i = 103.5$ mm. Run numbers 14-33–14-43: $p_{0,1} = 1047$ kPa, $T_0 = 426.9$ K, $\rho_\infty = 0.039$ kg/m^3.

5.4 Measurements of the Freestream Laser-Generated Perturbation with a PCB Probe

Similar multi-run profile measurements of the freestream laser-generated perturbation were made with a PCB probe. The only available probe was shorter so the measurements were made farther aft. The probe was positioned at a location of $z_{\text{probe}} = 2.145$ m, which corresponds to $\Delta z_i = 219.0$ mm. Fifteen separate y survey stations were used for the single probe survey. The mean pitot pressure $p_{0,2}$ was inferred using measurements of the total freestream pressure $p_{0,1}$ and the Rayleigh pitot formula.

Figure 5.16 shows an ensemble average of the measured response to the perturbation at each survey point, offset by an amount proportional to the y-location. The largest difference in the time of arrival of the perturbation is 3 μs for the ensemble-averaged time traces. For comparison, the ensemble-averaged Kulite measurements only showed a variation in the time of arrival 1–2 μs. Each time trace (constant y station) was as much as ± 5 K off of this average. This change in temperature may affect the convection time of the perturbation and thus creates a time of arrival variation in each of the survey points. A variation of ± 5 K in the stagnation temperature creates a variation of about 0.6% in the freestream velocity and about ± 1.6 μs change in the perturbation arrival time.

Figure 5.17 is a contour plot of the ensemble-averaged time traces shown in Figure 5.16. This figure shows a perturbation that is about the same length in the streamwise and spanwise directions. The PCB sensor had sufficient frequency response to be able to resolve the streamwise extent of the perturbation, unlike the Kulite sensor. The jitter in the time traces causes the contour plot of the perturbation to be irregularly shaped. The freestream perturbation was assumed to be roughly spherical to match in the deflectometry measurements conducted in the PCT. An approximation of the profile as a circle yields a perturbation with a diameter of about 8 mm.

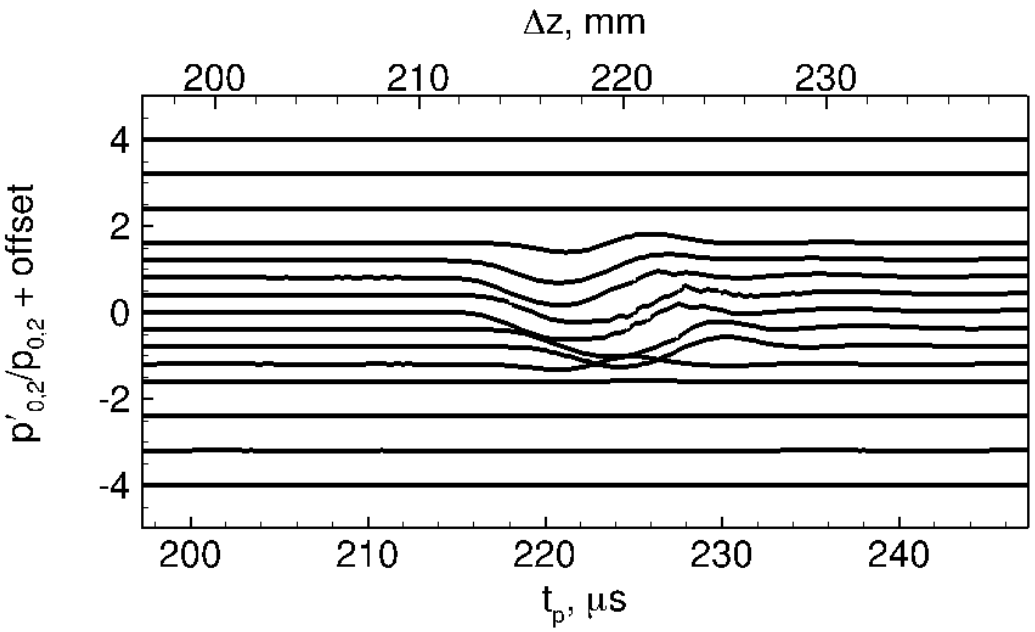

Figure 5.16. Ensemble averages of the PCB measurements of a laser-generated perturbation, offset by an amount proportional to the spanwise location of the measurement in the tunnel. Runs 16-21–16-33: $p_0 = 1022$ kPa, $T_0 = 412.8$ K, $\rho_\infty = 0.043$ kg/m^3, $M = 6.0$, $Re/m = 11.3 \times 10^6$/m.

Other factors, such as a large pitot probe size or the run-to-run variation in temperature may affect the accuracy of the measurements. The large sensor size could cause spatial averaging of the measurements of the perturbation and create uncertainty in the true dimension of the perturbation. The PCB sensor is 3.12 mm in diameter, while the measured perturbation is roughly 8 mm in diameter. The averaging effects of the bow shock in front of this pitot probe are also unknown. The stagnation temperature of the traces that make up the contour plot have an average of $T_0 = 412.8$ K, but the temperature can vary by as much as 5 K.

The magnitude of the perturbation measured by the PCB also appears to be much greater than the already-large magnitude measured by the Kulite sensor. The PCB measurements shown in Figure 5.17 is at stagnation conditions similar to the measurements shown in Figure 5.15, but they are taken at a probe location almost

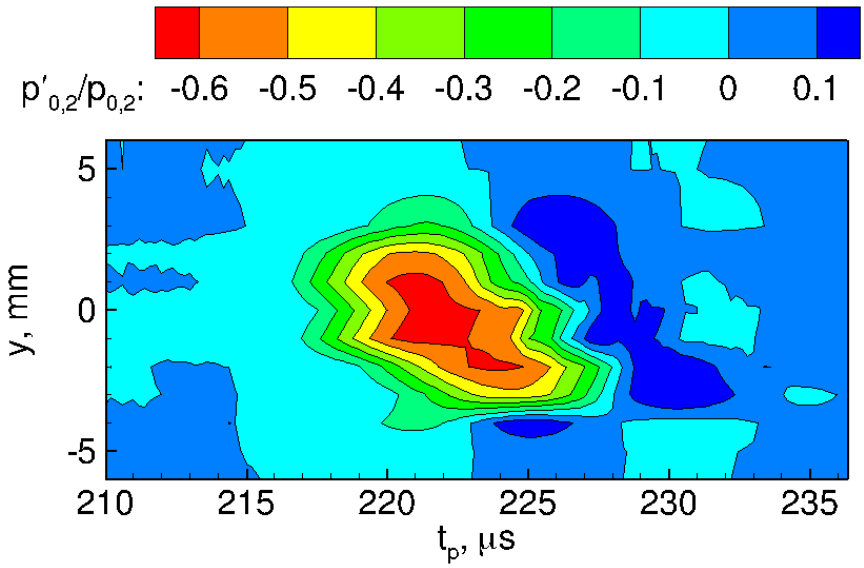

Figure 5.17. Contour plot from ensemble-averaged PCB probe measurements. Runs 16-21–16-33: $p_0 = 1022$ kPa, $T_0 = 412.8$ K, $\rho_\infty = 0.043$ kg/m^3, $M = 6.0$, $Re/m = 11.3 \times 10^6$/m.

twice as far downstream. The Kulite measurements give a maximum deficit of about $p'_{0,2}/p_{0,2} = -0.4$ while the PCB measurements give a maximum deficit of about $p'_{0,2}/p_{0,2} = -0.65$. This is a 63% increase in the amplitude of the thermal disturbance. A measurement farther downstream is expected to produce a slightly smaller amplitude disturbance because the perturbation has more time to cool. Instead, the amplitude of the freestream perturbation is larger.

The measurement with the PCB probe uses the factory-provided calibration and infers the pitot pressure from the freestream conditions. A dynamic calibration of the PCB sensor was not available at the time. The discrepancy in the amplitude measured by the Kulite sensor compared to the PCB sensor may be related to the lack of dynamic calibration. However, this amplitude difference is more likely caused by the difference in frequency response between the two sensors. The PCB sensor has a much higher frequency response than the Kulite sensors and can resolve the passing of a 8 mm perturbation traveling 874 m/s (the nominal freestream speed of the BAM6QT).

5.5 A Comparison of Measurements in the BAM6QT to Measurements in the PCT

The goal of the measurements in the PCT was to measure details of the freestream laser-generated perturbation in ways that were not possible in the BAM6QT. The PCT is a smaller scale tunnel, but has far longer run times than the BAM6QT. It is best to compare measurements directly between the two facilities to make sure the same freestream perturbation was generated in both. However, a direct comparison may not be possible because the measurements were made with different instrumentation. Kulite measurements were attempted in the PCT so that a direct comparison could be made. However, the Kulite used did not have a screen and large particles in the freestream destroyed the sensor. Thus, Kulite measurements were not feasible in the PCT at the time of the experiment.

To compare the measurements made in both facilities, sensors with similar frequency response will be used. These measurement techniques are fundamentally different, but the characteristics of the perturbation can still be gleaned from a combination of this information. This method compares the hot-wire measurements in the PCT to the Kulite measurements in the BAM6QT and the deflectometry measurements in the PCT to the PCB measurements in the BAM6QT. The perturbation size can be inferred from the different measurements and the perturbation shape can be determined from the higher-frequency response sensors.

Contour line plots of the measurements with a hot wire in the PCT and with a Kulite in the BAM6QT are shown in Figure 5.18. The direction in which the probes were traversed are also not the same, because they were fixed by the facility in which the measurements were made. The hot-wire measurements in the PCT occurred along the x-direction, which is approximately the direction of the laser beam path. The PCT only has optical access along the same axis as the probe traverse direction. The Kulite measurements in the BAM6QT occurred along the y-direction, which is approximately perpendicular to the laser beam path. The BAM6QT also has optical

access along the same axis as the probe traverse direction. However, there is no room to safely mount the perturbation-forming optics to match the PCT setup. Thus, the probe in the BAM6QT could only be traversed in a direction approximately 90° from the laser beam path.

The perturbation width in the x-direction is about 4 mm if the $E_0' = -0.05$ V contour line defines the boundary of the perturbation. The perturbation width in the y-direction at $\rho_\infty = 0.040$ kg/m^3 in the BAM6QT is about 8 mm if the $p_{0,2}'/p_{0,2} = -0.15$ contour line defines the boundary of the perturbation. The shape of the perturbation as measured by these two lower-frequency-response sensors are similar. The perturbation is a teardrop or pear shape with the wider end arriving at the probe first. This shape is typical of measurements with insufficient frequency response to resolve the passage of the perturbation.

Contour line plots of the deflectometry measurements in the PCT and the PCB measurements in the BAM6QT are shown in Figure 5.19. The deflectometry measurements in the PCT were made in the y-direction. This is because the deflectometry measurement was made by traversing a sensor across the schlieren image plane. This image plane is created by light beams running in the x-direction and is thus perpendicular to the optical axis. The PCB probe measurements in the BAM6QT were made in the y-direction like the Kulite measurements. The criterion of $\rho/\rho_\infty = 0.95$ was used to define the boundary of the perturbation in the PCT. The criterion of $p_{0,2}'/p_{0,2} = -0.15$ was used to define the boundary of the perturbation in the BAM6QT. The deflectometry measurements show that the freestream perturbation in the PCT at $\rho_\infty = 0.038$ kg/m^3 is about 3.5 mm in diameter. The PCB probe measurements show that the freestream perturbation in the BAM6QT at $\rho_\infty = 0.04$ kg/m^3 is about 8 mm in diameter.

Limitations of these comparisons exist. The amplitude of the disturbances here cannot be directly compared due to the use of different instrumentation in both tunnels. Furthermore the sensor sizes are all slightly different. The hot wire has a 2 μm diameter, the deflectometry measurements had about a 44 μm resolution, the

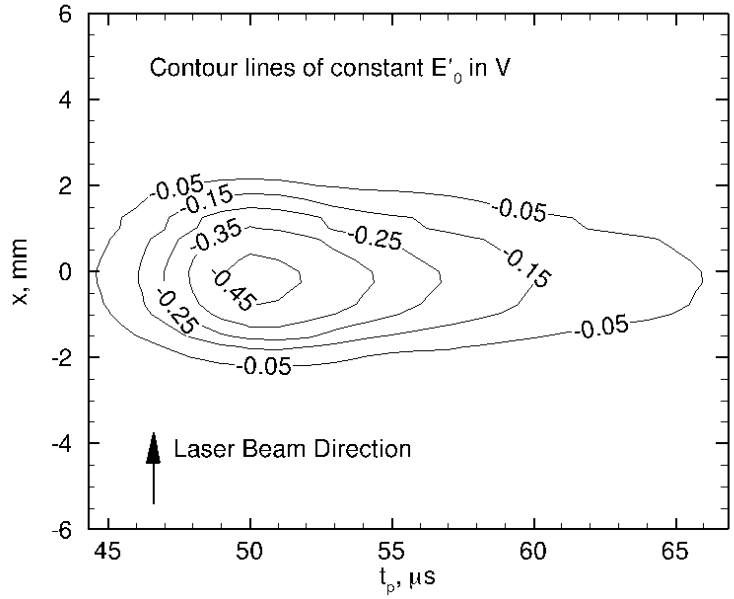

(a) Hot-wire measurement of freestream perturbation in PCT ($M = 3.42$) at $\rho_\infty = 0.038$ kg/m^3. Laser direction is from bottom to top.

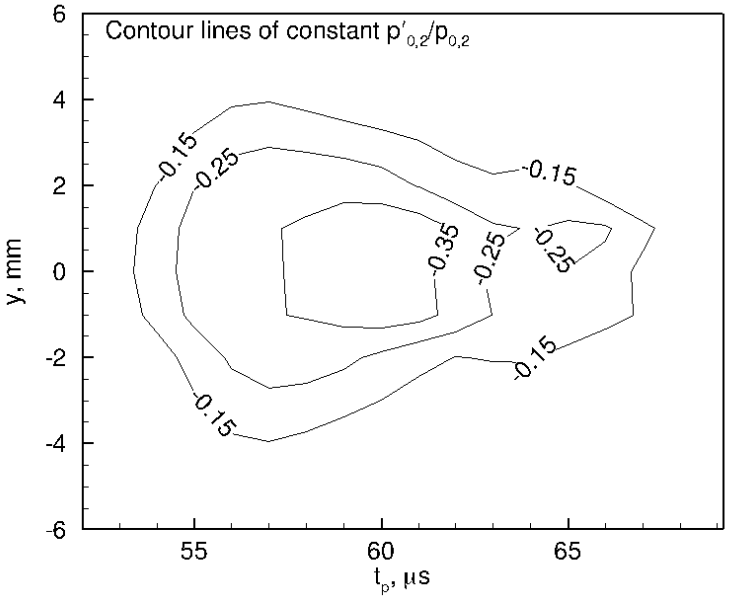

(b) Kulite measurement of freestream perturbation in BAM6QT ($M = 6$) at $\rho_\infty = 0.040$ kg/m^3. Laser direction is into the page.

Figure 5.18. Measurement of a freestream laser-generated perturbation with sensors of lower frequency response.

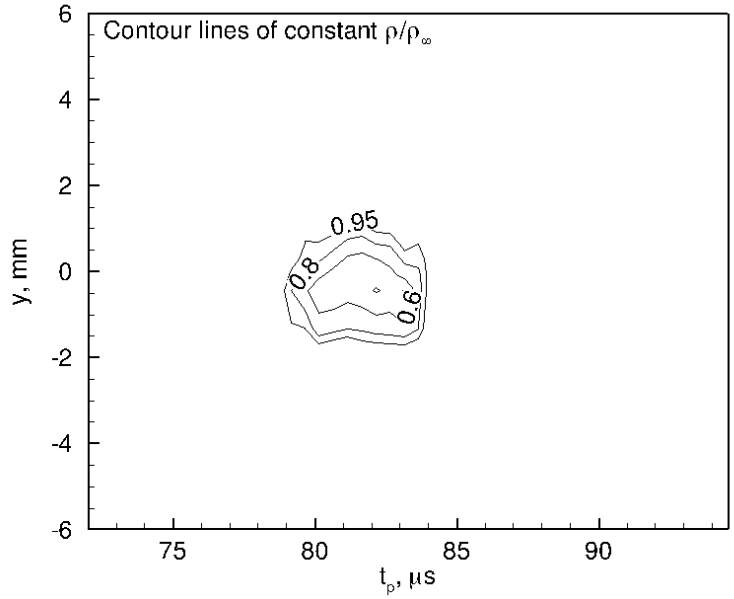

(a) Deflectometry measurement of freestream perturbation in PCT ($M = 3.42$) at $\rho_\infty = 0.038$ kg/m^3.

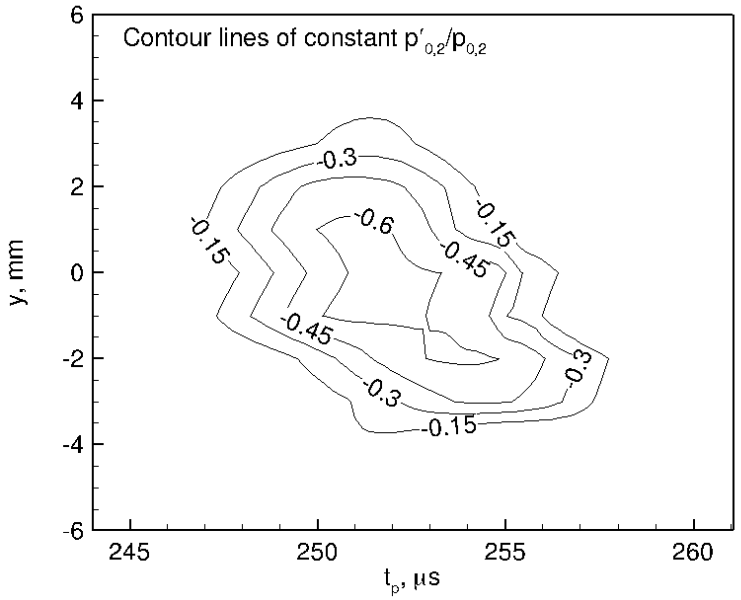

(b) PCB measurement of freestream perturbation in BAM6QT ($M = 6$) at $\rho_\infty = 0.040$ kg/m^3.

Figure 5.19. Measurement of a freestream laser-generated perturbation with sensors of higher frequency response. Laser beam path runs into page.

Kulite has a 1.6 mm diameter, and the PCB has a 3.1 mm diameter. Spatial averaging of measurements made with the larger sensors is possible. A moving average filter was applied to the hot-wire measurements shown in Figure 5.18(a) to mimic spatial averaging across a 1.5-mm window. Figure 5.20 shows the effects of the moving average filter. Little change is seen between Figures 5.18(a) and 5.20. Thus, it is unlikely that the difference in diameter is due entirely to spatial averaging effects.

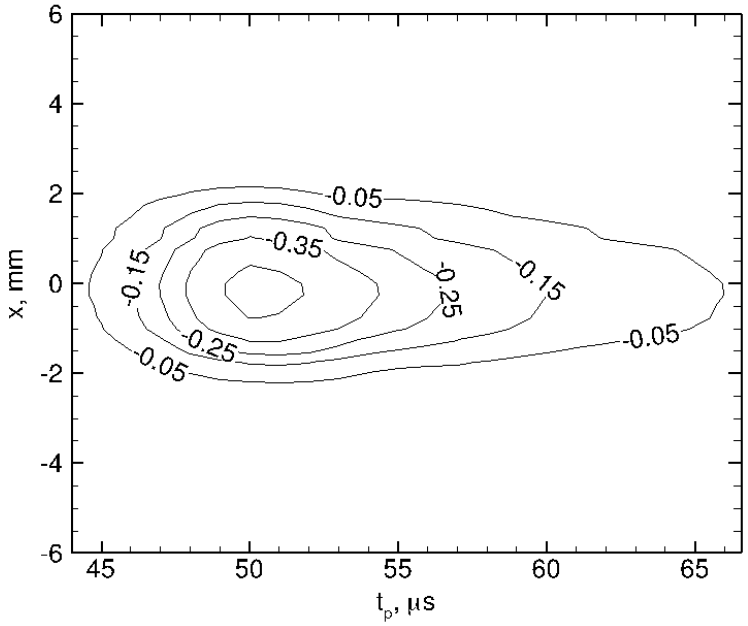

Figure 5.20. Contour plot of Figure 5.18(a) spatially averaged over 1.5 mm. Hot-wire measurement at $M = 3.42$, $\rho_\infty = 0.038$ kg/m^3.

The measurement of the diameter of the perturbation in the PCT at $\rho_\infty = 0.038$ kg/m^3 is about 4 mm, regardless of the instrumentation used. Likewise, the measurement of the diameter of the perturbation in the BAM6QT at $\rho_\infty = 0.040$ kg/m^3 is about 8 mm, regardless of the instrumentation used. However, despite the matched densities of the tunnel, the perturbation does not appear to be the same size. The perturbation characteristics may be affected by other tunnel conditions, such as Mach number or temperature. More measurements in PCT with a Kulite probe are desired to be able to make direct comparisons.

CHAPTER 6. MEASUREMENTS OF THE LASER PERTURBATION PASSING THROUGH AN OBLIQUE SHOCK

Measurements of the disturbance just after the oblique shock would help verify receptivity calculations. This type of measurement is difficult to make in the BAM6QT. The higher Mach number causes the angle of the oblique portion of the shock to lie closer to the body of the model. Many tunnel runs must also be made in order to create a suitable number of averages to resolve the disturbance in the tunnel, so off-body measurements with hot wires are not suitable for measuring the disturbance in the BAM6QT.

Measurements in the PCT can take advantage of the long run times at steady conditions. These long run times allow for detailed measurements of the laser-generated disturbance after it has been processed by an oblique shock. The measurements made in the PCT may not directly compare to those made in the BAM6QT, as discussed previously in Chapter 5.5. The smaller dimensions of the PCT also do not permit measurements on the actual model used in the BAM6QT. Thus, deflectometry measurements in the PCT were made for a wedge with a 15-degree half-angle. Measurements were made to determine if the disturbances follow the predicted trajectory and to determine if the disturbance amplitude changed as predicted by McKenzie et al. [26].

6.1 The Wedge Model

The wedge model was constructed from 6061-T6 aluminum and was 25.4 mm long and 25.4 mm wide. Measurements with a Keyence digital microscope showed that the manufactured model had a leading edge radius of about 41.7 μm and a half-angle of 14.8 degrees. To mount the wedge model in the PCT probe holder, a 76.2-mm-

long shaft protruded from the aft end of the wedge model. The shaft diameter was 6.35 mm.

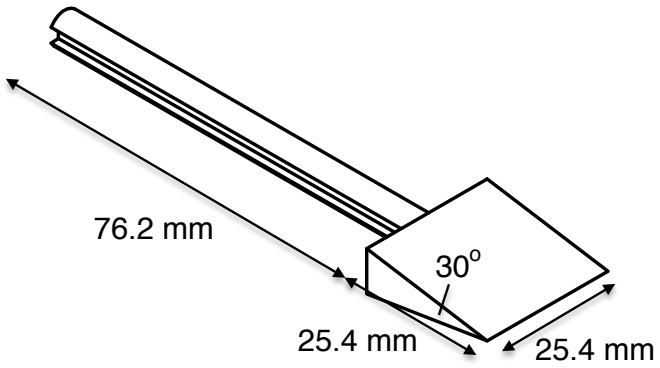

Figure 6.1. A drawing of the wedge model used for PCT measurements.

6.2 Expected Trajectory

Far upstream of the model, the disturbance is expected to traverse downstream in a straight line because the streamlines near the center of the tunnel are assumed to be perfectly horizontal. When the upstream thermal and acoustic disturbances arrive at the oblique shock, they are assumed to act according to Snell's law at the oblique shock. When any disturbance interacts with the shock wave, acoustic and thermal/vortical disturbances can be generated on the other side of the shock. For the sake of brevity, the entropy-vorticity disturbances behind the oblique shock will be referred to as a thermal disturbance, but have the possibility of containing both types of disturbances.

The angle of deflection for an entropy-vorticity wave is given by McKenzie et al. [26] as

$$\tan\theta_t = c\frac{M_{2n}}{M_{1n}}\tan\theta_i \tag{6.1}$$

where $c = a_2/a_1$ and a indicates the speed of sound in the region indicated by the subscript, M_n is the normal component of the Mach number relative to the oblique

shock, and θ_i is the incoming angle of the freestream disturbance measured relative to the perpendicular axis off of the oblique shock. The subscripts 1 and 2 on the right-hand side of Equation 6.1 indicate conditions in front of and behind the shock, respectively. The subscript i is indicative of the initial disturbance while the subscript t is indicative of the thermal disturbance that either passes through the shock or is generated by the disturbance passing through the shock. This is illustrated in the diagram in Figure 6.2 by the green and red arrows. The green arrow corresponds to the incoming disturbance. The red arrow corresponds to the trajectory of the deflected thermal disturbance.

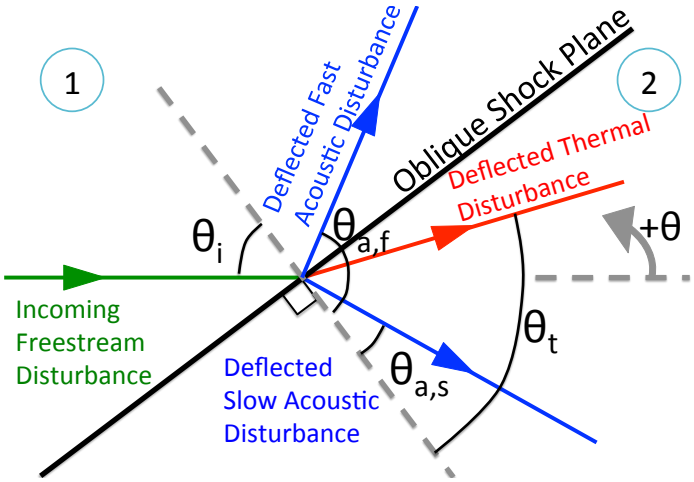

Figure 6.2. A diagram of the predicted trajectories of the disturbances generated after an oblique shock.

The deflection angle of an acoustic wave is given by

$$\cos\theta_a = \frac{-c^2\sin^2\theta_i\left(\pm M_{2n}\right) + \sqrt{M_{1n}^2\left[M_{1n}^2\cos^2\theta_i - c^2\sin^2\theta_i\left(1-M_{2n}^2\right)\right]}}{c^2\sin^2\theta_i M_{2n}^2 + M_{1n}^2\cos^2\theta_i} \tag{6.2}$$

where the positive sign in front of the first M_{2n} term corresponds to the slow acoustic wave generated by the shock, and the negative sign corresponds to the fast acoustic wave generated by the shock. In Figure 6.2, the trajectory of these disturbances is given by the blue arrows. The slow wave has the subscript s and the fast wave has the subscript f.

Figure 6.3 shows an overlay of only the wedge and predicted oblique shock over a schlieren image of the wedge in $M = 3.42$ flow. No laser perturbations were present in the flow for this image. The theoretical shock angle of a 15-degree wedge in Mach-3.42 flow is 29.6°. The predicted position of the oblique shock is given by the light blue dashed line. This prediction agrees fairly well with the dark line in the schlieren corresponding to the oblique shock until about $z = 88$ mm. The shock then began to curve due to the expansion fan radiated from the aft end of the wedge. This bending of the shock and presence of an expansion fan may result in differences between the actual and predicted trajectory of the disturbances downstream of the shock.

Nevertheless, theoretical trajectories were used to determine the best locations to make measurements in the PCT. The theoretical trajectories were overlaid on a schlieren picture of the wedge with no flow, as in Figure 6.4. The outline of the wedge is given in purple and the oblique shock generated by the wedge is given in a dashed light blue line. The location where the freestream disturbance is generated is given by the green star at (z, y) = (30.4, -7.00) mm. The trajectory of this disturbance, before it strikes the oblique shock, is given by a dashed green line. The trajectory of the thermal disturbance after the shock is given by the solid red line starting at (z, y) = (83.3, -7.00) mm with an angle of 9.3° from the horizontal axis. The trajectory of the slow acoustic disturbance is given by the dashed blue line with an angle of -12.1° from the horizontal axis. The trajectory of the fast acoustic disturbance is given by the dashed blue line with an angle of 76.2° from the horizontal axis. The points selected for the vertical surveys in the PCT are plotted on top of these lines as yellow dots.

6.3 Measurements

Previous chapters used a freestream speed to convert time traces to a relative distance (Equation 4.1). However, the measurements are now made behind a shock. A "particle" of air traveling through the shock would experience a change in velocity as it passes through the shock. The "particle" of air would also experience a deflection

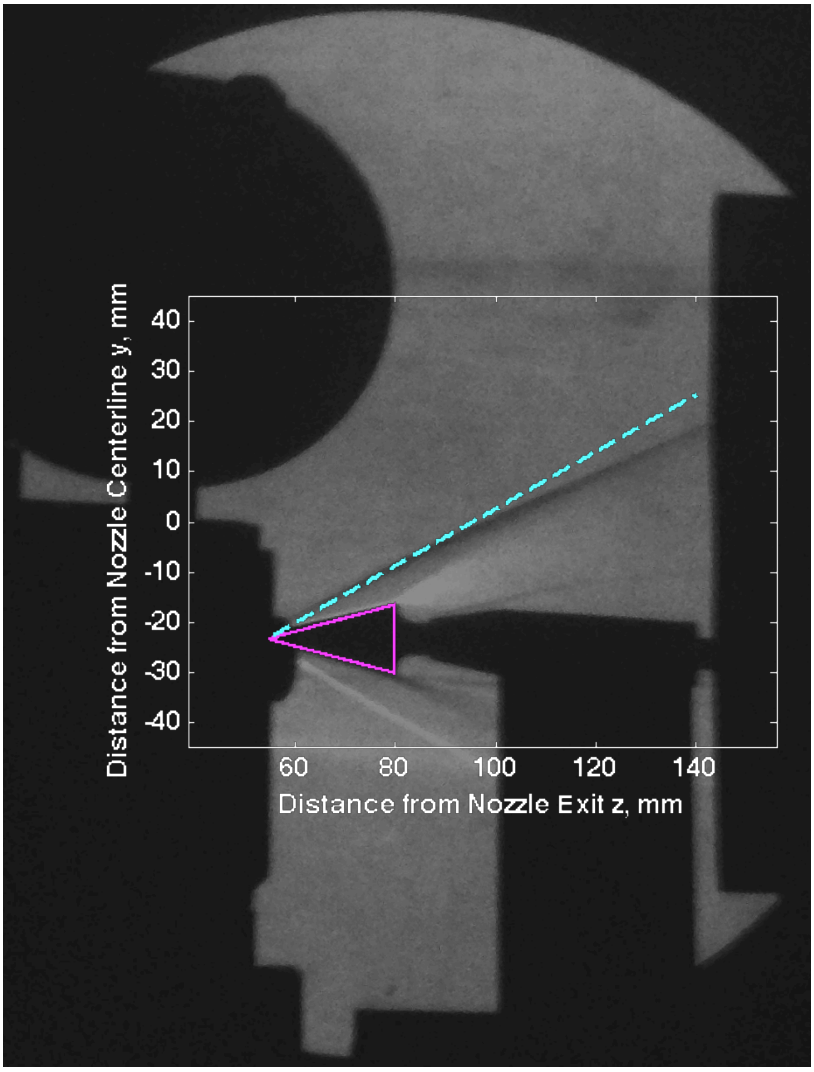

Figure 6.3. Schlieren image of 15-degree wedge in PCT with no laser perturbation. $p_0 = 96.7$ kPa, $T_0 = 311.0$ K, $M = 3.42$. Flow from left to right.

as it passes through the oblique shock. The streamlines prior to the oblique shock wave and after the oblique shock wave are straight. However, the streamlines after the oblique shock are at an angle to those prior to the shock. Thus, the relation between the time and relative distance that is associated with such time is no longer straightforward. A coordinate transformation for the following measurements was not attempted, but could perhaps be applied in the future.

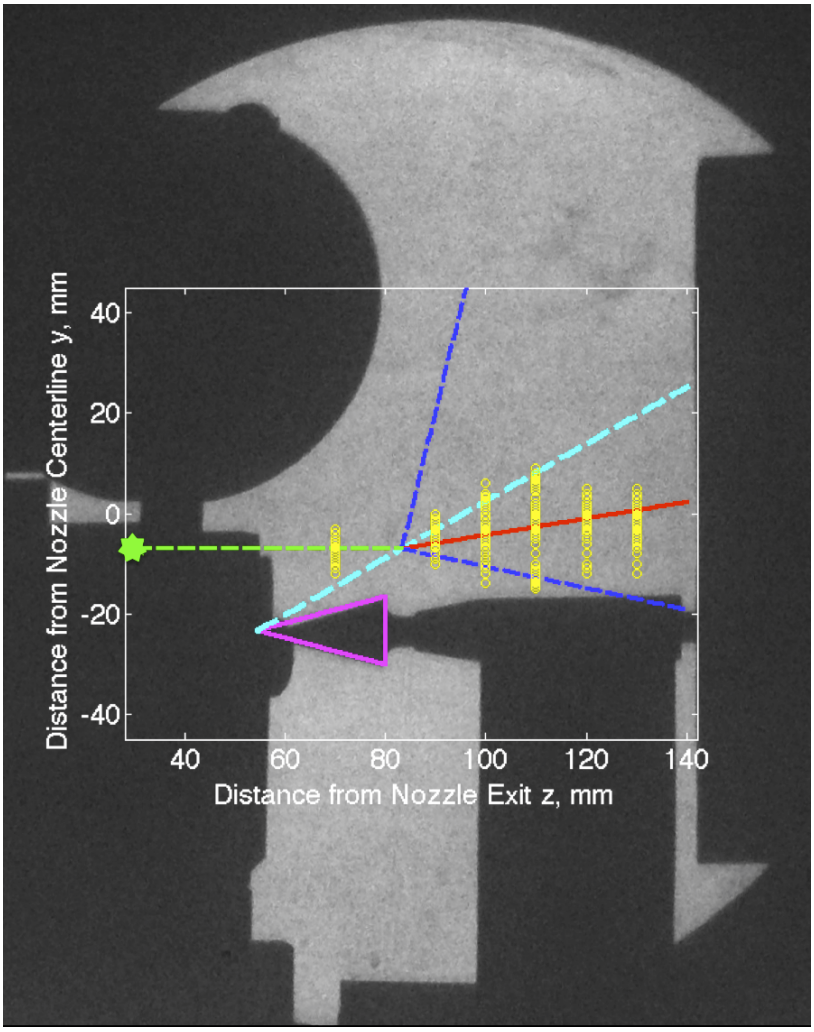

Figure 6.4. Predicted trajectory of the laser-generated disturbance overlaid on a picture of the wedge with survey locations in yellow. No flow.

Some of the surveys in the y-direction also traverse over the oblique shock or over the region influenced by the expansion fan. In these regions, the flow is not uniform. An application of the inverse Abel transform to these measurements requires that integration across the y-stations be made in an axisymmetric region. In regions of non-uniform flow, the perturbation is not expected to be axisymmetric. Thus, this chapter will only show measurements of deflection as a function of time.

6.3.1 Contour Plots of Deflection Measurements

This chapter shows contour plots of the deflection measurements made at the different z-stations shown in Figure 6.4. These contour plots were made in the same way as contour plots of measurements of the freestream perturbation. However, the horizontal axis in these plots is now a function of t_p, the time after a laser pulse was fired.

A contour plot of the disturbance upstream of the oblique shock is given in Figure 6.5. This measurement was made to confirm that the perturbation going into the oblique shock was similar to the freestream perturbation measured in Chapter 4. This plot is very similar to Figure 4.25, which shows deflection measurements of the freestream disturbance. The perturbation appears to consist of a region with positive Δ'_y and a region with negative Δ'_y. These indicate an axisymmetric perturbation because the two regions are about the same magnitude and shape. As expected, the perturbation used in this experiment is the same perturbation measured previously.

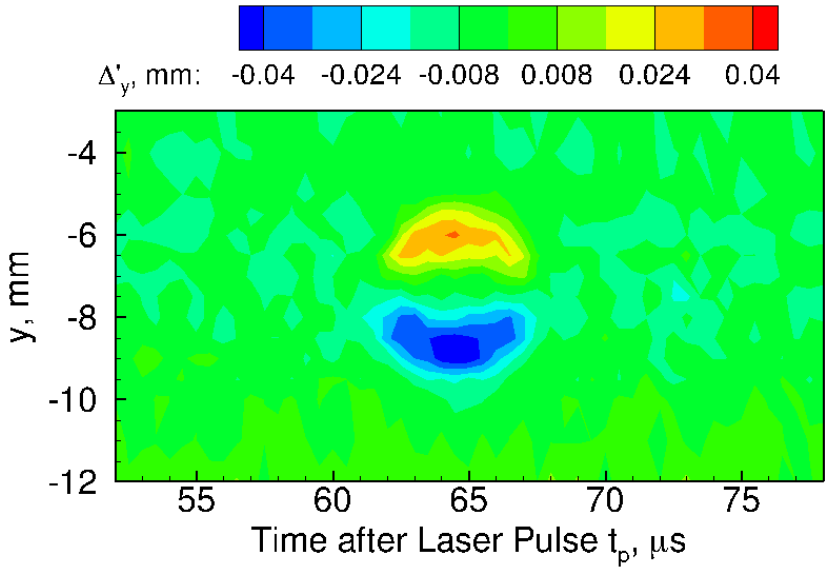

Figure 6.5. Deflectometry measurements of the disturbance upstream of the oblique shock wave at $z = 70$ mm. $p_0 = 97.5$ kPa, $T_0 = 310.9$ K, $\rho_\infty = 0.054$ kg/m^3, $M_\infty = 3.42$.

Figure 6.6 shows the contour plot of the deflection fluctuation measurements made at $z = 90$ mm. The contour levels in Figure 6.5 were chosen to match the levels in Figure 6.5. At this z-location, the y-stations in the survey are expected to pass through the shock, the thermal disturbance, and the weak acoustic disturbance. The predicted y-coordinate of these features are marked on Figure 6.6 by an a arrow. The theory suggests that the measurements at $z = 90$ mm pass through the oblique shock at $y = -3.25$ mm, the thermal disturbance at $y = -6.00$ mm, and an acoustic disturbance at $y = -8.40$ mm.

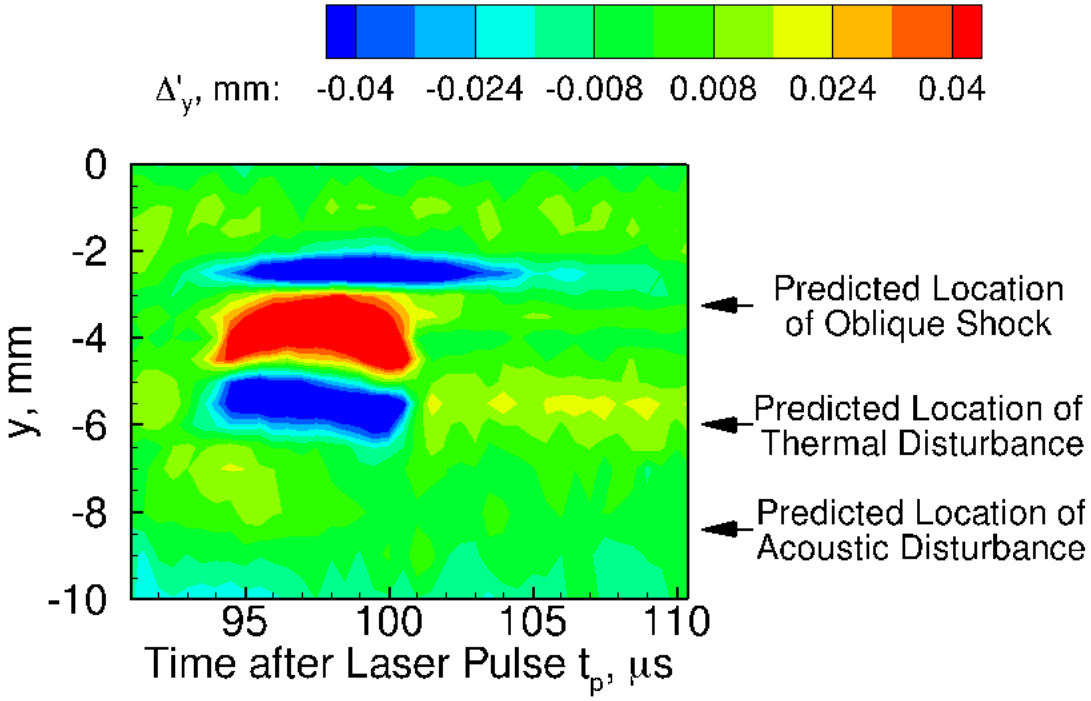

Figure 6.6. Deflectometry measurements near the intersection of the disturbance and the oblique shock wave at $z = 90$ mm. $p_0 = 97.5$ kPa, $T_0 = 310.9$ K, $\rho_\infty = 0.054$ kg/m^3, $M_\infty = 3.42$.

At a region between $y = -6.4$ and -2 mm, the deflection measurements saturate in the contour levels selected for Figure 6.6. Figure 6.7 shows the same contour plot with different contour levels to eliminate this saturation. The region at $y = -2.5$ mm shows negative deflection between 93.5–105 μs. This region may be associated with

the deflection of the oblique shock as the disturbance passes through, although that is unclear in this plot. Note that Figure 6.3 shows the oblique shock begins to curve at this measurement station. The region between $y = -6$ and -3 mm at $t_p = 93.5$–101 μs may be associated with the thermal disturbance. If this region is related to the thermal disturbance, it appears distorted when compared to the freestream disturbance. The acoustic disturbance is expected to pass through a location of $y = -8.4$ mm. No features in the contour plot indicate that this disturbance is detected with this measurement method. Computational comparisons are desired.

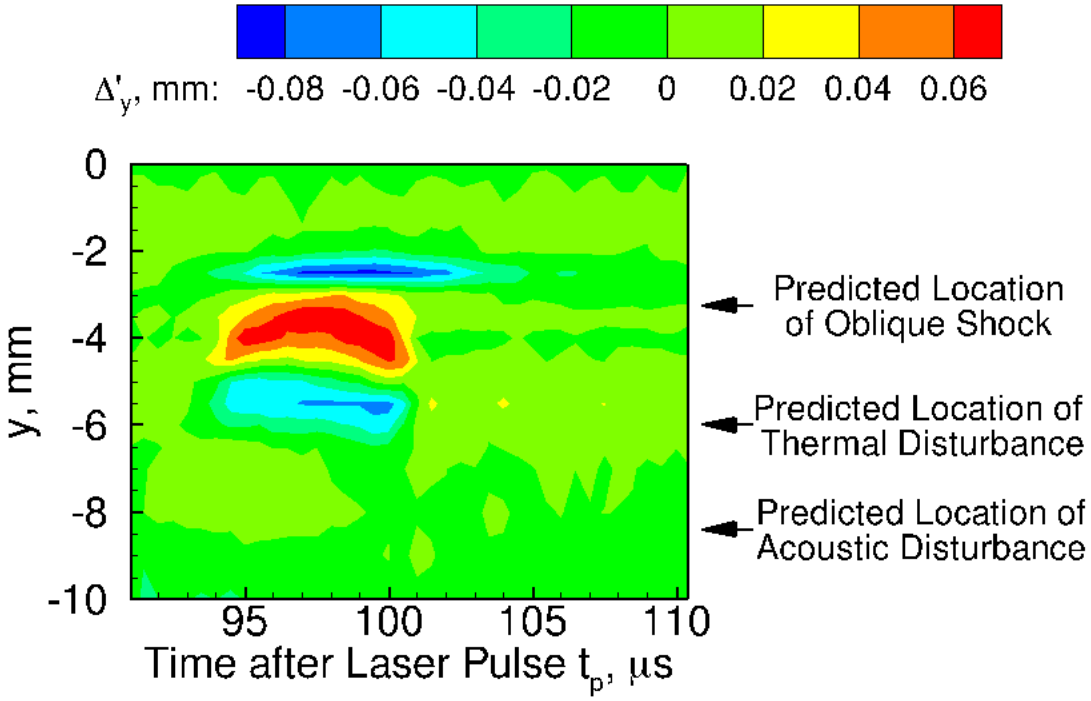

Figure 6.7. Deflectometry measurements unsaturated contour levels chosen for $z = 90$ mm. $p_0 = 97.5$ kPa, $T_0 = 310.9$ K, $\rho_\infty = 0.054$ kg/m^3, $M_\infty = 3.42$.

Figure 6.8 shows the deflection fluctuation measurements at $z = 100$ mm. At $z = 100$ mm, the oblique shock is expected to occur at $y = 2.50$ mm, the thermal disturbance is expected to occur at $y = -4.30$ mm, and the acoustic disturbance is expected occur at $y = -10.0$ mm. Again, some deflection is seen at a region between

$y = 1.0$ and 2.5 mm, lasting from 108.5–133.5 μs. This deflection is likely attributed to the shock deflecting as the disturbance passes through. The y-coordinate of this deflection is slightly less than the predicted location of the oblique shock. However, the oblique shock has started to curve at $z = 100$ mm (Figure 6.3). At a region between $y = -4.5$ and 0.0 mm, the disturbance is clearly seen again, although the shape of the disturbance appears distorted compared to the freestream measurements. It is possible that the disturbance is no longer axisymmetric at this location. The upper lobe of the thermal disturbance does not appear to be the complement of the lower lobe of the deflection fluctuation measurements. However, the diameter of this disturbance does not appear to differ from the diameter of the freestream disturbance. The acoustic disturbance does not appear to have been detected.

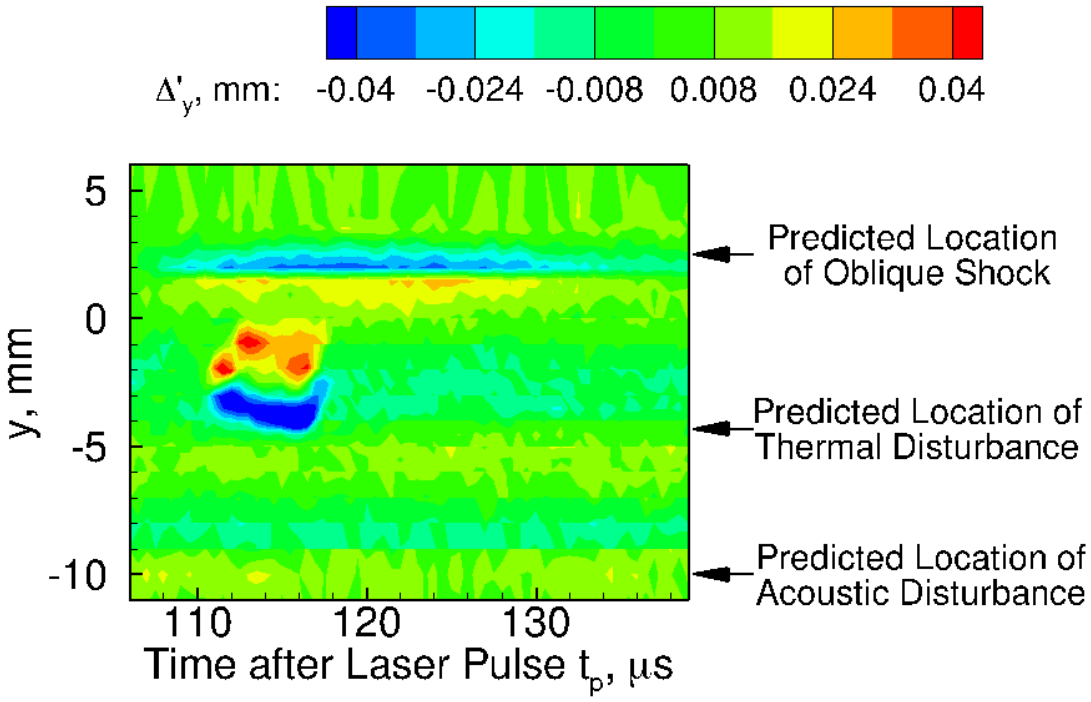

Figure 6.8. Deflectometry measurements near the intersection of the disturbance and the oblique shock wave, after the disturbance has passed through the oblique shock at $z = 100$ mm. $p_0 = 97.2$ kPa, $T_0 = 310.9$ K, $\rho_\infty = 0.054$ kg/m^3, $M_\infty = 3.42$.

Figure 6.9 shows a contour plot of deflectometry measurements at $z = 110$ mm. At $z = 110$ mm, the oblique shock is expected to pass through $y = 8.15$ mm, the thermal disturbance is expected to pass through $y = -2.50$ mm, and the acoustic disturbance is expected to pass through $y = -12.76$ mm. The oblique shock wave deflection is seen at $y = 6.5$ mm and lasts from about 123.3–148.5 μs after the laser pulse was fired. The thermal disturbance now appears to range from $y = -4.5$ to 1.25 mm and lasts from 126.0–133.5 μs after the laser pulse was fired. This disturbance also appears to have an irregular shape, with one portion of the disturbance lasting from 126.0–130.5 μs and a smaller portion of the disturbance lasting from about 130.5–133.5 μs. This smaller portion of the disturbance also appear to be slightly offset and rotated. The thermal disturbance no longer appears axisymmetric. Again, the acoustic disturbance does not appear to have been detected.

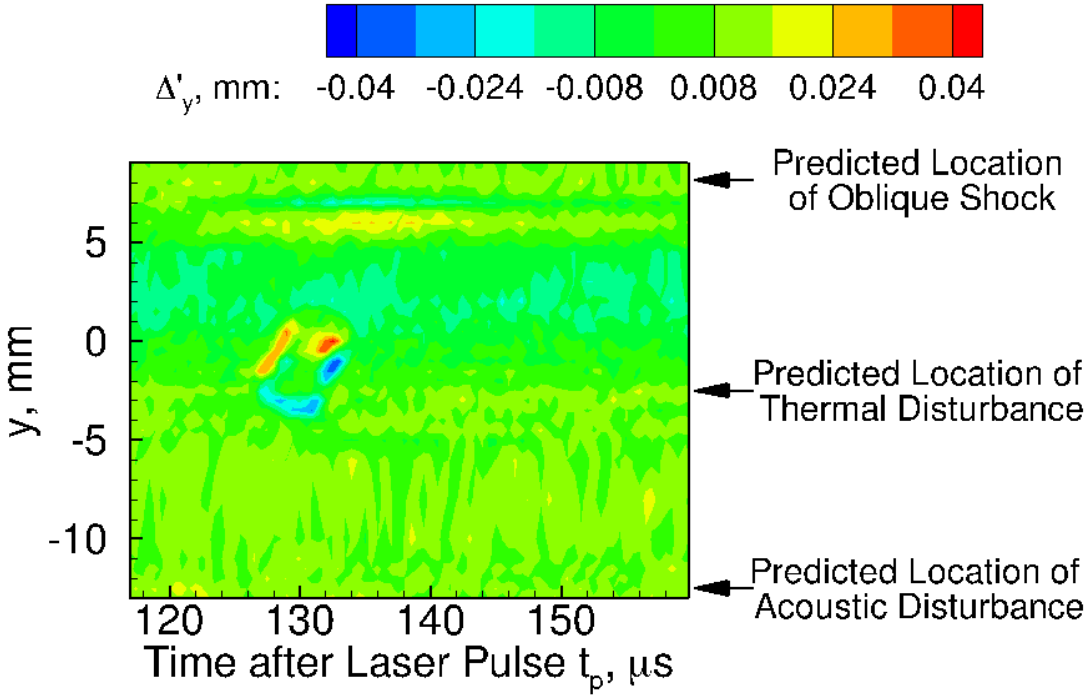

Figure 6.9. Deflectometry measurements after the disturbance has passed through the oblique shock wave at $z = 110$ mm. $p_0 = 97.7$ kPa, $T_0 = 311.0$ K, $\rho_\infty = 0.054$ kg/m^3, $M_\infty = 3.42$.

Measurements farther downstream at $z = 120$ and 130 mm are shown in Figures 6.10 and 6.11, respectively. These contour plots show a disturbance that appears to be dissipating. Note that the contour levels for the plots in Figure 6.10 and 6.11 are over a smaller range due to the lower signal in the measurements. This decrease in signal is expected. The same dissipation in signal with convection time was observed in the freestream measurements of the disturbance (Chapter 4). The farthest downstream measurements in Figure 6.11 appear to show alternating horizontal striations in the deflection fluctuation. These striations may be due to some unaccounted-for temperature variations which are magnified by the change in contour levels. These variations probably contribute to the SNR problems in the deflectometry measurements.

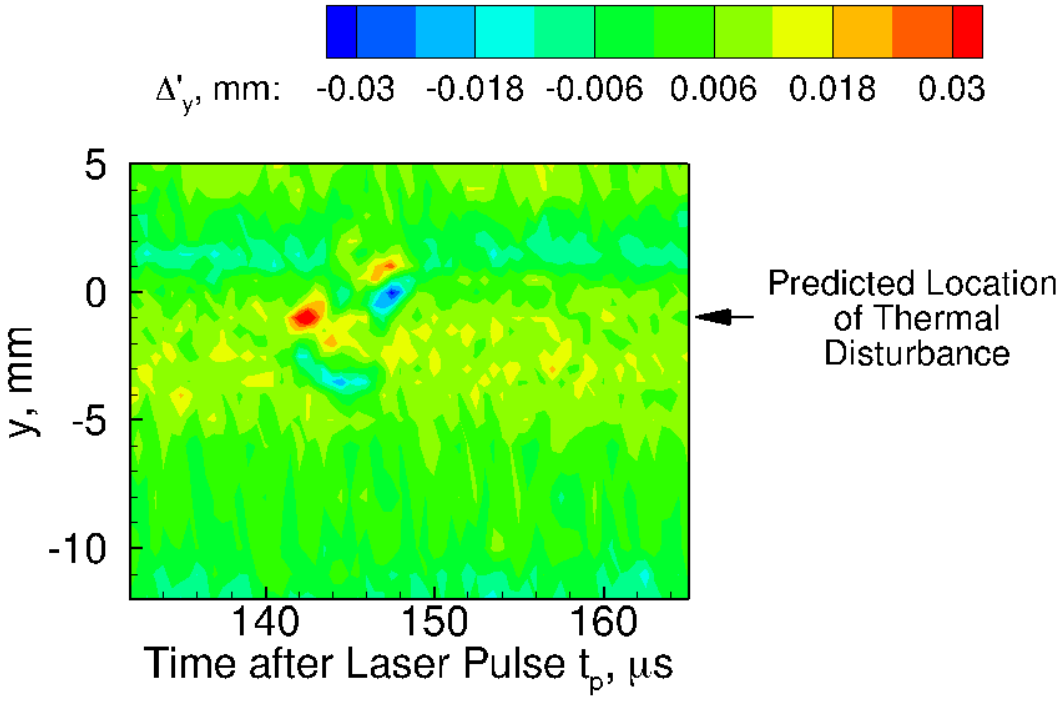

Figure 6.10. Deflectometry measurements downstream of the oblique shock wave at $z = 120$ mm. $p_0 = 97.2$ kPa, $T_0 = 311.0$ K, $\rho_\infty = 0.053$ kg/m^3, $M_\infty = 3.42$.

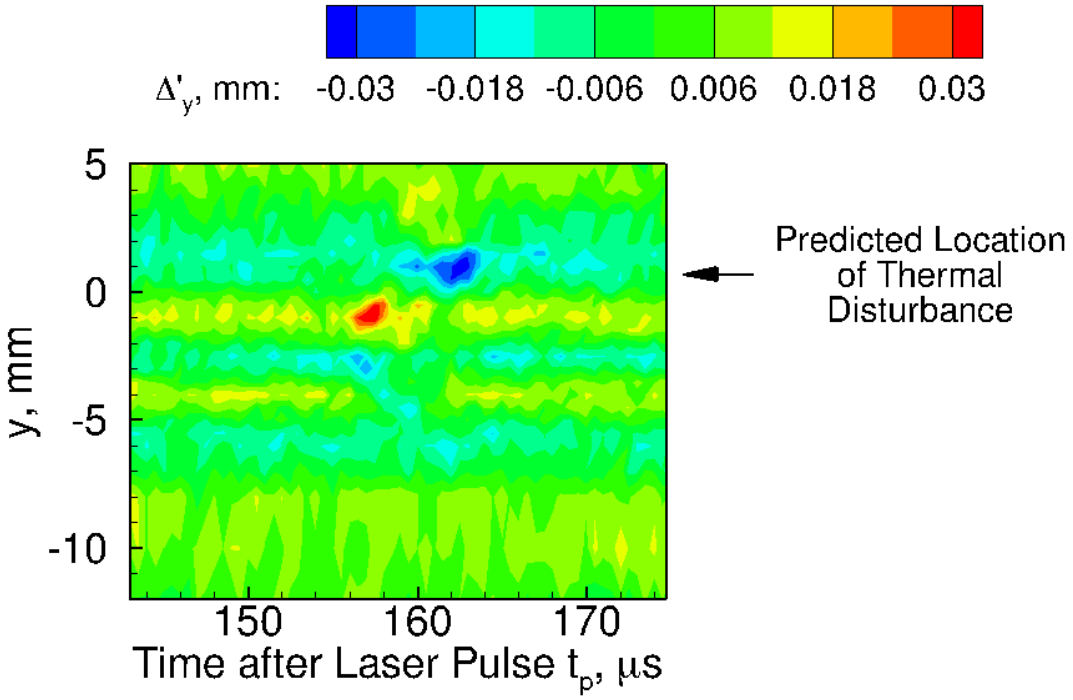

Figure 6.11. Deflectometry measurements downstream of the oblique shock wave at $z = 130$ mm. $p_0 = 97.4$ kPa, $T_0 = 311.0$ K, $\rho_\infty = 0.054$ kg/m^3, $M_\infty = 3.42$.

Similar measurements for the different z-stations were made at lower stagnation pressures. However, as the stagnation pressure decreases, the SNR also decreases. An example of the lack of clear measurements at these lower pressures is shown in Figure 6.12. Starting at about $z = 110$ mm at a freestream stagnation pressure of $p_0 = 68.5$ kPa and freestream stagnation temperature of $T_0 = 311.0$ K, barely any signal is detectable.

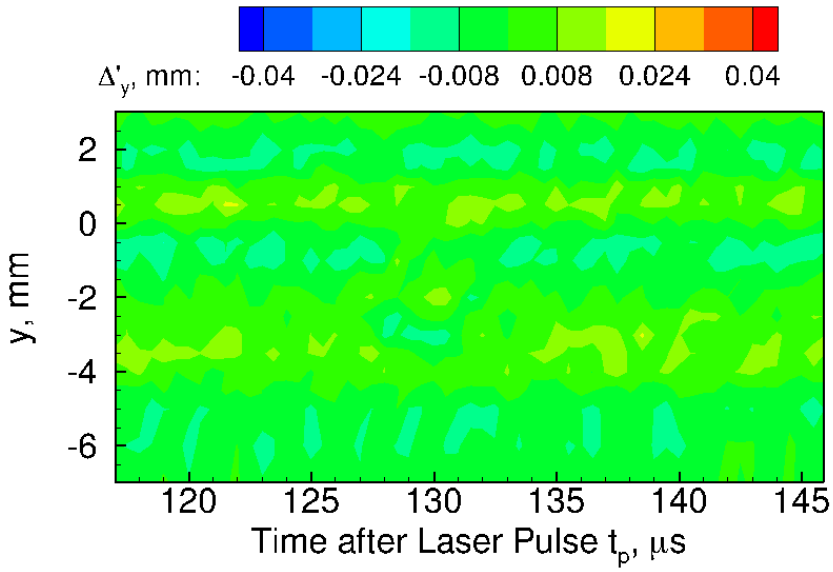

Figure 6.12. Deflectometry measurements with low SNR downstream of the oblique shock wave at $z = 110$ mm. $p_0 = 68.5$ kPa, $T_0 = 311.0$ K, $\rho_\infty = 0.054$ kg/m^3, $M_\infty = 3.42$.

CHAPTER 7. FORWARD-FACING CAVITY MEASUREMENTS

A forward-facing cavity was used to practice aligning the laser-generated perturbation to a model. The large nose diameter of the forward-facing cavity provided a larger target with which to align the perturbation, as compared to a sharp-nosed cone. The present study uses a cylindrical forward-facing cavity centered on the body axis [100, 101], similar to that used by Ladoon [24] and Segura [102]. However, this present study was the first to be conducted in a Mach-6 quiet tunnel.

The forward-facing cavity geometry is of interest for optically-guided interceptor missiles, cruise missiles, rockets, and self-propelled projectiles traveling at supersonic and hypersonic speeds. These vehicles with blunt-nose geometries typically fly at low altitude and high velocity, which can create stagnation regions with high heating. The concept of a supersonic forward-facing cavity to create pulsed sound waves was first studied by Hartmann [103]. The geometry used, now known as the Hartmann whistle, was capable of producing discrete acoustic frequencies. These frequencies matched closely to an "organ-pipe" frequency, which was dictated by the cavity dimensions and flow conditions.

A forward-facing cavity acts like a resonance tube. The pressure fluctuations have a dominant frequency approximated by resonance tube theory as:

$$\omega_{1n} = 2\pi f_{1n} = \frac{\pi a_0}{2L^*} \tag{7.1}$$

where ω_{1n} is the angular frequency of the resonance, f_{1n} is the frequency of the resonance, a_0 is the speed of sound in the cavity based on the stagnation temperature, L^* is the axial distance from the cavity base to the mean shock position $(L + \delta)$, L is the cavity depth, measured from the nose to the base of cavity, and δ is the mean shock standoff distance (between the nose and the mean shock position). The mean shock standoff distance is approximated using the arithmetic average of the correlation

value for a sphere and the correlation value for a flat-face cylinder at Mach 6 [104]. This correlation gives $\delta = 0.34D$.

A stable bow shock, when perturbed, is symmetric about the nose and exhibits small oscillations that damp. When the bow shock is stable, the oscillations of the bow shock drive the pressure fluctuations in the cavity [105]. The cavity pressure fluctuations are fairly small, similar to the freestream acoustic noise level. A stable cavity has a stable bow shock. At some critical cavity depth $(L/D)_{\text{crit}}$, pressure oscillations in the cavity can achieve self-sustained resonance. These large periodic oscillations do not damp and the cavity is assumed to be unstable. For the unstable cavity, the bow shock becomes unstable and exhibits an asymmetric shape or bulge [105].

A study of concave nose cones by Burbank and Stallings was the first to suggest that a forward-facing cavity in the stagnation region could be used as a passive method to reduce heating in the stagnation region [106]. A forward-facing cavity geometry was also tested in a hollow-nosed active seeker program [105] and a hit-to-kill endoatmospheric strapdown seeker [107]. Several groups showed 2–10 times less heat flux at the cavity base when a forward-facing cavity was placed in the stagnation region of a blunt body [105,107–110]. However, this only occurred when the cavity was stable [106, 111]. A separate study by Engblom et al. [112] suggested that although stable cavities produce less heating at the base of the cavity, they produce higher heating at the sharp lip of the cavity. Thus, the best design for the reduction of heat transfer in a forward-facing cavity is still an open issue. Regardless, the presence of large self-sustained pressure fluctuations are generally not ideal, particularly when critical payloads or sensing elements may be affected by structural fatigue, optical aberrations, etc.

Most early experimental work on forward-facing cavity geometries was conducted in conventional facilities, and thus, may not have simulated freestream flight conditions. A flight test of a cup (concave) nose over a range of $M = 2.5$–7.1 showed that the total heat input integrated over the surface of the nose was less than 60% of the theoretical value for a hemispherical (convex) nose [113]. The heat flux measurements

at and near the cavity base for the concave nose were up to 30 times less than those measured under stable cavity conditions in conventional wind tunnels. Lower heat transfer at the base of the concave nose cavity in flight indicates that the bow shock and cavity on this geometry are stable.

In the late 1990s, an experimental study in a Mach-4 quiet-flow tunnel was conducted to determine the effect of freestream noise on the cavity pressure fluctuations [24]. Ladoon et al. found that the pressure fluctuations in the cavity were an order of magnitude less under quiet-flow conditions than under noisy-flow conditions and showed damped resonance for shallow cavities. This discovery explained the flight test findings of Levine et al. [113]. It is likely that the freestream noise conditions in the Mach-4 quiet tunnel were more similar to that of the flight test. The reduction in freestream noise along with a stable cavity reduces the pressure fluctuation amplitudes in the base of the cavity. The reduction in unsteady oscillations is also thought to reduce the heat transfer, although the heat transfer was not measured.

Finding the critical depth of the cavity is useful for the design of forward-facing cavities. Ladoon's study at Mach-4 was unable to find a critical cavity depth at which the cavity pressure oscillations changed from stable to unstable. Ladoon assumed that this was because the model he tested did not have a deep enough cavity to find the critical depth using only the freestream noise in the tunnel. Thus, he used laser-generated perturbations to infer a critical cavity depth by extrapolation. The laser-generated perturbation is a large, impulsive disturbance that is capable of exciting the bow shock without altering the overall freestream flow quality. When a forward-facing cavity is excited with a perturbation and the cavity depth is less than critical, the pressure fluctuations damp exponentially with an envelope described as:

$$p' = C \exp\left(-\frac{\gamma}{2}t\right) \tag{7.2}$$

where C and $\gamma/2$ are constants found using a least-squares fit to the peaks of the pressure fluctuations [24]. Ladoon correlated the damping constant ($\gamma/2$) to the angular resonance frequency (ω_1) using a power law:

$$\frac{\gamma}{2} = A\left(\frac{1}{\omega_1}\right)^{-m} \tag{7.3}$$

where A and m are constants found through a least-squares fit. Ladoon then estimated the critical cavity depth using a linear extrapolation from the least-damped data point. This critical length was $(L/D)_{\text{crit}} = 2.7$.

In the late 2000s, Segura performed new experiments and found the critical depth for a forward-facing cavity [102]. The cavity depth was adjusted from $L/D = 0.5$–3.0 and the pressure fluctuations were compared for each depth tested. This provided a critical depth of $L/D = 1.2$ [102]. Segura's studies were conducted in the same facility that Ladoon used. However, the model was tested at a lower freestream pressure because the higher pressures were no longer quiet.

7.1 Forward-Facing Cavity Model

A diagram of the forward-facing cavity used in the BAM6QT is shown in Figure 7.1. The model is 38.10 mm in diameter, with a 19.05-mm-radius tip. The cavity is cylindrical and centered along the centerline of the model, with a diameter of 19.05 mm. The cavity depth on this model can be varied from $L/D = 0.00$–5.00 by changing the position of an insert within the model. This position is fixed with set screws. Unused holes are filled with set screws, which are fixed in place with tape and nail polish.

A Kulite XCQ-062-15A pressure transducer with a B-screen is mounted flush to the base of cavity. This sensor is also mounted on the centerline of the cavity. A B-screen is used to protect the transducer from particle impact. The resonant frequency of the Kulite pressure transducer is about 320 kHz. Previous studies show that the bandwidth of a Kulite XCQ sensor is nominally flat up to 20% of the resonant frequency [76, 77] while Kulite specifies that the nominally-flat bandwidth is only

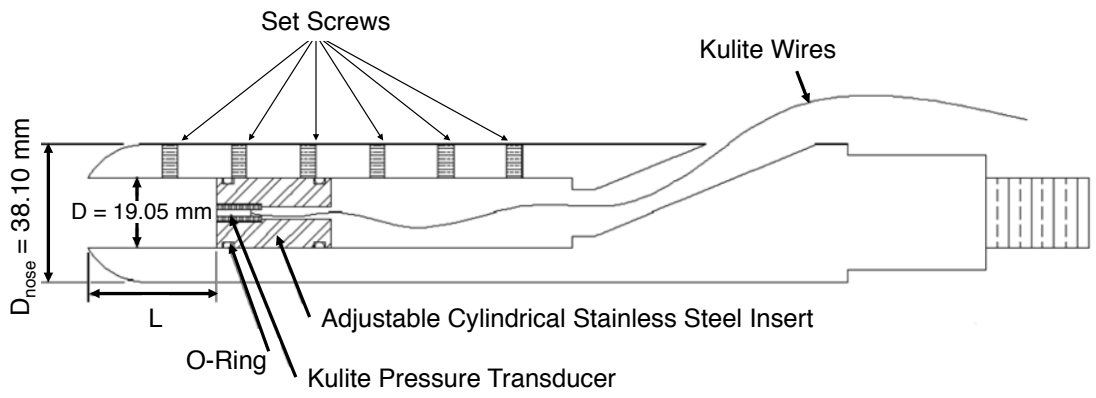

Figure 7.1. A diagram of the forward-facing cavity used.

20 kHz [75]. Regardless, this small bandwidth is sufficient for the frequencies seen in the forward-facing cavity, which do not exceed 5 kHz. The output signal of the transducer was amplified by a gain of 100, using a custom low-noise amplifier. The amplifier used a Texas Instruments INA103 amplifier chip, which has a -3 dB point at about 800 kHz [114].

The Kulite signal was acquired by a Tektronix DPO7054 with a sampling rate of 1 MHz. The Kulite signal was then low-pass filtered in post-processing with an 8-pole Butterworth filter with a cutoff frequency of 200 kHz to remove the resonant response of the Kulite. The roll-off of this Butterworth filter was about -3 dB at the cutoff frequency.

7.2 Cavity Response due to Natural Freestream Disturbances

In this section, the data shown do not include the effect of turbulent bursts on the nozzle wall nor the effect of freestream laser perturbations. The time data shown start at an arbitrary point after the tunnel starts, but remain in the first 2 seconds of the tunnel run. Only data from the first 2 seconds of the tunnel run was used

because previous measurements by Steen showed an increase in freestream acoustic noise after that time [92]. The frequency data shown in power spectral density plots is a result of breaking up a 0.1-s time sample into 10 segments and then ensemble-averaging the FFTs taken over each segment. A Welch spectrum estimation method with Blackman windows is used to determine the power spectral density. Up to 50% overlap was used for these windows. These parameters provide a frequency spacing of about 0.06 kHz.

7.2.1 Cavity Response to Natural Disturbances in Noisy Flow

Figure 7.2 shows an example of the response of a shallow cavity in noisy flow. Figure 7.3 shows an example of the response of a deep cavity in noisy flow. In the no cavity ($L/D = 0.00$) cases in both figures, the cavity is eliminated by sliding the adjustable cylindrical steel insert (Figure 7.1) until it lies flush with the rest of the nose.

In Figure 7.2(b), the fundamental cavity resonance peak at 3.85 kHz rises above the broadband frequency content, which remains at about the same level as the case where there is no cavity ($L/D = 0.00$). Using Equation 7.1, this frequency is about 5.4% different from the theoretical estimate of the fundamental cavity resonance frequency. The greatest difference between the theoretical and measured fundamental cavity resonance frequency was about 6% for all cavities tested. The error is presumably due to a combination of the estimate of the shock stand-off distance and the variation in the stagnation temperature from run to run.

Figure 7.3 shows the response of a deep cavity in noisy flow. The time response (Figure 7.3(a)) shows larger-amplitude pressure fluctuations in the cavity. The frequency content of these pressure fluctuations (Figure 7.3(b)) shows a fundamental peak at the resonance frequency of 1.53 kHz, and several harmonics at multiples of this frequency. This type of response is typical for a cavity experiencing self-sustained resonance. The normalized RMS amplitude of the pressure fluctuations at the fun-

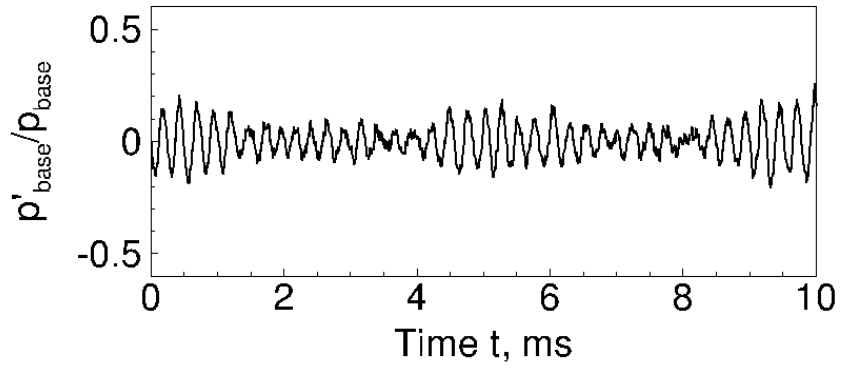

(a) Time response of a shallow cavity in noisy flow.

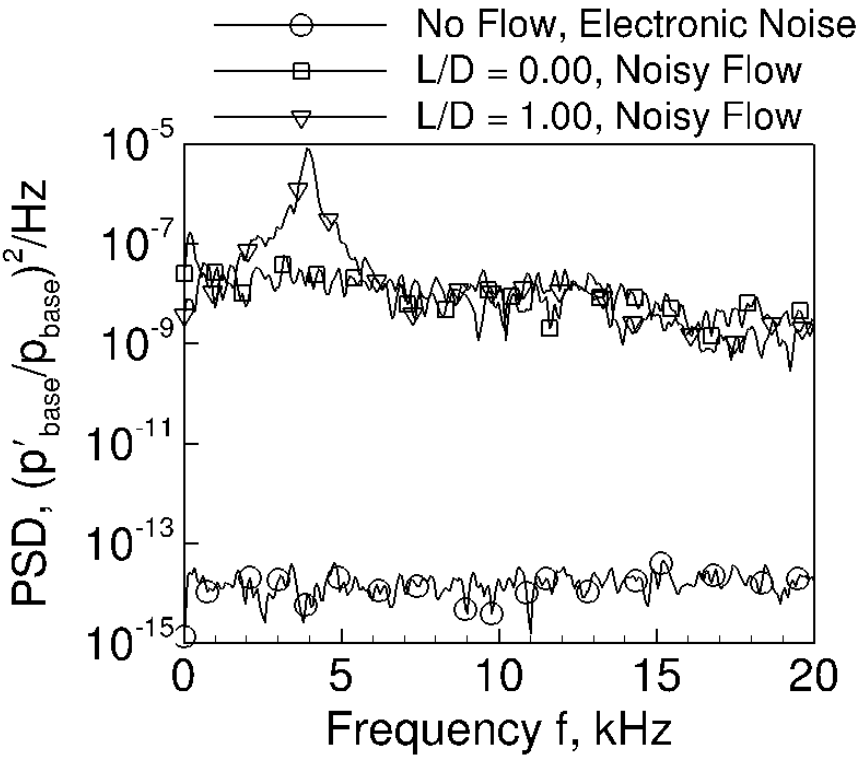

(b) Frequency response of a shallow cavity in noisy flow.

Figure 7.2. Damped cavity resonance: $L/D = 1.00$, $p_0 = 1072$ psia, $T_0 = 425.5$ K, Re/m $= 12.7 \times 10^6$/m, noisy flow (Run 9-05).

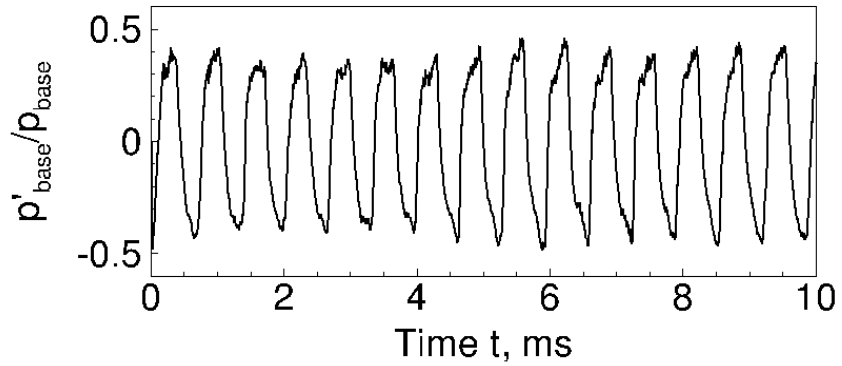

(a) Time response of a deep cavity in noisy flow.

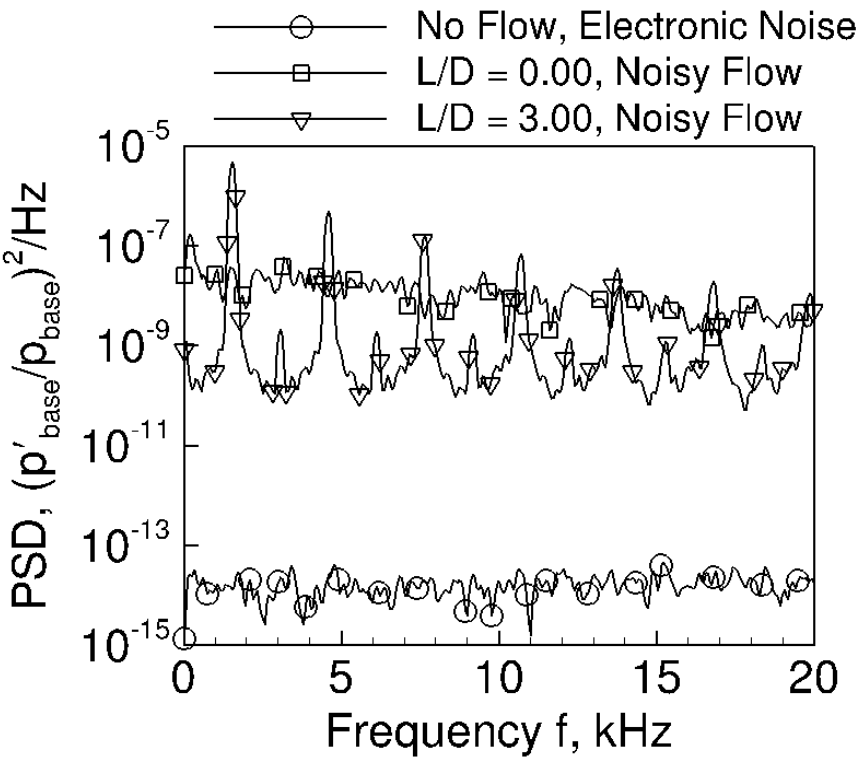

(b) Frequency response of a deep cavity in noisy flow.

Figure 7.3. Self-sustained cavity resonance: $L/D = 3.00$, $p_0 = 1078$ kPa, $T_0 = 424.4$ K, Re/m $= 12.8 \times 10^6$/m, noisy flow (Run 9-11).

damental frequency is roughly two orders of magnitude greater than the pressure fluctuations for the $L/D = 0.00$ case. However, the background frequency content for the $L/D = 3.00$ case appears to be lower than for the $L/D = 0.00$ case.

7.2.2 Cavity Response to Natural Disturbances in Quiet Flow

The response of the cavity in quiet flow is given in Figures 7.4 and 7.5. Note that there is a difference of two orders of magnitude in the y-axis on Figures 7.4(a) and 7.5(a). The RMS amplitude of the pressure fluctuations in the shallow cavity under quiet flow is two orders of magnitude lower than under noisy flow, requiring the re-scaling of the y-axis in Figure 7.4(a). However, the RMS pressure fluctuations in the deep cavity under quiet flow are about the same order of magnitude as under noisy flow, so Figure 7.5(a) did not require the same re-scaling. When the forward-facing cavity experiences self-sustained resonance in quiet flow, the RMS pressure fluctuations in the deep cavity ($L/D = 3.00$) are about 2.5 orders of magnitude higher, compared to shallow and zero-depth cavities.

The shallow cavity in quiet flow (Figure 7.4(b)) shows a single fundamental cavity resonance peak at 3.94 kHz, which is 3.2% different from the theoretical value. A small peak also exists at 1.26 kHz. The cause of this peak is unknown. The deep cavity (Figure 7.5(b)) shows a fundamental peak at 1.53 kHz with multiple higher harmonics. Unlike the noisy flow case, the background frequency content of the deep cavity in quiet flow is about an order of magnitude higher than the $L/D = 0.00$ case in quiet flow. The cause of this is not known.

A direct comparison of the frequency response of the shallow cavities is given in Figure 7.6. The peak frequency of the cavity resonance shifts with the cavity depth, as predicted by Equation 7.1. For shallow cavities, the cavity resonance is characterized by a single peak that rises above the noise, regardless of the magnitude of the freestream noise levels. An increase in freestream or broadband frequency content does not mask the resonance of the pressure fluctuations in the cavity. This

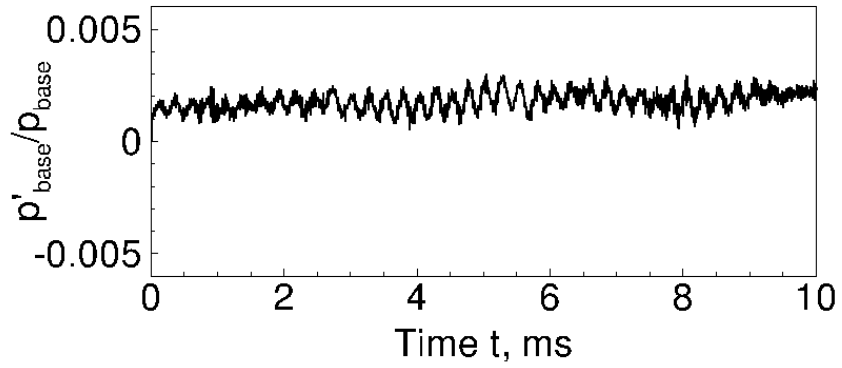

(a) Time response of a shallow cavity in quiet flow.

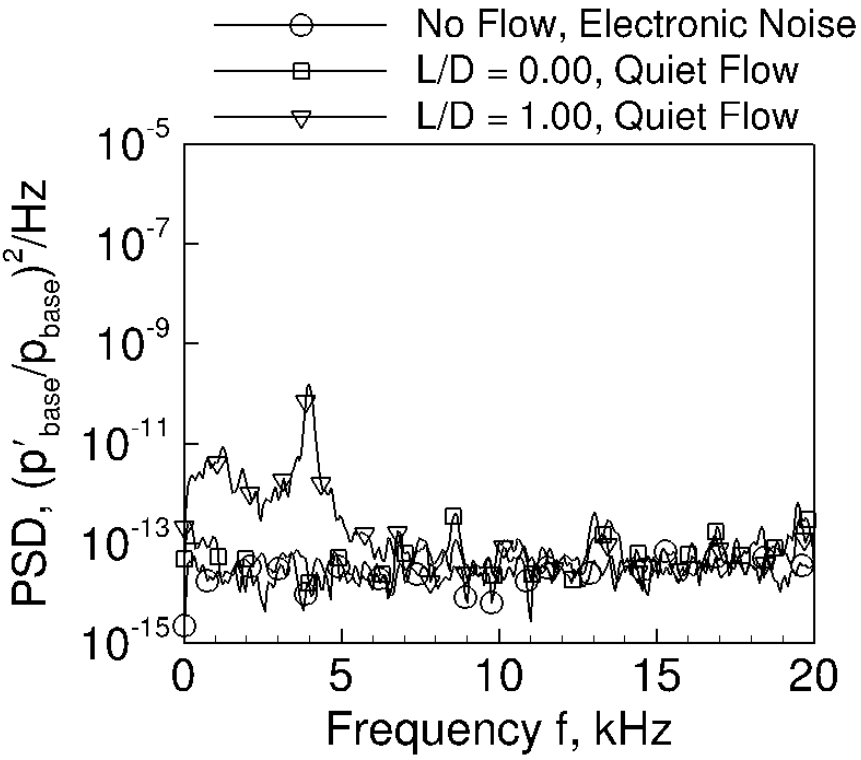

(b) Frequency response of a shallow cavity in quiet flow.

Figure 7.4. Damped cavity resonance: $L/D = 1.00$, $p_0 = 1072$ kPa, $T_0 = 425.5$ K, Re/m $= 12.7 \times 10^6$/m, quiet flow (Run 9-04).

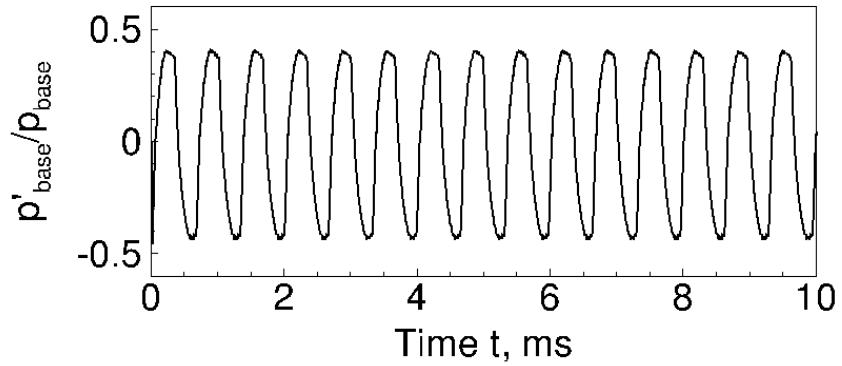

(a) Time response of a deep cavity in noisy flow.

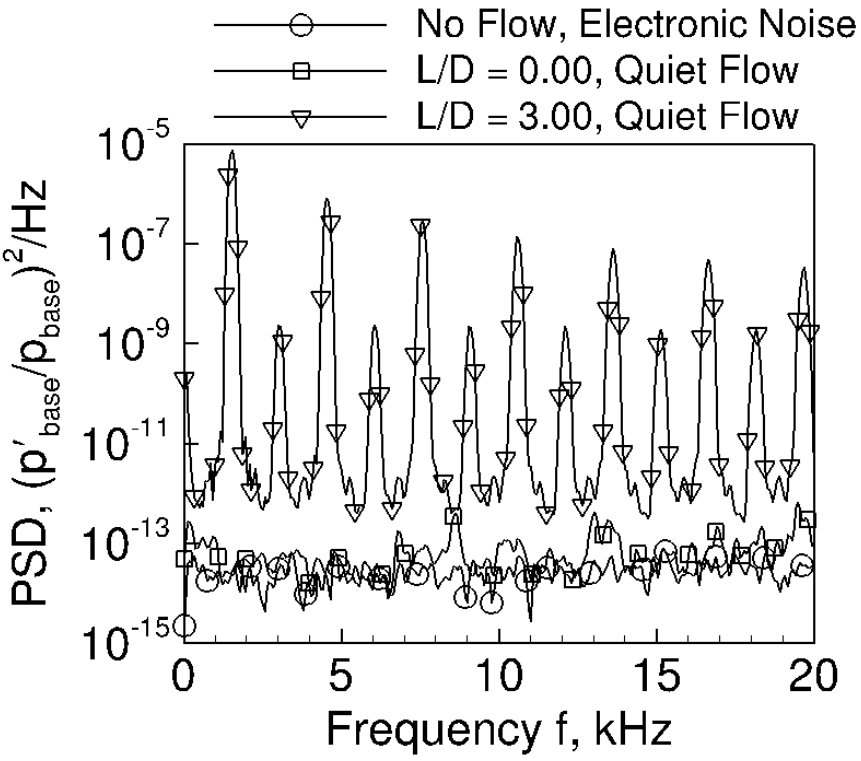

(b) Frequency response of a deep cavity in noisy flow.

Figure 7.5. Self-sustained cavity resonance: $L/D = 3.00$, $p_0 = 1059$ kPa, $T_0 = 424.0$ K, Re/m $= 11.7 \times 10^6$/m, quiet flow (Run 9-10).

indicates that the response of the system scales with the input to the system. Namely, the cavity acts as an amplifier of the incoming noise at the cavity resonance frequency.

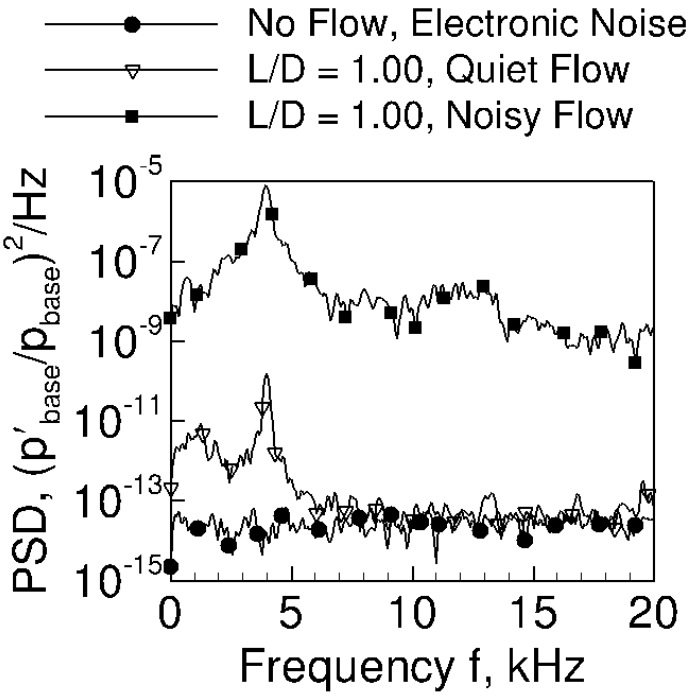

Figure 7.6. A comparison of frequency response for shallow forward-facing cavities (Runs 9-04 and 9-05).

A comparison of the spectra at a cavity depth of $L/D = 3.00$ is shown in Figure 7.7. These spectra show that the power spectral density at the fundamental and harmonics of the cavity resonance frequency are the same, regardless of the freestream noise level. However, the background noise level increases with the freestream noise, as seen in the damped cavity. It is likely that in the self-sustained resonance case, the cavity flow is in a saturated limit cycle, where a majority of the energy is contained in the fundamental frequency and harmonics.

The RMS amplitudes of the electronic noise and $L/D = 0.00$ cases were found by integrating spectra from 0–50 kHz. RMS amplitudes of cavity resonance are taken by integrating the spectra across the full width at half maximum (FWHM) of the fun-

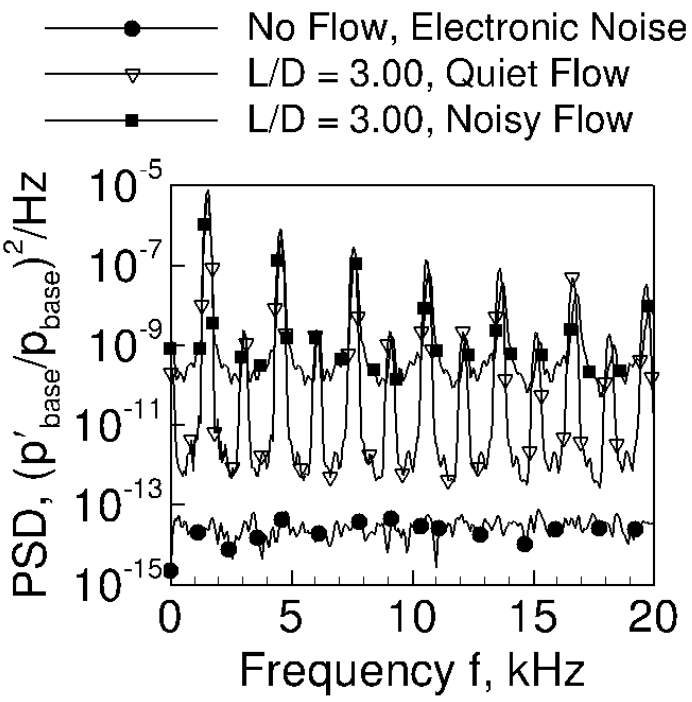

Figure 7.7. A comparison of frequency response for deep forward-facing cavities (Runs 9-10 and 9-11).

damental peak. This was done to ensure consistency in comparing the measurement of the RMS amplitude for both damped and self-sustained cavities. The deeper, self-sustained cavities exhibit large harmonics, which affect the RMS amplitude. Deeper cavities also tend to have a lower resonance frequency, so more harmonics appear in a smaller bandwidth. The RMS amplitudes of the peak cavity resonance frequency are given in Table 7.1.

Cavity depths between $L/D = 0.00$–5.00 were tested to find the critical cavity depth. The RMS amplitude of the fundamental resonance peak of the cavity pressure fluctuations was calculated for a variety of cavity depths. At the critical depth, the fluctuations should increase by orders of magnitude. Figure 7.8 shows that the RMS fluctuations increase by 1 order of magnitude in noisy flow and about 2.5 orders of magnitude in quiet flow at about $L/D > 1.2$. This value of the critical depth agrees

Table 7.1 RMS amplitudes of cavity resonance fundamental peak.

L/D	**Flow Condition**	p'_{base}/p_{base}
Electronic Noise		2.81×10^{-5}
0.0	Quiet	2.04×10^{-4}
0.0	Noisy	2.12×10^{-2}
1.0	Quiet	2.55×10^{-4}
1.0	Noisy	4.87×10^{-2}
3.0	Quiet	0.315
3.0	Noisy	0.283

with Segura's experiments at Mach 4 [102]. It is interesting to note that Ladoon tested cavity depths ranging well beyond $L/D = 1.2$ (from $L/D = 0.272$–1.984) in the same tunnel as Segura and could not find a critical cavity depth experimentally [24]. The Mach-4 quiet tunnel is no longer operational, so the Ladoon et al. experiment would not be easy to repeat.

The stability of these systems could also be determined from looking at the probability density function (PDF) of the response in the time domain. Rowley et al. found that stable cavities exhibit a probability density with a normal distribution. Unstable, limit-cycling cavities exhibit bimodal distributions [115]. Rowley et al.'s work concerns weapons-bay-like cavities rather than forward-facing cavities, but the comparison of probability densities should yield similar results. Example probability densities for cavities in quiet flow are given in Figure 7.9. The probability density for a shallow cavity is shown in Figure 7.9(a). The shape of the probability density function for this shallow cavity is normal, which indicates that the cavity is stable. The probability density for a deep cavity in quiet flow is given by Figure 7.9(b). The shape of this probability density function is bimodal, like that for a sine wave, which indicates that this type of cavity is unstable. Similar results are seen for cavities in noisy flow.

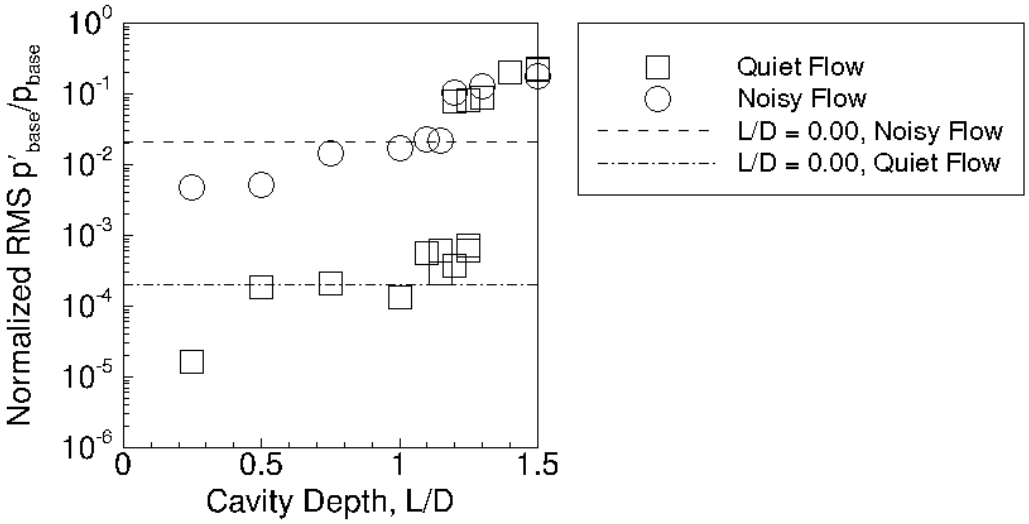

(a) Shallow Cavities, Semi-Log Plot.

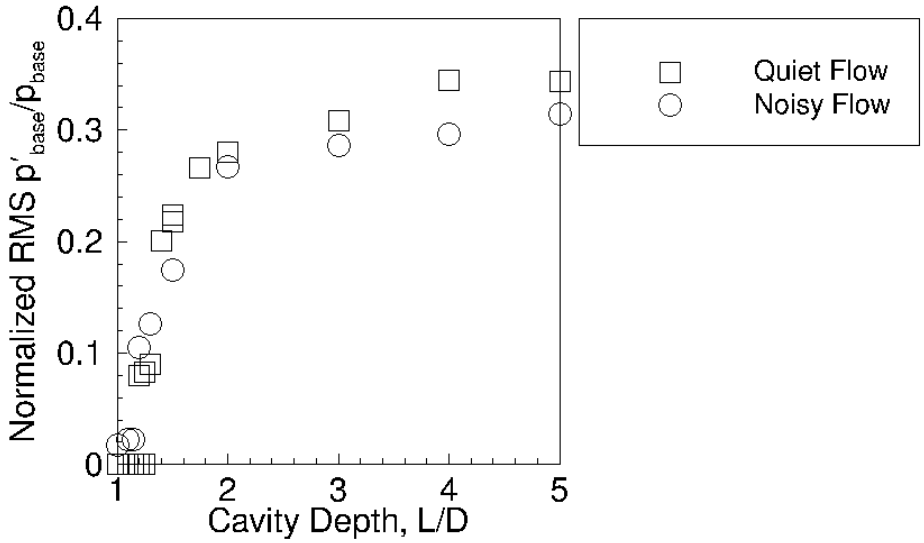

(b) Deeper Cavities, Linear Plot.

Figure 7.8. A comparison of RMS amplitudes of fundamental resonance peak for different cavity depths. $p_0 \approx 1060$ kPa, $T_0 \approx 425$ K, Re/m $\approx 12.5 \times 10^6$/m, quiet flow. Runs 9-04–9-15, 9-18–9-41.

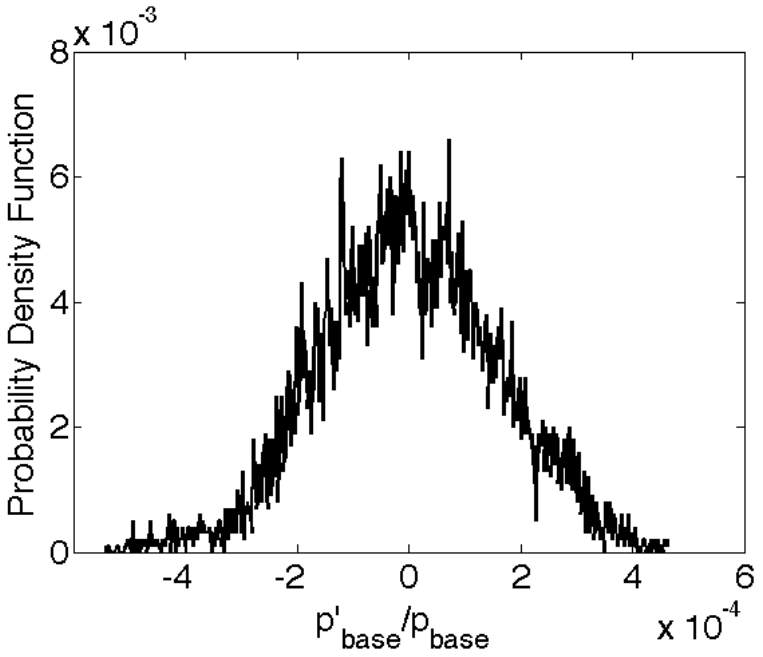

(a) For a damped cavity in quiet flow. Run 9-04: $L/D = 1.00$, $p_0 = 1072$ kPa, $T_0 = 425.5$ K.

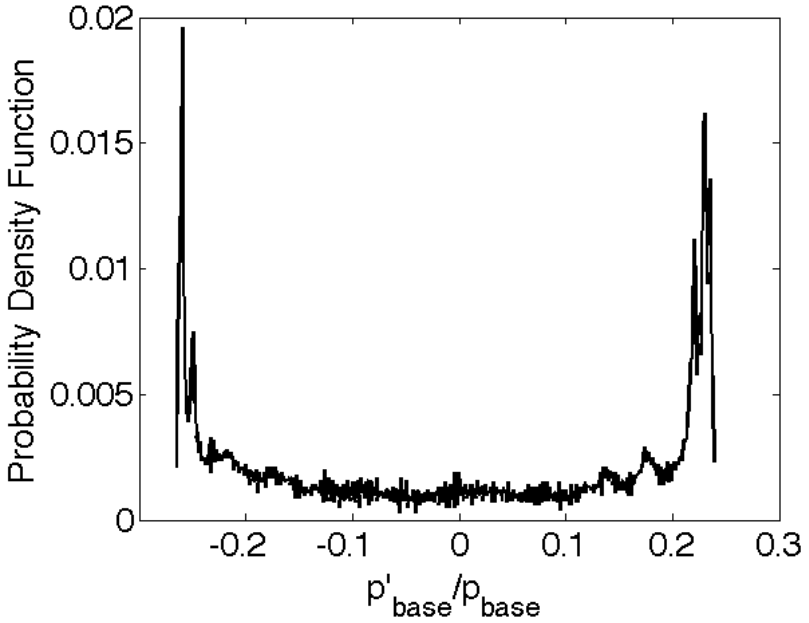

(b) For a self-sustained cavity in quiet flow. Run 9-10: $L/D = 3.00$, $p_0 = 1059$ kPa, $T_0 = 424.0$ K.

Figure 7.9. Probability density functions for cavities in quiet flow.

7.2.3 Effect of a Turbulent Spot on the Forward-Facing Cavity

Even at low Reynolds numbers, turbulent spots occasionally develop on the nozzle wall of the BAM6QT. These are typically infrequent if the boundary layer on the nozzle wall is laminar. However, at higher Reynolds numbers, turbulent spots develop more frequently on the nozzle wall and affect the freestream. A Mach wave precedes a turbulent spot on the nozzle wall. This wave can affect the bow shock in front of the model if it intersects the bow shock. A diagram of this effect is given in Figure 7.10.

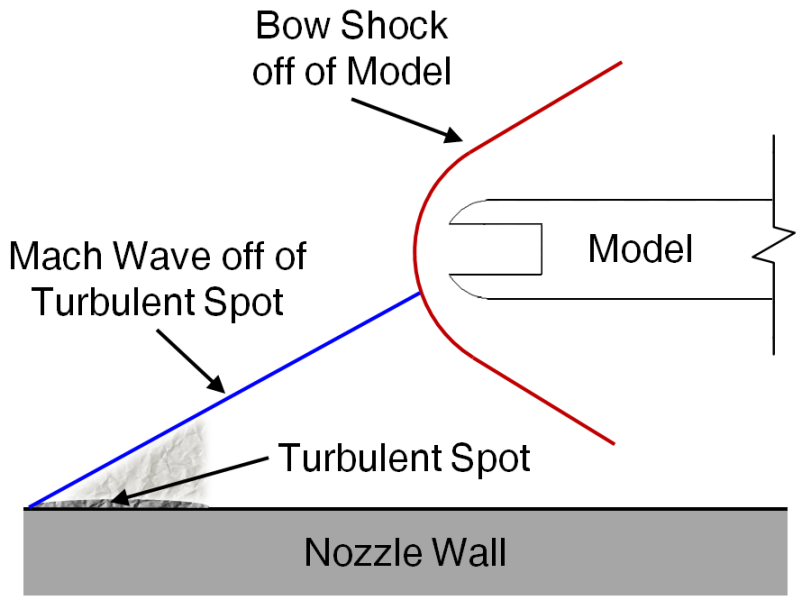

Figure 7.10. Diagram of the effect of a turbulent spot on a nozzle wall on a model in the tunnel.

Data shown previously in this chapter excludes data affected by turbulent spots. Figure 7.11 shows the response of the cavity to a turbulent spot on the nozzle wall. The blue trace is the voltage from a nozzle-wall hot film located 30 cm upstream of the nose of the model. The red trace is the calibrated pressure response of the cavity as a result of the passing turbulent spot. Note that the L/D here is near the critical depth, but the cavity yields a damped resonance. This may be due to small sensitivities in the flow near the critical depth. To study this effect in detail,

a controlled perturbation can be placed in the freestream of the tunnel using a laser perturber.

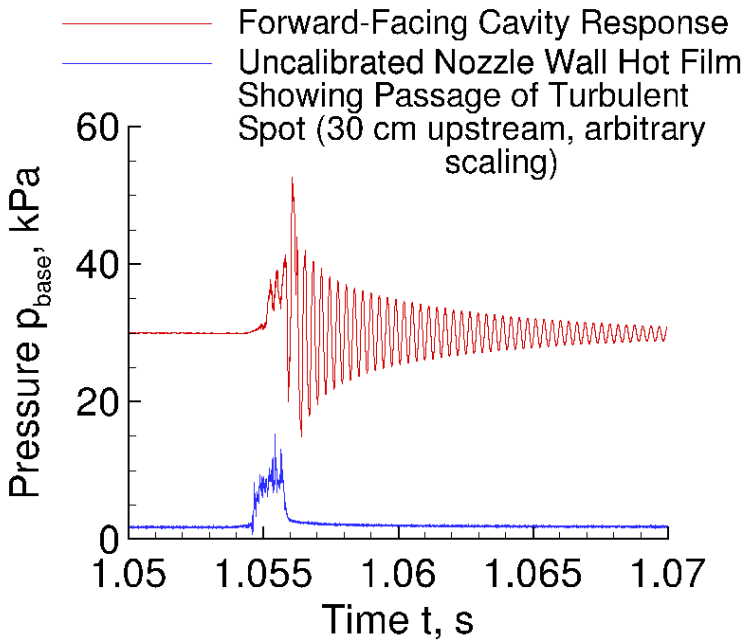

Figure 7.11. Effect of a turbulent spot on the nozzle wall on the forward-facing cavity. Run 9-40: $L/D = 1.25$, $p_{0,1} = 1026$ kPa, $T_0 = 425.1$ K, $M = 6.0$, quiet flow.

7.2.4 Cavity Resonance at Near-Critical Cavity Depths

The cavity exhibited signs of self-sustained resonance at the beginning of a run and then decayed before the end of the run, for cavity depths between $L/D = 1.00$ and 1.50. An example of this phenomenon is shown in Figure 7.12. This figure shows the measured cavity base pressure during a single tunnel run. In this example, the forward facing cavity experiences self-sustained resonance from when the tunnel starts at $t = 0$ s until about $t = 2.25$ s. The Reynolds number may have some effect on the critical cavity depth. At about $t = 3.25$ s, a turbulent spot passes on the nozzle wall. The effect of this turbulent spot decays, as seen previously for stable cavities.

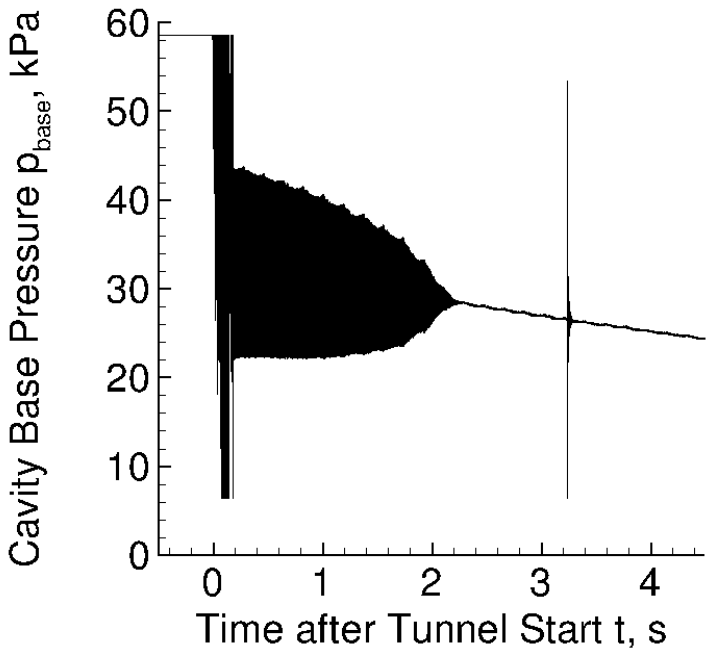

Figure 7.12. Example of decay from self-sustained resonance at near-critical cavity depths. Run 11-01: $L/D = 1.50$, $p_{0,i} = 1115.6$ kPa, $T_{0,i} = 439.2$ K, $M = 6.0$, quiet flow.

This effect was investigated by varying the Reynolds number based on cavity depth in two ways: by varying the cavity depth and by varying the initial stagnation pressure. The cavity Reynolds number is defined as

$$Re_L = \frac{\rho_\infty u_\infty L}{\mu_\infty} \tag{7.4}$$

where ρ_∞ is the density in the freestream, U_∞ is the freestream velocity, μ_∞ is the viscosity in the freestream, and L is the cavity depth. When only the cavity depth was varied, the initial stagnation pressure was held constant at about $p_{0,i} = 1115$ kPa. When the initial stagnation pressure was varied, the cavity depth was held constant at $L/D = 1.50$.

The criteria used to determine when self-sustained resonance appears to cease is when the cavity base pressure fluctuations drop below 1% of the mean cavity base pressure. Figure 7.13 shows a comparison of the cavity Reynolds number when the self-sustained resonance ceases ($Re_{L,stop}$) versus the initial cavity Reynolds number

($Re_{L,i}$). The y-axis is the cavity Reynolds number when self-sustained resonance ceases, in millions. The x-axis is the cavity Reynolds number at the start of the run, in millions. The Reynolds number when the self-sustained resonance ceases appears to be directly proportional to the initial cavity Reynolds number. A linear fit to the line has a coefficient of determination (R^2) of 0.973. The slope of this linear fit is about 0.87, which means that the self-sustained cavity resonance ceases for these critical cavity depths when the freestream Reynolds number drops by about 13%. The cause of this phenomenon is unknown.

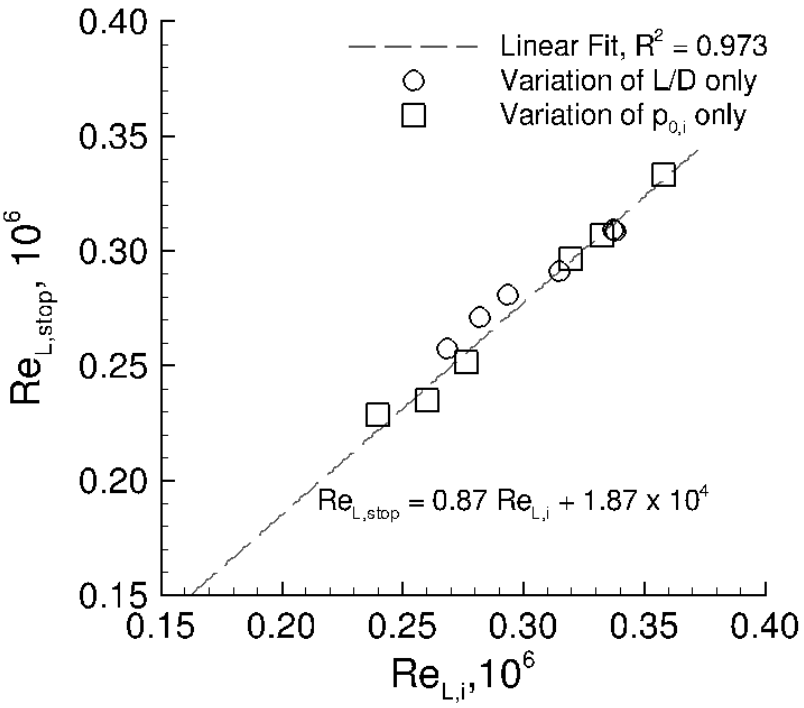

Figure 7.13. Cavity Reynolds number when the self-sustained resonance ceases, versus the initial cavity Reynolds number.

7.3 Cavity Response due to Laser-Generated Perturbations

Figure 7.14 shows the response of the forward-facing cavity when a laser-generated perturbation is created 56.0 mm upstream of the model nose. The cavity resonates

when the laser perturbation distorts the flow near the cavity nose, but damps out if $L/D < (L/D)_{\text{crit}}$. At higher stagnation pressures, more turbulent spots form in the nozzle wall boundary layer of the BAM6QT, which affects the data. Thus, in the amount of time during which the BAM6QT has quiet flow, fewer laser perturbations that were unaffected by the turbulent spots were available for analysis at the higher stagnation pressures. This reduced the number of time blocks available for analysis. All time data shown in this section are ensemble averages consisting of 5 different time blocks after a laser pulse.

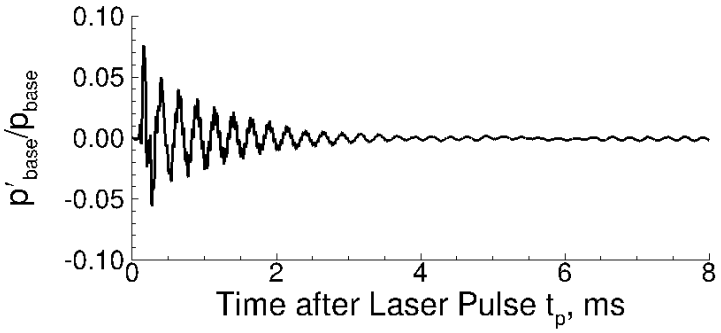

Figure 7.14. Ensemble average of laser shots 6–10 for Run 12-04: $L/D = 1.00$, $p_{0,1} = 1051$ kPa, $T_0 = 426.7$ K, $M = 6.0$, quiet flow, $\Delta z_i = 56.0$ mm.

The damping of the cavity response appears to have an exponential envelope. The exponential envelope can be fitted to the peaks using a least-squares method. The damping rate $\gamma/2$ can then be correlated to the characteristics of the cavity as in Ladoon's work [24]. An example is given in Figure 7.15.

Effect of Model Location

Two different model locations were tested. The first location placed the nose of the model at $z = 1.980$ m, $\Delta z_i = 56$ mm from the location where the perturbation is formed. This location was similar to the relative positioning used by Ladoon [24] in the PQFLT. However, the optical access for the laser perturber apparatus in the

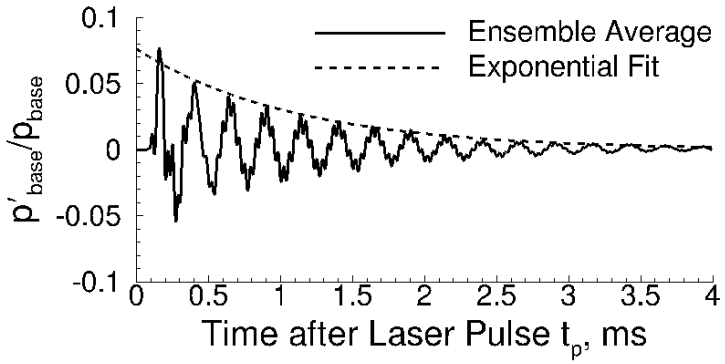

Figure 7.15. Sample data from Figure 7.14 with an exponential envelope fitted to the peaks. (Ensemble average of laser shots 6–10 for Run 12-04.)

BAM6QT is farther upstream. Thus, a location of $\Delta z_i = 56$ mm may have placed the blunt model in a region of nonuniform flow. The second model location was 0.375 m farther downstream at $z = 2.370$ m ($\Delta z_i = 430$ mm) to mitigate the effects of nonuniform flow. A diagram of the relative locations of the model and onset of uniform flow (dotted blue line) in the tunnel is given in Figure 7.16. The freestream perturbation is created near the center of the laser window, which is located at $z = 1.924$ m.

A close-up schematic of the far-forward positioning of the model is given in Figure 7.17. The theoretical Mach line designating the onset of uniform flow is given by a dashed blue line. The onset of uniform flow here is computed from the method of characteristics code used to design the tunnel [116]. The nozzle is still diverging at this location. The bow-shock standoff distance is approximated as $\delta = 0.34D$. The components of this schematic are drawn to scale, except for the laser-generated perturbation. This schematic shows that the laser-generated perturbation was offset from the center of the laser window by about 1 mm. This type of small offset occurs when the perturbation-forming optics are placed at a small angle from the flat window. The optics are placed at a small angle to reduce the likelihood of back-reflections on the flat window surface. This schematic shows that the placement of

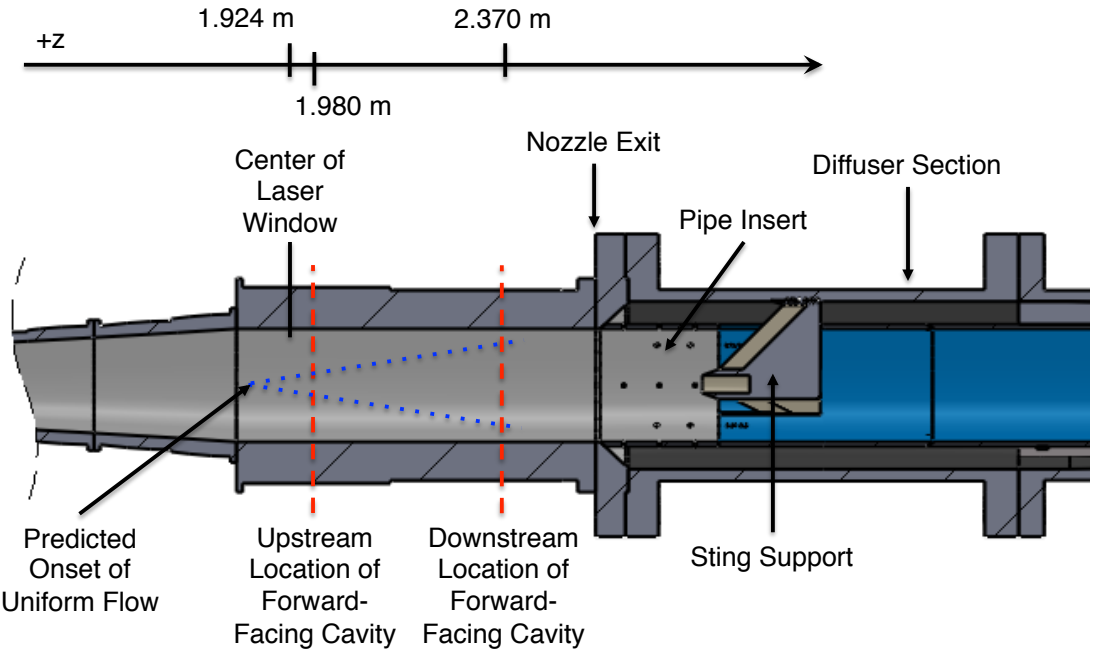

Figure 7.16. Schematic of model location with respect to the onset of uniform flow in the tunnel.

the forward-facing cavity model in the far-forward position places part of the nose of the model outside the region of uniform flow. However, the nozzle is very long relative to the exit diameter, so the flow properties change slowly near the nominal onset of uniform flow. Thus, the effects of nonuniform flow may not be significant.

When the model was placed farther downstream at $z = 2.370$ m, the response of the cavity to the laser perturbation did not resemble the cavity response seen by Ladoon. Figure 7.18 shows an example trace of the cavity response due to the perturbation at a farther aft location. While the later portions of the response appear similar, the initial response of the cavity to the laser perturbation does not appear to be the same. A laser perturbation can consist of a nearly-spherical thermal core surrounded by a weak spherical shock. The cavity response at the farther aft location appears to react to the different components of the laser-generated perturbation at

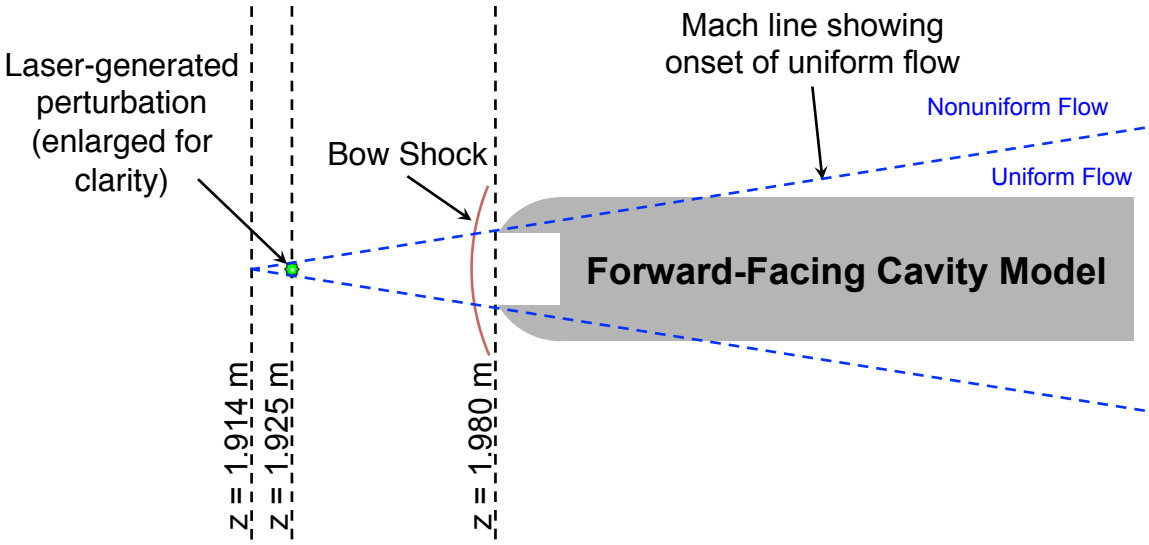

Figure 7.17. Close-up schematic of model in far-forward positioning ($z = 1.980$ m).

distinctly separate times, and thus has a different initial response. Since the latter portion of the cavity response to the perturbation appears to be the same as when the model is far upstream, the exponential envelope is fit to this portion of the response.

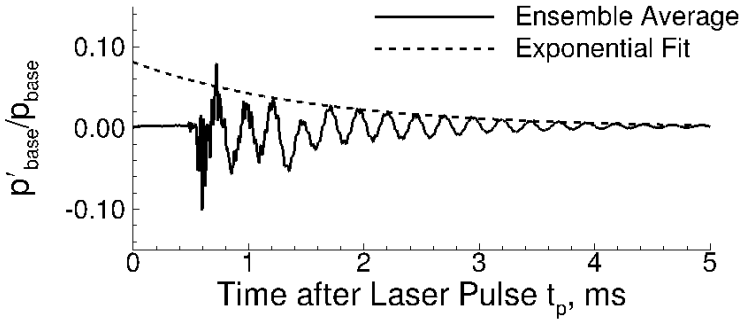

Figure 7.18. Ensemble average of laser shots 6–10 for Run 16-09: $L/D = 1.00$, $p_{0,1} = 1097$ kPa, $T_0 = 429.2$ K, $M = 6.0$, quiet flow, $\Delta z_i = 430$ mm, 5 averages.

Relation between Damping Constant and Resonance Frequency

Ladoon correlated the damping constant $\gamma/2$ to the inverse of the fundamental cavity resonance frequency $(1/\omega_1)$. Figure 7.19 shows this correlation for both Ladoon's data at Mach 4 (in squares) and the BAM6QT (in triangles and circles) for the model locations that were tested. The damping appears to occur at the same rate in the BAM6QT, regardless of the model's position in the tunnel. However, the data from BAM6QT and PQFLT fall on two different curves. The Reynolds numbers behind the shock wave in the current experiment were made to match those in Ladoon's experiment. However, the two experiments used models of different sizes and cavity diameters, and were performed under different stagnation conditions (pressures, temperatures, and Mach numbers). These parameters can affect ω_1 and probably also have some effect on $\gamma/2$. Thus, the data should not be expected to collapse on the same curve.

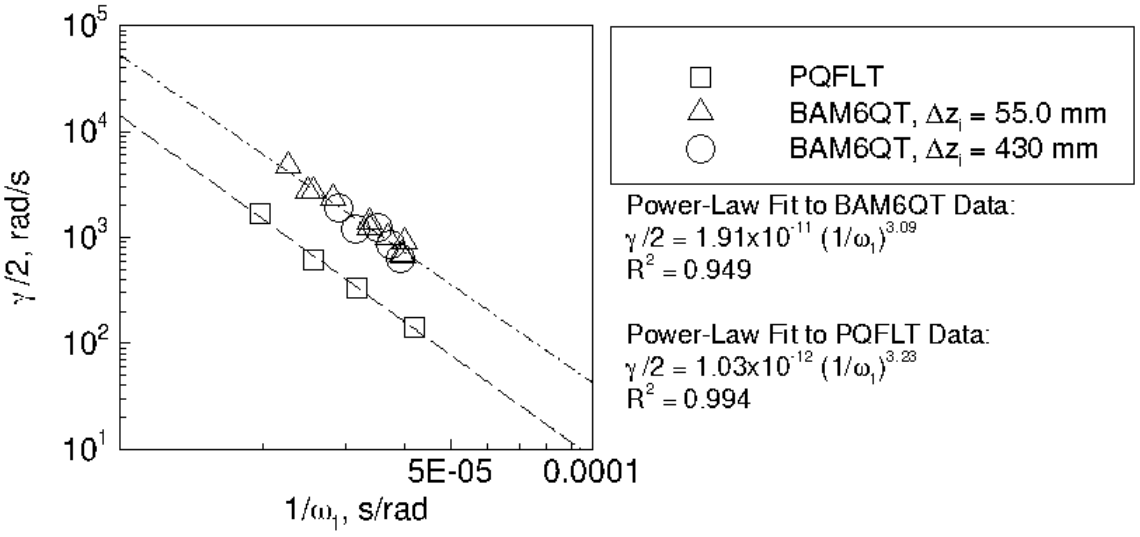

Figure 7.19. Correlation of the damping constant to the fundamental cavity resonance frequency for different Mach numbers.

Relation between Damping Constant and Cavity Depth

The correlation between the damping constant and the fundamental cavity resonance frequency appears to depend on a combination of Mach number and stagnation conditions. When the damping constant is plotted against the nondimensional cavity depth, the two data sets collapse, as shown in Figure 7.20. Ladoon's data at Mach 4 is plotted in squares while the Mach 6 data is plotted in triangles and circles. The data collapse on one curve, regardless of Mach number, stagnation temperature, etc. This implies that the damping characteristics of the cavity depend only on the non-dimensional cavity depth.

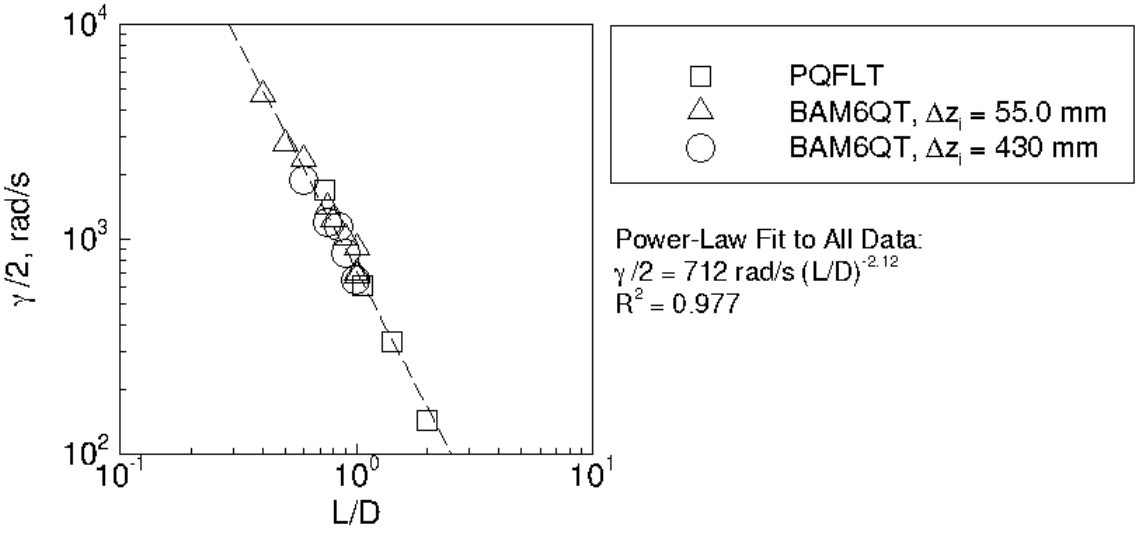

Figure 7.20. Correlation of the damping constant to the non-dimensional cavity depth for different Mach numbers.

7.4 Summary

Skill in aligning the perturbation to a downstream model was developed during this experiment. The laser perturber apparatus was also used in successful experiments with the forward-facing cavity. The laser perturbation impinging on the

forward-facing cavity at Mach 6 yielded measurements that were similar to those obtained by Ladoon [24]. Self-sustained cavity resonance appears at $L/D > 1.2$ in a forward-facing cavity geometry. In quiet flow, the onset of self-sustained resonance as the cavity depth is increased has a dramatic effect. The RMS pressure fluctuations in the cavity increase by 2.5 orders of magnitude in self-sustained resonance. In noisy flow, the RMS amplitude increase between damped and self-sustained resonance is only about 1 order of magnitude. However, the RMS amplitudes of the pressure fluctuations under self-sustained resonance are fairly similar for the two freestream noise levels.

The damping characteristics of sub-critical cavity depths can be examined by placing a freestream laser-generated perturbation upstream of the model. The perturbation supplies a large impulse, which excites the cavity resonance. The damping rates do not appear to be affected by the model's location in the tunnel. Furthermore, a comparison to measurements in a Mach-4, quiet-flow facility shows that $\gamma/2$ scales with L/D regardless of stagnation temperature and Mach number. This information could be useful in future designs of vehicles with forward-facing cavities.

CHAPTER 8. INTERACTION OF THE FREESTREAM LASER PERTURBATION WITH A FLARED CONE

The ultimate goal of this research was to measure the interaction of the freestream laser-generated perturbation with the boundary layer of a flared cone and to relate the boundary-layer instabilities to the freestream disturbances. Ideally, the amplitude and frequency content of the boundary-layer instabilities can be correlated to the amplitude of the freestream disturbances. A model could then be developed to show how the freestream disturbances create the boundary layer instabilities. This would provide great insight into the receptivity problem.

Chapters 4 and 5 contain detail about the freestream disturbance measurements. These measurements may not be sufficient to develop the amplitude-based theory of transition, but the present effort still reveals useful information. This current chapter discusses measurements of the boundary-layer instabilities on the flared cone. Surface pressure fluctuations beneath instability waves in a boundary layer are easily measured with pressure transducers. Thus, measurements of the effect of the freestream perturbation on the boundary-layer instabilities were made with surface-mounted pressure transducers. Measurements that are more complete and accurate are needed to help develop amplitude-based models of transition and some suggestions for future work are offered in the Chapter 9.

8.1 Flared Cone Model

A flared cone model was used because previous measurements showed that the natural instability waves on this model were very large. Natural transition also occurred under quiet flow on this model [10,117]. Other models, such as straight, slender cones, typically have small natural instability waves, which are difficult to measure

with surface-mounted pressure transducers and do not undergo natural transition in quiet flow. The flared cone model was therefore chosen to provide clear measurements of the instability waves.

The model was a body of revolution bounded by a circular arc with a 3-meter radius. The circular arc meets the hemispherical nosetip so that the curves lie tangent to each other. A schematic of this geometry is shown in Figure 8.1. The nosetip region and the frustum were manufactured as two separate components.

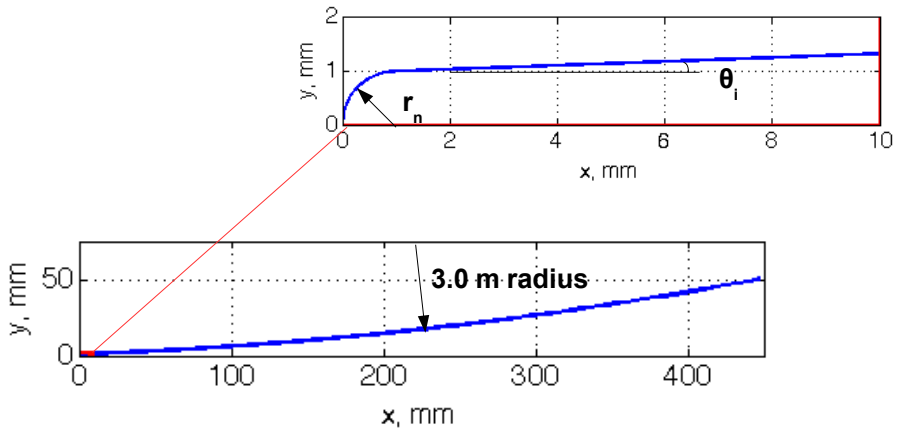

Figure 8.1. Schematic of the flared cone geometry, with detail of nosetip in inset.

The flared cone frustum was made from 6061-T6 aluminum round stock. This portion of the cone was 302.6 mm in length. The base of the cone was 99.5 mm in diameter. Fourteen 3.28-mm cylindrical ports were drilled into the frustum to allow for the installation of 3.12-mm-diameter sensors. Typically, these ports can be outfitted with fast pressure transducers or Schmidt-Boelter heat transfer gauges. The expected second-mode frequency is centered between 200–300 kHz, so sensors with a high-frequency response were required. PCB fast pressure transducers were thought to provide the most convenient and cost-effective method of measuring the response to the perturbation.

8.1.1 Nose Tips for the Flared Cone

The geometry of the nosetip is essentially a hemisphere that lies tangent to the circular-arc body of revolution. Two interchangeable nosetips are available for this model: a 1-mm-radius nosetip and a 0.16-mm-radius nosetip. Both nosetips were manufactured using 17-4PH stainless steel and a computer numerical control (CNC) lathe. The 1-mm-radius nosetip was approximately 143.1 mm long and is referred to as the blunt nosetip. A close-up picture of this nosetip is provided in Figure 8.2(a). A ruler with 1/64-inch divisions is visible in the lower portion of the image. Figure 8.2(a) shows that the blunt nosetip is not a perfect hemisphere, due to the limitations of the feasible manufacturing processes.

The sharp nosetip was made by supplying a CNC lathe with coordinates for an ideally sharp nosetip. However, due to manufacturing limitations, the nosetip broke at a location where the radius is about 0.16 mm. Technically, the nosetip is no longer sharp, but will be referred to as the "sharp nosetip" for simplicity. The final length of this nosetip is about 170.3 mm. A close-up picture of this sharp nose is shown in Figure 8.2(b). Part of a ruler with 1/64-inch divisions is visible in the upper portion of the image. The sharp nosetip was accidentally bent while in storage, but was re-straightened prior to these experiments. The straightness of this nosetip has not been measured due to its fragility. Table 8.1 provides a summary of the parameters illustrated in the inset in Figure 8.1 corresponding to each nosetip.

Table 8.1 Nosetip geometry parameters for the flared cone.

Nosetip	**Radius of Nosetip** r_n**, mm**	**Initial Opening Angle at Nose-Flare Junction** θ_i**, °**
Blunt	1	2
Sharp	0.16	1.47

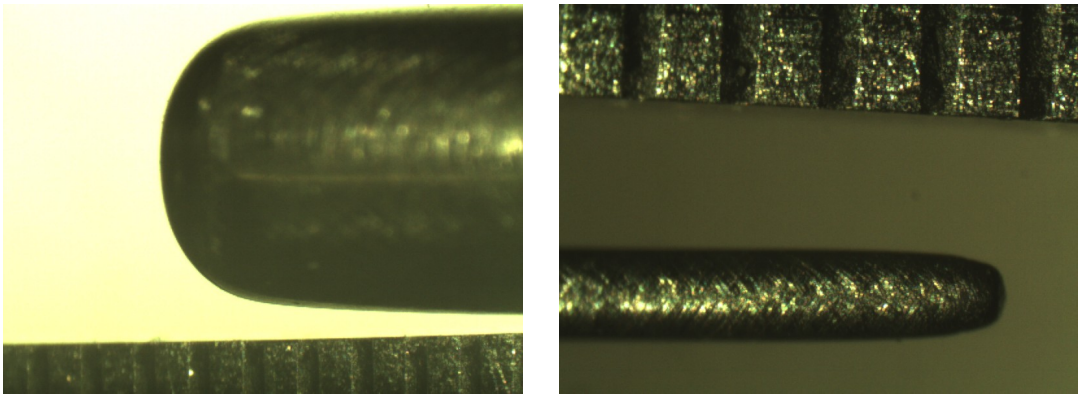

(a) $r_n = 1$ mm. (b) $r_n = 0.16$ mm.

Figure 8.2. Close-up pictures of interchangeable nosetips, taken with a microscope. Ruler has divisions every 1/64 inches.

8.1.2 Fast Pressure Transducer Placement

Fourteen PCB 132A31 sensors were mounted in the flared cone. Due to the limited number of long-memory Tektronix oscilloscopes, only 12 PCB sensors could be monitored at a time. The PCB transducers were sampled at 2 MHz for 5 seconds of the run time. The PCB measurements were converted to pressure using the factory calibration. Some discrepancies between the factory calibration and a dynamic calibration of the sensors have been noted in other experiments [77, 100]. The factory calibration for these sensors was used because a suitable dynamic calibration process had not yet been developed at the time of these experiments.

The PCB sensors were installed on three separate rays, 120° apart. Figure 8.3 shows eight sensors mounted in the main ray, which is referred to later as the 0° ray. The axial positions of the sensors on the ±120° rays match up with some of the sensors on the 0° ray. This creates three azimuthal arrays of sensors at different axial stations, which can be used to determine the angle of attack of the model. Small adjustments in angle of attack on the order of $< 1°$ are possible using the sting mount of the BAM6QT. The model is typically adjusted without the laser perturbation by trying to match the frequency and magnitude of second-mode wave peaks in the power

spectra for measurements in an azimuthal array of sensors. More on the process of alignment is given in the next section.

Figure 8.3. Picture of the flared cone model with blunt nose tip, showing fast pressure transducers mounted in the main (0°) ray.

The installation of these sensors in a flared cone model is not trivial. The large diameter of the sensors and the model curvature has the possibility of significantly affecting the surface roughness characteristics. Roughness profiles are taken with a Mitutoyo SJ-301 surface roughness tester. The surface roughness tester measures the profile of a surface by pulling a needle across the surface in a line and measuring the amount of deflection that the needle experiences. An example roughness profile is shown in Figure 8.4. This profile is a P-profile, meaning no high-pass filters are applied to the roughness profile. The minima at $\Delta x = 1.88$ and 4.97 mm correspond to the edges of the PCB. The cone frustum surface around the PCB sensor hole is at $\Delta x = 0$–1.88 mm and $\Delta x = 4.97$–7.5 mm. The average roughness height created by the sensors is between 20–30 μm. The maximum roughness height is reported by the SJ-301 to be 234 μm, but this is likely a measurement of the gap between the PCB sensor and cone frustum. For comparison, the step at the junction between the nosetip and cone frustum was only 12.5 μm.

The serial numbers, factory calibrations, and positions of the sensors used are given in Table 8.2. As many PCBs from the newest batch as possible were used in this experiment. This was done to ensure that the installed sensors were not damaged from previous use. An attempt was made to install sensors with matched

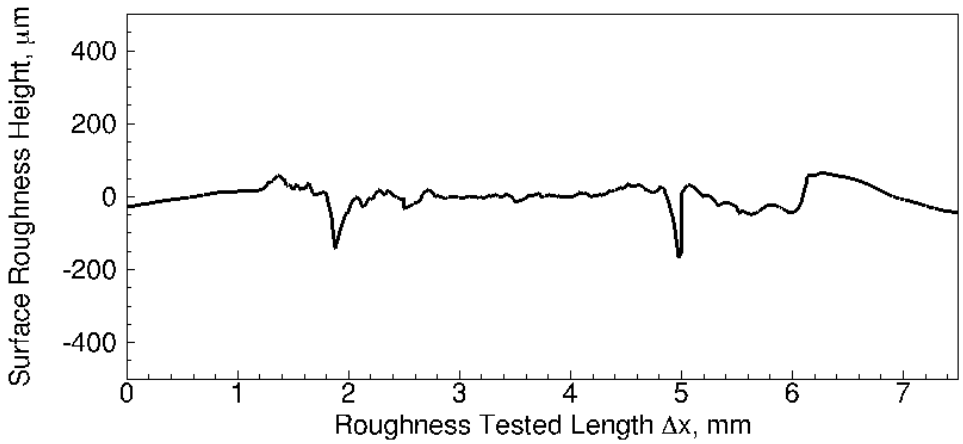

Figure 8.4. Roughness profile of a PCB sensor moutned in the flared cone model.

factory calibrations at the same axial station. Thus, sensors in the same azimuthal array had similar factory calibrations so that azimuthal comparisons could be made easily.

8.2 Alignment of the Model

The alignment process for this experiment required care, precision, and luck. The model must first be aligned to the flow to ensure that as little flow angularity as possible occurs relative to the model. Once the model is aligned to the flow without the laser-generated disturbance, its position is fixed in the tunnel and secured as best as possible with set screws. The laser-generated disturbance must next be aligned to the cone model. This is done with the flow off and with the aid of an alignment tool.

8.2.1 Alignment of the Model to the Flow

The model alignment to the flow was performed by analyzing the power spectra at three different azimuthal locations. In this particular experiment, there were three axial stations at which these spectra can be compared. For the blunt nosetip, these locations were x = 302, 351, and 403 mm from the nosetip. For the sharp nosetip,

Table 8.2 Table of PCB 132A31 sensors used.

$r_n = 1$ **mm** x, **mm**	$r_n = 0.16$ **mm** x, **mm**		**Ray** 0°	+120°	−120°
200	231	**Serial Number**	6599		
		Calibration, mV/psi	172.8		
250	281	**Serial Number**	6601		
		Calibration, mV/psi	181.4		
302	332	**Serial Number**	6656	6660	6664
		Calibration, mV/psi	173.5	175.5	179.6
325	355	**Serial Number**	6613		
		Calibration, mV/psi	172.0		
351	382	**Serial Number**	6658	6661	6665
		Calibration, mV/psi	166.3	163.8	162.7
378	409	**Serial Number**	6397		
		Calibration, mV/psi	167.0		
403	434	**Serial Number**	6659	6662	6617
		Calibration, mV/psi	157.2	158.0	155.1
420	451	**Serial Number**	6620		
		Calibration, mV/psi	147.2		

these locations were $x = 332$, 382, and 434 mm from the nosetip. All of these sensors were monitored during the alignment runs, so the spectra at all three azimuthal arrays were examined.

The model was aligned by first positioning the model so that the sting was at a 0° angle from the tunnel in the vertical plane. This was done using a PRO 3600 digital protractor with 0.01° precision. A preliminary run was performed with no laser-generated disturbances and the power spectra from the 3 different azimuthal locations at the three different axial stations were examined. For this experiment,

the blunt nosetip was used for the flow-alignment process. The sharp nosetip was accidentally bent and re-straightened, so the blunt nosetip was expected to be more axisymmetric.

The spectra of the measurements with no freestream laser perturbation were calculated using a 0.1-second time series at 1 s after the run starts. Time series with turbulent bursts were disregarded. The spectra were computed using a Welch spectrum estimation method. Each time series was split into 50 blocks, with Blackman windows applied to each of the 50 blocks. Up to 50% overlap was used on each of these blocks. Fast Fourier transforms (FFTs) were applied to each of the blocks, and then averaged together to create a power spectra.

An example of the spectra from a preliminary run is given in Figure 8.5. The second mode is a large peak over the frequencies of 230–285 kHz. There also appears to be a peak in the spectra at about 90–150 kHz at some of the azimuthal locations. The source of this peak is unknown, but it is around the same frequency as the expected first mode [117]. The peak may also be a subharmonic of the second mode, as suggested by Sivasubramanian et al. [68]. These spectra show that the second-mode amplitude is smaller along the $+120^\circ$ ray at $x = 302$ mm, and slightly larger on the -120° ray at $x = 403$ mm. The amplitude of the second mode peak on the -120° ray at $x = 351$ mm appears to be smaller than the other two sensors. The reason for this is unknown. The sensor was new, so it is unlikely that there was damage to this particular sensor from prior use.

A table of the RMS amplitudes of the second mode are given in Table 8.3. The use of the RMS amplitudes of the second mode may not be the best way to align the model, because there is some uncertainty in the calibrations of the PCB sensors. Thus, the RMS amplitudes were used as an additional check of alignment. A better determination of the alignment of the model was performed by examining the frequency and relative shape of the second-mode peak. The peak frequency of the second mode measured by each sensor for the alignment in Figure 8.5 is given in Table 8.4. The largest percent discrepancy in peak frequency is 7.1% at $x = 302$ mm.

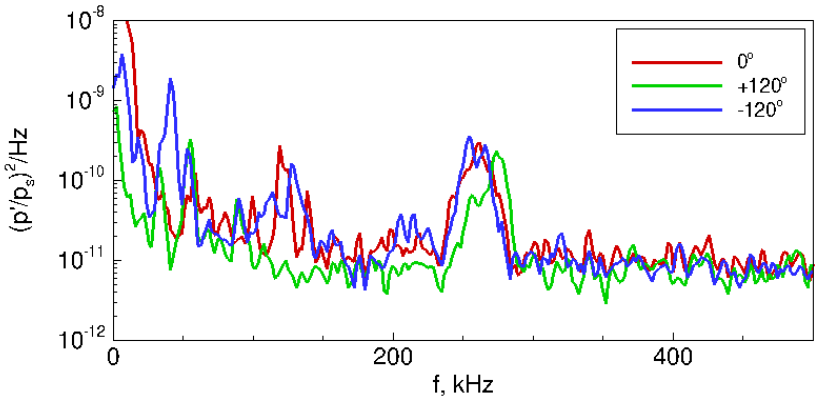

(a) $x = 302$ mm.

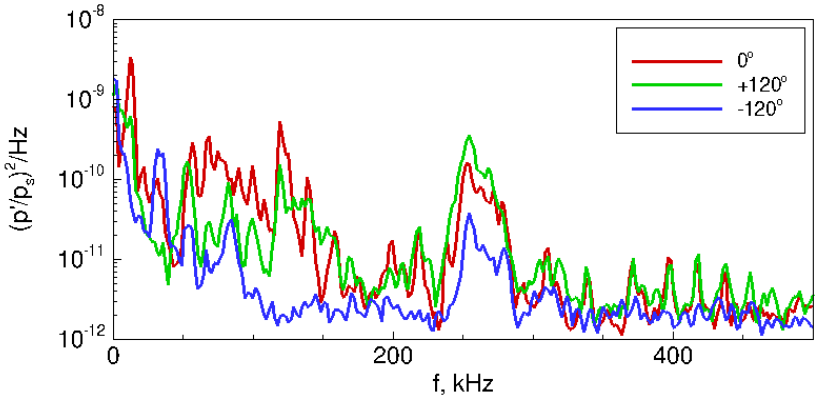

(b) $x = 351$ mm.

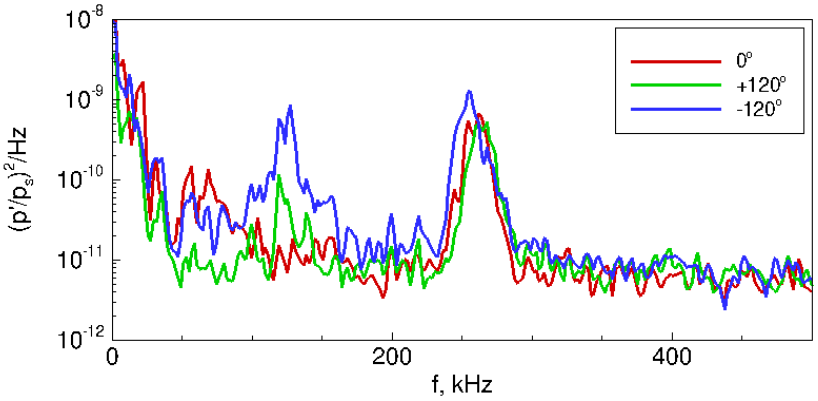

(c) $x = 403$ mm.

Figure 8.5. Power spectra of measurements from azimuthal arrays used for alignment of the model to the flow. $p_0 = 731.4$ kPa, $T_0 = 417.0$ K, $\rho_\infty = 0.032$ kg/m^3, $r_n = 1$ mm, $M = 6$. No laser-generated perturbation.

Table 8.3 RMS amplitudes of the second mode from a preliminary run for flared cone alignment to flow.

Sensor Location x, mm	$0°$ **Ray RMS Amplitude**	$+120°$ **Ray RMS Amplitude**	$-120°$ **Ray RMS Amplitude**
302	0.0020	0.0017	0.0020
351	0.0013	0.0020	0.0006
403	0.0030	0.0037	0.0038

Table 8.4 Peak frequency of the second mode from a preliminary run for flared cone alignment to flow.

Sensor Location x, mm	$0°$ **Ray 2nd Mode Peak Frequency, kHz**	$+120°$ **Ray 2nd Mode Peak Frequency, kHz**	$-120°$ **Ray 2nd Mode Peak Frequency, kHz**
302	261.7	273.4	253.9
351	251.9	253.9	253.9
403	261.7	267.5	255.9

The spectra suggested that the angle of attack of the model may need to be adjusted. The model was angled toward the $+120°$ ray because the RMS second-mode amplitudes appeared smaller on this ray at $x = 302$ and 403 mm. Ideally, there would be a way to make small systematic adjustments to the angle of attack. The current setup required the adjustment of the angle of attack through minor adjustments to the set screws in the sting support system. This was tedious and frustrating because there was no way to determine how much the sting moved with each adjustment.

The best alignment possible typically resulted in the spectra shown in Figure 8.6. The RMS amplitudes of the second mode, listed in Table 8.5, were still about the same as in the preliminary alignment run. However, the shape of the spectra at $x = 302$ mm and $x = 403$ mm, appeared to have more similar peaks across the

entire azimuthal array. In particular, Figure 8.5(a) shows that the second-mode peak in the spectra at +120° was a different shape than the peak at the other azimuthal locations. Figure 8.6(a) shows a second-mode peak that was more similar in shape to what was measured by the other sensors at the same axial station. This change indicated that the model was probably better aligned in Figure 8.6(a). Likewise, the shape of the second-mode peak at $x = 403$ mm on the −120° ray was more similar in Figure 8.6(c) than in Figure 8.5(c). The spectra do not appear to be similar in $x = 351$ mm for either run shown. Again, the cause of this discrepancy in the middle azimuthal array is unknown. Table 8.6 shows the second-mode peak frequency for the spectra in Figure 8.6. The largest percent discrepancy in peak frequency is about 3.0% at $x = 403$ mm.

Table 8.5 RMS amplitudes of the second mode from the best preliminary run for flared cone alignment to flow.

Sensor Location x, mm	**0° Ray RMS Amplitude**	**+120° Ray RMS Amplitude**	**−120° Ray RMS Amplitude**
302	0.0014	0.0012	0.0015
351	0.0013	0.0019	0.0006
403	0.0024	0.0027	0.0030

Table 8.6 Peak frequency of the second mode from the best preliminary run for flared cone alignment to flow.

Sensor Location x, mm	**0° Ray 2nd Mode Peak Frequency, kHz**	**+120° Ray 2nd Mode Peak Frequency, kHz**	**−120° Ray 2nd Mode Peak Frequency, kHz**
302	253.9	255.9	252.0
351	257.8	253.9	253.9
403	253.9	261.7	255.9

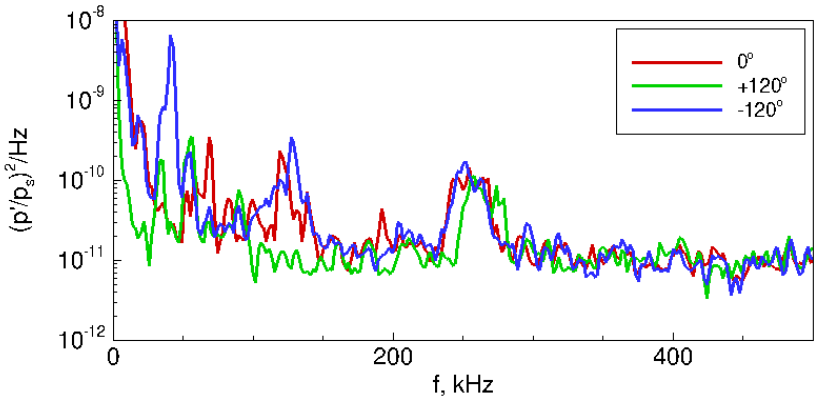

(a) $x = 302$ mm.

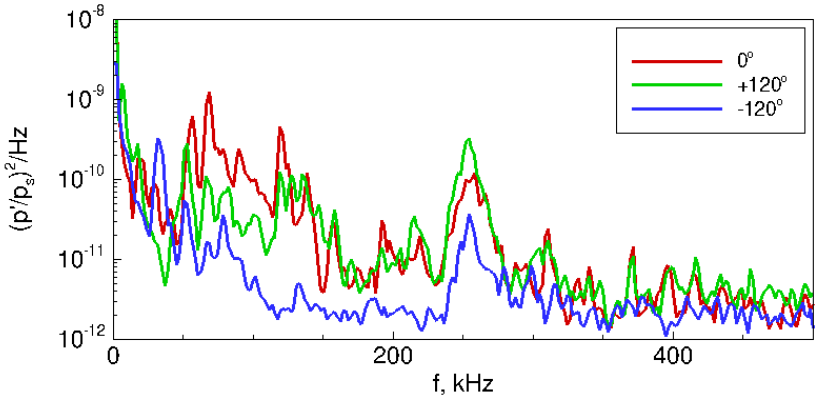

(b) $x = 351$ mm.

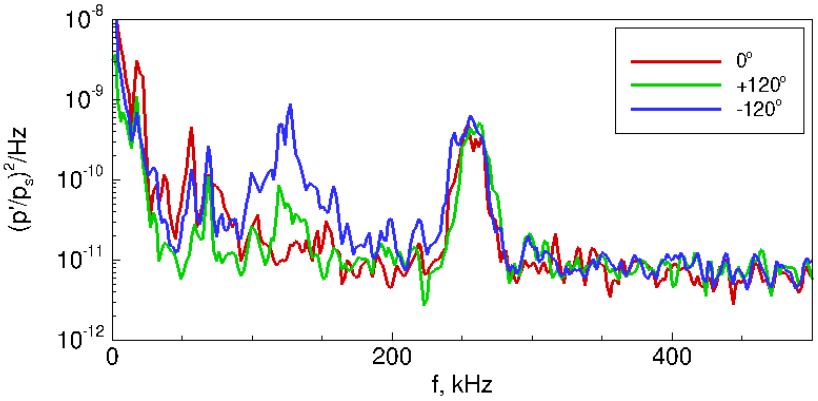

(c) $x = 403$ mm.

Figure 8.6. Power spectra of measurements from azimuthal arrays in best alignment of the model to the flow. $p_0 = 708.8$ kPa, $T_0 = 418.4$ K, $\rho_\infty = 0.031$ kg/m^3, $r_n = 1$ mm, $M = 6$. No laser-generated perturbation.

8.2.2 Alignment of the Laser-Generated Disturbance to the Model

Alignment of the laser-generated disturbance to the flared cone is also a difficult process. The laser-generated perturbation was typically created in the freestream of the tunnel and then allowed to convect downstream to interact with the flared cone model. Minor vibrations in each system may contribute to small errors in how the laser-generated disturbance interacts with the model.

A special tool was designed and built in the AAE machine shop to align the freestream laser-generated perturbation to the centerline axis of the flared cone. A photograph of this alignment tool mounted in the end of the flared cone model is shown in Figure 8.7. This alignment tool was a piece of stainless steel round stock with a 1/4-20 threading at one end and 1.5-mm-diameter holes precisely drilled in the other end. After aligning the model in the flow, the 1-mm-radius nosetip was unscrewed from the frustum, and replaced with the alignment tool. These 1.5-mm-diameter holes were used to press-fit a toothpick in the end.

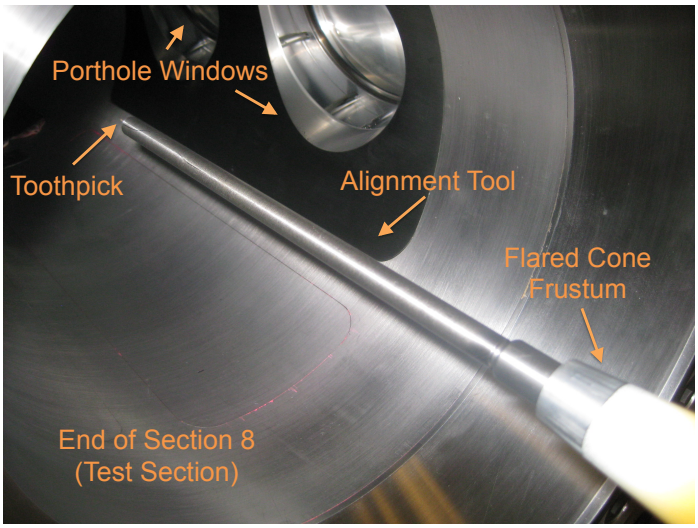

Figure 8.7. Photograph showing the alignment tool used for aligning the freestream laser disturbance to the flared cone model.

The perturbation-forming optics were first aligned at low laser power (long-pulse mode), so that the focus lay somewhere near the end of the toothpick. This was

checked by looking through a second set of windows, 90° from the laser beam axis. Figure 8.8(a) shows a typical example of how the alignment looked at low power. The end of the toothpick mounted at the end of the alignment tool was bright, due to the scattering of incident laser light.

The laser-generated disturbance was then checked at high power to make sure that the focus was actually located at the tip of the toothpick. The laser beam at low power can deceptively illuminate the end of the toothpick, even if the beam focus is not located exactly at the end of the toothpick. When the laser was turned to a higher power to generate the laser-induced disturbances, the initial alignment typically looked like Figure 8.8(b), where the laser disturbance was unintentionally offset from the alignment toothpick. Here, the laser-generated perturbation was close to being aligned, with the focus of the high-powered laser near the end of the toothpick. A careful re-positioning of the perturbation-forming optics was then required. The re-positioning of the optics was performed with rotational and translational stages.

When the disturbance was properly aligned to the centerline axis of the flared cone model, the laser-generated perturbation was created at the end of the toothpick, as shown in Figure 8.8(c). This alignment could then be checked by examining the toothpick mounted in the end of the alignment tool. Figure 8.9(a) shows a toothpick where the alignment was slightly offset. For reference, the toothpicks used for alignment are on the order of 1.5 mm in diameter. A red mark was used to mark the side of the toothpick aligned with the 0° ray. The end of the toothpick was slightly destroyed, having been ablated or burned by the laser-induced breakdown process.

The toothpick in Figure 8.9(a) shows that the laser-generated perturbation may have been formed a fraction of a millimeter lower than the centerline axis. Again, this slight misalignment required many more adjustments in the optical system until the proper alignment was achieved. In the course of this alignment process, several toothpicks may be destroyed. Figure 8.9(b) shows a close-up image of the toothpick mounted in the end of the alignment tool after the best alignment was achieved.

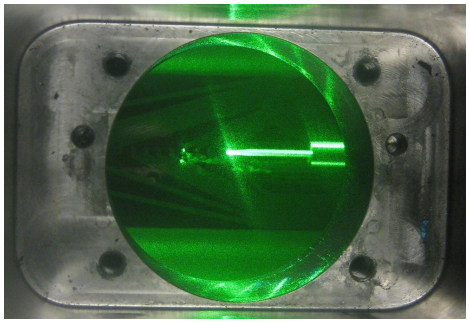

(a) Alignment at low laser power.

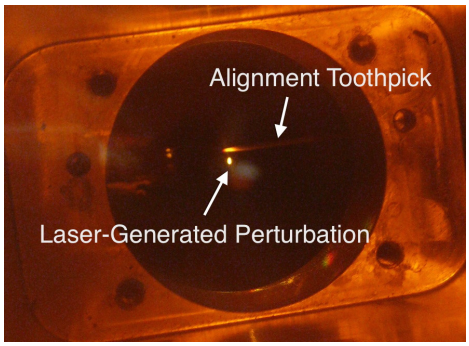

(b) Misalignment of the beam focus to the toothpick.

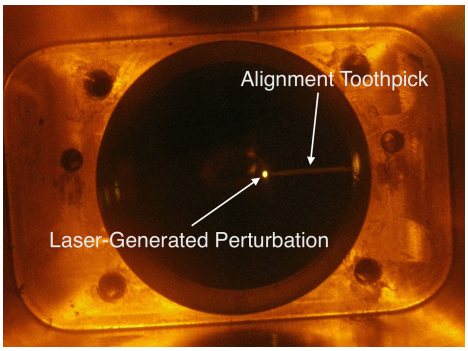

(c) Proper alignment of beam focus to the toothpick end.

Figure 8.8. Photographs showing the alignment of the laser beam to the toothpick mounted in the end of the alignment tool.

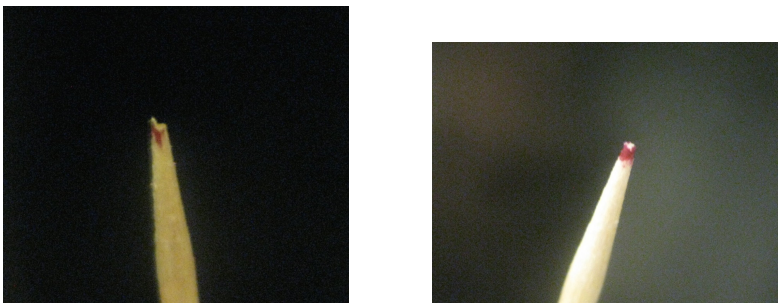

(a) Small error in alignment. (b) Better alignment.

Figure 8.9. Close-up photographs showing the alignment toothpick after a check of the alignment at higher power.

The best alignment provided an axisymmetric destruction pattern at the end of the toothpick.

The time of arrival of the laser-generated disturbances can also be used to check the alignment of the model to the disturbance. This can be done with or without flow. Both options have their advantages and disadvantages, but both options rely on the laser-generated perturbation being axisymmetric or having an axisymmetric effect on the model.

An example of the detection of the weak shock wave is shown in Figure 8.10. For this example, there is no flow and this was the best alignment achieved for positioning the perturbation on the cone centerline. In this plot, the time traces are offset by an amount proportional to the azimuthal distance of each sensor from the 0° ray. These time traces are only from the most forward azimuthal array at $x = 302$ mm. Data from the other azimuthal arrays looked similar, so only one array is shown here. Figure 8.10 shows that the weak shock arrived at the sensors at about $t_p = 1500\mu$s. A cross-correlation between the sensors shows that the largest delay was a 4.5 μs difference in arrival time between the $+120°$ and $-120°$ rays. An acoustic wave traveling at the speed of sound in quiescent air travels about 1.5 mm in 4.5 μs. This may indicate that the shock front is not perfectly axisymmetric about the cone centerline.

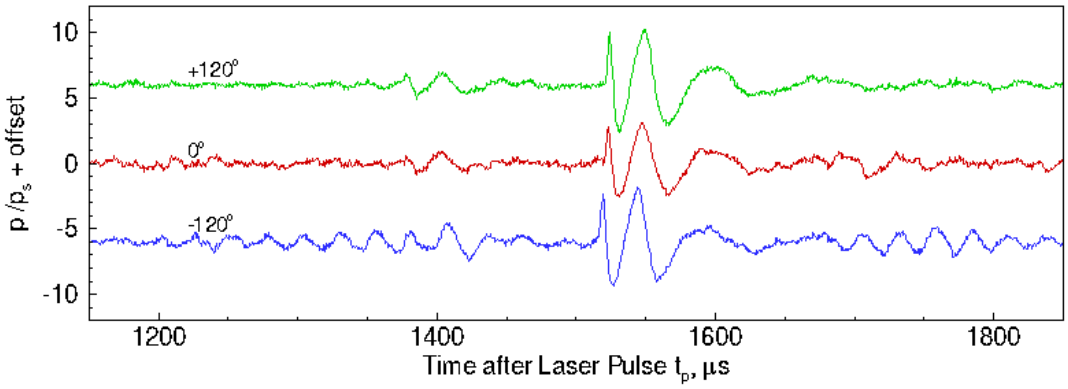

Figure 8.10. Time trace showing arrival of weak shock wave from laser-generated perturbation in $x = 302$ mm array. No flow. $p_0 = 21.3$ kPa, $T_0 = 426.4$ K.

8.3 Measurements of the Second Mode using PCB Sensors

To monitor the axial growth of the second-mode instability, the eight PCB sensors along the 0° ray were used. To monitor the azimuthal relationship between the sensors, three azimuthal sensor arrays at three different axial stations were used. The factory calibrations for the PCB sensors were used to convert voltages to pressure fluctuations (p'). The pressure fluctuation measurements were normalized by a computed surface pressure (p_s). Unlike a straight cone model, the surface pressure on a flared cone changes with each sensor station due to the presence of a pressure gradient.

The time traces were typically low-pass filtered in post-processing with a digital 8-pole Butterworth filter, with a cutoff at 800 kHz. An example of a single trace is shown in Figure 8.11. In this figure, the black trace is the signal read by the PCB sensor. The green trace is the signal output by the laser to indicate that a high-powered pulse has been fired ("Q-SW Sync Signal"). The low-frequency pulse at the beginning of the black trace between 0.1–0.3 s was not always detectable or repeatable. The signal conditioners used with the PCB sensors are high-pass filtered at 11 kHz. Thus, they occasionally eliminate the low-frequency pulse. The cause of this pulse was likely due to the electromagnetic activity that occured when the laser

perturbation was formed. Schmisseur [43] showed a similar electronic spike in his hot-wire measurements. However, the peak in the hot-wire measurements was much sharper and more repeatable.

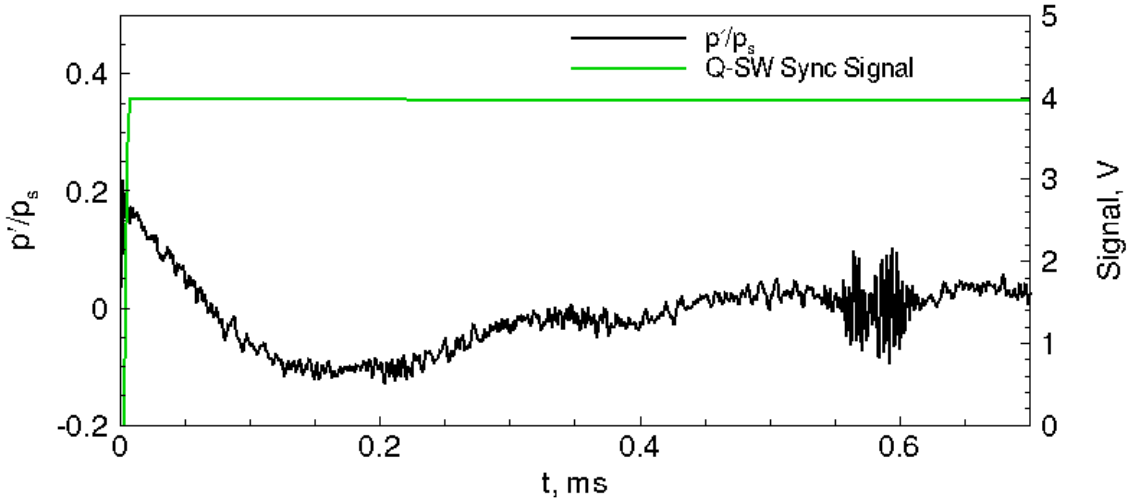

Figure 8.11. Example time trace of response to laser perturbation. $r_n = 0.16$ mm, $p_0 = 534.3$ kPa, $T_0 = 428.3$ K, $Re/m = 5.81 \times 10^6$/m, $x = 231$ mm, $M = 6$, quiet flow (Laser shot 10 in Run 19-47).

8.3.1 Test Conditions for the Experiment

Test conditions that could be varied for this experiment included changes in the nosetip radius, changes in the stagnation pressure, and changes in the alignment of the freestream disturbance. Limitations in the test conditions exist. Here, the possible test conditions are discussed and the feasible ranges are given.

Both the 1-mm-radius (blunt) nosetip and the 0.16-mm-radius (sharp) nosetip are used for this experiment. Ideally, Reynolds number sweeps would be run for each nosetip. However, the conditions at which each nosetip could be run were limited by separation on the BAM6QT nozzle wall, small-amplitude waves, and transition on the flared cone model. At freestream stagnation pressures below about 500 kPa,

the sharp nosetip had a tendency to cause separation in the nozzle-wall boundary layer. This boundary layer separation was probably caused by a shock/boundary layer interaction. The boundary layer does reattach during the run, but this reduces the effective run time. At freestream stagnation pressures above about 655 kPa, the wave packets at the end of the cone start to transition. This limits the useful stagnation pressures at the higher end.

For the blunt nosetip, similar restrictions at the higher pressures exist. However, for the blunt nosetip, the upper limit occurs at about 865 kPa. The lower limit in freestream stagnation pressure for the blunt nosetip is determined by the amplitude of the freestream disturbance. The laser perturbation can be formed at stagnation pressures as low as 310 kPa. However, at freestream stagnation pressures below about 690 kPa, the disturbance on the surface of the cone is not measurable above the noise.

The alignment of the freestream laser-generated disturbance was varied to determine its effect. The nominal alignment of the freestream disturbance was to the centerline axis of the flared cone. The freestream laser-generate disturbance was also generated either 1.5 mm or 3.0 mm from the centerline axis. Each off-axis alignment of the perturbation could place the perturbation closer to either the 0° ray, the +120° ray, or the −120° ray.

8.3.2 Forms of Data Analysis for Surface Pressure Measurements

A large amount of data was collected as part of the present experiment. For the current set of measurements, a total of 14 PCB sensors were installed in the model. Data from only 12 PCB sensors could be recorded during any one run, due to limitations in the number of long-memory oscilloscopes. Each of these sensors was sampled at 2 MHz. The set of measurements described in the previous section occurred over a total of 47 different runs. A table of the conditions is listed in Appendix E.

The data from this experiment could be analyzed in a number of different ways. These include:

1. Tracking the time of arrival of a single laser-induced perturbation at each axial station.
2. Tracking the growth of a single laser-induced perturbation in the streamwise direction.
3. Using the measured disturbance amplitude to estimate an initial amplitude.
4. Tracking the amplitude differences in the disturbance for a single laser-induced perturbation in the azimuthal direction.
5. Tracking the shot-to-shot variation of the disturbance time of arrival at each sensor station.
6. Using the shot-to-shot variation of the disturbance time of arrival at each sensor to develop ensemble averages of the disturbance.
7. Relating the changes in the shot-to-shot time of arrival of the disturbance to decreasing freestream conditions of the BAM6QT.
8. Relating the amplitude of the disturbance on the surface of a cone to the decreasing freestream conditions of the BAM6QT.
9. Relating the amplitude of the disturbance on the surface of a cone to the freestream amplitude of the disturbance.
10. Relating the wave packet amplitude variation to the time of arrival variation.
11. Applying short-time Fourier transforms to determine the changes in frequency content of the wave packet over time.
12. Performing a wavelet analysis to determine time of arrival of the generated disturbance.
13. Repeating the above analyses for each nosetip to determine nosetip effects.

Not all of these types of analyses could be performed for every bit of available data because it is time-consuming. Only some of these analyses will be reported here and only some of the sensors at the aft end of the cone will be used in the analyses.

Much of the data analysis must be automated due to the amount of available data. The nature of some of the available data makes the automation process difficult. For example, the determination of shot-to-shot variation in time of arrival could not be done in an automated fashion for cases where the generated wave packet is nearly the same amplitude as the natural disturbances. This occurs for measurements on the farther upstream sensors and at the farther downstream sensors. At the farther upstream sensors, the disturbances are too small to be measured. At the farther downstream sensors, the natural waves are large.

8.4 Evolution of a Laser-Generated Disturbance in the Axial Direction

Typical time traces of the signal from the PCB sensors in response to a single laser-generated perturbation are shown in Figures 8.12 and 8.13. These data are all from the sensors mounted on the 0° ray. The time scale for t_p originates when the laser pulse is fired. The time traces are offset by an amount proportional to the distance between the sensor and the nose tip. Figure 8.12 shows that the perturbation produced a wave packet on the blunt cone, but this wave packet was not detectable until the aft end of the cone, around $x = 351$ mm. The packet occasionally exhibits a double- or triple-burst feature.

The packet appears similar in shape to the computations by Terwilliger [67] of a nonlinear wave packet on the flared cone model. The double-burst feature was also seen in computations by Salemi [118] for a linear wave packet on a 5° cone in a high-enthalpy flow. In Salemi's computations, the double-burst feature is attributed to the dispersion of instabilities with different phase speeds. It is not clear that this explanation would also be applicable to the flared cone.

Figure 8.13 shows that the perturbation produced a larger wave packet on the sharp model, and the perturbation was detected by all of the sensors. The wave packet at $x = 231$ and 332 mm took on a double-burst shape. The wave packet at $x = 355$ mm may have been a double burst merging into a single burst. The sensors at the

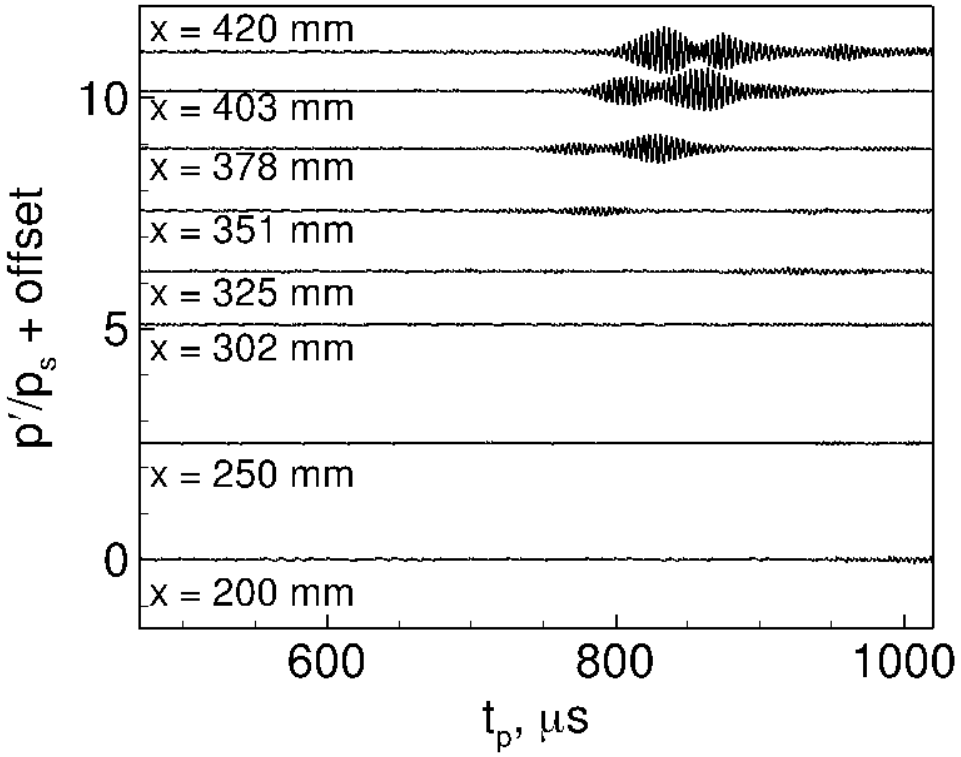

Figure 8.12. The measured response to a single freestream laser-generated disturbance. $r_n = 1$ mm, $p_0 = 740.3$ kPa, $T_0 = 427.9$ K, $Re/m = 8.06 \times 10^6$/m (Laser shot 8 in Run 19-44).

aftmost stations ($x = 434$ and 451 mm) on the sharp nosetip measured a wave packet with characteristics of breakdown. Again, this wave packet shape is characteristic of a nonlinear wave packet and was seen in computations by Terwilliger [67, pp. 108,109].

The differences in the axial development of the freestream disturbance seem to show some effects of nosetip bluntness. Computational studies by Balakumar show that blunter nosetips have a lower receptivity coefficient to acoustic plane waves [28]. The freestream laser perturbation does not appear to generate a wave packet that is large enough to be measurable on the blunt flared cone until a location of $x = 351$ mm. On the other hand, the sharp flared cone shows an effect of the freestream perturbation in the most upstream sensor location of $x = 231$ mm, despite being at a lower Reynolds number. This effect may be due to either (1) a change in receptivity,

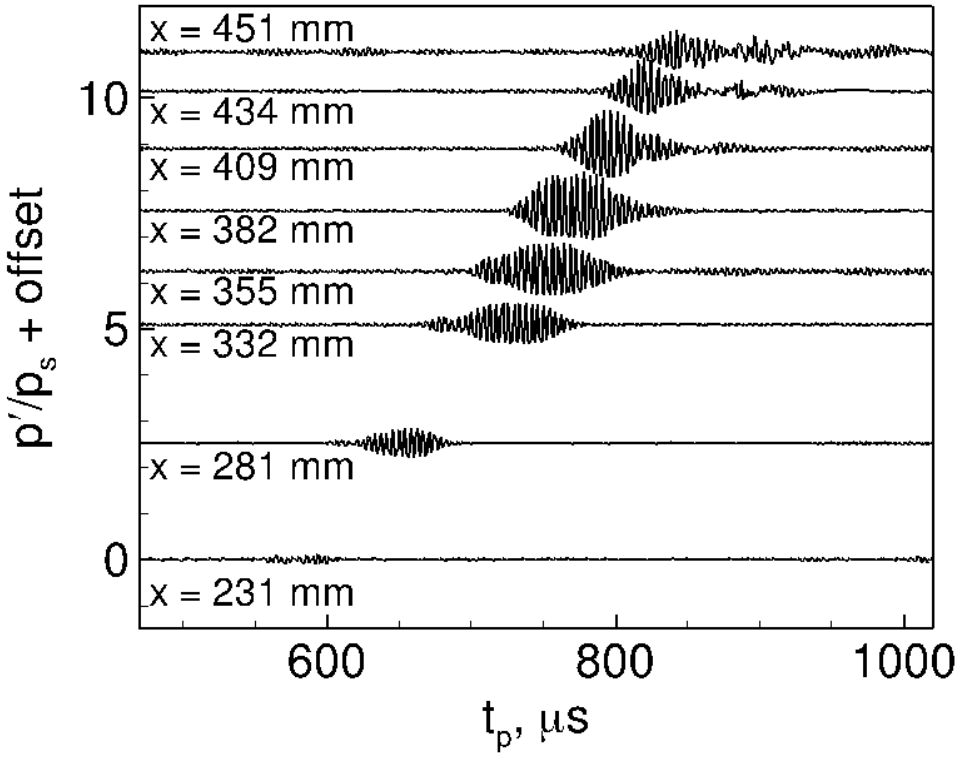

Figure 8.13. The measured response to a single freestream laser-generated disturbance. $r_n = 0.16$ mm, $p_0 = 534.3$ kPa, $T_0 = 428.3$ K, $Re/m = 5.81 \times 10^6$/m (Laser shot 10 in Run 19-47).

(2) a change in the freestream amplitude of the perturbation, or (3) the reduced amplification of the second-mode waves on the blunt cone. Freestream measurements in Chapter 4 showed a change in the amplitude and size of the perturbation with a change in freestream conditions.

The different nosetips can only be run over a very limited range of stagnation pressures. The overlap between these pressures are typically only at the very beginning of a run for the sharp nosetip and at the very end of a run for the blunt nosetip. Conditions from Run 19-45 and Run 19-46 are shown in Figure 8.14. These two runs correspond to the lowest freestream stagnation pressure for the blunt flared cone and the highest freestream stagnation pressure for the sharp flared cone, respectively. The perturbation is again aligned to the centerline of the flared cone for these two runs.

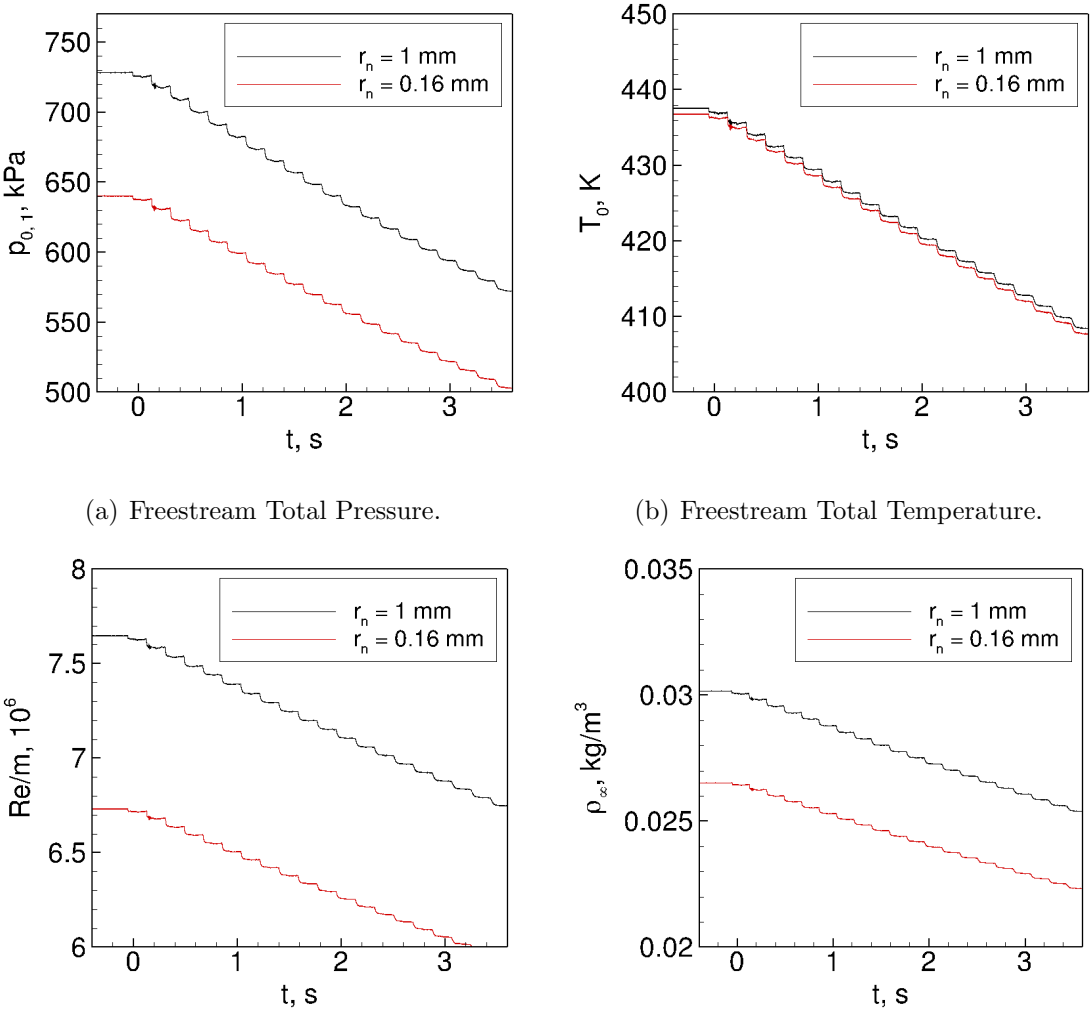

(a) Freestream Total Pressure.

(b) Freestream Total Temperature.

(c) Freestream Unit Reynolds Number.

(d) Freestream Density.

Figure 8.14. Plots showing the variation in conditions over the run for Run 19-45 ($r_n = 1$ mm) and Run 19-46 ($r_n = 0.16$ mm).

The total pressure is measured using a Kulite transducer mounted in the driver tube. The total temperature is inferred from the measurement of freestream total pressure and the initial total temperature using the isentropic relations (Equation 2.1). The unit Reynolds number is calculated using

$$Re/m = \frac{\rho u}{\mu} = \frac{p_{0,1}}{\mu\sqrt{T_0}}\sqrt{\frac{\gamma}{R}}M\left[1+\frac{\gamma-1}{2}M^2\right]^{-\frac{\gamma+1}{2(\gamma-1)}} \tag{8.1}$$

where $\gamma = 1.4$ is the ratio of specific heats, $R = 287$ J/kg-K is the gas constant, the total pressure $p_{0,1}$ is measured, the viscosity μ is calculated using a Sutherland law for viscosity, and the total temperature T_0 is inferred from the isentropic relations. The freestream density is also inferred from the measurement of total pressure and the isentropic relations:

$$\rho_\infty = \frac{p_1}{RT_1} = \frac{p_1}{p_{0,1}}\frac{1}{R}\frac{T_0}{T_1} \tag{8.2}$$

where p_1 is the freestream static pressure and T_1 is the freestream static temperature.

Comparisons of the nosetips should be made by matching the freestream density, assuming once more that the amplitude of the freestream disturbance is largely governed by this flowfield parameter, and not the other parameters. The freestream density seen by the blunt flared cone at $t = 2.600$ s is the same as the maximum freestream density seen by the sharp flared cone. The freestream density seen by the sharp flared cone at $t = 0.8611$ s is the same as the minimum freestream density seen by the blunt flared cone. Thus, the blunt cone response to laser pulses fired after $t = 2.600$ s are compared to the sharp cone response to laser pulses fired before $t = 0.8611$ s, since the impinging freestream perturbation should be nearly the same.

The freestream noise increases near the end of Run 19-45 and nozzle-wall boundary layer separation is possible at the beginning of Run 19-46. An uncalibrated nozzle-wall hot film was used to determine if either scenario occurred for the two runs analyzed here. The nozzle-wall hot film traces associated with the overlapping freestream density in these runs is given in Figure 8.15. The large downward spikes in the traces that occur every 0.1 s correspond with the laser generated perturbation formed in the BAM6QT freestream. These spikes are related to electromagnetic interference

created either during the laser-induced breakdown process or by the Nd:YAG laser power supply.

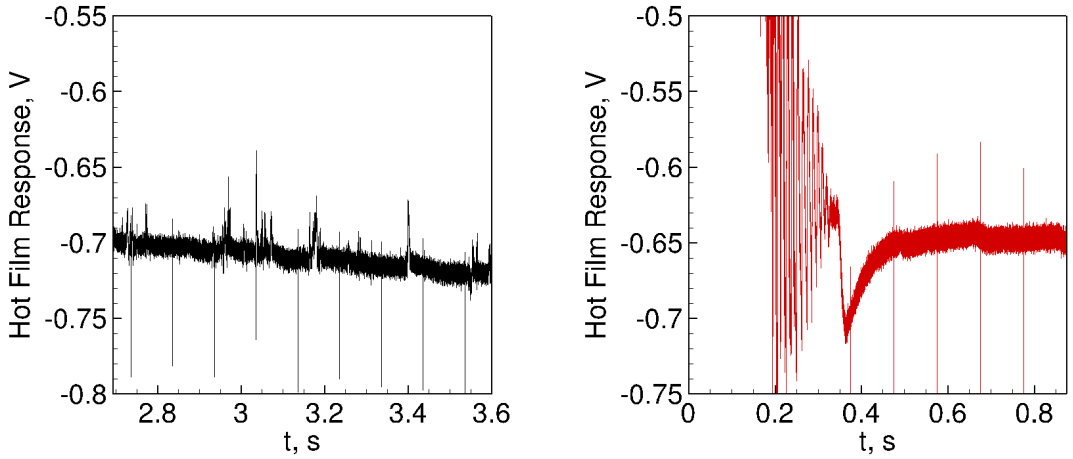

(a) $r_n = 1$ mm (Run 19-45). (b) $r_n = 0.16$ mm (Run 19-46).

Figure 8.15. Uncalibrated nozzle-wall hot-film traces at overlapping conditions for the blunt and sharp flared cone model.

Figure 8.15(a) shows small upward peaks that are similar in shape to small turbulent spots. These appear at $t = 2.727$, 2.772, 2.966, 3.036, 3.074, 3.177, and 3.400 s. Figure 8.15(b) shows that the flow establishes after about $t = 0.3650$ s. Thus, the best comparison of these two nosetips at similar freestream densities should occur at $t = 2.836$ s for the blunt cone and at $t = 0.5748$ s for the sharp nosetip. The freestream density is about 0.026 kg/m^3 for both models at these times.

The effect of the laser pulse on the blunt cone is shown in Figure 8.16. This figure corresponds to the laser pulse that was fired at $t = 2.836$ s. Again, the effect of the freestream laser-generated perturbation was small, and undetectable in all but the aftmost sensors. The scaling on this plot was half the scaling used on Figure 8.12. The wave packet shape in Figure 8.16 at $x = 403$ mm still exhibits the double-burst shape seen in Figure 8.12, but the wave packet at $x = 420$ mm does not exhibit the triple-burst shape. This change in shape may be due to the changes in freestream condition, but the cause is not clear.

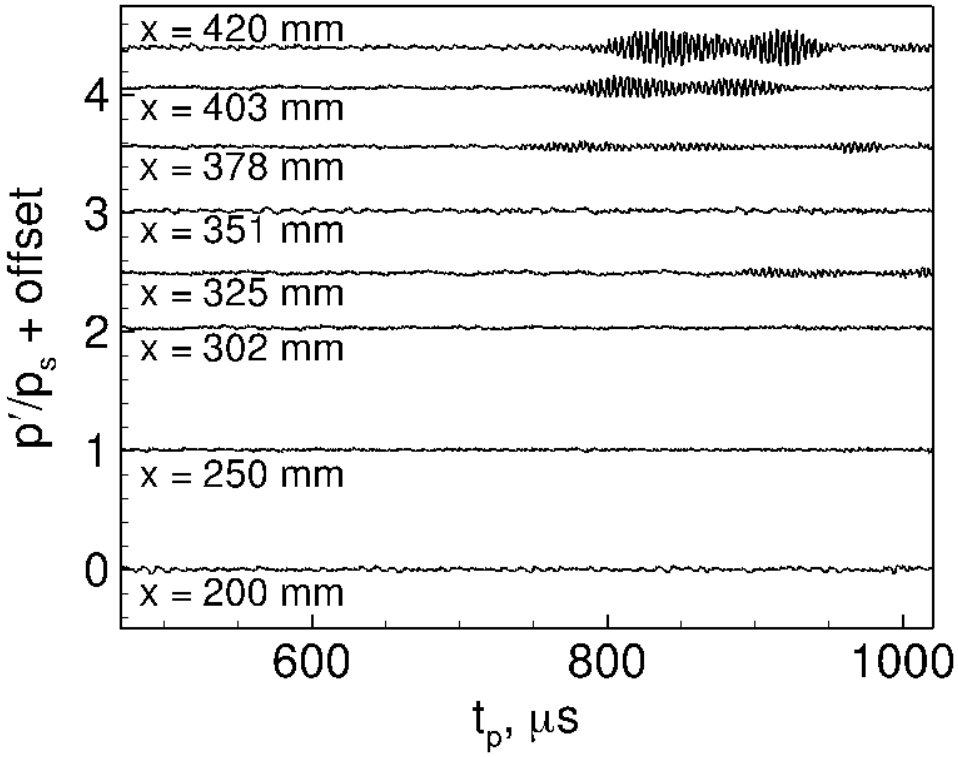

Figure 8.16. The measured response to a freestream laser-generated disturbance. $r_n = 1$ mm, $p_0 = 599.5$ kPa, $T_0 = 411.1$ K, $Re/m = 6.98 \times 10^6$/m, $\rho_\infty = 0.026$ kg/m^3 (Laser shot 28 in Run 19-45).

The effect of the laser pulse fired at $t = 0.5748$ s on the sharp cone is shown in Figure 8.17. The wave packet generated by the freestream laser perturbation was again seen in all the sensor traces, but appears to be larger. The larger amplitude was expected because the freestream density in Run 19-46 (Figure 8.17) is 10% higher than in Run 19-47 (Figure 8.13). The wave packets also still exhibited the double- or triple-burst shape and experienced nonlinear breakdown at the last three sensor stations. The natural freestream disturbances appear to be much larger at $x = 355$ mm than any other location. The cause of this increase is unknown, because it is not apparent in the other sensors nor in the later time traces.

Figures 8.16 and 8.17 show that the wave packet on the blunt model is smaller than the wave packet on the sharp model. Balakumar's study of the receptivity of

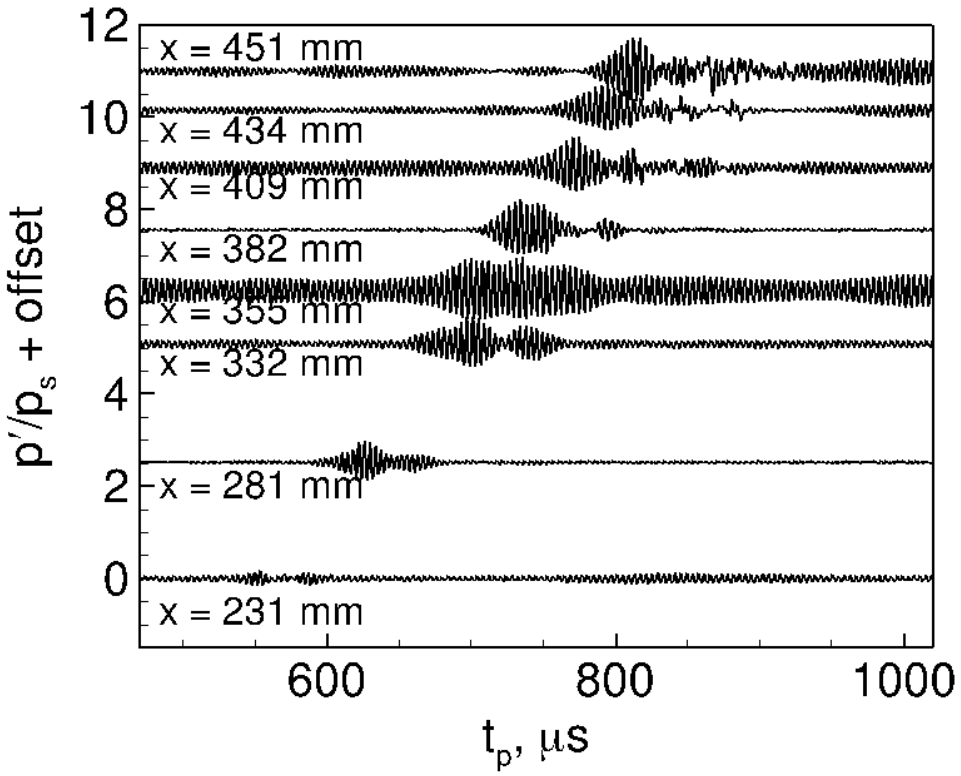

Figure 8.17. The measured response to a freestream laser-generated disturbance. $r_n = 0.16$ mm, $p_0 = 615.1$ kPa, $T_0 = 431.8$ K, $Re/m = 6.59 \times 10^6$/m, $\rho_\infty = 0.026$ kg/m^3 (Laser shot 5 in Run 19-46).

nosetip bluntness to planar acoustic waves suggests that sharp nosetips should have higher receptivity than blunt nosetips [28]. It is possible that the blunt nosetip is also less receptive to the discrete freestream thermal disturbance, and thus, also generates a smaller wave packet. However, the instability growth on the sharp model differs from that on the blunt model, so the cause of the discrepancy in the amplitude of the wave packet is not known.

8.4.1 Time of Arrival Analysis

Detection of the wave packet in the time trace is crucial for several of the analyses listed in Section 8.3.2. It was thus important to develop an automated method

of detecting the time of arrival of the wave packet, to determine the speed of the boundary-layer disturbance and to determine any variations in arrival time. The time of arrival can also be used to find a window for spectral analysis of the wave packet.

Time of Arrival Variation along the Axial Direction to Calculate Speed

The speed of the disturbance was determined by looking at the data from each sensor along an axial ray. This was best done by looking at the ray with the most sensors: the 0° ray. To expedite this process, a cross-correlation method was used to determine the time offset between the arrival of the wave packet at the most downstream station and the farther upstream stations. A 1000-point (500 μs-long) window around the wave packet was taken to reduce the possibility that large disturbances would interfere with the cross-correlation method. This window was initially placed around the wave packet manually to determine an acceptable algorithm. After the packet-finding algorithm was refined, the window was found automatically. The best window was positioned by setting the first point of the window 200 μs before the arrival time of the wave packet. The window is marked by the squares in Figure 8.18.

The cross-correlation method worked fairly well with the sharp nosetip. The method worked especially well for the first usable shot of a run, because the amplitude of the disturbance decreases as the run increases. As the run continued, the amplitude of the laser perturbation decreased, as did the wave packet amplitudes. On the blunt nosetip, the wave packet was not detectable in the most upstream sensors, so this method did not work well for this condition. An example of the effectiveness of this cross-correlation method is given in Figures 8.19 and 8.20, which correspond to the runs shown in Figures 8.12 and 8.13. The time of arrival calculated using the cross-correlation method is given by red squares for each sensor location. A solid blue line is used to show the linear least-squares fit to the time of arrival points.

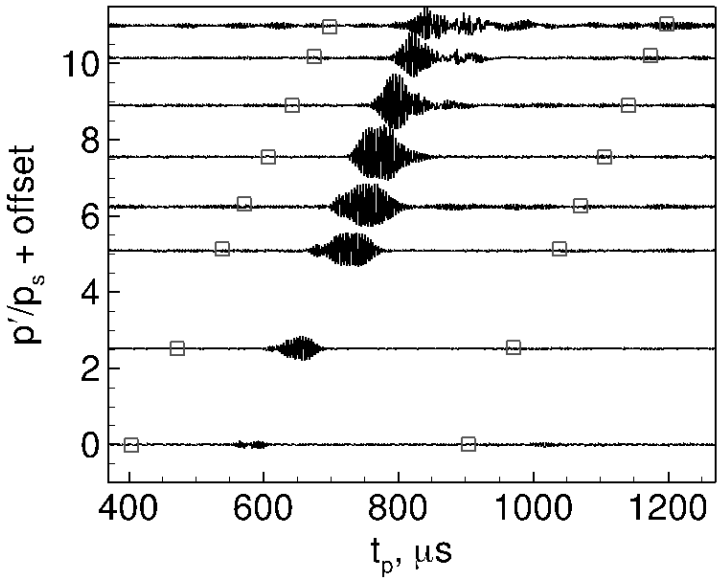

Figure 8.18. Figure 8.13 with markers showing the edges of the windows used for cross-correlations and spectral analysis (Run 19-47).

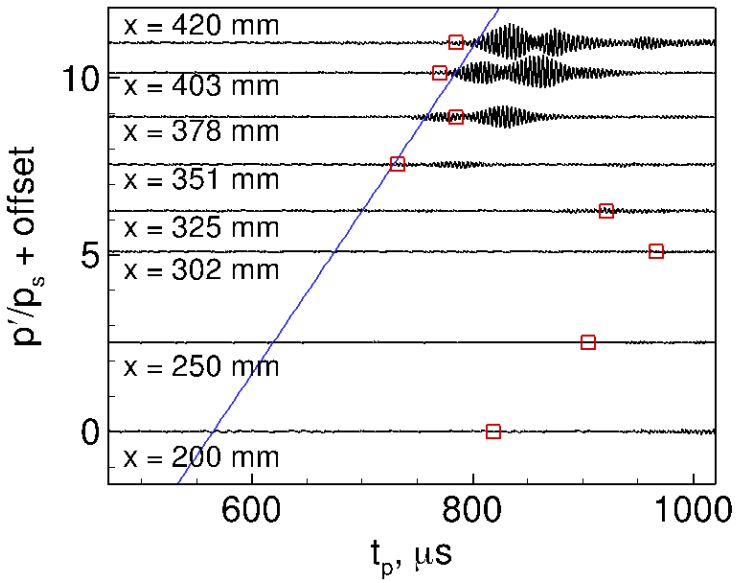

Figure 8.19. Figure 8.12 with markers showing the time of arrival found with cross-correlation (Run 19-44).

In Figure 8.19, the wave packet generated by the freestream laser perturbation was too small to be measured by the most upstream sensors. The cross-correlation method only worked for the last sensors under these conditions, but appeared to have trouble detecting the arrival of the disturbance at $x = 378$ mm. A linear least-squares fit to find the speed was made to the last four sensors only, as shown by the blue line in Figure 8.19.

In Figure 8.20, the wave packet was large, so the cross-correlation method worked fairly well at detecting the wave packet at all sensor locations. Small discrepancies were seen in the detection of the start of the wave packet. The cross-correlation method measures the delay between the most prominent feature seen in the time traces. Thus, the method may have picked out the maximum amplitude of the wave packet instead of its time of arrival.

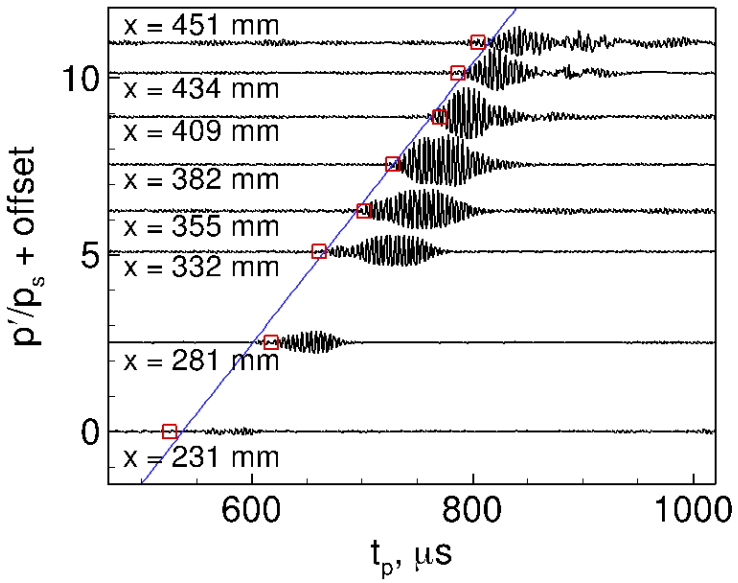

Figure 8.20. Figure 8.13 with markers showing the time of arrival found with cross-correlation (Run 19-47).

Another method of finding the time of arrival was to use a thresholding method. The time of arrival of the wave packet at each axial station was defined as the time at which the pressure fluctuations reach 10% of the maximum pressure fluctuation

amplitude. A windowing function was also used in this method to eliminate any effects of the large low-frequency pulse seen in Figure 8.11. The thresholding method applied to the same two cases shown previously in Figures 8.12 and 8.13 is shown in Figures 8.21 and 8.22, respectively.

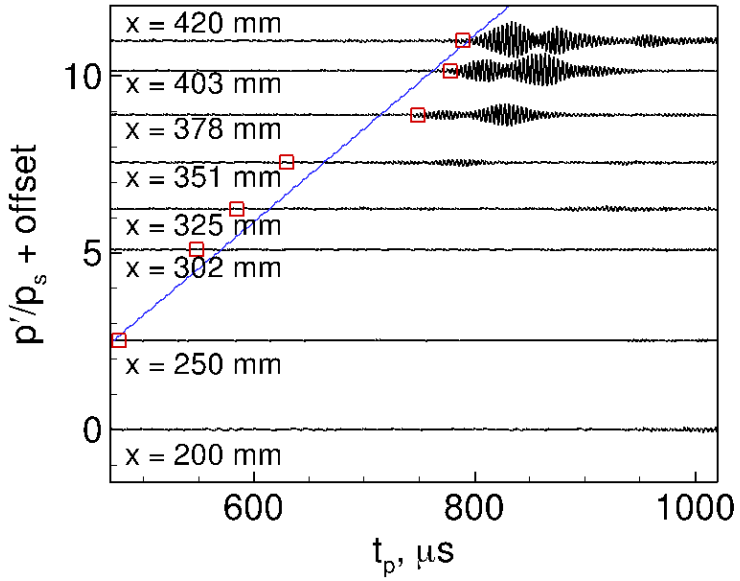

Figure 8.21. Figure 8.12 with markers showing the time of arrival found with thresholding (Run 19-44).

This thresholding method worked slightly better for some of the wave packets, and worse for others. Again, when the wave packet amplitude was on the same order as the freestream disturbances, it was difficult to separate the start of the wave packet from the freestream noise. In Figure 8.21, the wave packet arrival was detected clearly in the response of the three aftmost sensors, but not in the response of sensor at $x = 351$ mm. In Figure 8.22, the thresholding method appears to be a poorer method for finding the wave packets, as compared to the cross-correlation method. The threshold value could be refined, but this would require the manual analysis of more data. This manual analysis is undesirable, due to the quantity of data available.

Other methods, such as a wavelet analysis, could be applied to finding these wave packets. However, these methods will have similar problems when the amplitude of

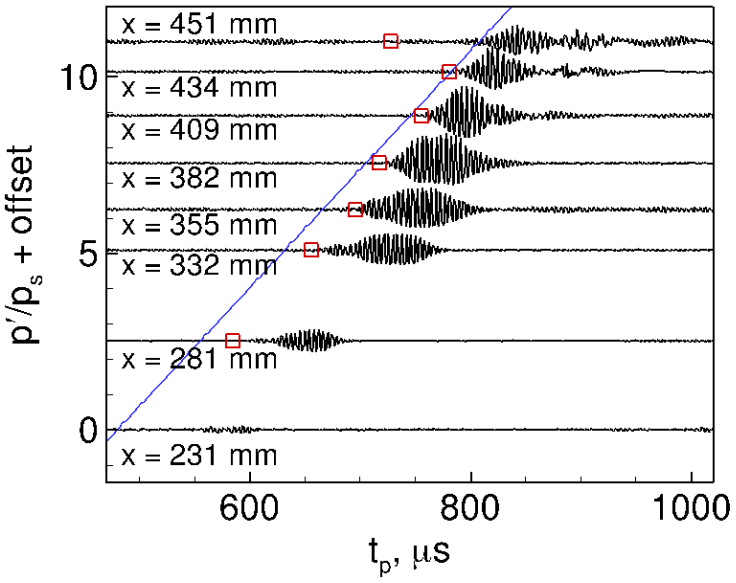

Figure 8.22. Figure 8.13 with markers showing the time of arrival found with thresholding (Run 19-47).

the natural waves is on the same order as the forced waves. Further work may need to be done in order to improve the packet-finding method for such waves. Thus, the cross-correlation method will be used at present for time-dependent analyses, and only the wave packets that have a large enough amplitude to be detected will be analyzed.

The data from the first four usable laser shots within the same run were processed with the cross-correlation method for each nosetip. The measurements where the disturbances and the cross-correlation method did not seem to agree were disregarded. A compilation of the data from these four laser shots was used to find the speed of the disturbance. A linear least squares fit showed that the speed of the wave packet for the 1-mm-radius nosetip (Figure 8.12) is about 804 m/s and the speed of the wave packet for the 0.16-mm-radius nosetip (Figure 8.13) is about 847 m/s. According to computations by Johnson [117], the edge velocity is 780 m/s at the aft end of the blunt flared cone. According to computations by Gronvall [10], the edge velocity is 840 m/s at the aft end of the sharp flared cone. The measurements are

1–3% higher than the computations, which implies that the wave packet is traveling faster than the computed edge velocity. This discrepancy may be due to the fact that the computations were performed at somewhat different conditions than the measurements. There are also many different ways to define the edge of the boundary layer, so the packet may be traveling at a speed associated with a streamline farther from the wall than in the computations.

Shot-to-Shot Changes in Wave Packet Arrival Time

Figure 8.23 shows the pressure measurements from the PCB sensor installed at $x =$ 420 mm on the 0° ray for the 1-mm-radius nosetip. These measurements correspond to laser shots 8–22 in Run 19-24. The response after each laser shot is offset by an amount proportional to the time at which the laser pulse is fired. The measured response to each laser-generated perturbation appeared to change from shot to shot. Each freestream laser perturbation appeared to generate wave packets of different amplitude. The time of arrival of each of the wave packets also appeared to change by as much as 20–30 μs. The changes in arrival time seen in the present experiment are similar to the changes in arrival time seen in Schmisseur's work [43, Figure 7.4].

A cross-correlation method was used to determine the amount of change in the wave packet arrival time. The cross-correlation method compared each laser shot to the first usable laser shot in a run. Figure 8.24 shows the measured response at $x = 420$ mm after laser shots 8–22 in Run 19-24. Again, each laser shot is offset by an amount proportional to the time after the tunnel starts. The time of arrival detected by the cross-correlation is marked by a black square. The detected time of arrival was plotted on top of the time traces after each laser shot to check the accuracy of the cross-correlation method.

Figure 8.25 shows the change in the wave packet arrival time plotted against the time during the tunnel run. This was done to determine if the change in arrival time was dependent on the run time as it is in the freestream. As the run time

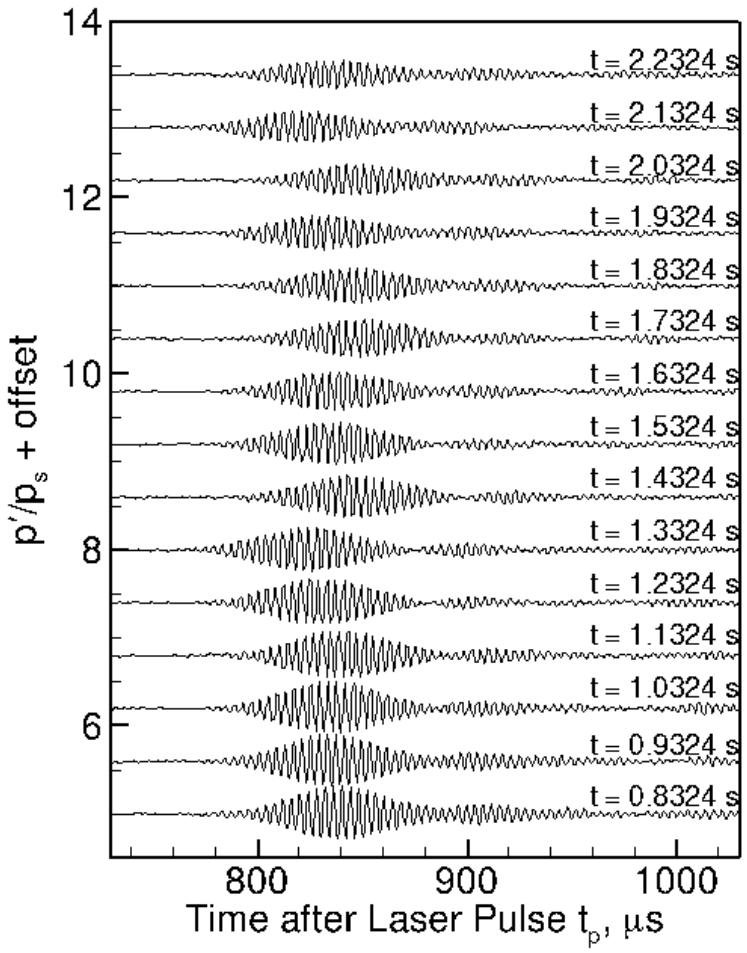

Figure 8.23. Plot of the measured response to each of the laser-generated disturbances at $x = 420$ mm on the 0° ray. Time traces are offset by an amount proportional to the time at which the laser pulse occurs. $p_0 = 685.0$–635.2 kPa, $T_0 = 422.6$–404.2 K, $M = 6$, $r_n = 1$ mm (Run 19-24).

increases, the freestream velocity decreases, so the perturbation might take longer to convect. Unlike the changes in arrival time seen in the freestream (Figure 5.8), the wave packet arrival time did not appear to increase with the decreasing tunnel conditions. However, for this particular run, the time of arrival variation appeared larger toward the end of the run than at the beginning of the run.

Previous measurements by Salyer [25] showed up to 20-μs variation in arrival time, which was caused by flaws in the triggering of the oscilloscopes. To determine if the

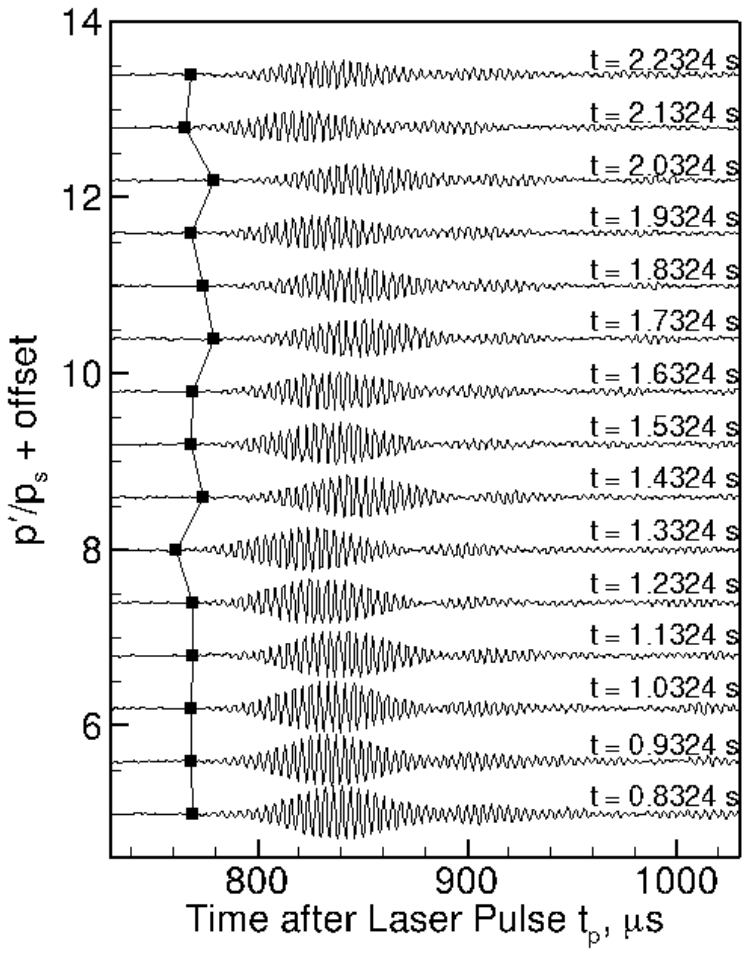

Figure 8.24. Plot of the measured response to each of the laser-generated disturbances at $x = 420$ mm on the 0° ray with shot to shot variation in time of arrival markers. $p_0 = 685.0$–635.2 kPa, $T_0 = 422.6$–404.2 K, $M = 6$, $r_n = 1$ mm (Laser shots 8–22 in Run 19-24).

observed change in time of arrival was also caused by the electronics, a check of the oscilloscope trigger setup was performed. A 10-Hz square wave was generated by an Agilent 33220A Function Generator and recorded by the oscilloscopes during a tunnel run. The Nd:YAG laser was not used during this run, but the setup of the electronics was otherwise the same. An example of the square wave is shown in Figure 8.26. The time of arrival of the square wave pulse is marked by a black dot.

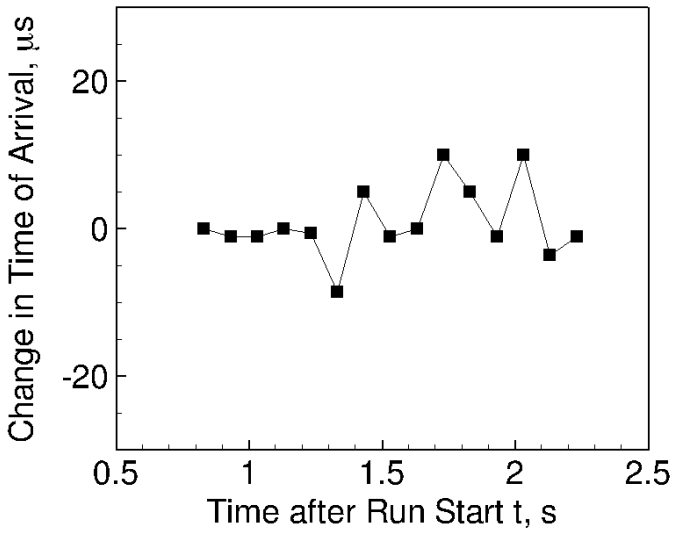

Figure 8.25. Plot of the shot-to-shot variation in time of arrival against time after the tunnel starts. p_0 = 685.0–635.2 kPa, T_0 = 422.6–404.2 K, $M = 6$, $r_n = 1$ mm, $x = 420$ mm on the 0° ray (Run 19-24).

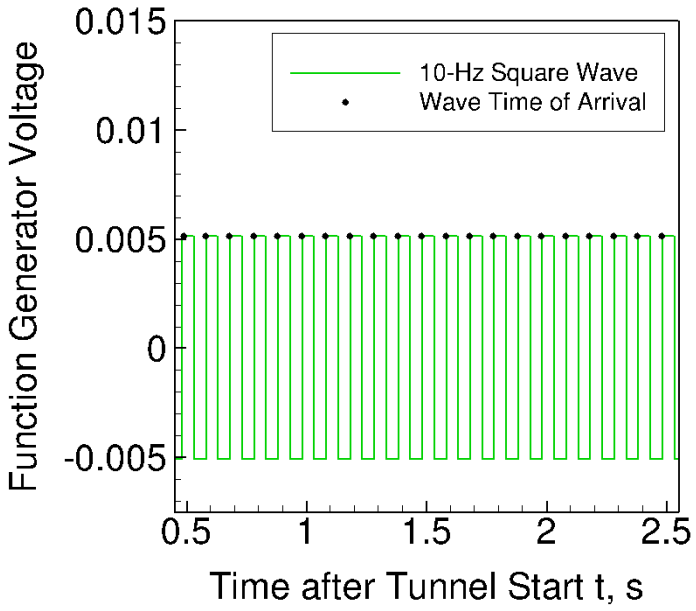

Figure 8.26. Square wave signal used to determine electronic jitter contribution to time of arrival variation.

The change in the time of arrival of the square-wave pulse was examined by comparing:

- The measurement on Channel 1 on Oscilloscope 1 (a Tektronix DPO 7054) to Channel 1 on each oscilloscope (Figure 8.27(a)).
- The measurement on Channel 1 of each oscilloscope to the generated square wave (Figure 8.27(b)).
- The measurement on Channel 1 of Oscilloscope 3 (a Tektronix DPO 7104) to each of the other channels on Oscilloscope 3 (Figure 8.27(c)).
- The measurement on each channel of Oscilloscope 3 to the generated square wave (Figure 8.27(d)).

Figure 8.27 shows that there is no change in time of arrival due to how the oscilloscopes are triggered. This shows that the changes in time of arrival were probably not associated with the oscilloscope electronics.

Due to the lack of evidence that the changes in wave packet arrival time were caused by the oscilloscope electronics, other options were considered. The time of arrival variations may also have been caused by a misalignment of the freestream disturbance to the flared cone. Small misalignments of the disturbance may be caused by a variety of factors, such as flow angularity, vibrations in the sting, vibrations in the optical setup, etc. Furthermore, the vibrations in the sting or in the optical setup may cause small transient changes in the angularity of the model compared to the flow.

Cases where the perturbation was purposely offset from the centerline axis of the flared cone model were examined to determine the effect of alignment on the time of arrival of the wave packet. Considering only the most aft sensor on the 0° ray, three different alignment configurations were examined:

- The freestream disturbance aligned to the centerline of the flared cone.
- The freestream disturbance offset 1.5 mm from the centerline of the flared cone toward the 0° ray.

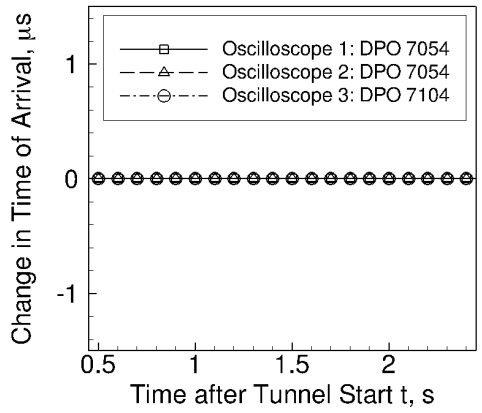

(a) Change in time of arrival in Channel 1 of each oscilloscope.

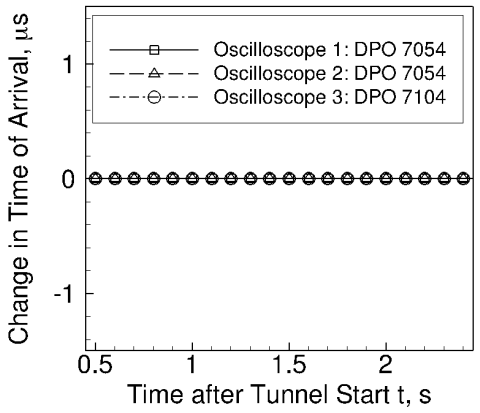

(b) Change in time of arrival in Channel 1 of each oscilloscope compared to square wave.

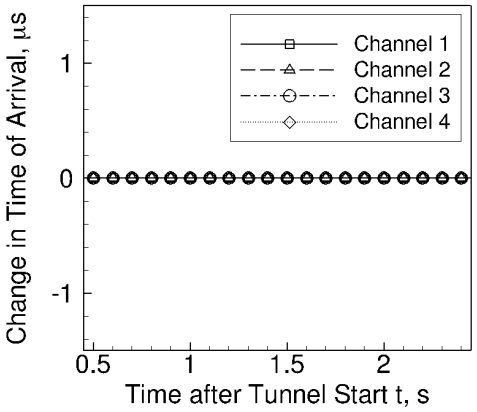

(c) Change in time of arrival in each channel of Oscilloscope 3.

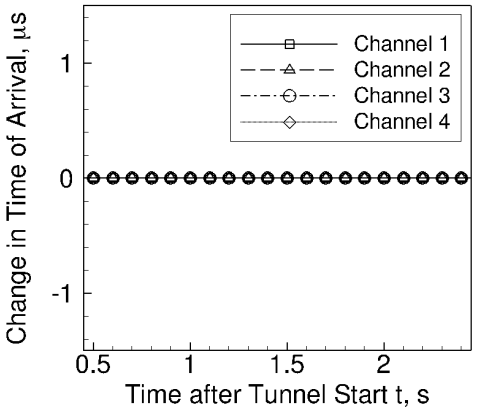

(d) Change in time of arrival in Oscilloscope 3, compared to square wave.

Figure 8.27. Change in time of arrival between oscilloscopes and channels.

- The freestream disturbance offset 3.0 mm from the centerline of the flared cone toward the 0° ray.

These three different alignments are examined for both the 1-mm-radius nosetip and the 0.16-mm-radius nosetip. The run numbers compared are given in Table 8.7. The changes in time of arrival were calculated by cross-correlating each laser shot to the first usable laser shot that was aligned to the model centerline. Thus, the change in time of arrival is calculated with respect laser shot number 8 in Run 19-08 for the

1-mm-radius nosetip and with respect to laser shot number 10 in Run 19-07 for the 0.16-mm-radius nosetip.

Table 8.7 Run numbers used for comparing variation in arrival times for different alignment offsets toward the 0° ray.

Offset Amount, mm	$r_n = 1$ **mm**	$r_n = 0.16$ **mm**
0	Run 19-08	Run 19-07
1.5	Run 19-12	Run 19-10
3.0	Run 19-36	Run 19-38

Figure 8.28 shows the shot-to-shot change in arrival time for the wave packet. These data correspond to measurements made on the 1-mm-radius nosetip model. Statistics on the change in time of arrival are given in Table 8.8. The mean and standard deviation of the change in arrival time are given for each offset in alignment. As the offset increases, the mean change in arrival time increases. This may mean that as the offset increases, the wave packet takes a longer time to convect to the model. As the offset increases, the standard deviation also increases slightly.

Table 8.8 Statistics on the changes in arrival time plotted in Figure 8.28. $r_n = 1$ mm.

Offset in Alignment, mm	**Mean Change in Arrival Time, μs**	**Standard Deviation in Arrival Time, μs**
0	0.8	4.7
1.5	12.3	5.7
3.0	19.2	8.6

Figure 8.29 shows the shot-to-shot change in arrival time for the wave packet. These data correspond to measurements made on the 0.16-mm-radius nosetip model. The mean and standard deviation of the changes in arrival time are given in Table 8.9. As the offset from the centerline increases, the mean change in arrival time increases,

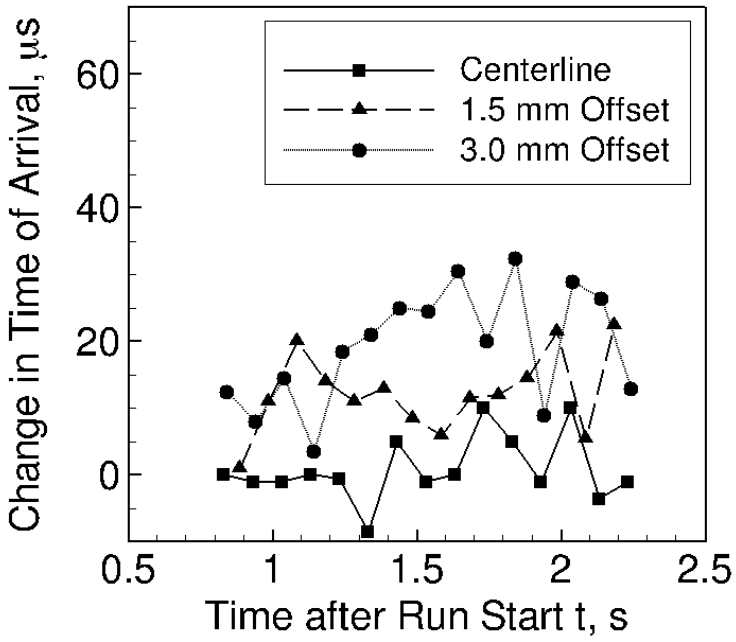

Figure 8.28. Changes in the wave packet arrival time for various alignments, relative to laser shot number 8 in Run 19-08. $p_0 \approx 720$ kPa, $T_0 \approx 435$ K, $M = 6$, $r_n = 1$ mm, $x = 420$ mm on the 0° ray (Runs 19-08, 19-12, 19-36).

but the standard deviation remains about the same. Again, the increase in the mean is probably related to a longer convection time. It is not clear why the standard deviation does not change with the offset in alignment to the 0.16-mm-radius nose.

Table 8.9 Statistics on the changes in arrival time plotted in Figure 8.29. $r_n = 0.16$ mm.

Offset in Alignment, mm	**Mean Change in Arrival Time, μs**	**Standard Deviation in Arrival Time, μs**
0	3.3	7.3
1.5	21.2	8.6
3.0	25.6	7.8

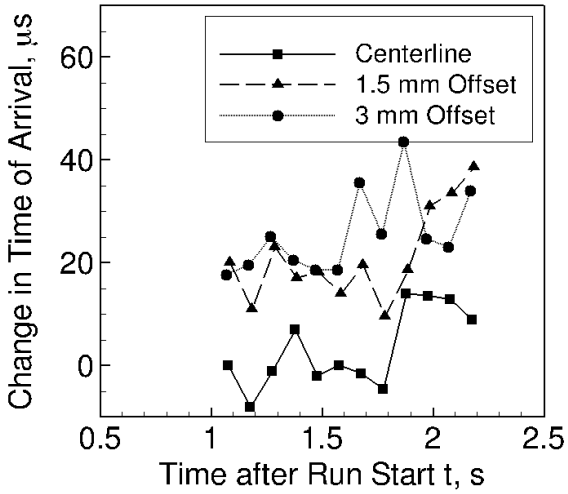

Figure 8.29. Changes in the wave packet arrival time for various alignments, relative to laser shot number 10 in Run 19-07. $p_0 \approx$ 515 kPa, $T_0 \approx 414$ K, $M = 6$, $r_n = 0.16$ mm, $x = 451$ mm on the 0° ray (Runs 19-07, 19-10, 19-38).

The magnitude of the mean change in arrival time is large for the small offsets in alignment. If the perturbation were assumed to travel in a straight line at the nominal freestream speed of 874 m/s, a 20 μs change in arrival time is equivalent to a change in distance of 17.5 mm. This distance is not reasonable if considering vibrational displacement of the model. The straight-line distance between the location where the perturbation is formed and the most aft sensor only changes by about 10 μm when the perturbation is offset 3 mm from the centerline. In reality, the perturbation speed probably changes and its trajectory is not a straight line because it must pass through a shock and an entropy layer. However, this still does not adequately explain why the arrival time of the wave packet changes so greatly.

The standard deviation of the change in arrival time shows the variation in the arrival time. This statistical parameter may show the small variations in alignment caused by small vibrations in the model position or optical mounts. The standard deviation ranges from 4.7–8.6 μs. Using the nominal freestream speed of 874 m/s, an equivalent distance to these time scales is about 4.1–7.2 mm. This means that the

linear distance that the perturbation travels would have to vary by about 4.1–7.2 mm. Again, these distances are large, but the perturbation probably does not travel in a straight line.

Another possibility is that the formation of the freestream laser perturbation changes slightly from shot to shot. The number of ionized particles may change from shot to shot if the density is not perfectly uniform. A method of observing or determining the shot-to-shot formation of the freestream perturbation has not been developed. However, measurements of the freestream perturbation in Chapter 5 show that the standard deviation in the arrival time is 1.2 μs. This phenomenon will have to be carefully studied further through both experiment and computation.

Another unexplained phenomenon was the variation in time of arrival between sensors along the same ray. An example of this is provided in Figure 8.30. For this particular run, the freestream laser perturbation was aligned 1.5 mm off of the centerline of the flared cone toward the 0° ray (Run 19-09). The measured response to the freestream laser perturbations at $t = 1.1604$ (laser shot 11) and $t = 1.2604$ s (laser shot 12) after the tunnel run has started are plotted here. The measured responses to laser shots 11 and 12 at $x = 231$ mm are given in Figure 8.30(a) and offset by a constant of 0.2. The measured responses to laser shots 11 and 12 at $x = 451$ mm are given in Figure 8.30(b) and offset by a constant of 1.1. Note that this constant offset is larger at $x = 451$ mm because the amplitude of the wave packet is larger at the farther downstream station.

Figure 8.30(a) shows that the wave packet created in laser shot 11 took longer to arrive at $x = 231$ mm than the wave packet created in laser shot 12. Figure 8.30(b) shows that the wave packet created in laser shot 11 took less time to arrive at $x = 451$ mm than the wave packet created in laser shot 12. This change implies that the wave packet created in laser shot 11 traveled faster than the wave packet created in laser shot 12. The phenomenon was not observed in every run, nor for every condition.

Measurements by Schmisseur in the PQFLT [43] suggest that this time of arrival variation is not a phenomenon present only in the BAM6QT or in this experiment.

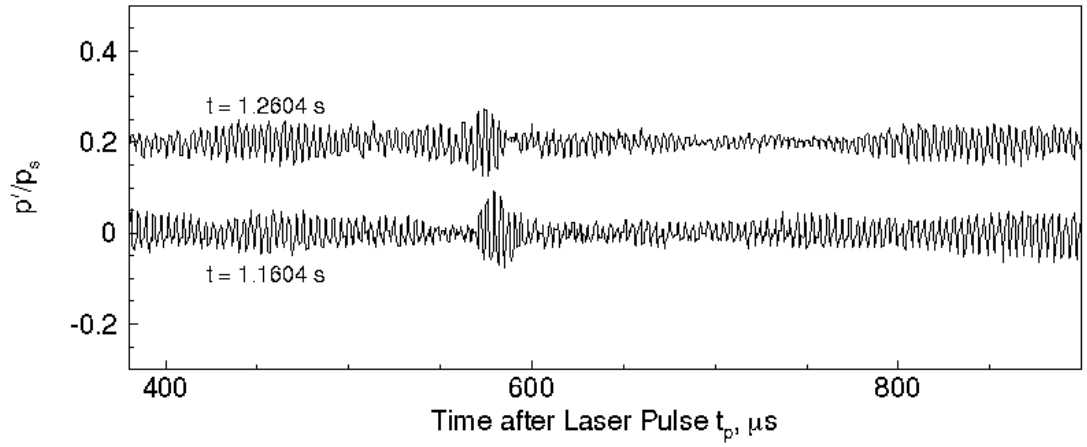

(a) $x = 231$ mm, $t = 1.1604$ s and $t = 1.2604$ s.

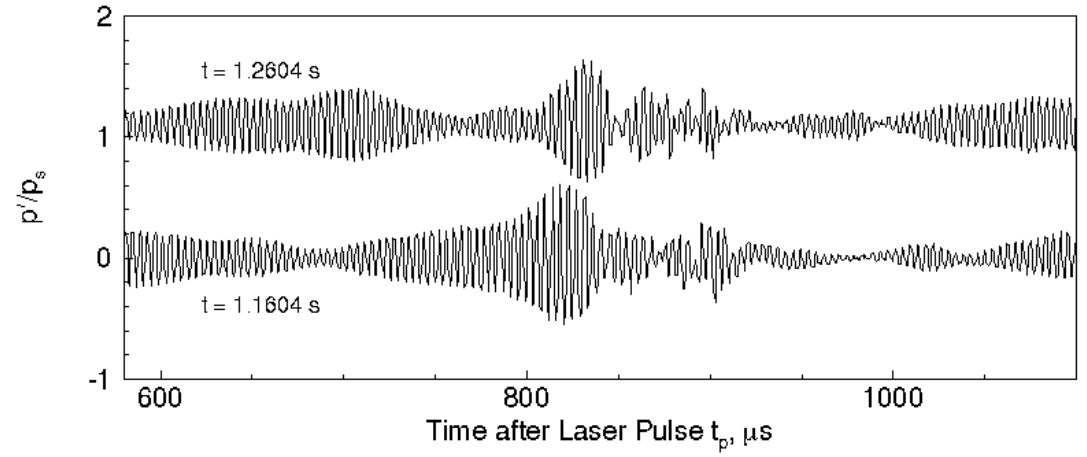

(b) $x = 451$ mm, $t = 1.1604$ s and $t = 1.2604$ s.

Figure 8.30. Time of arrival variation between sensors. Freestream disturbance aligned to 0° ray at a 1.5-mm offset, $r_n = 0.16$ mm, $p_0 = 565$ kPa, $T_0 = 423.0$ K, $M = 6$ (Laser shots 11 and 12 for Run 19-09).

Computations might be able to verify the suspicion that the time of arrival variation is due to a small alignment offset. Other explanations for the change in arrival time of the wave packet may also exist.

8.4.2 Frequency and Amplitude Analysis

A single fast Fourier transform (FFT) was taken of the wave packet after each laser shot to measure the RMS amplitude of these wave packets as they grow. As many as 12–15 FFTs were then averaged together to form power spectra. The windows used for these FFTs were the same as shown previously in Figure 8.18. A Welch spectrum estimation method with Blackman windows was used for the time bracketed by the two squares. When the responses from multiple laser pulses were used, the FFTs of each wave packet were averaged together to form a power spectrum. However, the laser-generated disturbances appeared to produce wave packets of varying amplitude and structure, so an average of the FFTs may not be representative of the spectral content in a single wave packet.

The spectral analysis of the response to a single laser perturbation was fairly noisy. Thus, it was desirable to try to smooth out the power spectra. Figure 8.31 shows FFTs from several different laser shots in a single run. The FFTs of the wave packets from different portions of the run look similar despite the differences in amplitude and structure of each wave packet. This similarity shows that an average of the FFTs from each wave packet generated in the run can produce representative power spectra. Even after averaging together 12–15 FFTs, the spectra appeared noisy. A zero-phase moving average filter was applied to the averaged FFTs in post-processing to smooth out the displayed data. This filter had a window size of 5 points and processes the data points in the forward and reverse directions.

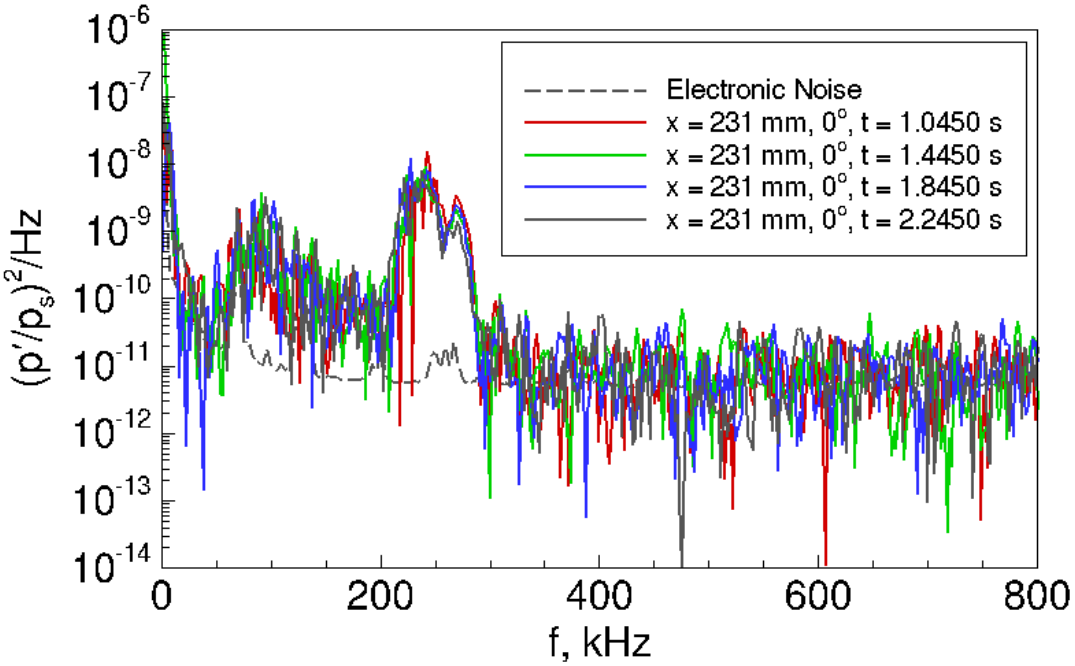

Figure 8.31. Several different FFTs for $r_n = 0.16$ mm, $x = 231$ mm. Laser shots 10, 14, 18, and 22 for Run 19-47: $p_0 = 534.3$ kPa, $T_0 = 428.3$ K, $Re/m = 5.81 \times 10^6$/m.

Power Spectra Showing the Axial Evolution of a Wave Packet

The power spectra for the traces shown in Figures 8.12 and 8.13 are shown in Figures 8.32(a) and 8.32(b), respectively. These power spectra are generated by averaging the FFTs from 12 different wave packets in the same run. The spectral analysis method yields a frequency spacing of 2 kHz. The peak of the second-mode frequency band stays relatively constant at about 250 kHz for the blunt nosetip and at about 230 kHz for the sharp nosetip. The difference in peak frequencies is likely due to the slightly lower stagnation pressures used in the run for the sharp nosetip. The second-mode frequency band in the power spectra remains relatively constant with increasing axial distance. The constant frequency is due to the nearly-constant boundary layer thickness, which develops as a result of the pressure gradient created by the flare [117].

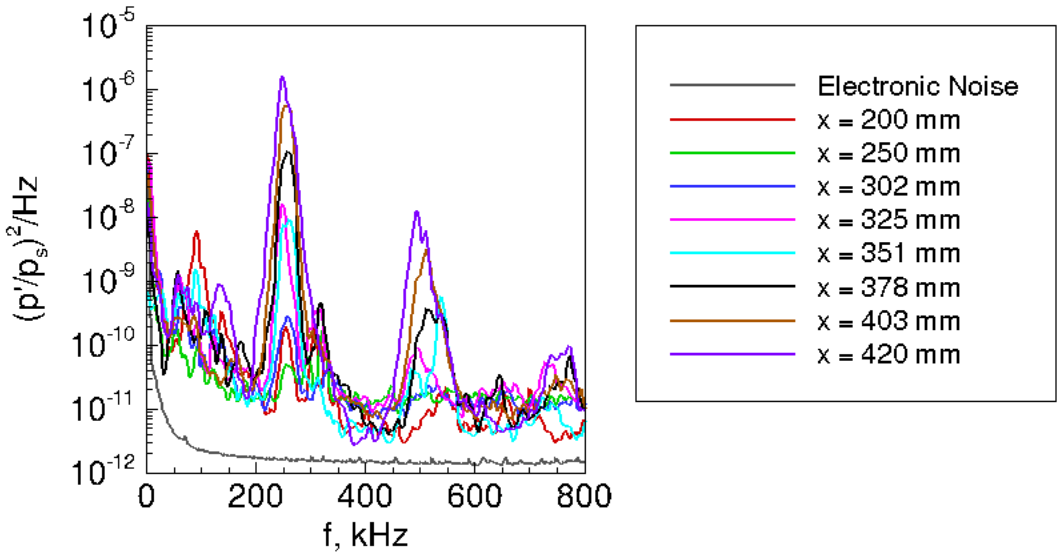

(a) Run 19-44: $r_n = 1$ mm, $p_0 = 706.9$ kPa, $T_0 = 422.3$ K, $Re/m = 7.86 \times 10^6$/m.

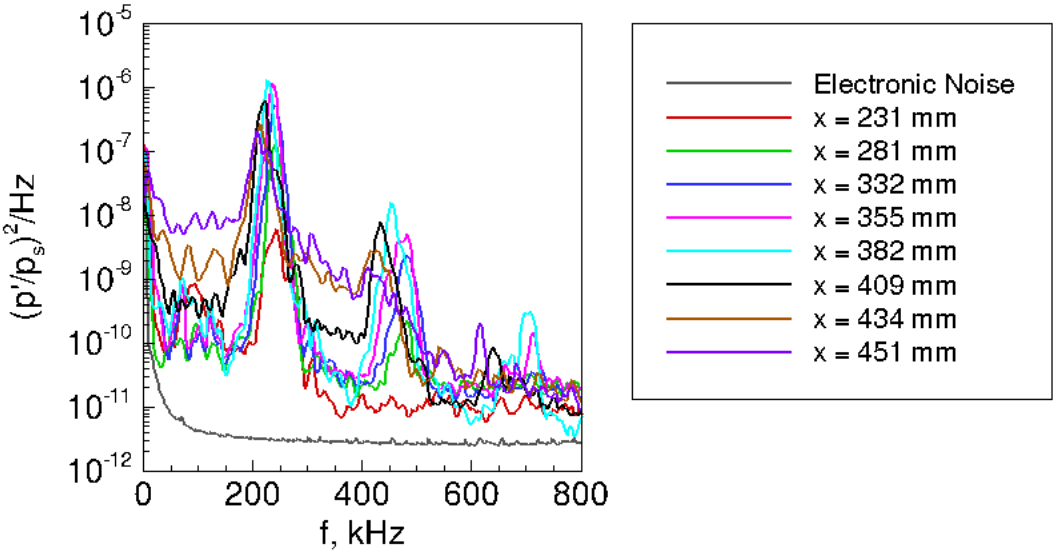

(b) Run 19-47: $r_n = 0.16$ mm, $p_0 = 534.3$ kPa, $T_0 = 428.3$ K, $Re/m = 5.81 \times 10^6$/m.

Figure 8.32. Spectral analysis of wave packet at various axial stations on the 0° ray.

In Figure 8.32(a), the spectra at $x = 325$ mm and farther-aft stations show the presence of a harmonic. The wave packet was larger than the natural waves only at $x = 351$ mm and downstream. Coincidentally, the time traces which showed measurable wave packets in Figure 8.12 exhibited a double-burst shape. The spectra at the corresponding stations show a large second-mode peak and at least one harmonic peak. This suggests that the multi-burst shape may be related to the nonlinearity of the wave packet. A peak at 91 kHz appears in the spectra at $x = 200$ mm. This is less than half of the second-mode peak frequency, so it is probably not a subharmonic. This peak also does not appear to grow with increasing Reynolds number. At $x = 250$ mm, the peak at 91 kHz disappears and a 60 kHz peak appears. This 60 kHz peak was seen at farther aft stations and displayed little or no growth. The spectral content at $x = 420$ mm shows an additional peak that appears at 132 kHz. This peak is slightly more than half the second-mode peak frequency of 250 kHz, but may be a subharmonic.

Figure 8.32(b) shows that the axial growth of the wave packet on the sharp nosetip is different from that of the blunt nosetip. The first axial station at which a PCB sensor was installed ($x = 231$ mm) appears to have a peak located in the frequency band where the second mode is expected, at about 230 kHz. There does not appear to be a higher harmonic in the spectra for the wave packet at this location. However, the spectra at $x = 231$ mm shows a peak at 86 kHz. This peak behaves similarly to the 91 kHz peak on the blunt cone because it only appears in the first sensor station. At $x = 332$ mm, the 86 kHz peak disappears and a peak appears at 68 kHz. The 68 kHz peak persists until at least $x = 382$ mm. Farther aft sensors do not appear to detect the lower-frequency peak, but this could be due to the increase in the broadband frequency content.

The harmonic of the second mode appears farther upstream on the blunt model than on the sharp model. On the sharp model, the harmonic first appears at $x = 281$ mm. On the blunt model, the harmonic may be present in the first trace, but the spectra are not clear. On the sharp model, a higher harmonic to the second mode

at about 750 kHz also appears to rise out of the background frequency content at $x = 355$ mm. At $x = 382$ mm, the second-mode peak shifts to about 225 kHz. At $x = 409$ mm, the second-mode peak shifts to about 217 kHz. The harmonic peaks also shift down in frequency with the fundamental peak. At $x = 409$ mm, an increase in the broadband frequency content also begins to occur. This increase in the broadband frequency content indicates that breakdown has started to occur. The second harmonic peak at 750 kHz disappears by $x = 434$ mm. This may indicate that the flow is starting to transition on the flared cone. It is possible that as transition begins, the boundary layer thickens and shifts the second-mode peak to a lower frequency. The time traces in Figure 8.13 show that the wave packet at $x = 409$ mm is slightly shorter than the packet at $x = 332$ mm. This is probably because the wave packet has begun to breakdown at $x = 409$ mm.

The spectra for Run 19-45 and 19-46 are given in Figures 8.33(a) and 8.33(b). These were the runs used to compare data at the same freestream density, so only data from a few laser shots can be used for the power spectra. Only 3 FFTs were averaged to compute these spectra.

The spectra in Figure 8.33(a) show that the second-mode peak frequency is now 226 kHz. The harmonic peak at 457 kHz is present as far upstream as $x = 351$ kHz and as far downstream as $x = 420$ mm. The harmonics are again indicative of nonlinear growth. The lower-frequency peaks behave similarly to the higher-pressure data seen in Figure 8.32(a). The 91 kHz peak only appears in the spectra at $x = 200$ mm, a peak at about 67 kHz appears in the farther aft sensors, and a peak at about 130 kHz appears at $x = 420$ mm. Since the 91 kHz peak does not appear to change with decreased freestream conditions, it is unlikely that this peak is related to anything in the boundary layer. The other lower-frequency peaks at around 67 kHz and 130 kHz change slightly with the decreased conditions, but their cause is again unknown.

The spectra for Run 19-46 (Figure 8.33(b)) are similar to the spectra for Run 19-47 (Figure 8.32(b)). The stagnation pressure for Run 19-46 is about 10% higher than for Run 19-47. Thus, the spectra change accordingly. The second-mode peak

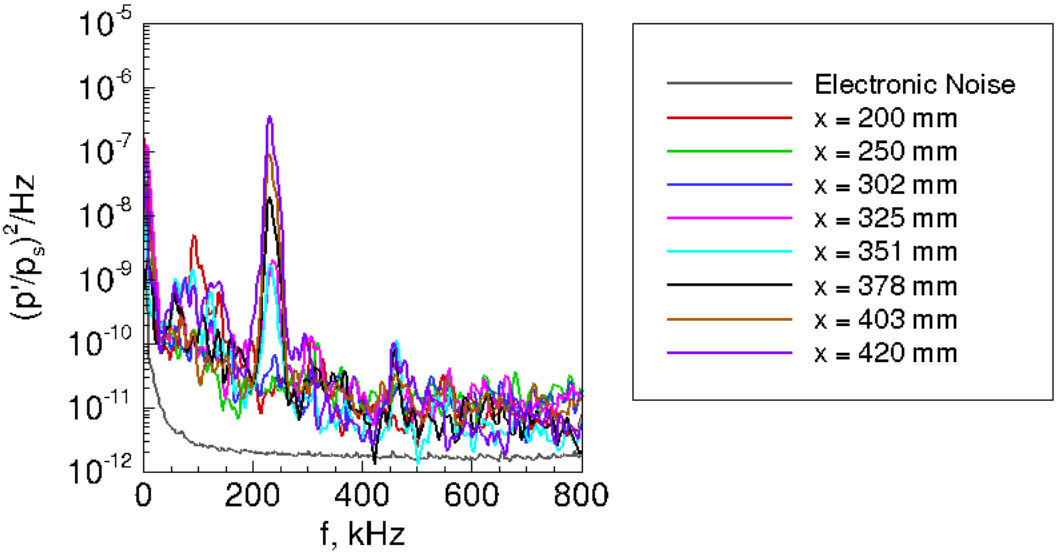

(a) Run 19-45: $r_n = 1$ mm, $p_0 = 599.5$ kPa, $T_0 = 411.1$ K, $Re/m = 6.98 \times 10^6$/m.

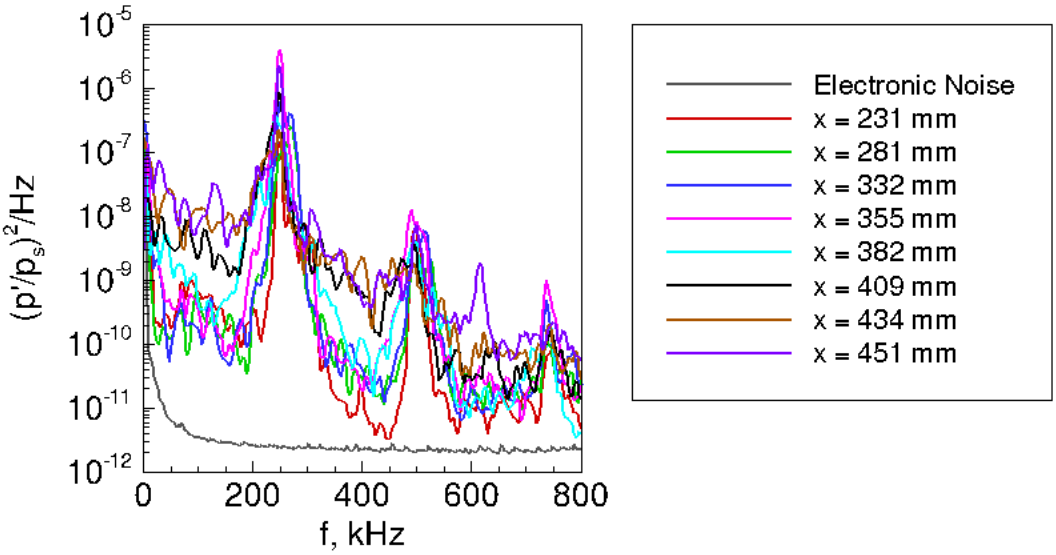

(b) Run 19-46: $r_n = 0.16$ mm, $p_0 = 615.1$ kPa, $T_0 = 431.8$ K, $Re/m = 6.59 \times 10^6$/m.

Figure 8.33. Spectral analysis of wave packet at various axial stations on the 0° ray. $\rho_\infty = 0.026$ kg/m^3.

frequency is now at about 248 kHz. The spectra show a first and second harmonic peak at 489 and 737 kHz, respectively. These harmonics persist from the first sensor station at $x = 231$ mm through to the last sensor station at $x = 451$ mm. However, the background frequency content begins to increase as far upstream as $x = 382$ mm. This increase in background frequency content indicates that transition onset has moved forward with the increase in stagnation pressure, as expected. The lower-frequency peaks seen in Figure 8.32(b) are not as clear in Figure 8.33(b).

RMS Amplitudes of the Wave Packet Compared to N-Factor Computations

The RMS amplitudes of the wave packet in the second-mode frequency band were found by first integrating the spectra between about 230–270 kHz for the blunt nosetip and about 200–240 kHz for the sharp nosetip. Then, the square root of the integrated value was taken to be the RMS amplitude. This procedure was performed for each FFT of the response to a laser shot. The RMS from each FFT was then averaged to yield the RMS amplitudes presented here.

The computation of the N-factor uses the growth of only the most amplified frequency, so narrow integration limits are used to try to match the computations as best as possible. The N-factor computed in STABL [10, 117] for the corresponding axial locations is also tabulated for comparison. The computations for the sharp nosetip used a total pressure of $p_0 = 620.5$ kPa, a total temperature of $T_0 = 433$ K, and a wall temperature of 300 K. The computations for the blunt nosetip used a total pressure of $p_0 = 965.3$ kPa and a total temperature of $T_0 = 433$ K.

The experimental RMS amplitudes were calculated using the spectra in Figures 8.32(a) (Run 19-44) and 8.33(b) (Run 19-46). The run conditions of these two cases matched the computation conditions more closely than other runs. The RMS amplitudes of the second-mode frequencies are provided in Tables 8.10 and 8.11. The N-factors correspond to slightly different conditions, but they can still provide a gen-

eral idea of how the second mode is computed to grow on the flared cone for each nosetip. When compared to the tabulated RMS amplitudes, the experimental measurements do not match the linear computation. This is expected because the spectra show large harmonics in the spectral content, indicating nonlinear growth.

Table 8.10 RMS amplitudes for Run 19-44 and N factors computed in STABL for the second mode on the blunt ($r_n = 1$ mm) cone.

x, mm	$p'/p_s \times 10^2$	**Computed** N	e^N
200	0.212	2.4	11.02
250	0.186	4.8	121.5
302	0.392	7.6	1.998×10^3
325	0.954	9.0	8.103×10^3
351	2.67	10.6	4.013×10^4
378	9.38	12.2	1.988×10^4
403	14.0	13.8	9.846×10^4
420	10.1	14.8	2.676×10^6

Table 8.11 RMS amplitudes for Run 19-46 and N factors computed in STABL for the second mode on the sharp ($r_n = 0.16$ mm) cone.

x, mm	$p'/p_s \times 10^2$	**Computed** N	e^N
231	3.75	5.4	221.4
281	6.30	7.3	1.480×10^3
332	8.93	9.3	1.094×10^4
355	20.4	10.2	2.690×10^4
382	7.33	11.4	8.932×10^4
409	10.1	12.6	2.966×10^5
434	5.30	13.8	9.846×10^5
451	14.9	14.6	2.191×10^6

To compare the measured RMS amplitudes to the computed N-factors, each RMS amplitude was normalized by the RMS amplitude at the first location. Figure 8.34 compares the RMS amplitude to the N-factor for the blunt nose at $p_0 = 706.9$ kPa and for the sharp nose at $p_0 = 615.1$ kPa. The normalized RMS amplitudes are given by the open squares, with corresponding values on the right vertical axis. The N-factor computation from STABL is given by the solid line, with corresponding values on the left vertical axis. The scaling of the right vertical axis is the same as the left vertical axis, but the right axis is shifted so that the points fall close to the computation. For the blunt nosetip case, the right axis is shifted so that the point at $x = 302$ mm matches the computation. For the sharp nosetip case, the right axis is shifted so that the point at $x = 231$ mm matches the computation.

The blunt nosetip measurements show that the first three locations on the compression cone have roughly the same RMS amplitudes. It is unlikely that this could be caused by insufficient vertical resolution on the oscilloscopes. The vertical resolution of the oscilloscope was about 12 bits. The vertical scaling was set to 1 mV per division for the channels recording measurements from the first three sensor locations. The maximum and minimum recorded voltage on these channels was about ± 2 mV for Run 19-44. The constant RMS in the first three sensor stations could also be due to the inability of the sensor to detect changes in the RMS amplitude at these magnitudes. In fact, Casper was not able to resolve measurements of the second mode under quiet flow when the N-factors were less than 4 [80]. At farther downstream stations, the RMS measurements follow the N-factors found in STABL fairly well, until about $x = 378$ mm. When compared to the spectra in Figure 8.32(a), it is evident that the wave packet is nonlinear at this station and possibly at farther upstream stations. When the waves are nonlinear, their growth does not match the linear computations.

Similarly, for the sharp nosetip, the RMS amplitudes do not appear to grow as predicted by the linear computation of N-factor. The spectra in Figure 8.33(b) show that the first and second harmonic appear at all axial stations, and thus, the wave

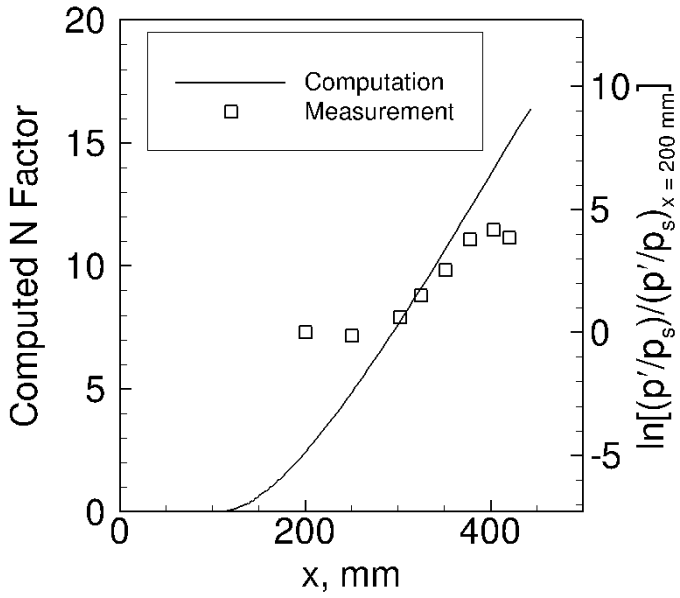

(a) $r_n = 1$ mm. Measurements from Run 19-44.

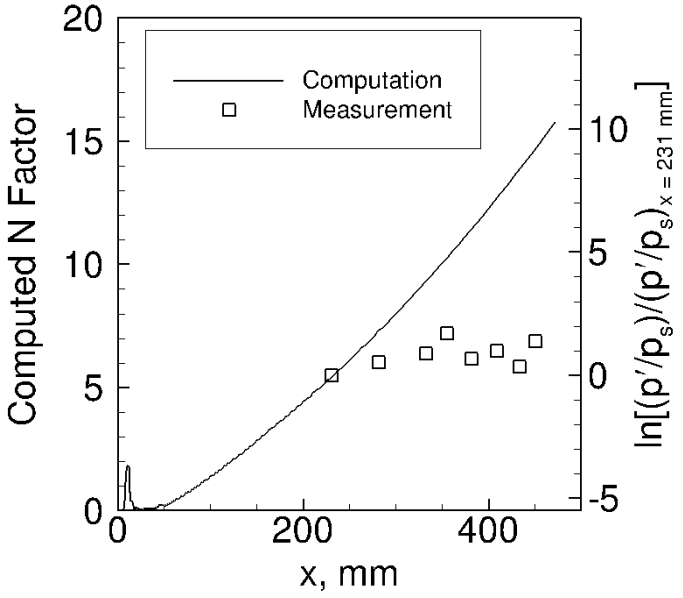

(b) $r_n = 0.16$ mm. Measurements from Run 19-46.

Figure 8.34. A comparison of RMS amplitudes of the second mode to the N factors computed in STABL.

packet is highly nonlinear at all of these stations. The large RMS amplitudes of the second-mode frequency remains relatively constant at all axial stations. This indicates that the wave packet is probably saturated at all of these stations.

The right vertical axis in Figure 8.34(a) was shifted upward more than the right vertical axis in Figure 8.34(b). This seems to indicate that the initial amplitude on the blunt nose is smaller than on the sharp nose. An initial amplitude can be inferred if the scaling of the RMS amplitudes to the computations is assumed to match Figure 8.34.

On the blunt nosetip, the wave packet at $x = 325$ mm is assumed to be in the linear growth regime and to have a significant SNR. The RMS amplitudes are normalized by the RMS amplitude at $x = 200$ mm, but the match to the N-factor is taken at $x = 325$ mm. This means that the computation of the initial amplitude must consider the RMS amplitude of the wave packet at $x = 325$ mm as well as the RMS amplitude of the wave packet at $x = 200$ mm. To calculate the initial disturbance, the following equation was used

$$\ln\left(\frac{A_1}{A_0}\right) = N - \ln\left(\frac{A_2}{A_1}\right) \tag{8.3}$$

where A_0 is the initial amplitude of the wave packet, $A_1 = 1.276 \times 10^{-3}$ Pa is the RMS amplitude of the wave packet at $x = 200$ mm, $A_2 = 0.0127$ Pa is the amplitude of the wave packet at $x = 325$ mm, and $N = 9.0$ is the computed N-factor matched at $x = 325$ mm. The amplitudes used here are not normalized because the surface pressure changes at each sensor station. For the blunt nosetip, the initial disturbance amplitude is calculated to be $A_0 = 1.57 \times 10^{-3}$ Pa, which is $3.51 \times 10^{-6} p_\infty$.

On the sharp nosetip, a wave packet that may still be in the linear region is harder to find. The power spectrum of the pressure fluctuations at the first sensor station ($x = 231$ mm) show the presence of a second harmonic. The presence of this harmonic indicates that the wave packet is already nonlinear at $x = 231$ mm. A computation of the initial disturbance amplitude with this data will not be accurate. Nevertheless, the initial amplitude can computed with Equation 8.3, letting $N = 5.4$ and $A_2 =$

$A_1 = 0.0186$ Pa be the RMS amplitude of the wave packet at $x = 231$ mm. This yields an initial disturbance amplitude of $A_0 = 8.42 \times 10^{-2}$ Pa, which is $2.34 \times 10^{-4} p_\infty$.

From this analysis, the sharp nosetip appears to have an initial amplitude almost 2.5 orders of magnitude larger. Balakumar's work comparing the receptivity of sharp and blunt nosetips suggests that a sharp nosetip should have a receptivity coefficient almost 3 orders of magnitude larger than the blunt nosetip [28]. The general agreement of the measurements shown here to Balakumar's study is encouraging. The residual discrepancies may be (1) because Balakumar calculated receptivity for planar acoustic waves, (2) the use of different computational conditions, or (3) the experimental data lacks a linear growth region for the sharp nosetip.

Change in Wave Packet Amplitude Over the Run Time

The amplitude of the generated wave packet appears to change over the course of a tunnel run. This amplitude varies from laser shot to laser shot, so it is unclear if this variation is due to the changing tunnel conditions or due to variations in the laser perturber setup. The following analysis only uses the blunt nosetip data from Run 19-23. Only data from the sensor at $x = 378$ mm on the 0° ray is shown here. This sensor was chosen because the wave packet may not yet be nonlinearly saturated at $x = 378$ mm, but is still large enough to be measurable for the entire run. A similar analysis is not conducted for the sharp nosetip because the wave packet generated in the boundary layer on the sharp model appears to be saturated at even the first sensor location. The RMS amplitudes of the second-mode disturbance over time are measured by integrating the spectra over the second-mode bandwidth and taking the square root, as before.

It is suspected that the RMS amplitudes of the wave packet change due to the changing freestream conditions. Changing freestream conditions will affect the amplitude of the freestream laser perturbation, as seen in Chapter 4. A comparison between the freestream perturbation amplitude and the wave packet RMS amplitude

can be made to determine if this is the case. However, a direct comparison is not possible because the measurements of the perturbation in the BAM6QT freestream are at a higher density than the flared cone measurements. Nevertheless, a qualitative comparison can be made.

The amplitude of the freestream laser perturbation is calculated by finding the estimated energy of the perturbation. The estimated impulse is the same as used in Chapter 5, an integration of the pressure measurement across the perturbation (Equation 5.4). Only the amplitudes measured by the PCB sensor are used because the Kulite sensors do not have a high enough frequency response to be able to resolve the passage of the perturbation in the freestream. The PCB measurements are plotted with the RMS amplitude of the wave packet on the blunt flared cone in Figure 8.35. The amplitude of the freestream disturbances corresponds to the right vertical axis. The RMS amplitude of the wave packet in the boundary layer corresponds to the left vertical axis. The axes here are scaled arbitrarily to show that the same trend occurs in both sets of data. Figure 8.35 shows the same relative decrease in both the second-mode amplitude on the blunt flared cone and the amplitude of the freestream disturbance. Thus, the decreasing freestream disturbance magnitude causes a decreasing wave packet amplitude over time.

8.5 Azimuthal Measurements of the Developing Disturbance

To determine the symmetry and the controllability of the perturbation, three azimuthal arrays were monitored. Each of these arrays contains three sensors, spaced 120° apart. Both the blunt nosetip and the sharp nosetip were used in these measurements. The alignment of the laser perturbation to the cone was not adjusted between the blunt nosetip runs and the sharp nosetip runs. This was done to maintain as consistent an alignment as possible between the two nosetips. Given the axisymmetry of the cone, a perfect alignment of a perfectly axisymmetric freestream perturbation to

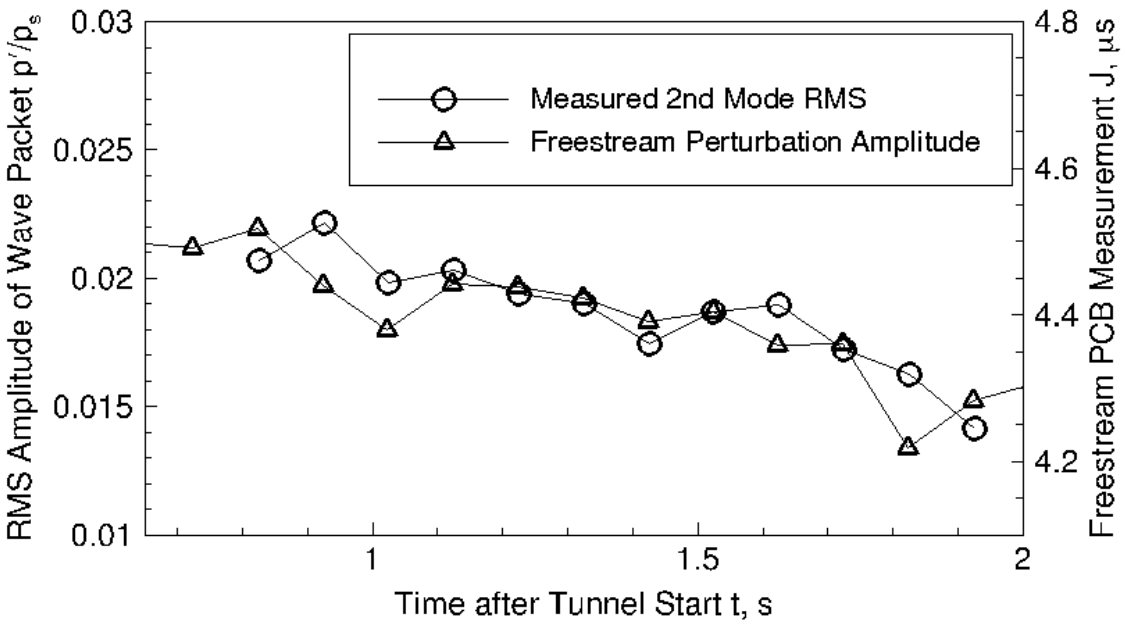

Figure 8.35. A comparison of the wave packet amplitude on the blunt flared cone to the freestream perturbation amplitude.

the cone centerline should produce an axisymmetric response of the boundary layer. Thus, each sensor on the azimuthal arrays should show a similar response.

On the blunt cone, the azimuthal arrays are located at axial stations of $x =$ 302 mm, 351 mm, and 403 mm. On the sharp cone, the azimuthal arrays are located at axial stations of $x = 332$ mm, 382 mm and 434 mm. The laser perturbation was aligned to the cone in the following configurations:

1. Along the centerline axis of the cone.
2. 1.5 mm from the cone centerline, toward the 0° (main) ray.
3. 1.5 mm from the cone centerline, toward the −120° ray.
4. 1.5 mm from the cone centerline, toward the +120° ray.
5. 3 mm from the cone centerline, toward the 0° (main) ray.
6. 3 mm from the cone centerline, toward the −120° ray.
7. 3 mm from the cone centerline, toward the +120° ray.

The time traces shown in the following sections are now offset by an amount proportional to the azimuthal location of the sensor.

8.5.1 Measurement of Axisymmetry: Perturbation Aligned to the Cone Centerline

To check symmetry, the perturbation was aligned upstream of the cone, along the centerline of the cone. The time traces from the azimuthal arrays for the blunt nosetip are shown in Figure 8.36. The wave packet is difficult to detect at the most upstream azimuthal sensor array at $x = 302$ mm (Figure 8.36(a)). Some increase in amplitude is seen at about $t = 900$ μs. However, this increase occurs too late to be the result of the laser perturbation. These could be large natural waves. The second array at $x = 351$ mm shows what appears to be a small wave packet near $t = 700$ μs. After this wave packet passes over the sensors, an increase in the fluctuation amplitude is again seen in the sensors. At the aftmost azimuthal sensor array at $x = 403$ mm, the wave packet is seen clearly in all of the sensors. The wave packet appears to be larger in the $\pm 120^\circ$ rays than in the 0° ray. Futhermore, the wave packet in the 0° ray also appears to show a double-burst structure.

The frequency content of the traces are also analyzed using the power spectral density, as computed using methods discussed at the beginning of Section 8.4.2. Figure 8.37 shows the spectral content at each azimuthal array. The power spectra show second-mode peaks that have nearly the same frequency, but the magnitude of the peaks again show asymmetric amplitudes. A peak near 130 kHz is observed in some of the spectra, but not all. The 130 kHz peak appears in the 0° and -120° sensors at $x = 302$ mm. Then, the 130 kHz peak appears in the 0° and $+120^\circ$ sensors at $x = 351$ mm. Finally, the 130 kHz peak appears in the -120° and $+120^\circ$ sensors at $x = 403$ mm. The change in azimuthal stations at which this peak appears may indicate the presence of an instability traveling obliquely. However, not enough azimuthal sensors were used to state this with any conviction.

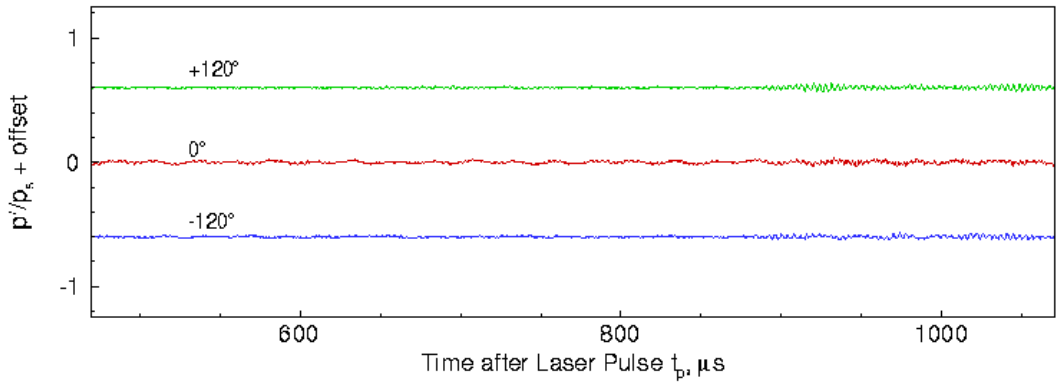

(a) $x = 302$ mm.

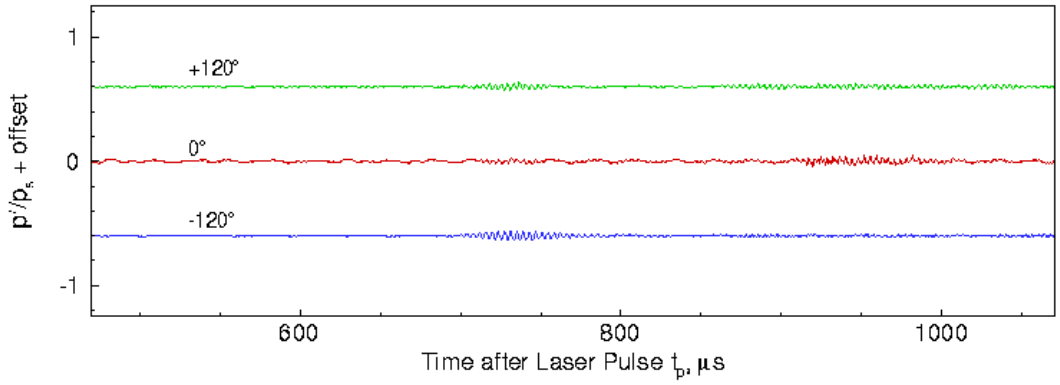

(b) $x = 351$ mm.

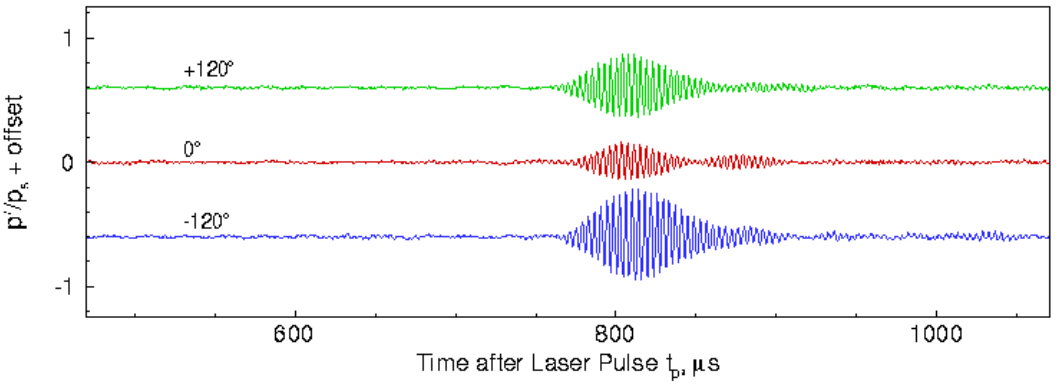

(c) $x = 403$ mm.

Figure 8.36. Time traces from azimuthal arrays of the effect of a laser perturbation for $r_n = 1$ mm. Perturbation aligned to cone centerline. Run 19-03: $p_0 = 748.1$ kPa, $T_0 = 431.9$ K, $Re/m = 8.02 \times 10^6$/m.

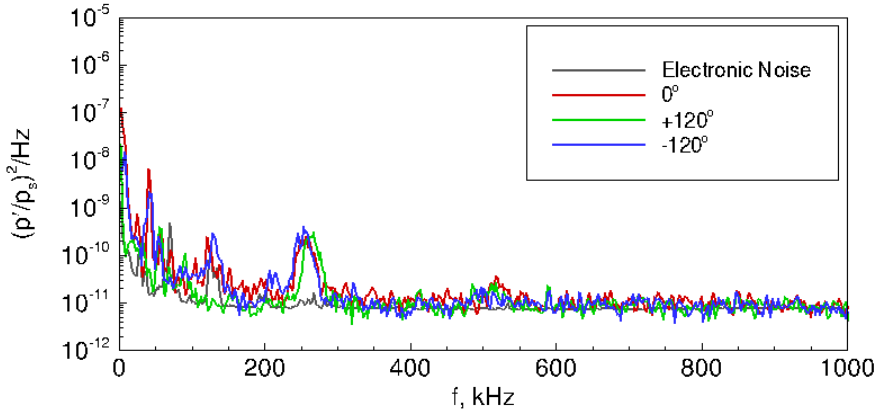

(a) $x = 302$ mm.

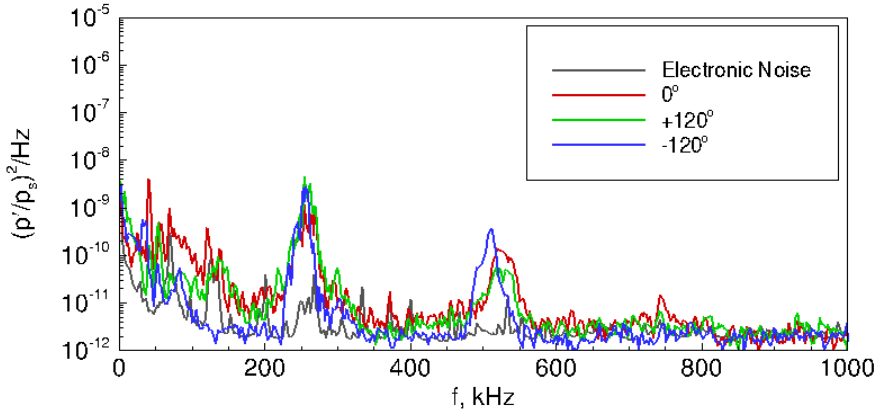

(b) $x = 351$ mm.

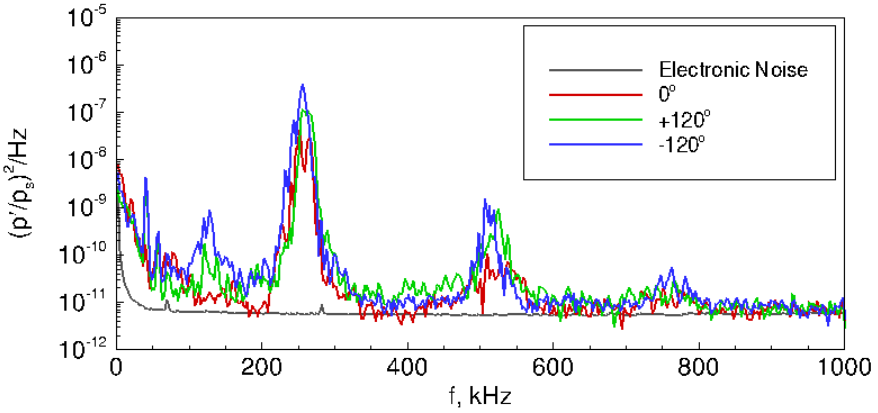

(c) $x = 403$ mm.

Figure 8.37. Spectra from azimuthal arrays for $r_n = 1$ mm. Perturbation aligned to cone centerline. Run 19-03: $p_0 = 748.1$ kPa, $T_0 = 431.9$ K, $Re/m = 8.02 \times 10^6$/m.

The sharp nosetip was also used when the perturbation was aligned to the centerline axis. The time traces from the three azimuthal sensor arrays are shown in Figure 8.38. The first azimuthal sensor array (Figures 8.38(a) and 8.39(a)) detects the wave packet in the boundary layer of the sharp nosetip. This implies that the amplitude of the wave packet is larger than on the 1-mm-radius nosetip. This first sensor array also shows that the wave packet amplitude on the 0° ray at $x = 332$ mm is smaller than on the other two rays. This amplitude discrepancy is similar to the amplitude discrepancy seen at $x = 403$ mm on the blunt cone. Farther aft sensors show perturbations that are relatively similar in amplitude between the different rays, but slightly different in shape. For the sharp nosetip, the waves become nonlinearly saturated.

The spectra from the three azimuthal sensor arrays are shown in Figure 8.39. The presence of several large harmonics are seen in each of the stations. The amplitude of the second mode and its harmonics appear larger than on the blunt cone. In particular, the presence of large harmonics at $x = 332$ mm suggests that the wave packet at $x = 332$ mm may be nonlinearly saturated. Amplitude comparisons between these saturated wave packets become less useful.

8.5.2 Off-Axis Investigations

Initial measurements on the cone surface of the effect of the off-axis perturbation used an offset of about 1.5 mm. The perturbation was then offset by 3.0 mm toward each ray of sensors because an offset of 1.5 mm was suspected to be too small to cause a detectable change in the boundary layer instabilities. When the perturbation was created off the centerline of the model, a clear and significant change was seen for the blunt nosetip, but not for the sharp nosetip.

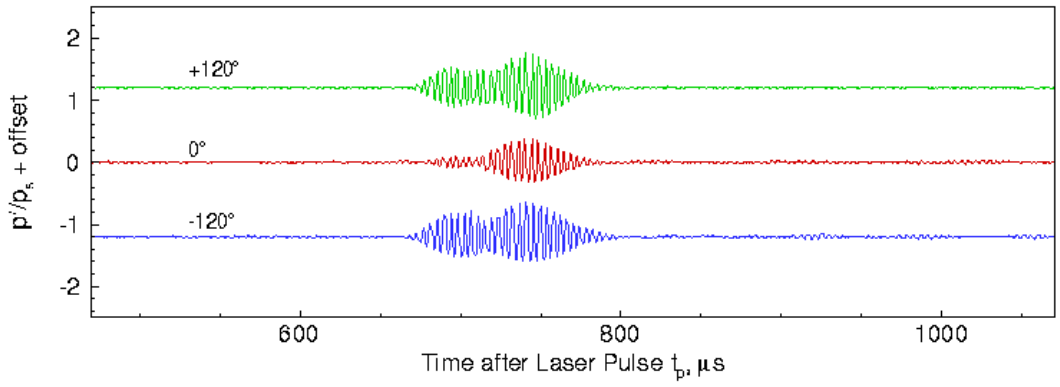

(a) $x = 332$ mm.

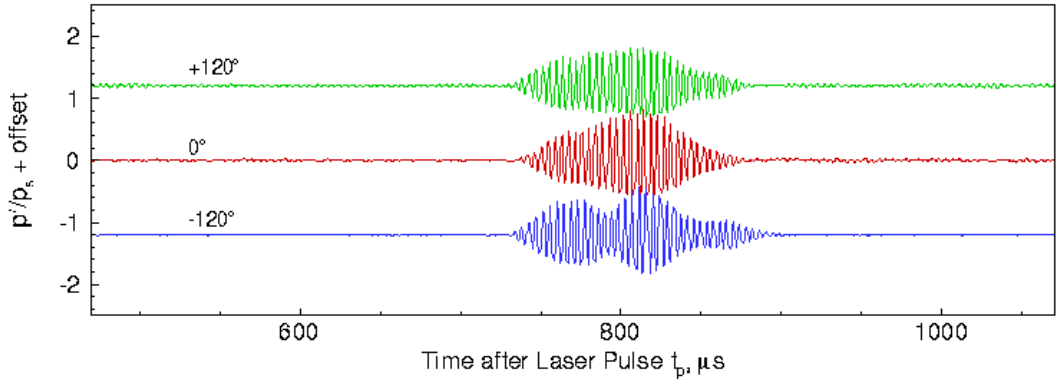

(b) $x = 382$ mm.

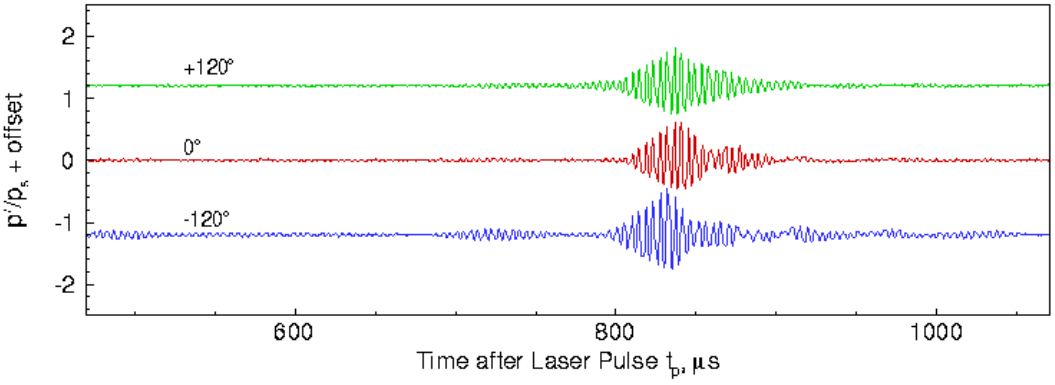

(c) $x = 434$ mm.

Figure 8.38. Time traces from azimuthal arrays of the effect of a laser perturbation for $r_n = 0.16$ mm. Perturbation aligned to cone centerline. Run 19-07: $p_0 = 535.8$ kPa, $T_0 = 424.1$ K, $Re/m = 5.92 \times 10^6$/m.

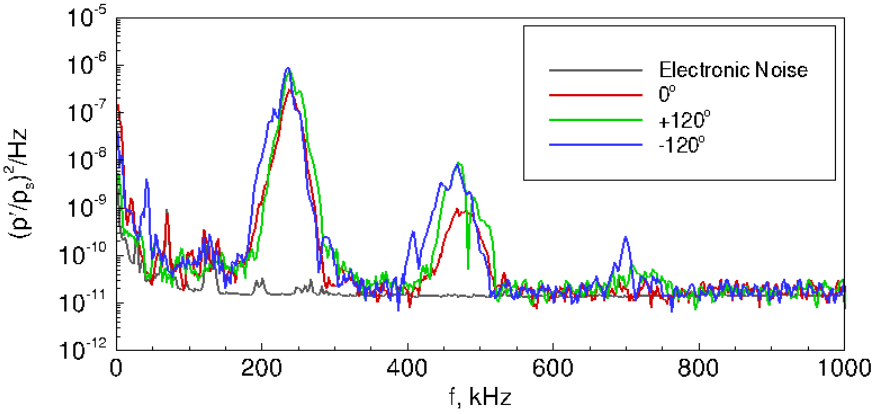

(a) $x = 332$ mm.

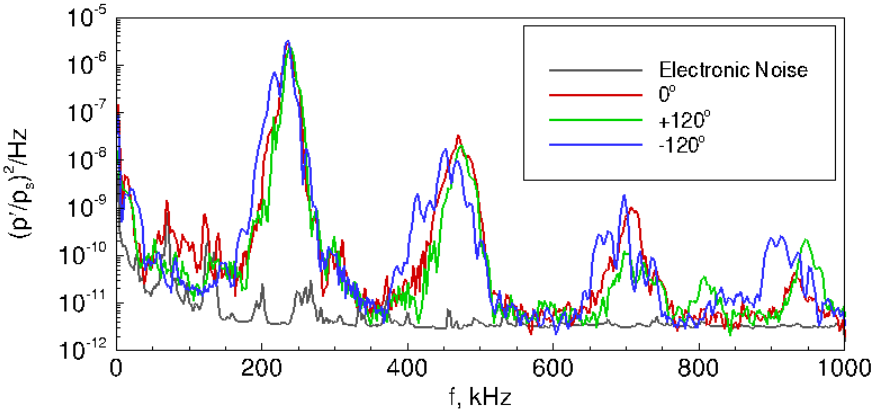

(b) $x = 382$ mm.

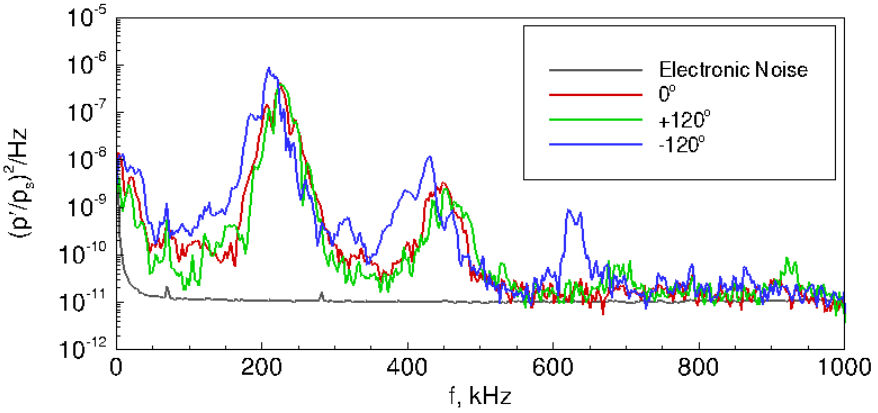

(c) $x = 434$ mm.

Figure 8.39. Spectra from azimuthal arrays for $r_n = 0.16$ mm. Perturbation aligned to cone centerline. Run 19-07: $p_0 = 535.8$ kPa, $T_0 = 424.1$ K, $Re/m = 5.92 \times 10^6$/m.

1.5-mm Offset from the Model Centerline

When the perturbation is aligned 1.5 mm off-axis toward the 0° ray, a visible effect is seen in the time traces for the blunt model in Figure 8.40. The sensor along the 0° ray measures a larger amplitude wave packet than the other sensors at $x = 403$ mm. A smaller but similar effect is observed at $x = 351$ mm. Figure 8.41 shows that the offset of the perturbation does not change the time trace nearly as much on the sharp nosetip. This lack of change implies that the blunt nosetip is more sensitive to the offset than the sharp nosetip. This implication is contrary to intuition. The sharp nosetip provides a much smaller target than the blunt nosetip, so the precision of the alignment to this nosetip should affect where the freestream laser perturbation interacts with the model's flow-field. However, it is possible that the wave packet in Figure 8.41 is saturated so that any small setup changes would not greatly change the amplitude of the wave packet.

The spectral content of the wave packet measurements are given by Figures 8.42 and 8.43. The spectral content of the wave packets on the blunt model at $x = 351$ and 403 mm shows a larger second mode and larger harmonic amplitudes at 0° than in the other two rays. The spectral content of the wave packets on the sharp model does not show much difference between the three azimuthal sensor locations. The spectral content of the wave packets on the sharp model consist of much larger harmonics than the blunt model. The RMS amplitudes of the wave packets on the sharp model are almost an order of magnitude larger than on the blunt model, except at the most aft azimuthal array.

Similar data were acquired when the freestream perturbation was aligned with a 1.5 mm offset from the cone centerline toward the +120° ray. Figure 8.44 shows that the wave packet on the $+120h^{\circ}$ ray on the blunt model has a larger amplitude than the wave packet on the other rays until $x = 403$ mm. At $x = 403$ mm, the amplitudes are similar, perhaps because of nonlinear saturation or breakdown. The response of the wave packet on the sharp model remains fairly axisymmetric, as shown in Figure 8.45.

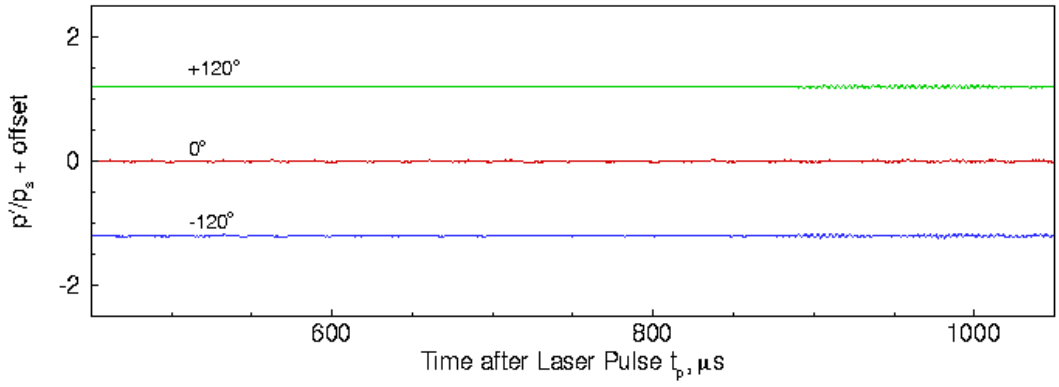

(a) $x = 302$ mm.

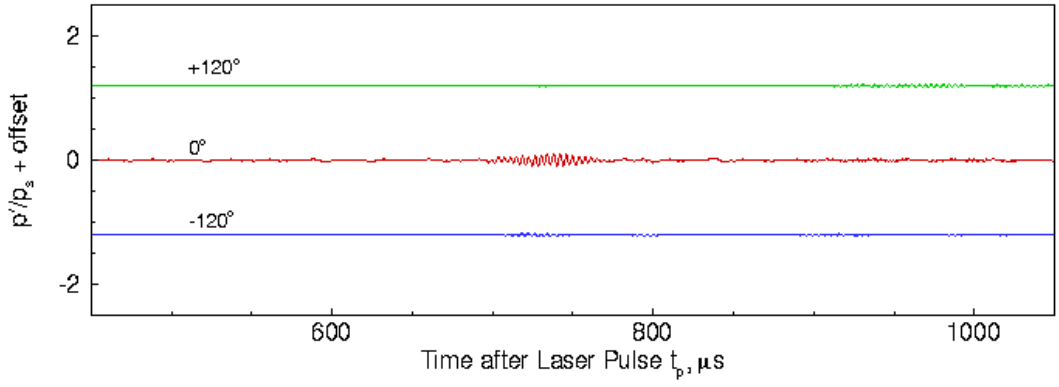

(b) $x = 351$ mm.

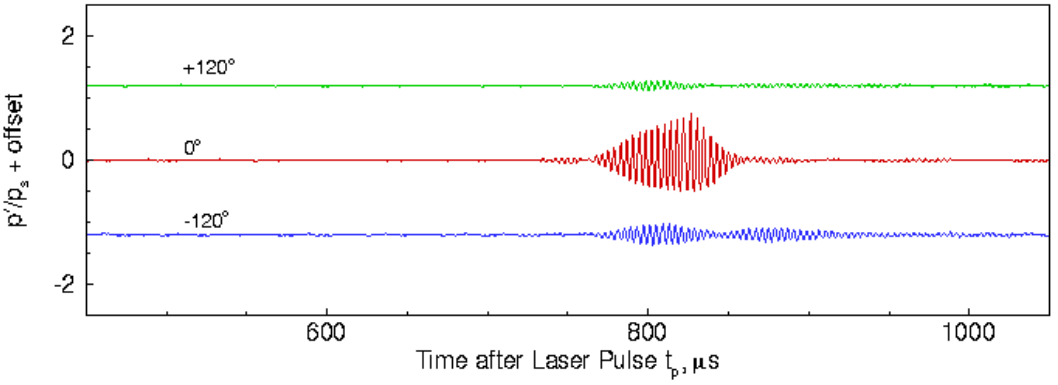

(c) $x = 403$ mm.

Figure 8.40. Time traces from azimuthal arrays of the effect of a laser perturbation for $r_n = 1$ mm. Perturbation generated 1.5 mm closer to 0° ray. Run 19-11: $p_0 = 734.6$ kPa, $T_0 = 429.9$ K, $Re/m = 7.93 \times 10^6$/m.

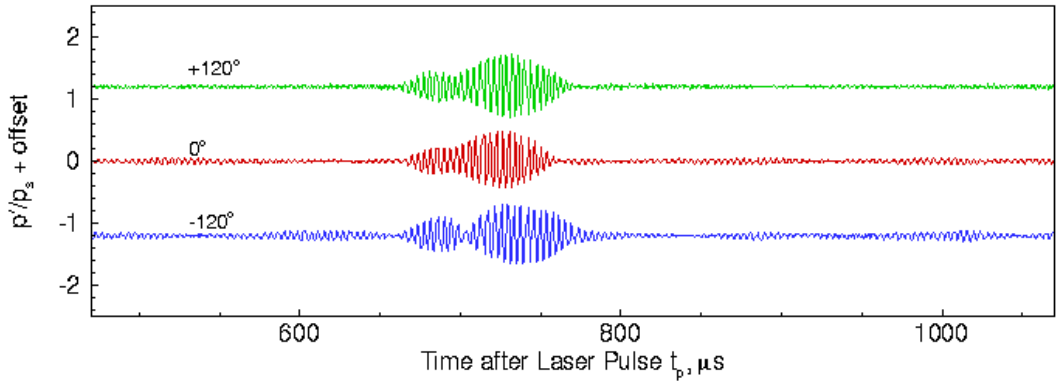

(a) $x = 332$ mm.

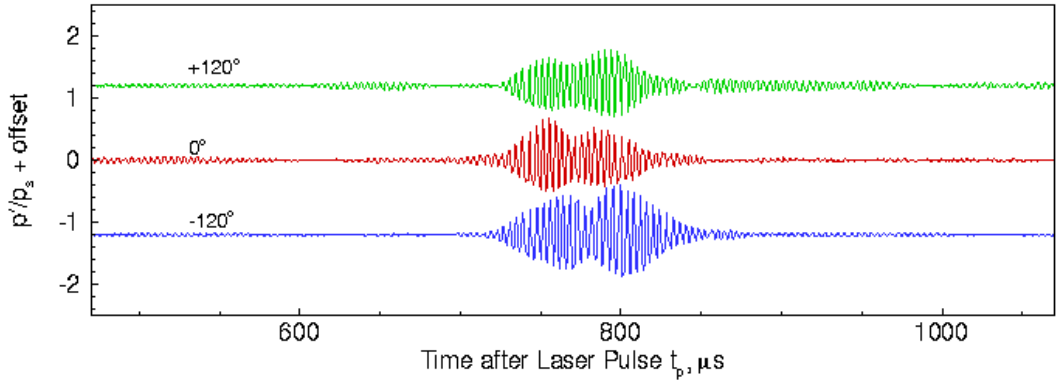

(b) $x = 382$ mm.

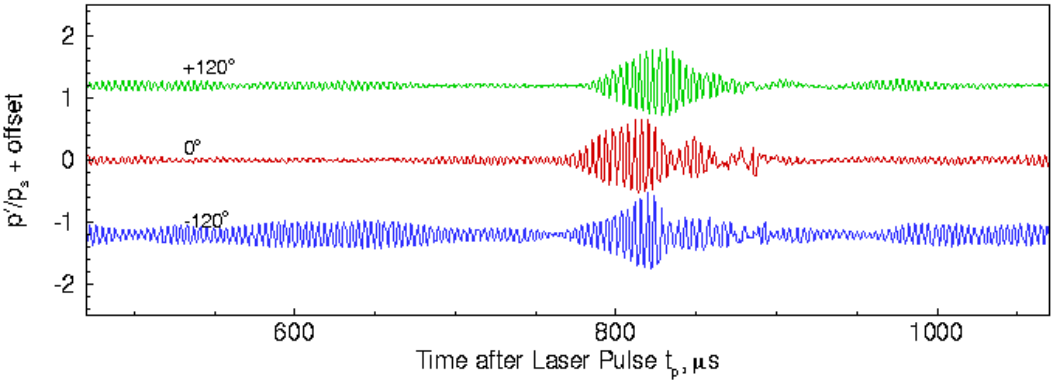

(c) $x = 434$ mm.

Figure 8.41. Time traces from azimuthal arrays of the effect of a laser perturbation for $r_n = 0.16$ mm. Perturbation generated 1.5 mm closer to 0° ray. Run 19-09: $p_0 = 586.4$ kPa, $T_0 = 427.3$ K, $Re/m = 6.40 \times 10^6$/m.

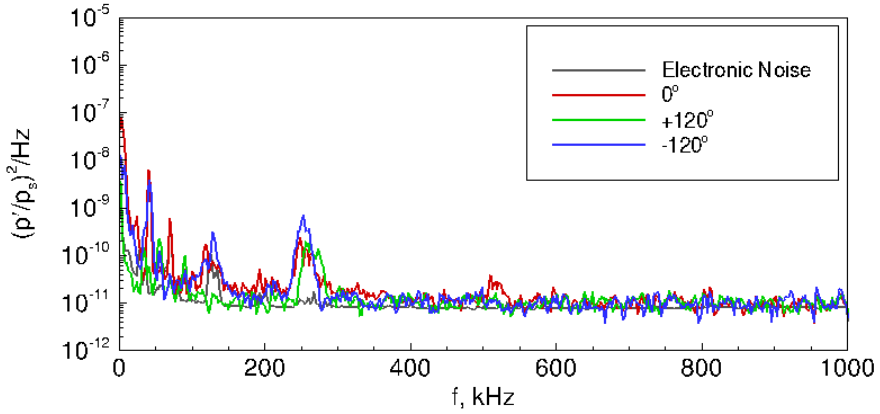

(a) $x = 302$ mm.

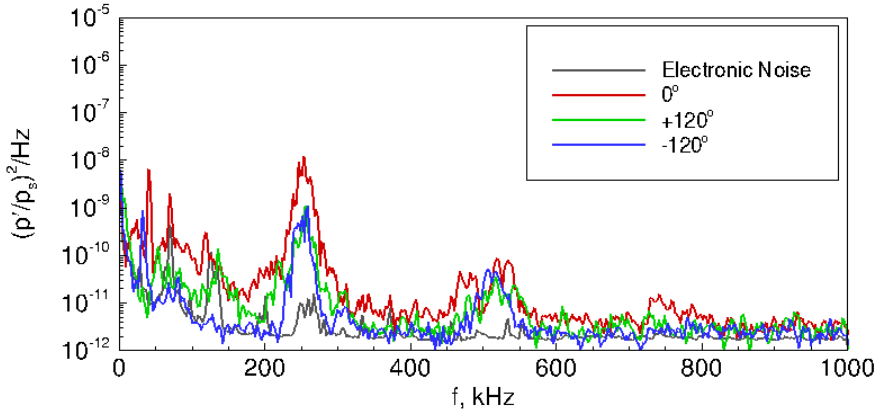

(b) $x = 351$ mm.

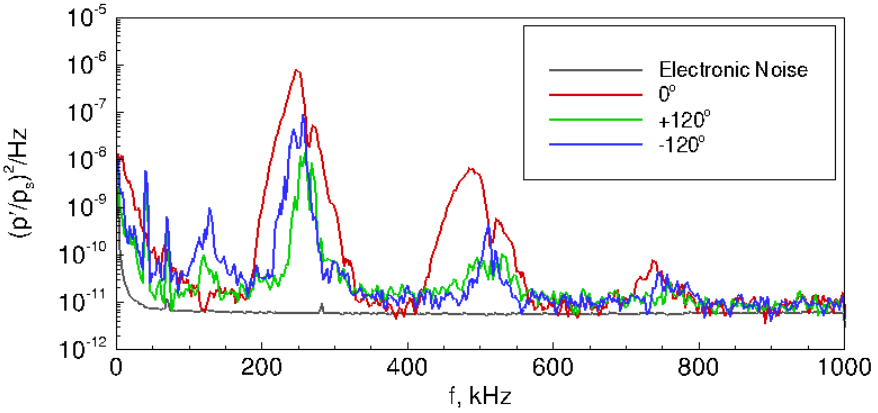

(c) $x = 403$ mm.

Figure 8.42. Spectral from azimuthal sensors for $r_n = 1$ mm. Perturbation generated 1.5 mm closer to 0° ray. Run 19-11: $p_0 = 734.6$ kPa, $T_0 = 429.9$ K, $Re/m = 7.93 \times 10^6$/m.

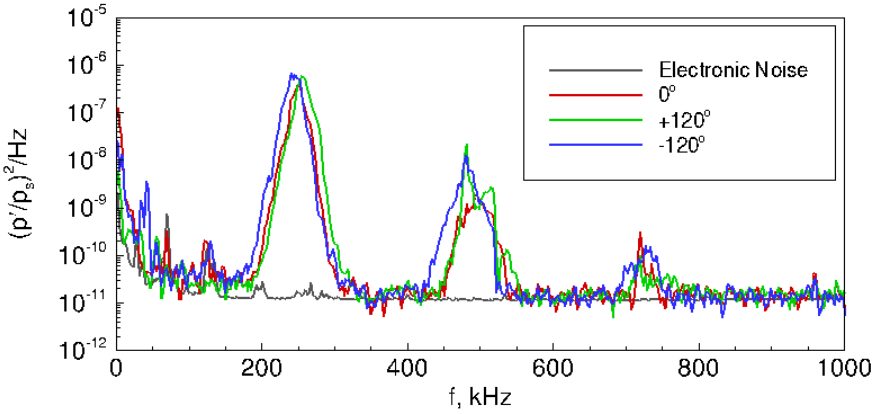

(a) $x = 332$ mm.

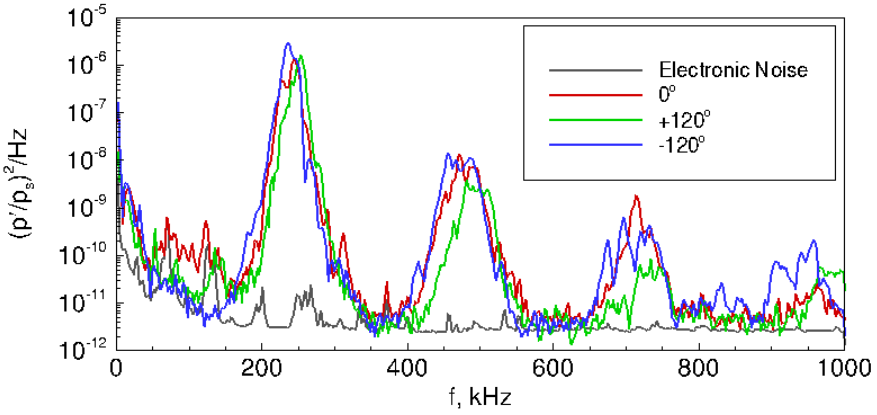

(b) $x = 382$ mm.

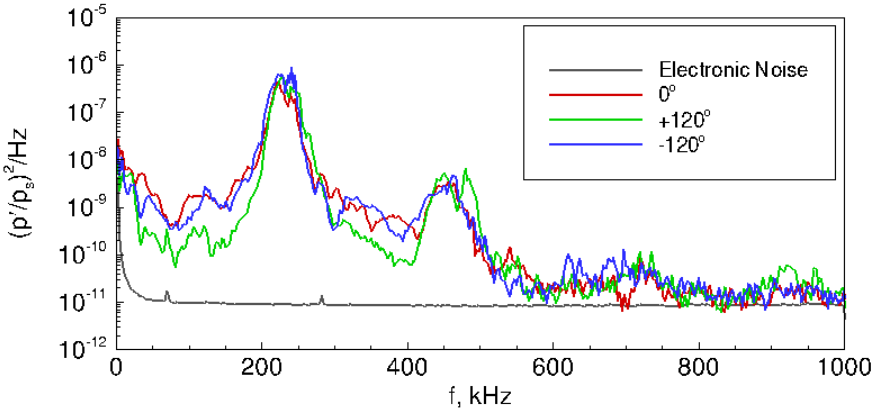

(c) $x = 434$ mm.

Figure 8.43. Spectra from azimuthal sensors for $r_n = 0.16$ mm. Perturbation generated 1.5 mm closer to 0° ray. Run 19-09: $p_0 = 586.4$ kPa, $T_0 = 427.3$ K, $Re/m = 6.40 \times 10^6$/m.

The spectra for the wave packet on the blunt model in Figure 8.46 show transitional and turbulent flow over the +120° ray at axial stations of $x = 351$ mm and 403 mm, respectively. There is a possible shift in the peak frequency for the +120° ray on the sharp model, but otherwise, the spectra for the sharp model in Figure 8.47 are fairly axisymmetric.

When the freestream perturbation is aligned to the −120° ray, however, the effect is different than for the other two alignments. The sensor on the −120° ray shows a transitional or turbulent wave packet in the blunt model (Figure 8.48). The sensor on the −120° ray has a slightly different shape on the sharp model (Figure 8.49), but otherwise still appears fairly axisymmetric. The power spectra for the wave packet on the blunt model in Figure 8.50 shows that the wave packet is transitional at $x = 302$ mm and turbulent at $x = 351$ mm and 403 mm. Figure 8.51 shows that the wave packet on the sharp model along the −120° ray is large and possibly transitional at $x = 332$ mm, transitional at $x = 382$ mm, and turbulent at $x = 434$ mm. This is a larger difference compared to the previous cases. The difference is not obvious in the time traces.

The 1.5-mm-offset freestream disturbance only appears to cause an effect on the sharp model when it is aligned toward the −120° ray. This effect may be caused by some defect or other asymmetry in the model near the −120° ray causing early transition on that side. The sharp nosetip is extremely slender and fragile. Thus, it is very difficult to fabricate it axisymmetrically and to maintain the straightness of the nosetip. The sharp nosetip was accidentally bent and re-straightened in the past, and it is possible that this has some effect on the model.

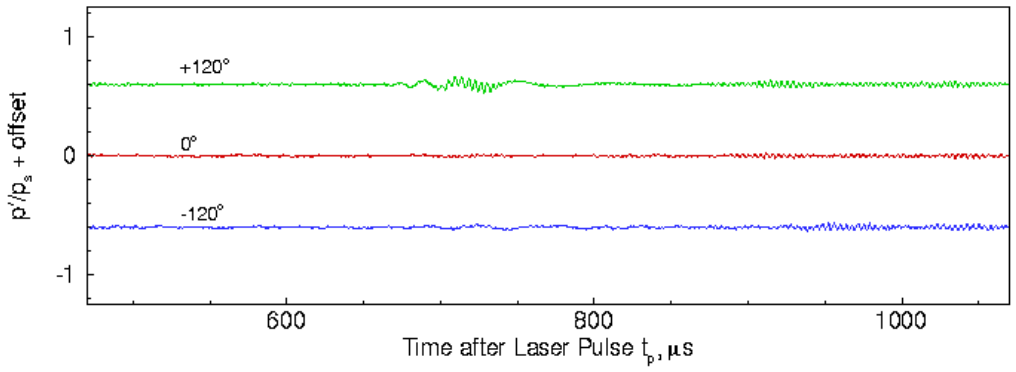

(a) $x = 302$ mm.

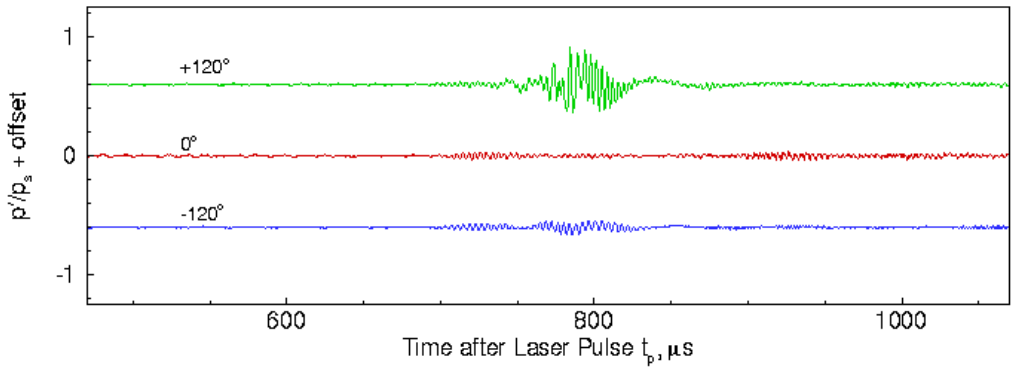

(b) $x = 351$ mm.

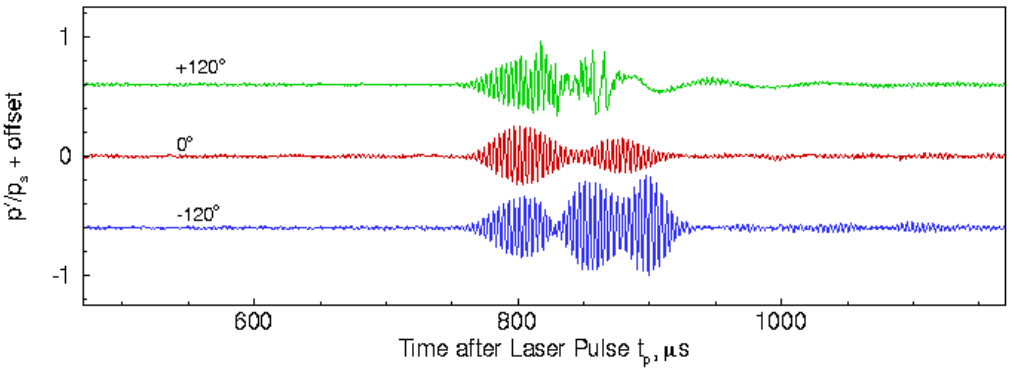

(c) $x = 403$ mm.

Figure 8.44. Time traces from azimuthal arrays of the effect of a laser perturbation for $r_n = 1$ mm. Perturbation generated 1.5 mm closer to +120° ray. Run 19-15: $p_0 = 744.6$ kPa, $T_0 = 429.7$ K, $Re/m = 8.05 \times 10^6$/m.

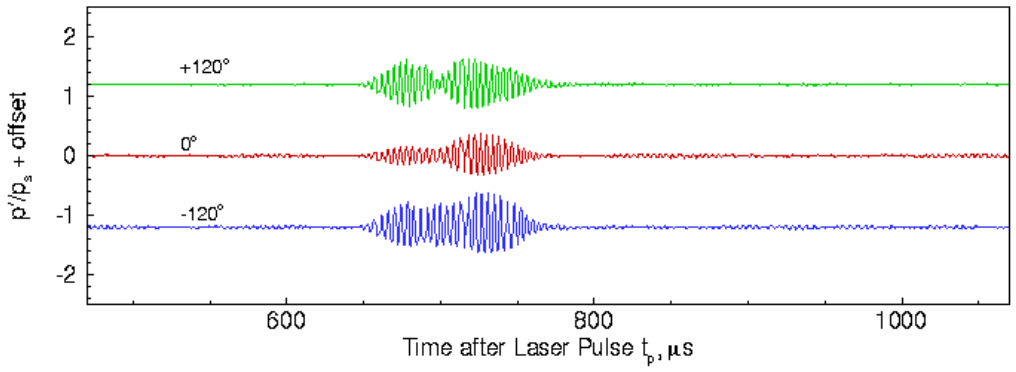

(a) $x = 332$ mm.

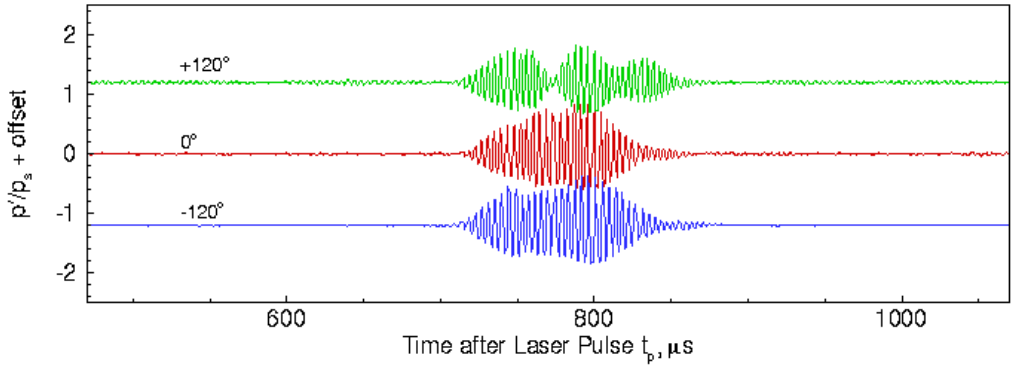

(b) $x = 382$ mm.

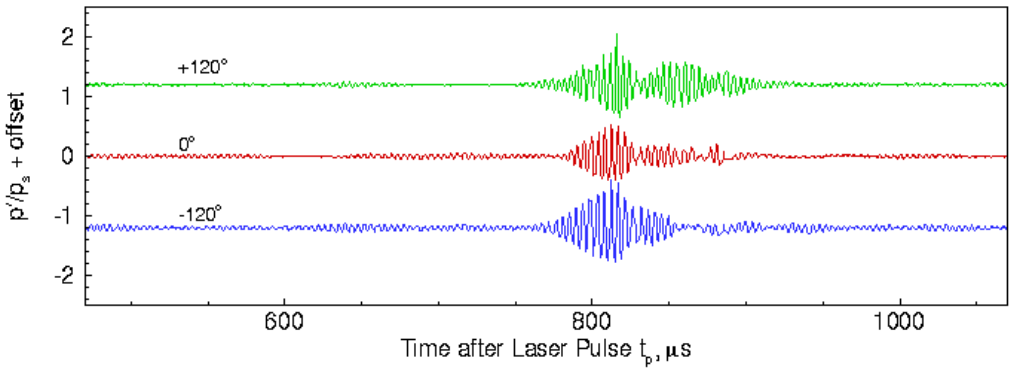

(c) $x = 434$ mm.

Figure 8.45. Time traces from azimuthal arrays of the effect of a laser perturbation for $r_n = 0.16$ mm. Perturbation generated 1.5 mm closer to +120° ray. Run 19-14: $p_0 = 536.1$ kPa, $T_0 = 430.2$ K, $Re/m = 5.78 \times 10^6$/m.

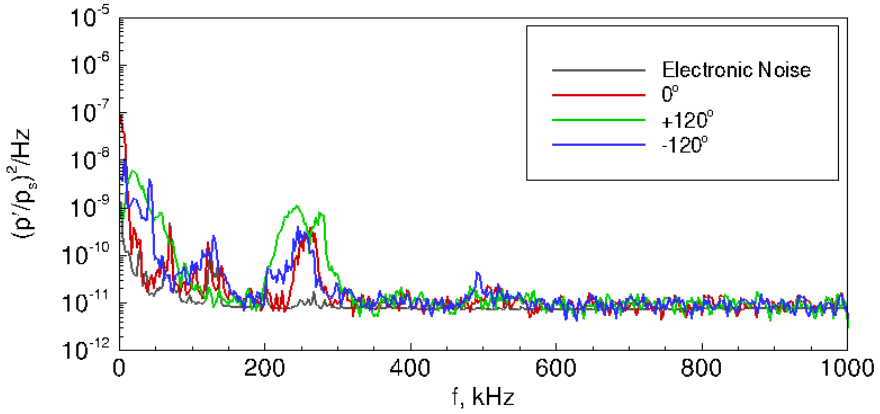

(a) $x = 302$ mm.

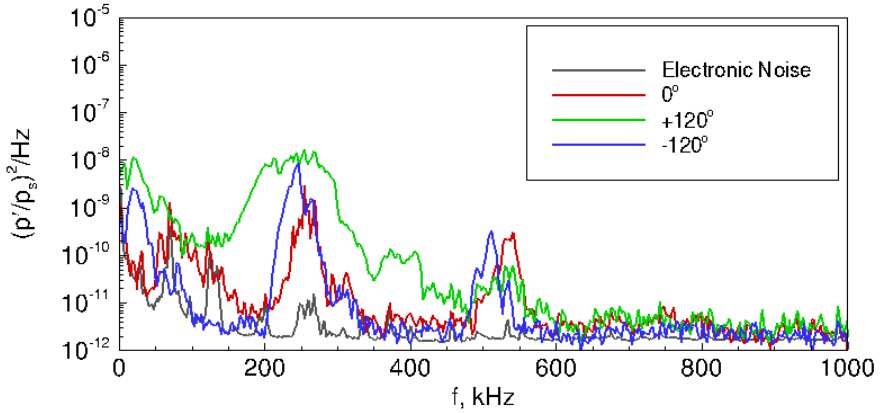

(b) $x = 351$ mm.

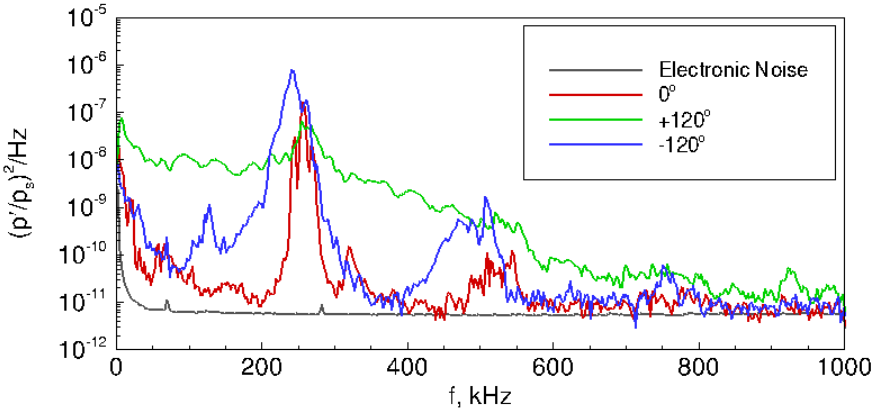

(c) $x = 403$ mm.

Figure 8.46. Spectra from azimuthal sensors for $r_n = 1$ mm. Perturbation generated 1.5 mm closer to +120° ray. Run 19-15: $p_0 = 744.6$ kPa, $T_0 = 429.7$ K, $Re/m = 8.05 \times 10^6$/m.

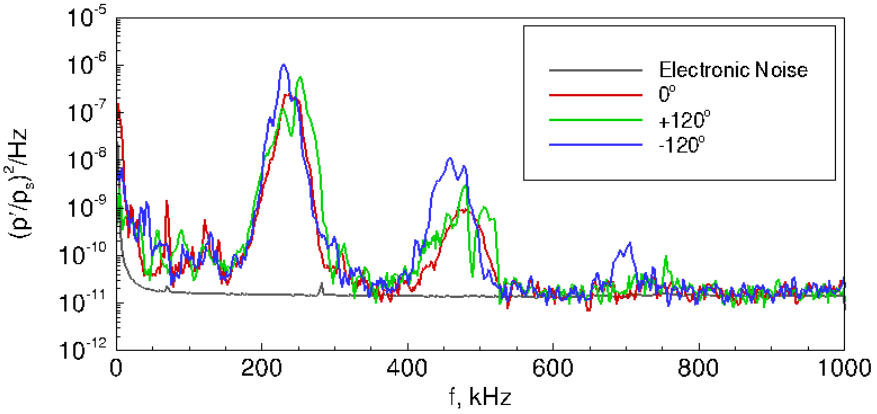

(a) $x = 332$ mm.

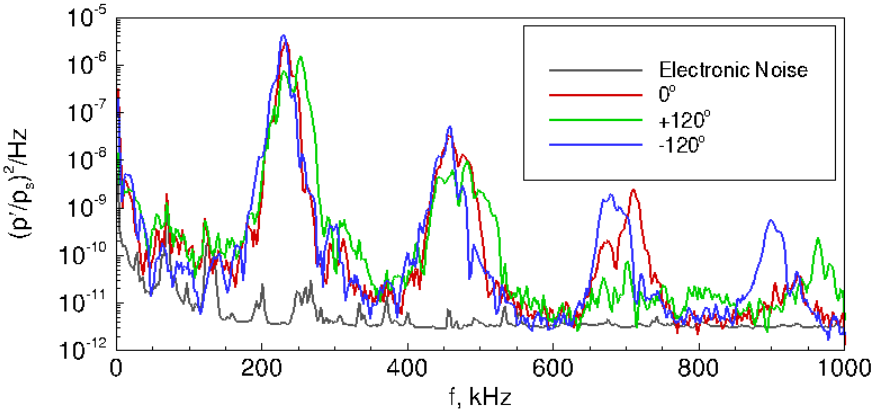

(b) $x = 382$ mm.

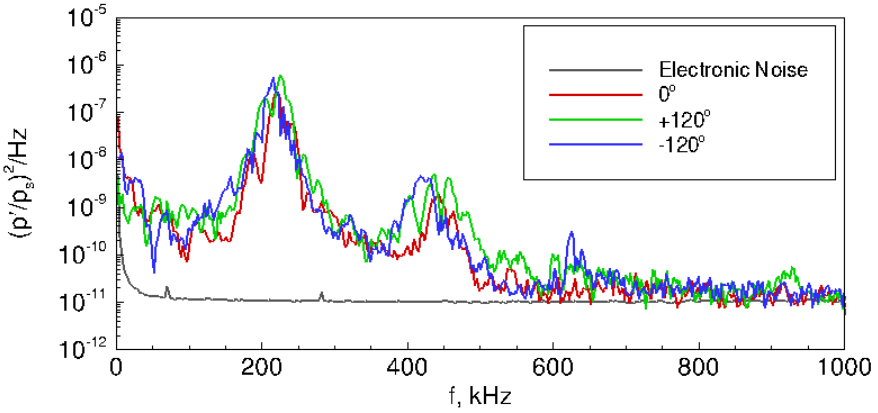

(c) $x = 434$ mm.

Figure 8.47. Spectra from azimuthal sensors for $r_n = 0.16$ mm. Perturbation generated 1.5 mm closer to +120° ray. Run 19-14: $p_0 = 536.1$ kPa, $T_0 = 430.2$ K, $Re/m = 5.78 \times 10^6$/m.

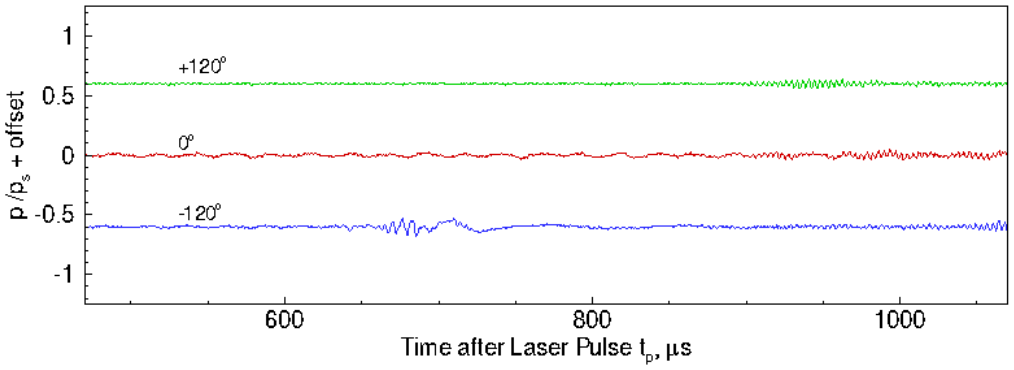

(a) $x = 302$ mm.

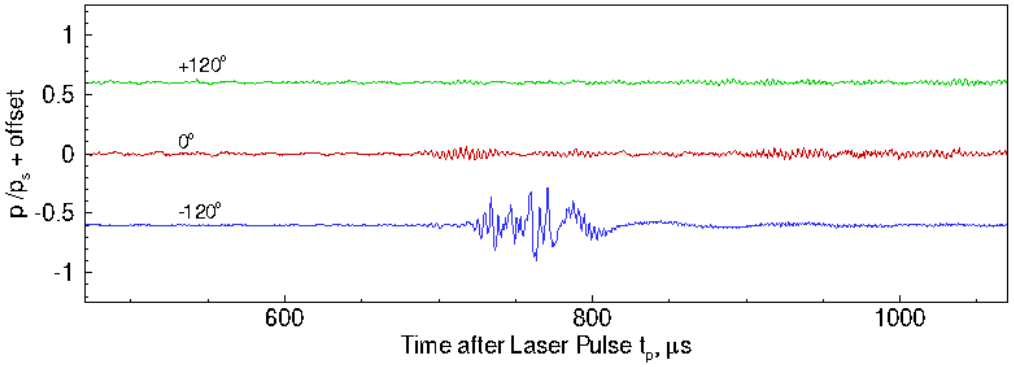

(b) $x = 351$ mm.

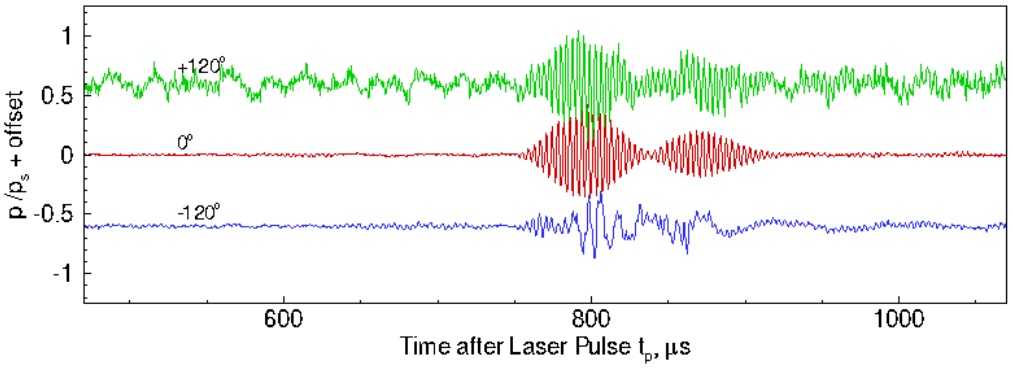

(c) $x = 403$ mm.

Figure 8.48. Time traces from azimuthal arrays of the effect of a laser perturbation for $r_n = 1$ mm. Perturbation generated 1.5 mm closer to $-120°$ ray. Run 19-17: $p_0 = 743.9$ kPa, $T_0 = 430.7$ K, $Re/m = 8.01 \times 10^6$/m.

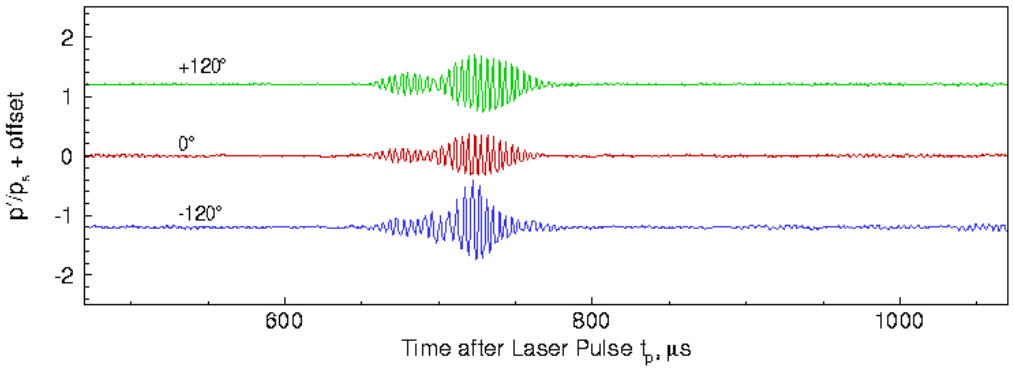

(a) $x = 332$ mm.

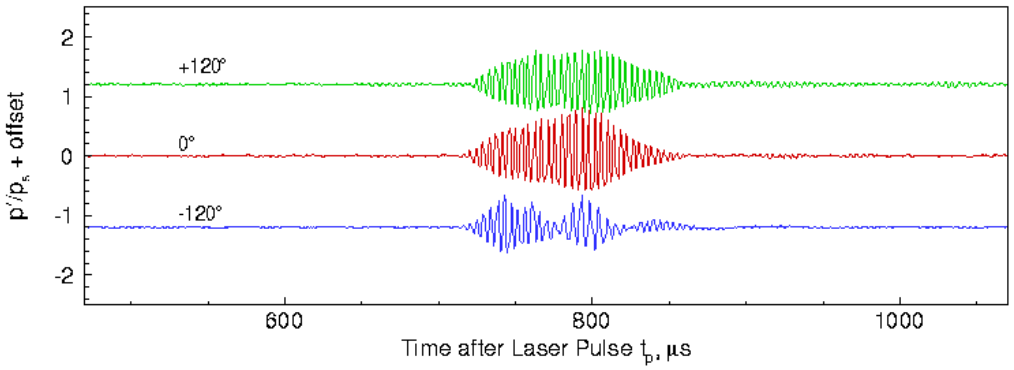

(b) $x = 382$ mm.

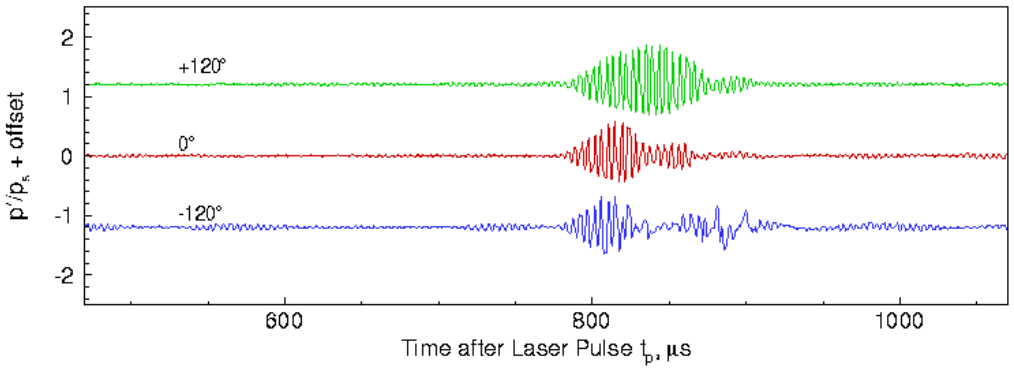

(c) $x = 434$ mm.

Figure 8.49. Time traces from azimuthal arrays of the effect of a laser perturbation for $r_n = 0.16$ mm. Perturbation generated 1.5 mm closer to $-120°$ ray. Run 19-20: $p_0 = 531.6$ kPa, $T_0 = 425.4$ K, $Re/m = 5.85 \times 10^6$/m.

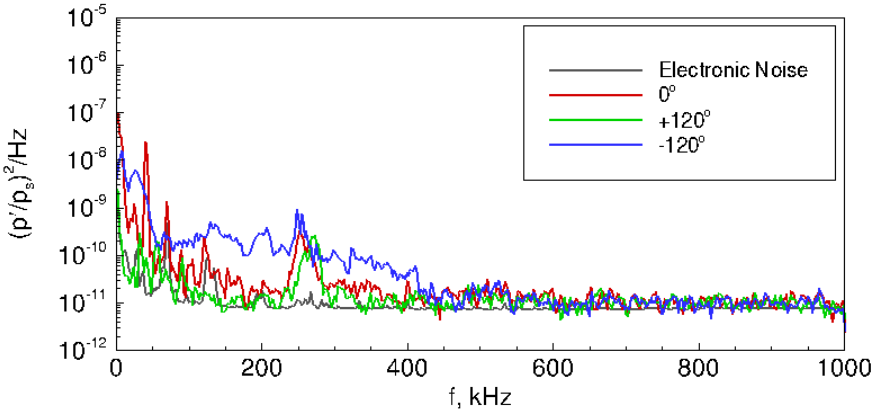

(a) $x = 302$ mm.

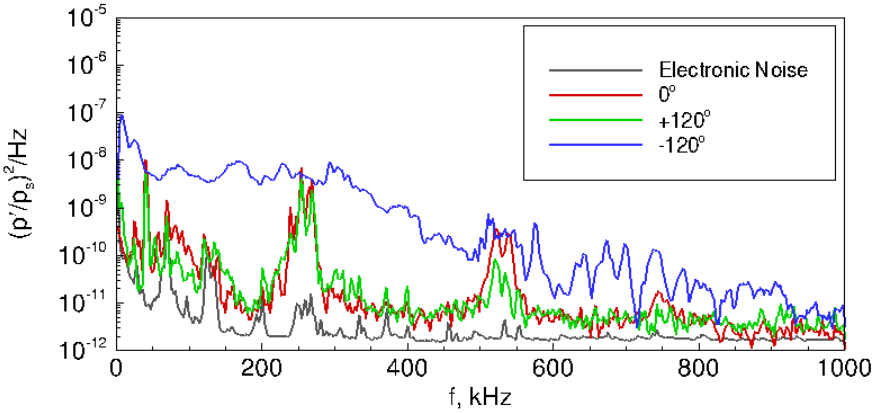

(b) $x = 351$ mm.

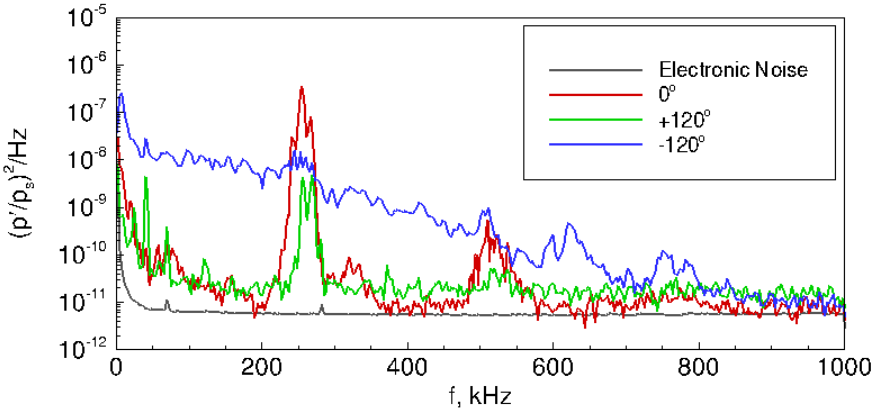

(c) $x = 403$ mm.

Figure 8.50. Spectra from azimuthal sensors for $r_n = 1$ mm. Perturbation generated 1.5 mm closer to $-120°$ ray. Run 19-17: $p_0 = 743.9$ kPa, $T_0 = 430.7$ K, $Re/m = 8.01 \times 10^6$/m.

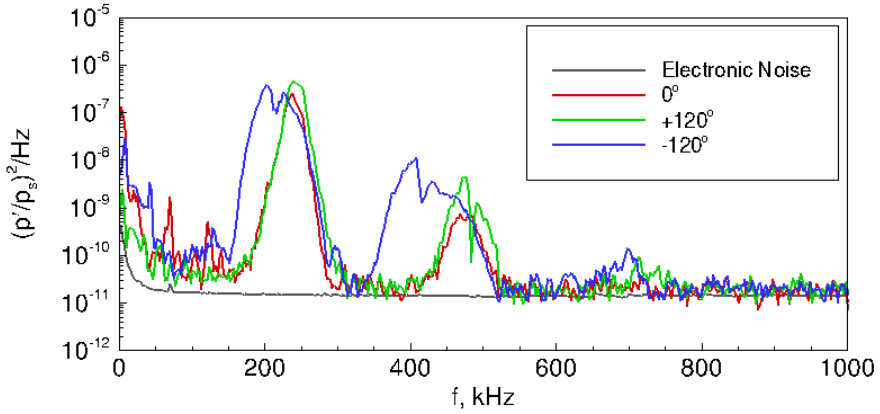

(a) $x = 332$ mm.

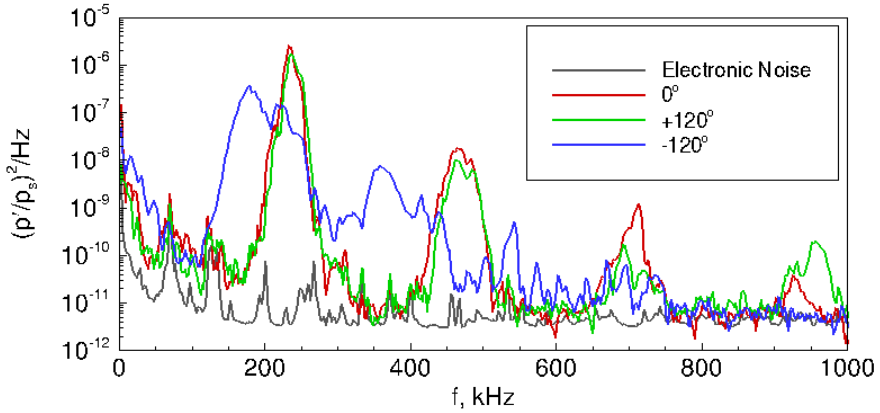

(b) $x = 382$ mm.

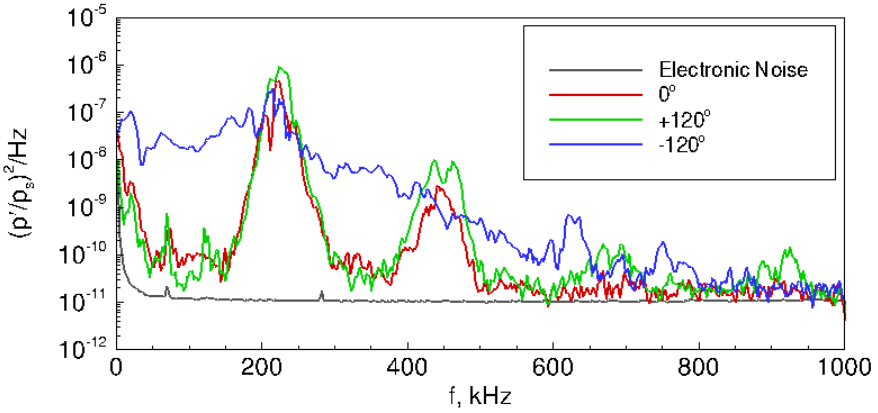

(c) $x = 434$ mm.

Figure 8.51. Spectra from azimuthal sensors for $r_n = 0.16$ mm. Perturbation generated 1.5 mm closer to $-120°$ ray. Run 19-20: $p_0 = 531.6$ kPa, $T_0 = 425.4$ K, $Re/m = 5.85 \times 10^6$/m.

3.0-mm Offset from the Model Centerline

The freestream perturbation was also aligned to be offset 3.0 mm from the flared cone centerline, upstream of the model. The time traces for when the perturbation is aligned toward the 0° ray are shown in Figure 8.52 for the blunt nosetip and Figure 8.53 for the sharp nosetip. The blunt nosetip case shows a wave packet on the 0° ray that looks like a turbulent spot, which is different from the 1.5-mm-offset case. When the perturbation was only offset by 1.5 mm from the cone centerline, the wave packet on the 0° ray was more like a large-amplitude wave packet. Figure 8.53 shows that the time traces of the wave packet on the sharp model is still fairly axisymmetric.

The power spectra of the data shown in Figures 8.52 and 8.53 are shown in Figure 8.54 and 8.55, respectively. Figure 8.54 shows that the wave packet on the blunt model is at least transitional along the 0° ray at $x = 302$ mm. The broadband frequency content on the 0° ray is large at all axial stations. The wave packet acts similarly to the on-axis case along the other two rays at ±120°. Figure 8.55 shows the spectra for the sharp nosetip. On the 0° ray, the wave packet does not appear to be turbulent. However, the spectra show that the 0° wave packet at $x = 434$ mm may be transitional. The spectra at the other azimuthal stations do not show much difference when compared to each other.

Similar effects are seen when the perturbation is created toward the other sensor rays at ±120° from the main ray. Figure 8.56 shows the time traces when the perturbation is offset toward the +120° ray on the blunt model and Figure 8.57 shows the corresponding spectra. Figure 8.58 shows the time traces when the perturbation is offset toward the +120° ray on the sharp model and Figure 8.59 shows the corresponding spectra. Figure 8.60 shows the time traces when the perturbation is offset toward the −120° ray on the blunt model and Figure 8.61 shows the corresponding spectra. Figure 8.62 shows the time traces when the perturbation is offset toward the −120° ray on the sharp model and Figure 8.63 shows the corresponding spectra.

The alignment of the freestream perturbation does not appear to have much of an effect on the sharp model, except when it is aligned toward the -120° ray. When the perturbation is aligned toward the +120 or 0° rays on the sharp model, the wave packet exhibits symmetry around the azimuth of the cone. The spectra in Figure 8.63 (Run 19-39) show that the alignment of the perturbation toward the -120° ray produces a second-mode peak with a wider bandwidth on that ray than seen on the other rays. The second-mode peak spreads as the distance downstream is increased, and eventually, by $x = 434$ mm, the broadband frequency content starts to rise. Looking back to the 1.5-mm-offset alignment, Figure 8.51 (Run 19-20) shows similar spectra. The alignment of the perturbation toward the -120° ray produces a broader second-mode peak with a shifted peak frequency at $x = 332$ mm. The background frequency content rises until finally, at the most downstream station, there is a broadband increase in the frequency content and the wave packet breaks down by $x = 434$ mm. No adjustments were made to the model between each alignment configuration and no adjustments were made between nosetip changes for each alignment configuration. The order in which the nosetips were tested was also arbitrary. There may be some consistent asymmetry in the flow field or on the model itself near the -120° ray.

The data in these plots all show the same effect: for the blunt nosetip, the freestream laser perturbation generates a larger wave packet along the ray toward which it is aligned. The sharp model does not show the same effect when the perturbation is intentionally offset from the centerline. The laser perturbation generates a nonlinear wave packet on the sharp nosetip. Because the wave packet amplitude is already saturated, it does not show as significant a change in amplitude when the perturbation is aligned off-axis, except when the perturbation is aligned toward the -120° ray. There may be some small defect on the sharp nosetip near the -120° ray creating this discrepancy. Breakdown of this wave packet occurs earlier on the ray toward which the laser perturbation was aligned.

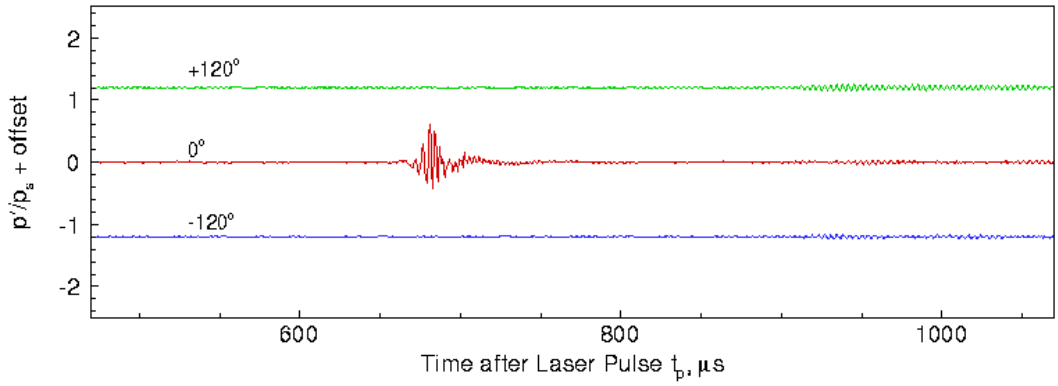

(a) $x = 302$ mm.

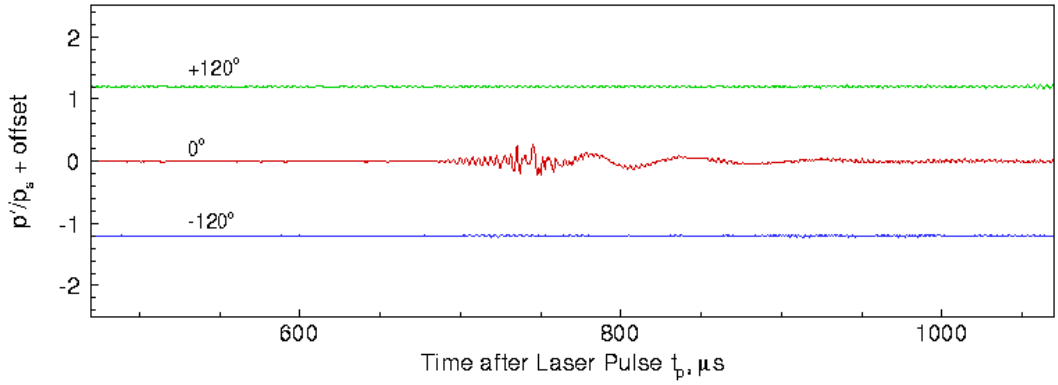

(b) $x = 351$ mm.

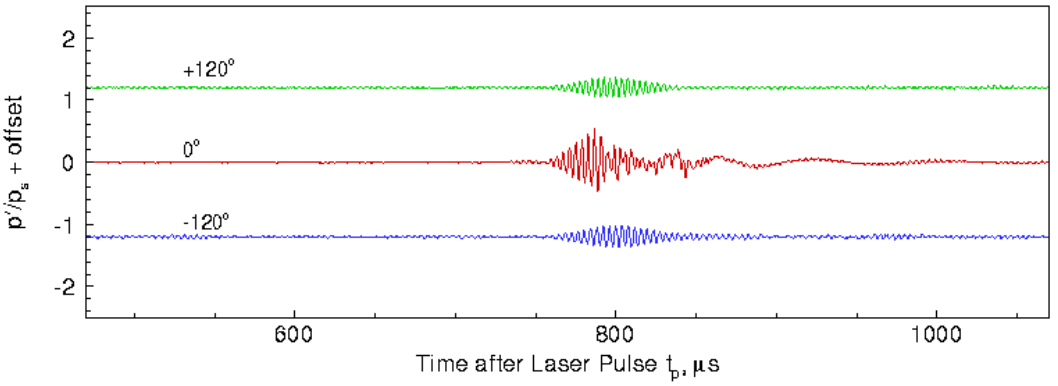

(c) $x = 403$ mm.

Figure 8.52. Time traces from azimuthal arrays of the effect of a laser perturbation for $r_n = 1$ mm. Perturbation generated 3 mm closer to 0° ray. Run 19-35: $p_0 = 749.9$ kPa, $T_0 = 431.5$ K, $Re/m = 8.05 \times 10^6$/m.

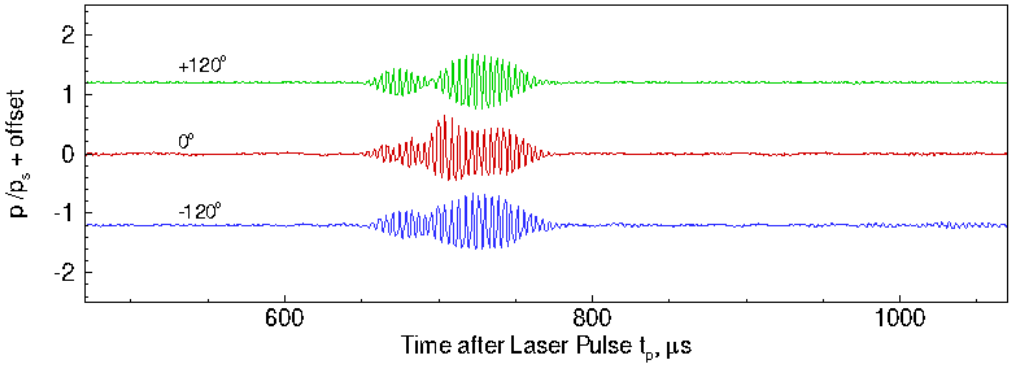

(a) $x = 332$ mm.

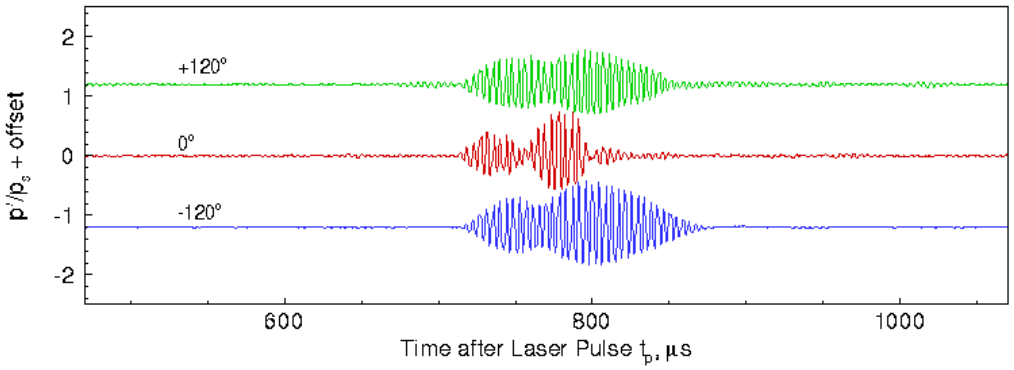

(b) $x = 382$ mm.

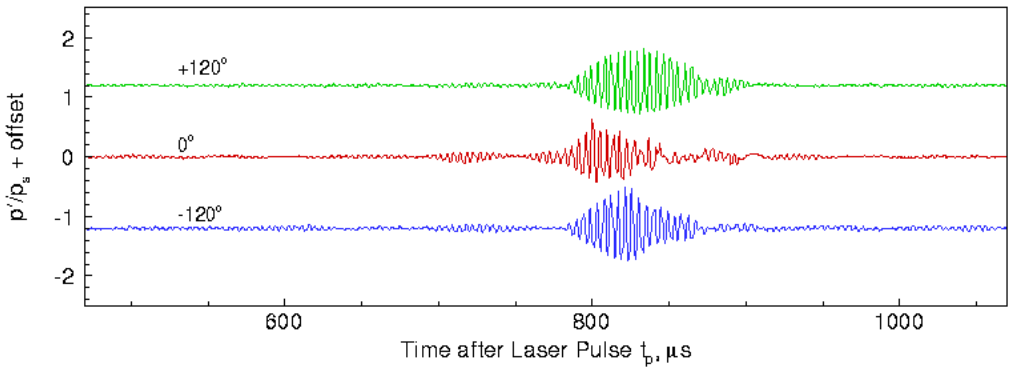

(c) $x = 434$ mm.

Figure 8.53. Time traces from azimuthal arrays of the effect of a laser perturbation for $r_n = 0.16$ mm. Perturbation generated 3 mm closer to 0° ray. Run 19-38: $p_0 = 533.9$ kPa, $T_0 = 427.5$ K, $Re/m = 5.82 \times 10^6$/m.

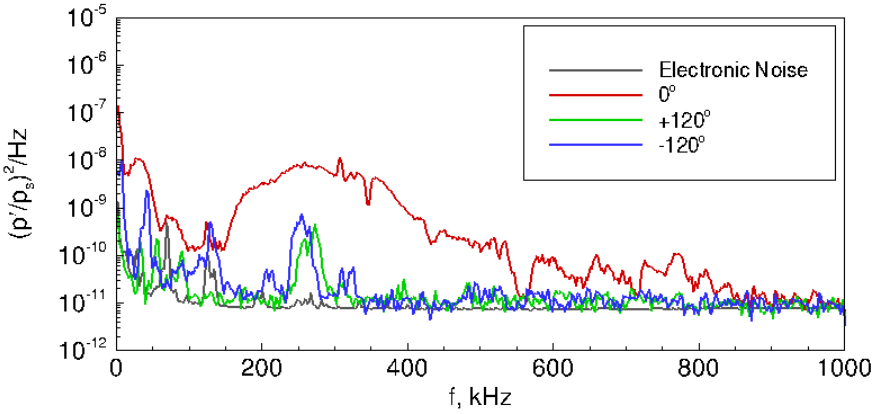

(a) $x = 302$ mm.

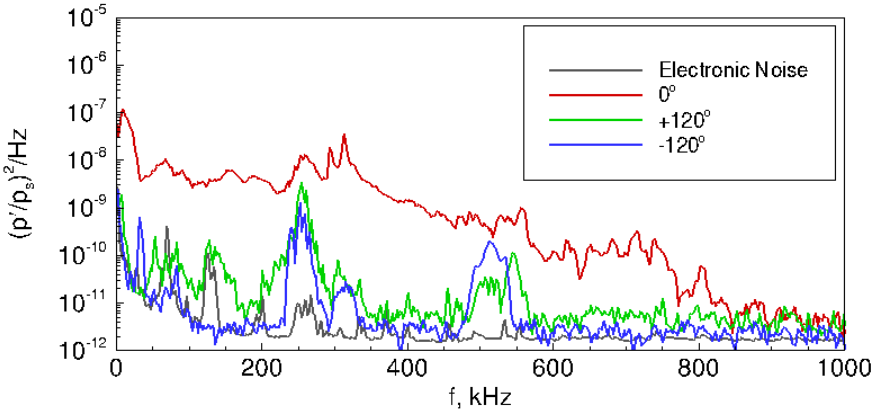

(b) $x = 351$ mm.

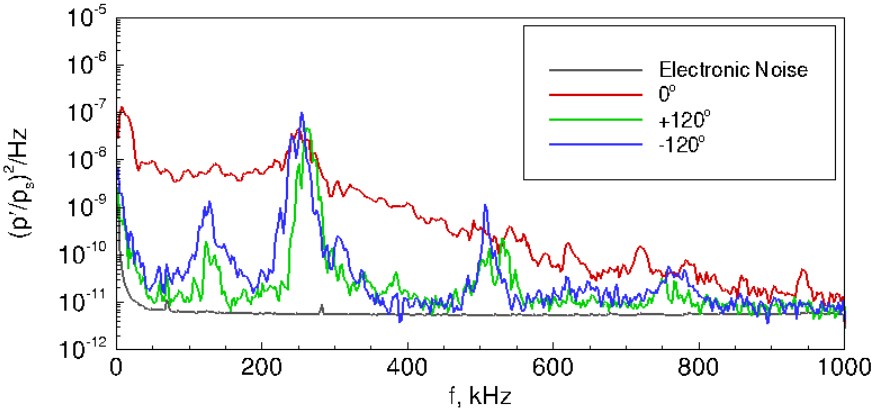

(c) $x = 403$ mm.

Figure 8.54. Spectra from azimuthal sensors for $r_n = 1$ mm. Perturbation generated 3 mm closer to 0° ray. Run 19-35: $p_0 = 749.9$ kPa, $T_0 = 431.5$ K, $Re/m = 8.05 \times 10^6$/m.

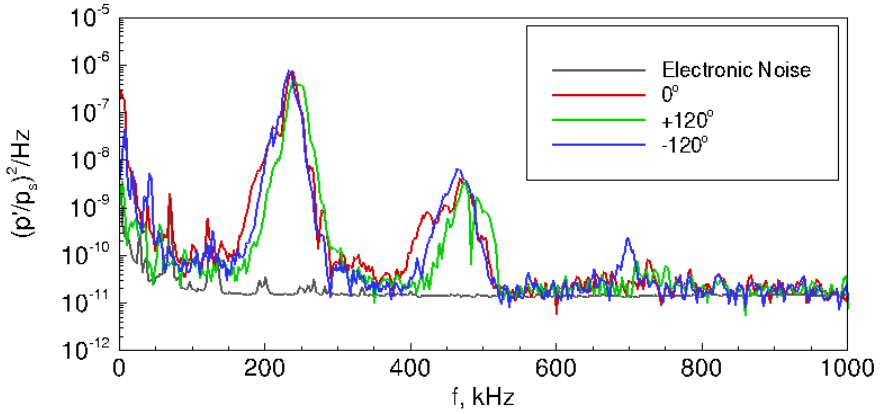

(a) $x = 332$ mm.

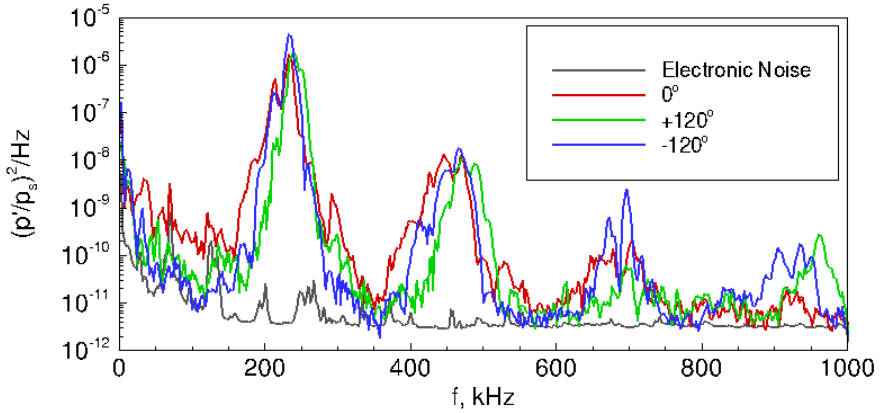

(b) $x = 382$ mm.

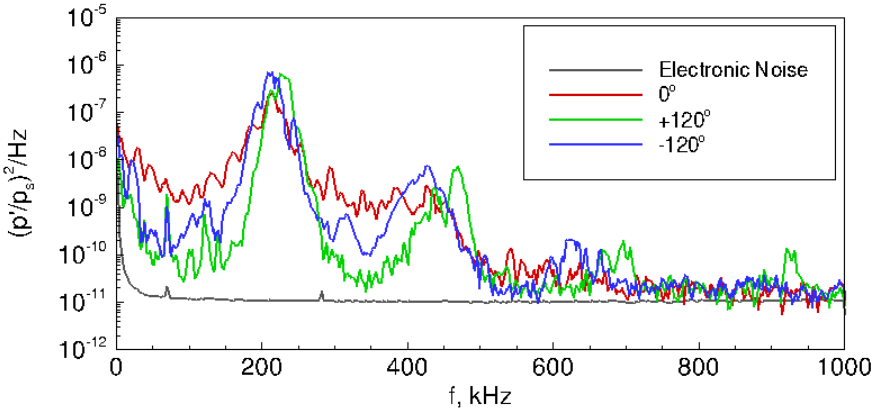

(c) $x = 434$ mm.

Figure 8.55. Spectra from azimuthal sensors for $r_n = 0.16$ mm. Perturbation generated 3 mm closer to 0° ray. Run 19-38: $p_0 = 533.9$ kPa, $T_0 = 427.5$ K, $Re/m = 5.82 \times 10^6$/m.

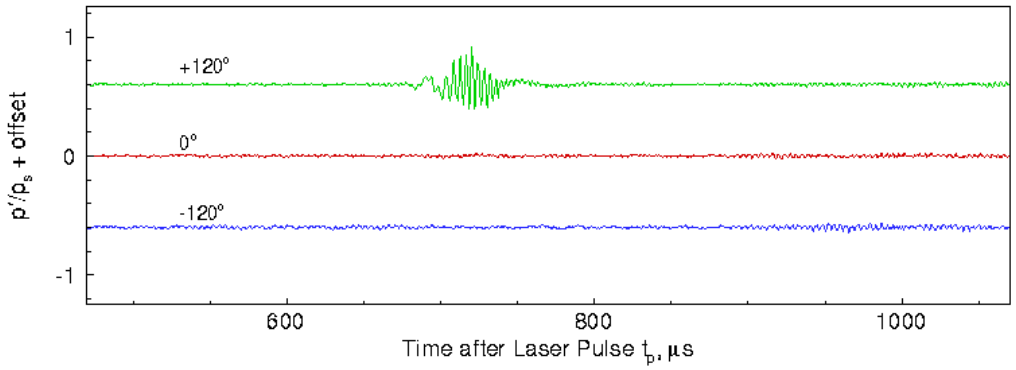

(a) $x = 302$ mm.

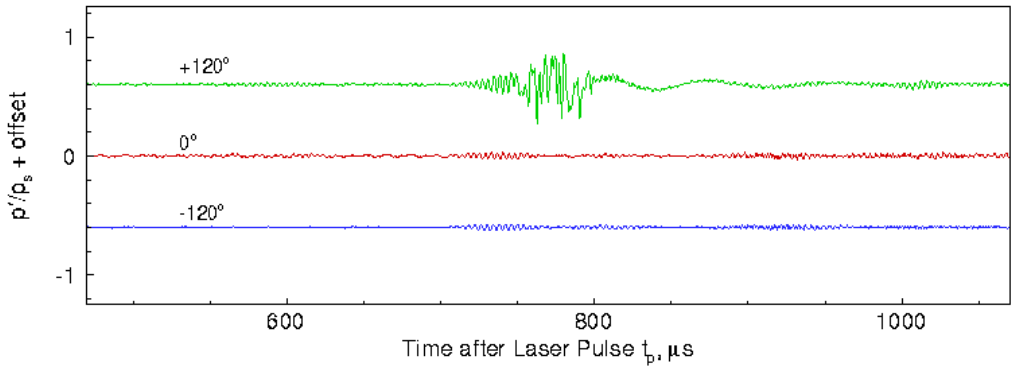

(b) $x = 351$ mm.

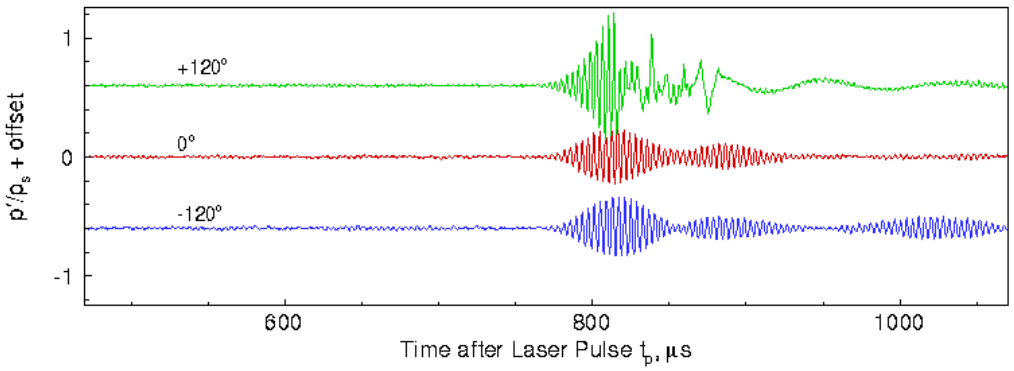

(c) $x = 403$ mm.

Figure 8.56. Time traces from azimuthal arrays of the effect of a laser perturbation for $r_n = 1$ mm. Perturbation generated 3 mm closer to +120° ray. Run 19-26: $p_0 = 744.2$ kPa, $T_0 = 429.4$ K, $Re/m = 8.05 \times 10^6$/m.

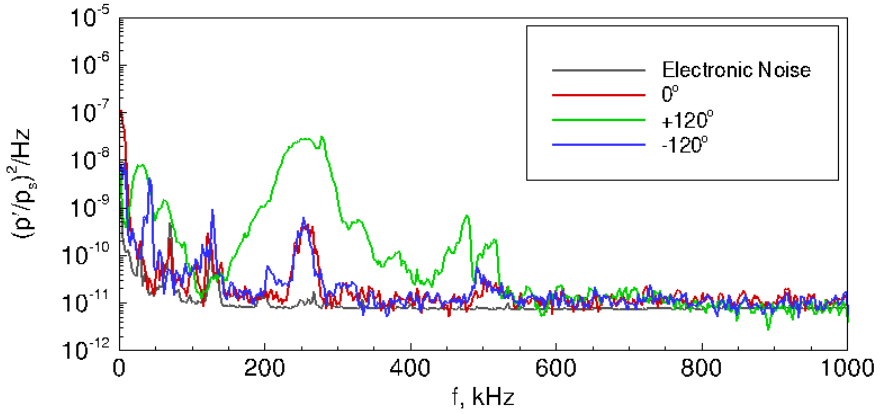

(a) $x = 302$ mm.

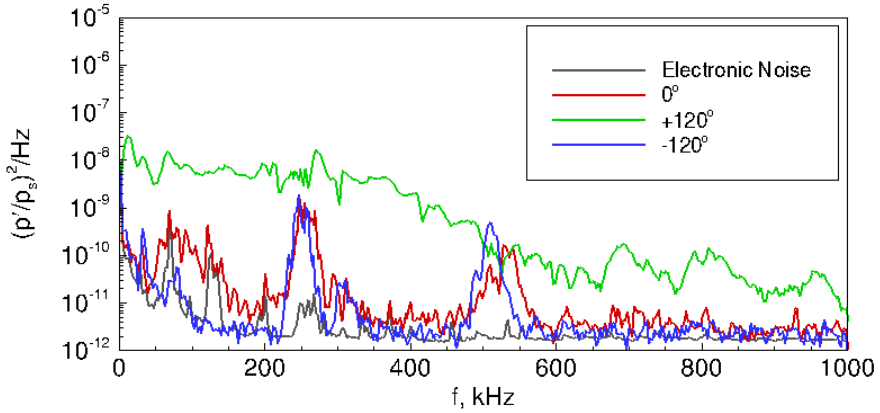

(b) $x = 351$ mm.

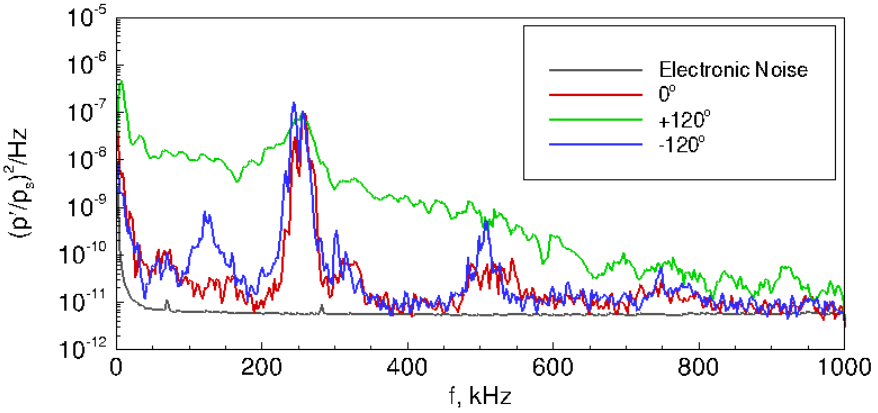

(c) $x = 403$ mm.

Figure 8.57. Spectra from azimuthal sensors for $r_n = 1$ mm. Perturbation generated 3 mm closer to +120° ray. Run 19-26: $p_0 = 744.2$ kPa, $T_0 = 429.4$ K, $Re/m = 8.05 \times 10^6$/m.

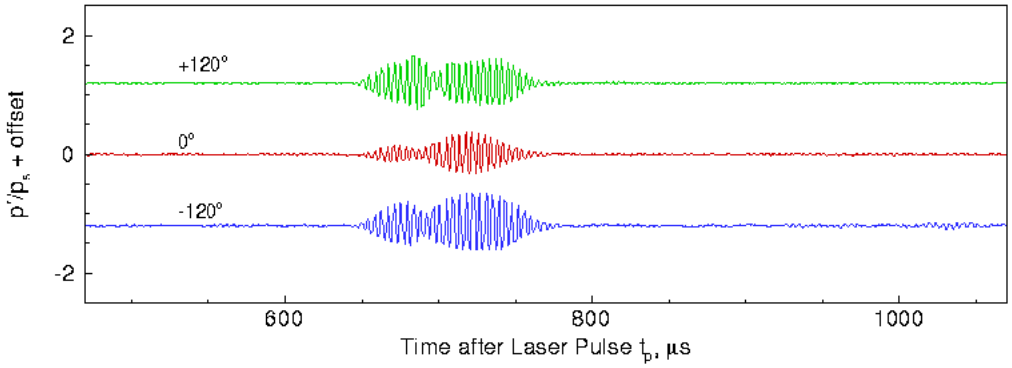

(a) $x = 332$ mm.

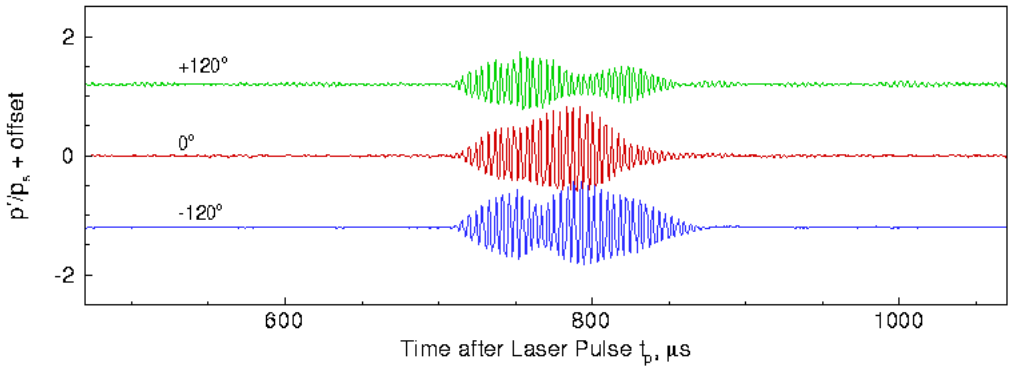

(b) $x = 382$ mm.

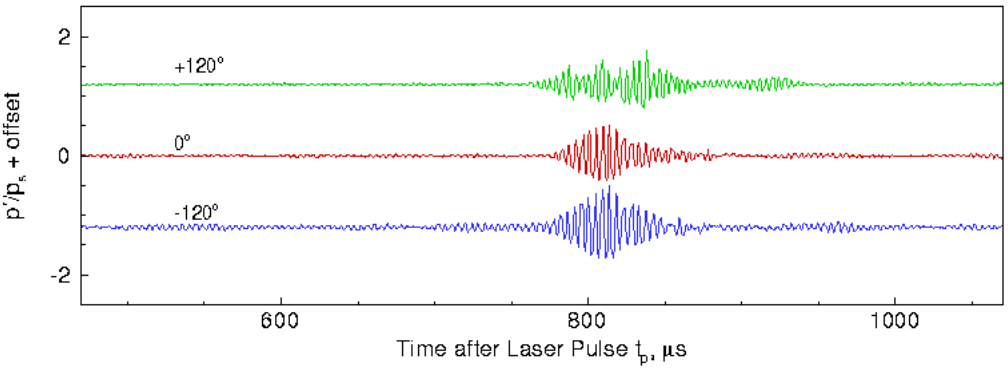

(c) $x = 434$ mm.

Figure 8.58. Time traces from azimuthal arrays of the effect of a laser perturbation for $r_n = 0.16$ mm. Perturbation generated 3 mm closer to +120° ray. Run 19-29: $p_0 = 536.9$ kPa, $T_0 = 424.5$ K, $Re/m = 5.92 \times 10^6$/m.

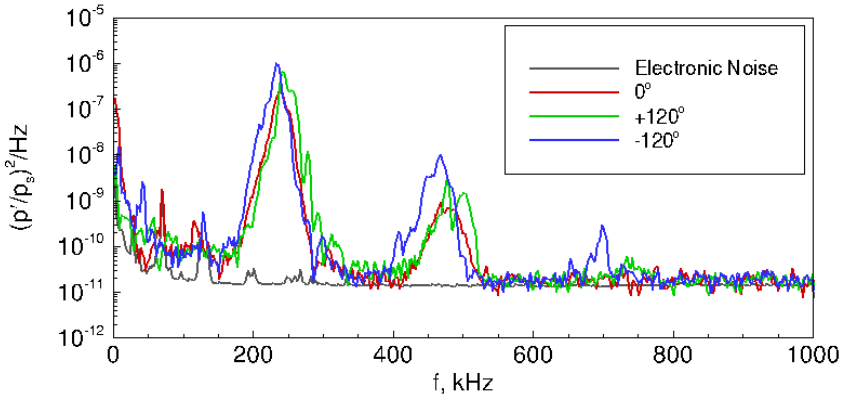

(a) $x = 332$ mm.

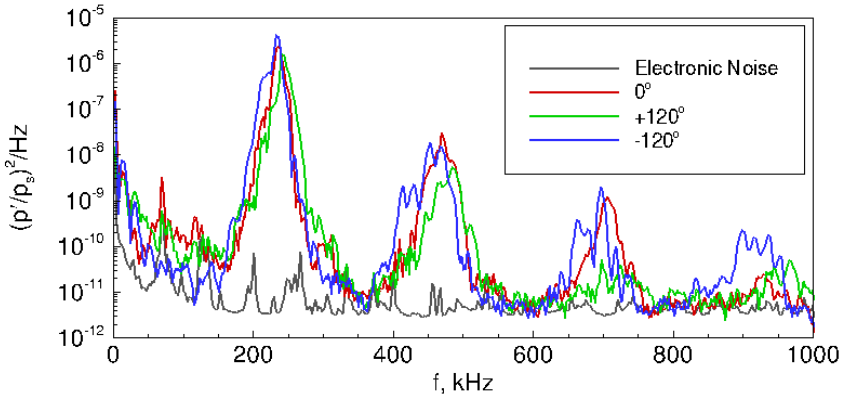

(b) $x = 382$ mm.

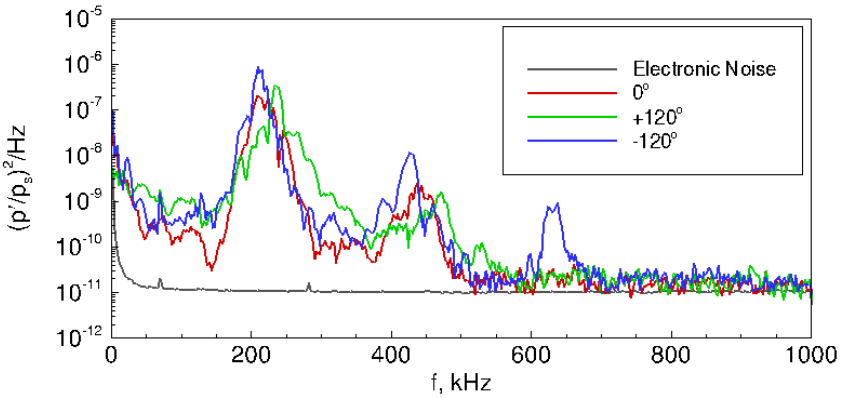

(c) $x = 434$ mm.

Figure 8.59. Spectra from azimuthal sensors for $r_n = 0.16$ mm. Perturbation generated 3 mm closer to +120° ray. Run 19-29: $p_0 = 536.9$ kPa, $T_0 = 424.5$ K, $Re/m = 5.92 \times 10^6$/m.

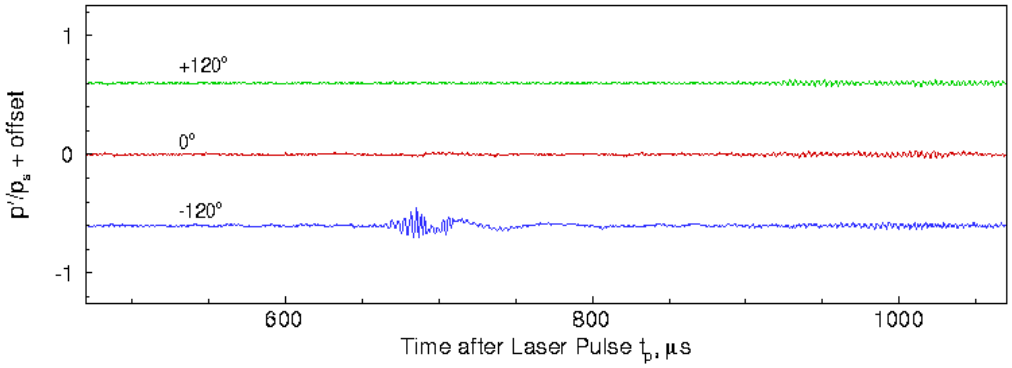

(a) $x = 302$ mm.

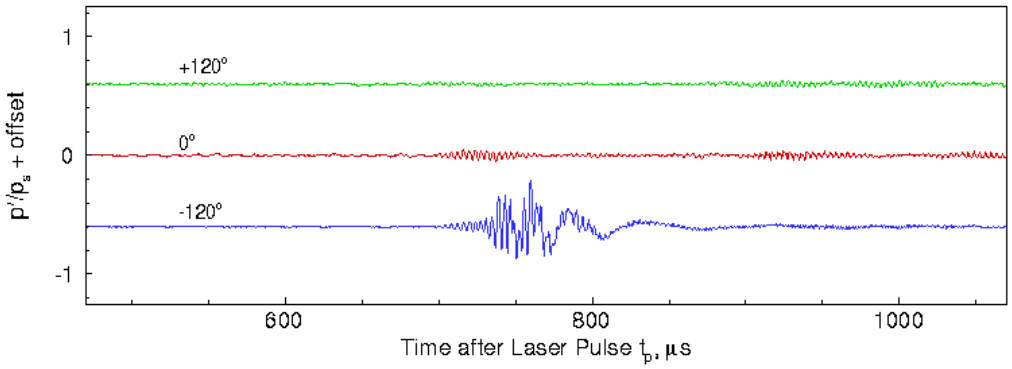

(b) $x = 351$ mm.

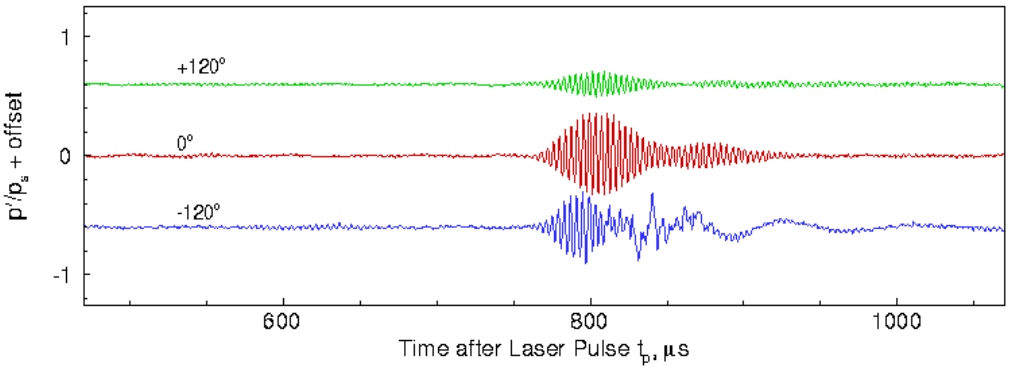

(c) $x = 403$ mm.

Figure 8.60. Time traces from azimuthal arrays of the effect of a laser perturbation for $r_n = 1$ mm. Perturbation generated 3 mm closer to $-120°$ ray. Run 19-41: $p_0 = 744.8$ kPa, $T_0 = 429.0$ K, $Re/m = 8.07 \times 10^6$/m.

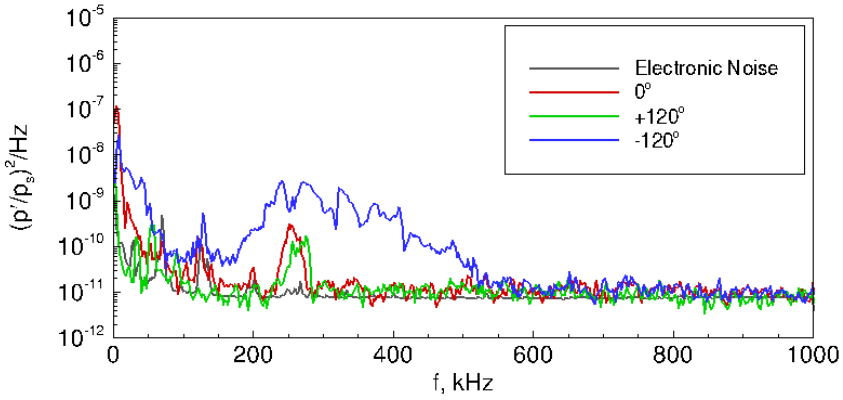

(a) $x = 302$ mm.

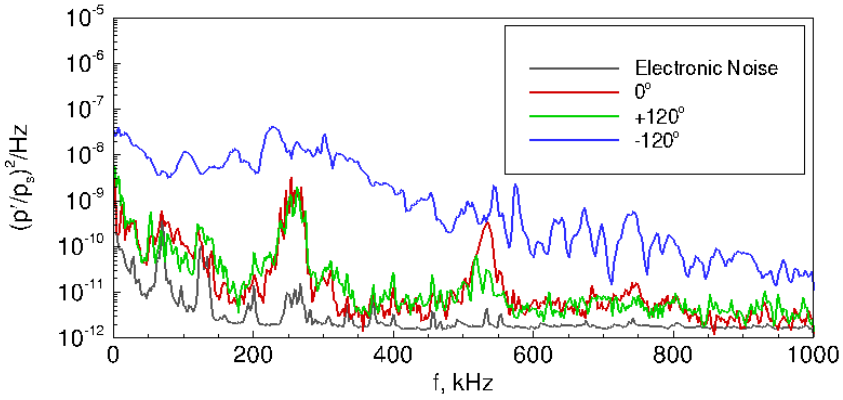

(b) $x = 351$ mm.

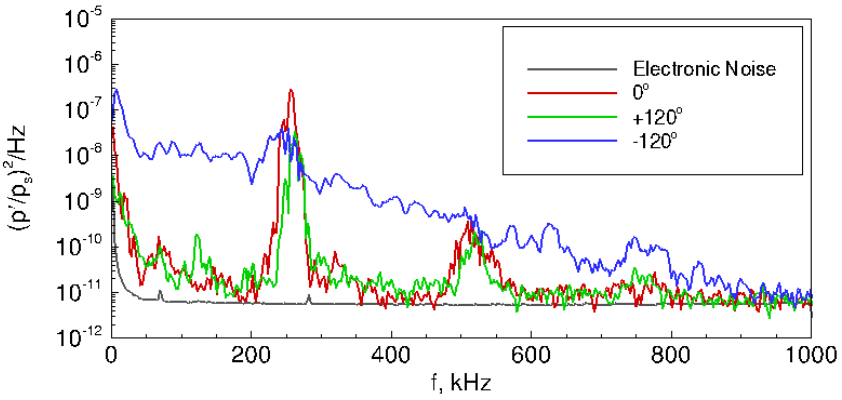

(c) $x = 403$ mm.

Figure 8.61. Spectra from azimuthal sensors for $r_n = 1$ mm. Perturbation generated 3 mm closer to $-120°$ ray. Run 19-41: $p_0 = 744.8$ kPa, $T_0 = 429.0$ K, $Re/m = 8.07 \times 10^6$/m.

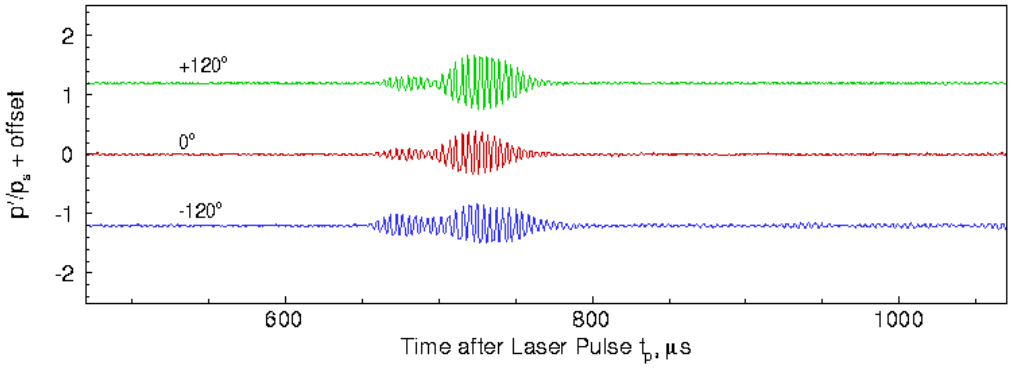

(a) $x = 332$ mm.

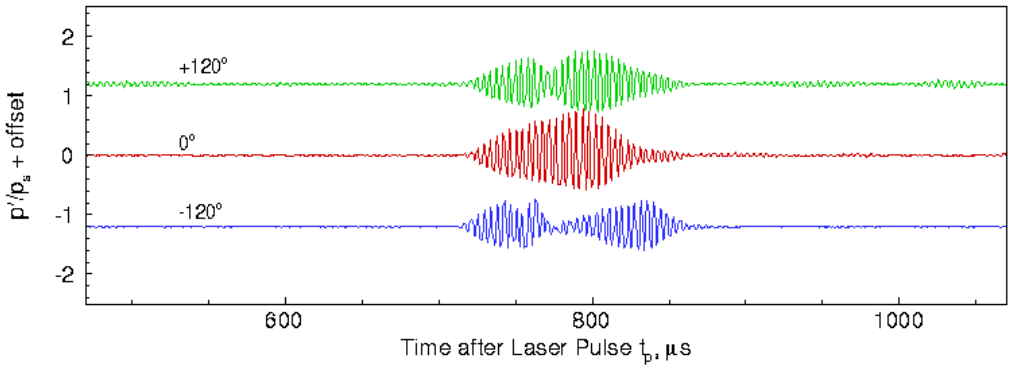

(b) $x = 382$ mm.

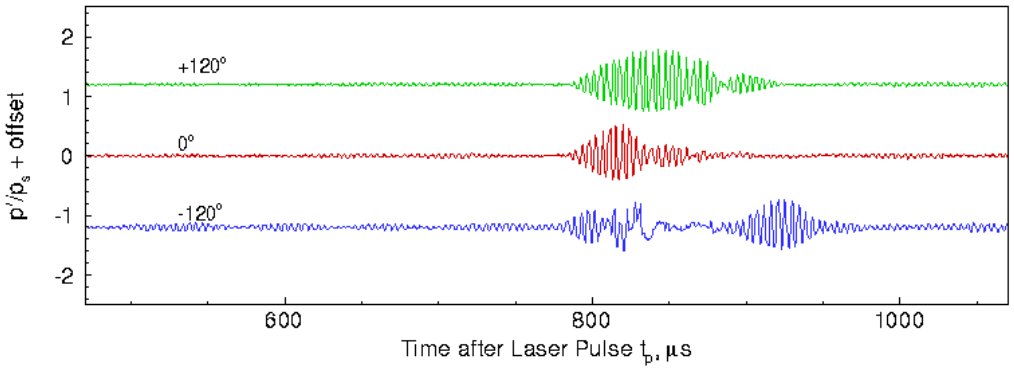

(c) $x = 434$ mm.

Figure 8.62. Time traces from azimuthal arrays of the effect of a laser perturbation for $r_n = 0.16$ mm. Perturbation generated 3 mm closer to $-120°$ ray. Run 19-39: $p_0 = 535.4$ kPa, $T_0 = 426.6$ K, $Re/m = 5.86 \times 10^6$/m.

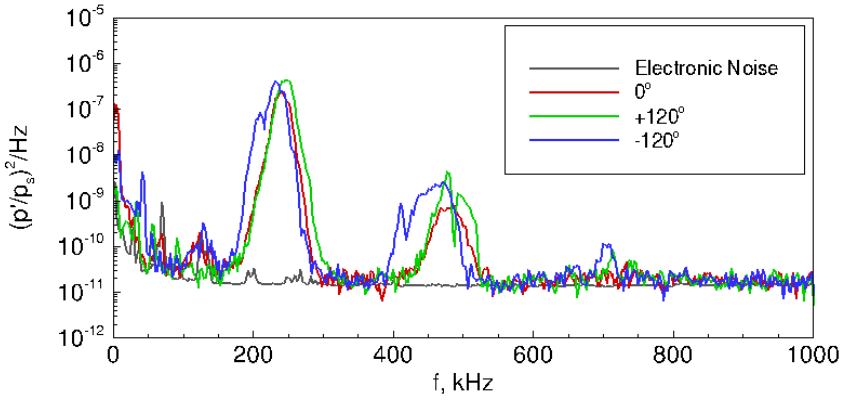

(a) $x = 332$ mm.

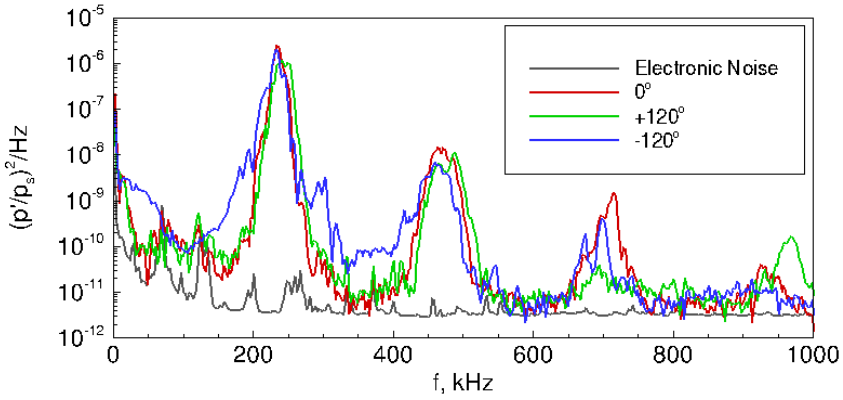

(b) $x = 382$ mm.

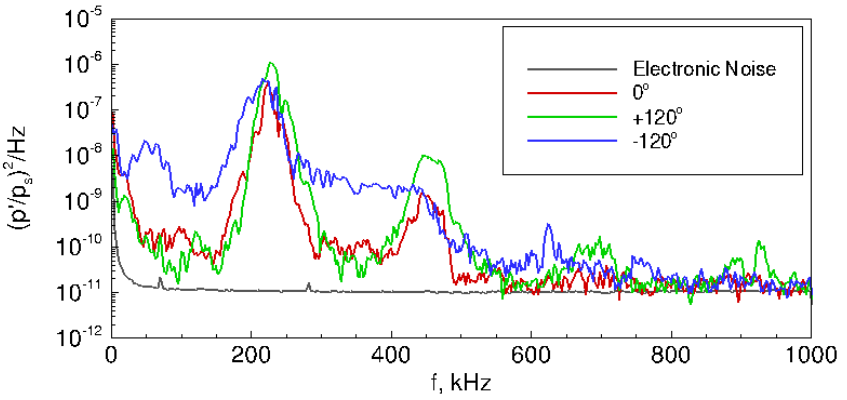

(c) $x = 434$ mm.

Figure 8.63. Spectra from azimuthal sensors for $r_n = 0.16$ mm. Perturbation generated 3 mm closer to $-120°$ ray. Run 19-39: $p_0 = 535.4$ kPa, $T_0 = 426.6$ K, $Re/m = 5.86 \times 10^6$/m.

8.6 Comparison of the Data to Measurements by Others

Previous measurements by Schmisseur show a single peak in the near-surface measurements at the back of the elliptic cone [43, Figure 7.4]. No clear wave packet was measured in his experiments. As in the current data set, the shape of the boundary layer disturbance appears to vary from shot to shot, and the time of arrival of the disturbance also appears to vary from shot to shot. A similar time of arrival variation was not seen in Salyer's measurements [25]. This may be due to the fact that Salyer primarily used hemisphere and forward-facing cavity geometries. Measurements on these models were made primarily in the stagnation region, and thus, may not show the time of arrival variations seen on the surface of a cone-type model.

Heitmann generated a wave packet in the boundary layer of a 7-degree straight cone using the weak shock wave of the laser perturbation [60]. The laser perturbation was generated behind the oblique shock of the cone and the pulse energy of the laser was decreased to produce different wave packet amplitudes. As a result, these wave packet amplitudes were much smaller than the amplitudes in the present experiment. Furthermore, the shape of the wave packets in Heitmann's experiment was different when compared to the wave packet shape in the present experiment, except in the low-energy cases. The wave packets show some distortion in Heitmann's experiments, but this distortion is attributed to the large energy of the laser perturbation and possible effects of the plasma in the perturbation. When the freestream perturbation amplitude was reduced, a shot-to-shot variability in phase and amplitude of the wave packets was observed by Heitmann [119]. This shot-to-shot variability is similar to the time of arrival variation seen in the BAM6QT for the flared cone. However, Heitmann uses an unseeded laser to create the laser perturbation, so the variability in his experiment may also be caused by the limited repeatability of the laser perturbation.

Schmisseur estimated the thermal amplitude of the perturbation to be roughly 100 K greater than the freestream, which may be large enough to cause nonlinear receptivity [43]. For example, the linear receptivity computations by Huang et al. [41]

use a thermal disturbance with an amplitude of 52.8×10^{-4} K. The perturbation diameter is on the order of 2–8 mm, depending on the freestream conditions. Many of the existing computations use a plane-wave disturbance to compute receptivity, so the present understanding of "large" versus "small" amplitude disturbances may not easily translate to localized perturbations. It is possible that the integrated effect of the laser perturbation is still small enough to cause linear receptivity.

The measurements made by Schmisseur showed a large disturbance in the boundary layer, but no wave packets were generated. The PQFLT was limited in Reynolds number range, and thus was not able to show how the laser-generated disturbance would have developed farther downstream. The highest freestream unit Reynolds number run by Schmisseur occurred at 4.24×10^6/m. Measurements at the aft end of Schmisseur's elliptic cone yielded an equivalent Reynolds number of $Re_x = 640,000$ or $Re_{x,\infty} = 538,500$. A freestream Reynolds number of $Re_{x,\infty} = 538,500$ in the BAM6QT occurs at about 77 mm from the flared cone nosetip. The flared cone model was not able to accommodate sensors farther upstream than 200 mm from the blunt nosetip. In fact, the blunt nosetip itself is about 140 mm long. Perhaps at some farther upstream location, where the Reynolds number matched Schmisseur's experiments, the same large disturbance would have been measured instead of the wave packet.

Direct numerical simulations (DNS) of a nonlinear wave packet on a flared cone were made by Terwilliger [67]. Although the conditions of the experiment do not match the conditions of the computation, some qualitative comparisons can be made. Terwilliger used a slot for wall blowing and suction to generate a nonlinear wave packet on the surface of the flared cone model in his DNS studies. The slot had dimensions of 0.24 mm by 2 mm and was placed at $x = 174$ mm. The forcing amplitude $v'/u = 0.03$ is the magnitude of the wall-normal velocity at the suction-blowing slot. The wave packets predicted by Terwilliger's computation exhibit a double-burst shape, similar to those seen in the experiment. However, the double-burst shape appeared as far upstream as the first sensor station in the experiment, while Terwilliger only saw

the double-burst feature toward the farther downstream end of the computational domain. This suggests that the wave packet generated in the flared cone boundary layer by the freestream laser perturbation may be more nonlinear than the wave packet generated on the surface computed by Terwilliger.

Computations by Huang et al. [41] used a perturbation about 5 orders of magnitude less than Schmisseur's estimate of the perturbation temperature. Huang's computations were for the same model used in the BAM6QT, but at slightly different mean flow conditions. Despite the differences between the computation and the experiment, many similarities between the two studies exist. The wave packet shapes match fairly well. Several of the computed packet shapes also exhibit a double-burst structure, which is seen clearly in the experiment. Furthermore, the spectra match fairly well when the Reynolds numbers are matched. It is not clear why the studies produce such similar results despite the orders-of-magnitude difference in the modeled freestream perturbation.

8.7 Summary

The large freestream laser perturbation was capable of generating nonlinear wave packets in the boundary layer of the flared cone model. The frequency content of the wave packet in the boundary layer was similar to the natural dominant frequencies of the flared cone. Surprisingly, the initial amplitudes of the wave packet disturbance were very small, despite the large freestream perturbation. The wave packet grew nonlinearly with increasing distance from the nosetip. The wave packet on the blunt model was smaller than on the sharp model. It is not clear whether this is due to the smaller growth rates of the second-mode waves on the blunt model, or to a lower receptivity. More computations are desired to help interpret this result. The speed of the wave packet in the boundary layer was measured to be 1–3% higher than the computed boundary layer edge velocity. This discrepancy may be caused by the time of arrival method used to calculate the wave packet speed.

The wave packet in the boundary layer of the sharp nosetip was highly nonlinear and broke down at the aft end of the cone at lower Reynolds numbers than for the blunt cone. The power spectra of the wave packet on the sharp model showed a large second-mode peak and large first and second harmonics. A lower-frequency peak was also observed in the spectra at about 130 kHz. The presence of this peak may indicate the presence of a subharmonic. The presence of a subharmonic would indicate that the perturbation experiences an N- or H-type nonlinear resonance. However, this peak does not appear to shift with changes in the freestream Reynolds number or with changes in the second-mode frequency. Again, it is not yet clear whether the larger waves on the sharp model are due to a larger receptivity, to larger growth rates, or to both effects.

When the freestream laser perturbation is offset from the flared cone centerline, a large effect is observed on the blunt model while almost no effect is observed on the sharp model. This implies that the blunt model is more sensitive to small errors in alignment than the sharp model. The sensitivity of the blunt model to the alignment of the perturbation is not intuitive. Again, further studies of this effect are desired.

The freestream of the BAM6QT provided a disturbance field with very little acoustic noise and the freestream laser perturbation is a repeatable controlled perturbation. These conditions are unique. The BAM6QT was one of only 3 known quiet hypersonic tunnels at the time this dissertation was written and the only one with optical access far upstream. As always, more data are desired, but unique hypersonic facilities like the BAM6QT have limited availability. The present thesis provides the first set of experiments with a controlled freestream perturbation impinging on a hypersonic model to generate second-mode wave packets. These wave packets amplify linearly and nonlinearly, and in some cases, break down to turbulence.

Although the measurements are challenging to make and limited in completeness and accuracy, they provide a significant step toward the characterization of this complex problem. The characterization of the freestream laser perturbation is not as complete as desired, due to the difficulty of this high-frequency measurement. Quan-

titative measurements were made in the freestream to characterize the perturbation and quantitative measurements were made of the surface pressure fluctuations. The data set acquired here yielded a large amount of information that has not been previously observed. The flared cone experiment sheds light on the receptivity, linear and nonlinear growth, and breakdown to turbulence of a controlled freestream perturbation. Computational comparisons are required to make the best use of these measurements.

CHAPTER 9. SUMMARY AND RECOMMENDATIONS

Few experiments have been performed to understand the process of receptivity. These experiments require careful control and difficult measurements. In the measurements described in this dissertation, a laser-generated perturbation was created in the freestream of a wind tunnel, then allowed to convect downstream to interact with a model. The freestream laser perturbation was characterized in two different tunnels: the NASA LaRC PCT and the Purdue University BAM6QT. Then, the laser perturbation was characterized after it had passed through an oblique shock. Next, this perturbation was placed upstream of a forward-facing cavity model in the BAM6QT to develop the skill required to align the perturbation with a downstream cone model. Finally, the freestream laser perturbation was placed upstream of a flared cone model in the BAM6QT. Instabilities in the boundary layer created by the freestream perturbation were measured with surface-mounted pressure sensors. None of these measurements were as accurate or complete as desired, but many of these measurements are the first of their kind.

The experiment presented in this dissertation yielded surprising results. Measurements of the freestream disturbance showed a large discrete thermal perturbation. However, calculations of the initial amplitude of the wave packet disturbance generated in the boundary layer were very small. Another unexpected result was that the blunt nosetip appeared to be more sensitive to the alignment of the freestream disturbance to the model centerline. When the freestream disturbance was deliberately offset from the model centerline, a larger wave packet was generated on the side toward which the disturbance was offset. These new results show some unexpected effects of the freestream disturbance and raise questions about the current understanding of receptivity.

9.1 Summary

Measurements with pressure probes were made in the freestream of the BAM6QT at Purdue University to characterize this disturbance. However, more detailed measurements were desired, so the freestream characterization measurements were also made in the PCT at NASA LaRC. Hot wire and deflectometry measurements were made in the PCT, but the measurements were not as clear as desired. The technology that can be used to measure these disturbances is still insufficient to provide measurements to the fidelity desired. Nevertheless, these measurements showed that the freestream disturbances decrease in amplitude as the freestream temperature and density decrease. They also showed that the laser-generated disturbance is roughly spherical. The amplitude of the disturbance was also large enough to be locally nonlinear, creating around a 65% deficit in the probe-measured characteristics.

Measurements were also carried out behind an oblique shock in the PCT. A physical interpretation of the disturbance was difficult due to a lack of axisymmetry in the disturbance after passing through the shock. However, the measurements agreed well with McKenzie and Westphal's predictions of the trajectory of entropic/vortical disturbances through an oblique shock. The experimental data could be compared to a computation of this flow if one becomes available.

Next, the disturbance was placed in front of a forward-facing cavity to show that the laser perturber apparatus worked as expected and to develop the skill required to align a freestream perturbation to a model in the BAM6QT. The alignment of the disturbance to a forward-facing cavity was relatively simple compared to a sharper-nosed model. The forward-facing cavity showed that the disturbance appears to generate the same type of response seen previously by Salyer [37] and Segura [102]. Historical data were also combined with present-day data to create a correlation between the damping coefficient and the cavity depth. This correlation was independent of Mach number.

Finally, the freestream laser perturbation was placed upstream of a flared cone model in the BAM6QT. Schmisseur's measurements on a 4:1 elliptic cone raised suspicion that the freestream perturbation may not produce measurable instability waves [43]. However, the present measurements showed that the large freestream perturbation generated wave packets in the boundary layer. These wave packets were both linear and nonlinear, and occasionally broke down to turbulence. The wave packets also had the same frequency as the natural second-mode waves and convected with about the same speed as the edge velocity.

The spectral content of the wave packets appeared to consist of a second-mode instability and sometimes one or more higher harmonics. The RMS amplitude of the second-mode bandwidth was compared to linear computations of wave growth. The measured RMS amplitudes deviated from the linear computations in most cases. It remains difficult to measure instabilities above the background noise when they are small enough to be linear. An attempt at finding the initial amplitude of the second-mode disturbance was also performed. For the blunt nosetip, the estimated initial amplitude was about 3.51×10^{-6} times the freestream static pressure. For the sharp nosetip, the estimated initial amplitude was about 2.34×10^{-4} times the freestream static pressure. These initial amplitudes are very low, and thus, suggest linear receptivity despite the large localized amplitude of the freestream disturbance.

When the freestream perturbation was purposely offset from the centerline axis of the flared cone, the laser-generated disturbance appeared to generate a large wave packet on the blunt model, along the ray toward which the perturbation was aligned. This large-amplitude wave packet often became transitional or turbulent. The sharp model did not show as large an effect of the offset in the perturbation. The already large-amplitude wave packet was likely saturated at the measurement stations, so changes in the alignment may not be as effective. Computational and theoretical studies are needed to interpret the data better, and to make the best use of it.

9.2 Suggestions for Future Work

Many parameters in the experiment were not explored to their full potential. Hypersonic receptivity experiments are very difficult to plan and execute. Accurate and complete measurements will remain challenging for a long time. Systematic variation of the many relevant flow parameters will also require many studies over a long period of time. The present measurements have suggested many possible improvements. These include:

1. Determine whether the receptivity process that creates a wave packet in the boundary layer of a flared cone is linear or nonlinear. The amplitude of the perturbation is locally large, and yet appears to generate small initial disturbances. A computational study could be done to determine how large a localized disturbance must be to no longer produce linear receptivity. The peak amplitude of the thermal disturbance of the freestream appears large enough to create some kind of bypass transition. However, this is not the case, as a wave packet is clearly generated in the flared cone boundary layer. Our understanding of discrete disturbances is not as complete as it is for planar disturbances. Further computational and theoretical studies are desired to complement this data set.

2. Further characterization of the freestream disturbances could also be gathered for the receptivity measurements. Several freestream disturbance measurements were made in the BAM6QT, but they were at higher stagnation pressures than used for the flared cone experiment. The freestream disturbance characterization measurements were made prior to the measurements on the flared cone, so the limitations on the usable Reynolds number range for the flared cone were not known at the time. Further measurements of the freestream perturbation should be made in the BAM6QT at similar Reynolds numbers. These perturbations should also be made with better instrumentation. Higher-frequency measurements of the laser perturbation in the freestream might be performed

with more quantitative instrumentation, such as the laser differential interferometer, in order to better characterize the perturbation.

3. Further computations of the nonlinear breakdown process of the wave packet are also desired. The mechanism which causes transition on the flared cone is not clear. The spectra indicate the presence of a low-frequency peak, which may be a subharmonic. However, this peak does not appear to change with changes in conditions, so its contribution to the breakdown process is unclear.

4. When the perturbation is generated on the centerline axis, the freestream disturbances produce a wave packet. However, when this disturbance is offset, the wave packet appears to look more like a turbulent spot. This phenomenon has not been previously seen and more experiments and computational studies may help to reveal the cause.

5. A straight 7-degree half-angle cone model could be used for future receptivity studies. The natural waves are large on the flared cone model and can make the laser-generated disturbance difficult to discern from the natural waves. Furthermore, the natural waves tend to saturate fairly early, which may not allow for enough of a change to be detected when using laser-generated disturbances. However, past studies on a 7-degree cone show that natural transition is never seen in quiet flow. Also, the second mode may not be large enough to be measurable on this model, even with the presence of the laser-generated disturbance. To be certain, trial experiments need to be conducted on this model.

6. An apparatus to make very small angle of attack or yaw adjustments in a systematic manner would benefit future experiments in the BAM6QT. Alignment of the model to the freestream flow can be tedious and require several runs, which takes time. To reduce the amount of time spent aligning the model, a method of making small systematic adjustments in the angle of attack or yaw angle would benefit all models that require careful alignment to the flow.

7. A method of creating smaller freestream disturbances is desired. This may be possible by using a faster laser with a shorter pulse duration. Ideally, a laser perturber would allow for precise adjustments in amplitude over a wide range. This would allow for studies of amplitude effects.

8. A large amount of data were acquired in the experiment where the freestream laser-generated disturbance was deposited in front of the flared cone. While several different types of data analysis were applied to this data set, not all of the analysis was completed. Several options discussed in Section 8.3.2 could be completed over the next several years.

LIST OF REFERENCES

LIST OF REFERENCES

[1] M. V. Morkovin. Critical evaluation of transition from laminar to turbulent shear layers with emphasis on hypersonically traveling bodies. Technical report, Air Force Flight Dynamics Laboratory, Wright-Patterson Air Force Base, OH, Mar 1969. Technical Report AFFDL-TR-68-149.

[2] S. P. Schneider. Flight data for boundary-layer transition at hypersonic and supersonic speeds. *Journal of Spacecraft and Rockets*, 36(1):8–20, Jan–Feb 1999.

[3] S. P. Schneider. Hypersonic laminar-turbulent transition on circular cones and scramjet forebodies. *Progress in Aerospace Sciences*, 40(1–2):1–50, Feb 2004.

[4] L. M. Mack. Boundary-layer stability theory. Part B. Technical report, Jet Propulsion Laboratory, Pasadena, CA, May 1969. Doc. 900-277.

[5] A.M.O. Smith and N. Gamberoni. Transition, pressure gradient and stability theory. Technical report, Douglas Aircraft Division, Aug 1956. Report No. ES 26388.

[6] J. L. van Ingen. The e^n method for transition prediction. Historical review of work at TU Delft. AIAA Paper 2008-3830, Jun 2008.

[7] S. P. Schneider. Effects of high-speed tunnel noise on laminar-turbulent transition. *Journal of Spacecraft and Rockets*, 38(3):323–333, May–Jun 2001.

[8] S. P. Schneider. Development of hypersonic quiet tunnels. *Journal of Spacecraft and Rockets*, 45(4):641–664, Jul–Aug 2008.

[9] S. P. Schneider. Effects of roughness on hypersonic boundary-layer transition. *Journal of Spacecraft and Rockets*, 45(2):193–209, Mar–Apr 2008.

[10] D. C. Berridge, A. Chou, C. A.C. Ward, L. E. Steen, P. L. Gilbert, T. J. Juliano, S. P. Schneider, and J. E. Gronvall. Hypersonic boundary-layer transition experiments in a Mach-6 quiet tunnel. AIAA Paper 2010-1061, Jan 2010.

[11] W. H. Saric, H. L. Reed, and E. J. Kerschen. Boundary-layer receptivity to freestream disturbances. *Annual Review of Fluid Mechanics*, 34:291–319, 2002.

[12] D. C. Berridge, K. M. Casper, S. J. Rufer, C. R. Alba, D. R. Lewis, S. J. Beresh, and S. P. Schneider. Measurements and computations of second-mode instability waves in three hypersonic wind tunnels. AIAA Paper 2010-5002, Jun 2010.

[13] J. M. Kendall. Wind tunnel experiments relating to supersonic and hypersonic boundary-layer transition. *AIAA Journal*, 13(3):290–299, Mar 1975.

[14] A. V. Fedorov. Laminar turbulent transition in a hypersonic boundary layer: Receptivity and instability pre-history. Technical report, Moscow Institute of Physics and Technology, Jul 1997. European Office of Aerospace Research and Development, Special Project SPC-96-4024, DTIC Accession Number ADA328847.

[15] E. Reshotko. Boundary-layer stability and transition. *Annual Review of Fluid Mechanics*, 8:311–349, Jan 1976.

[16] M. E. Goldstein. The evolution of Tollmien-Schlichting waves near a leading edge. *Journal of Fluid Mechanics*, 127:59–81, 1983.

[17] A. Fedorov. Transition and stability of high-speed boundary layers. *Annual Review of Fluid Mechanics*, 43:79–95, 2010.

[18] L. M. Mack. Linear stability theory and the problem of supersonic boundary-layer transition. *AIAA Journal*, 13(3):278–289, Mar 1975.

[19] M. R. Schopper. A model for the noise radiated by turbulent boundary layers and its interaction with laminar layers in supersonic flow. AIAA Paper 1979-1523, Jul 1979.

[20] M. R. Schopper. Interaction of aerodynamic noise with laminar boundary layers in supersonic wind tunnels. NASA Contractor Report 3621, National Aeronautics and Space Administration, Apr 1984.

[21] L. S.G. Kovasznay. Turbulence in supersonic flow. *Journal of Aerospace Sciences*, 20(10):657–674,682, Oct 1953.

[22] A. V. Fedorov and M. V. Kozlov. Receptivity of high-speed boundary layer to solid particulates. AIAA Paper 2011-3925, Jun 2011.

[23] M. V. Morkovin. Note on the assessment of flow disturbances at a blunt body traveling at supersonic speeds owing to flow disturbances in free stream. *Journal of Applied Mechanics*, 27(2):223–229, Jun 1960.

[24] D. W. Ladoon, S. P. Schneider, and J. D. Schmisseur. Physics of resonance in a supersonic forward-facing cavity. *Journal of Spacecraft and Rockets*, 35(5):626–632, Sep–Oct 1998.

[25] T. R. Salyer. *Laser Differential Interferometry for Supersonic Blunt Body Receptivity Experiments*. PhD thesis, School of Aeronautics & Astronautics, Purdue University, West Lafayette, IN, May 2002.

[26] J. F. McKenzie and K. O. Westphal. Interaction of linear waves with oblique shock waves. *Physics of Fluids*, 11(11):2350–2362, Nov 1968.

[27] K. Kara, P. Balakumar, and O. A. Kandil. Effects of nose bluntness on hypersonic boundary-layer receptivity and stability over cones. *AIAA Journal*, 49(12):2593–2606, Dec 2011.

[28] P. Balakumar and M. A. Kegerise. Receptivity of hypersonic boundary layers over straight and flared cones. AIAA Paper 2010-1065, Jan 2010.

[29] A. Fedorov and A. Tumin. High-speed boundary-layer instability: Old terminology and a new framework. *AIAA Journal*, 49(8):1647–1657, Aug 2011.

[30] P. Balakumar. Receptivity of a supersonic boundary layer to acoustic disturbances. *AIAA Journal*, 47(5):1069–1078, May 2009.

[31] P. Balakumar and M. A. Kegerise. Receptivity of hypersonic boundary layers to acoustic and vortical disturbances. AIAA Paper 2011-0371, Jan 2011.

[32] J. M. Kendall. Boundary layer receptivity to freestream turbulence. AIAA Paper 1990-1504, Jun 1990.

[33] A. A. Maslov, A. N. Shiplyuk, A. A. Sidorenko, and D. Arnal. Leading-edge receptivity of a hypersonic boundary layer on a flat plate. *Journal of Fluid Mechanics*, 426:73–94, 2001.

[34] M. Wiegel and R. W. Wlezien. Acoustic receptivity of laminar boundary layers over wavy walls. AIAA Paper 1993-3280, Jul 1993.

[35] K. M. Casper. *Pressure Fluctuations Beneath Instability Wave Packets and Turbulent Spots in a Hypersonic Boundary Layer*. PhD thesis, School of Aeronautics & Astronautics, Purdue University, West Lafayette, IN, Aug 2012.

[36] J. D. Schmisseur, S. H. Collicott, and S. P. Schneider. Laser-generated localized freestream perturbations in supersonic and hypersonic flows. *AIAA Journal*, 38(4):666–671, Apr 2000.

[37] T. R. Salyer, S. H. Collicott, and S. P. Schneider. Characterizing laser-generated hot spots for receptivity studies. *AIAA Journal*, 44(12):2871–2878, Dec 2006.

[38] D. Heitmann. *Transitionsuntersuchungen in hypersonischen Grenzschichten mit laserinduzierten Störungen*. PhD thesis, Institüt fur Strömungsmechanik (Institute of Fluid Mechanics), Technische Universität Braunschweig, Braunschweig, Germany, 2011.

[39] Y. Huang and X. Zhong. Numerical study of laser-spot effects on boundary-layer receptivity for blunt compression-cones in Mach-6 freestream. AIAA Paper 2010-4447, Jun 2010.

[40] Y. Huang and X. Zhong. Numerical study of freestream hot-spot perturbation on boundary-layer receptivity for blunt compression-cones in Mach-6 flow. AIAA Paper 2011-3078, Jun 2011.

[41] Y. Huang and X. Zhong. Parametric study of boundary-layer receptivity to freestream hot-spot perturbation over a blunt compression cone. AIAA Paper 2014-774, Jan 2014.

[42] J. B. McGuire. Fluid dynamic perturbations using laser induced breakdown. Master's thesis, School of Aeronautics & Astronautics, Purdue University, West Lafayette, IN, Aug 1994.

[43] J. D. Schmisseur. *Receptivity of the Boundary Layer on a Mach-4 Elliptic Cone to Laser-Generated Localized Freestream Perturbations*. PhD thesis, School of Aeronautics & Astronautics, Purdue University, West Lafayette, IN, Dec 1997.

[44] National Institute of Standards and Technology. Computational chemistry comparison and benchmark database. Online Database, Release 15b, `http://cccbdb.nist.gov/`, Aug 2011. NIST Standard Reference Database 101. Last accessed May 2012.

[45] F. L. Pedrotti, S. J., L. S. Pedrotti, and L. M. Pedrotti. *Introduction to Optics*. Pearson Education, Inc., San Francisco, 3rd edition, 2007.

[46] G. V. Ostrovskaya and A. N. Zaĭdel'. Laser spark in gases. *Soviet Physics Uspekhi*, 16(6):834–855, May–Jun 1974.

[47] A. Camire. Quotations QART1752 and QART1753 from Spectra-Physics, Nov 2010.

[48] D. S. Smith and R. G. Tomlinson. The effect of mode beating in laser-produced gas breakdown. *Applied Physics Letters*, 11(73):73–75, Aug 1967.

[49] R. G. Adelgren, G. S. Elliott, D. D. Knight, A. A. Zheltovodov, and T. J. Beutner. Energy deposition in supersonic flows. AIAA Paper 2001-0885, Jan 2001.

[50] C. Grey Morgan. Laser-induced breakdown phenomena. *Scientific Progress*, 65(257):31–50, Spring 1978.

[51] R. A. Armstrong, R. A. Lucht, and W. T. Rawlins. Spectroscopic investigation of laser-initiated low-pressure plasmas in atmospheric gases. *Applied Optics*, 22(10):1573–1577, May 1983.

[52] V. I. Eremin, L. V. Norinskii, and V. A. Pryadein. Frequency dependence of the threshold of optical breakdown in air in the ultra-violet band. *JETP Letters*, 13(8):307–310, 1971.

[53] N. Kawahara, E. Tomita, T. Nakayama, Y. Ikeda, and A. Nishiyama. Spatial and temporal characteristics of laser-induced air plasma. AIAA Paper 2006-1461, Jan 2006.

[54] K. Mori, K. Komurasaki, and Y. Arakawa. Energy transfer from a laser pulse to a blast wave in reduced-pressure air atmospheres. *Journal of Applied Physics*, 95(11):5979–5983, Jun 2004.

[55] C. M. Limbach and R. B. Miles. Simultaneous temperature, density and velocity measurements in laser-generated plasmas by Rayleigh and filtered Rayleigh scattering. AIAA Paper 2014-0143, Jan 2014.

[56] N. Glumac, G. Elliott, and M. Boguszko. Temporal and spatial evolution of the thermal structure of a laser spark in air. AIAA Paper 2005-0204, Jan 2005.

[57] N. Glumac and G. Elliott. The effect of ambient pressure on laser-induced plasmas in air. AIAA Paper 2006-0399, Jan 2006.

[58] L. I. Sedov. *Similarity and Dimensional Methods in Mechanics*. Academic Press, 2nd edition, 1959. Translated by A. G. Volkovets.

[59] G. Taylor. The formation of a blast wave by a very intense explosion: I. Theoretical discussion. *Proceedings of the Royal Society of London. Series A, Mathematical and Physical Sciences.*, 201(1065):159–174, Mar 1950.

[60] D. Heitmann and R. Radespiel. Simulations of boundary-layer response to laser-generated disturbances at Mach 6. *Journal of Spacecraft and Rockets*, 50(2):305–316, Mar–Apr 2013.

[61] A. V. Fedorov, A. A. Ryzhov, and V. G. Soudakov. Numerical and theoretical modeling of supersonic boundary-layer receptivity to temperature spottiness. AIAA Paper 2011-3077, Jun 2011.

[62] M. V. Morkovin, E. Reshotko, and T. Herbert. Transition in open flow systems—a reassessment. *Bulletin of the American Physical Society*, 39(9), 1994.

[63] P. S. Klebanoff, K. D. Tidstrom, and L. M. Sargent. The three-dimensional nature of boundary-layer instability. *Journal of Fluid Mechanics*, 12(1):1–34, Jan 1962.

[64] Y. S. Kachanov. Physical mechanisms of laminar-boundary-layer transition. *Annual Review of Fluid Mechanics*, 26:411–482, Jan 1994.

[65] A. Thumm, W. Wolz, and H. Fasel. Numerical simulation of spatially growing three-dimensional disturbance waves in compressible boundary layers. In *Proceedings of the Third IU-TAM Symposium on Laminar-Turbulent Transition*, Toulouse, France, Sep 1989.

[66] C.-L. Chang and M. R. Malik. Oblique-mode breakdown and secondary instability in supersonic boundary layers. *Journal of Fluid Mechanics*, 273:323–360, 1994.

[67] N. Terwilliger. Numerical investigation of boundary layer instability modes on a compression cone at Mach 6. Master's thesis, Department of Aerospace and Mechanical Engineering, The University of Arizona, 2011.

[68] J. Sivasubramanian and H. F. Fasel. Growth and breakdown of a wave packet into a turbulent spot in a cone boundary layer at Mach 6. AIAA Paper 2012-0085, Jan 2012.

[69] J. W. Hofferth, R. D. W. Bowersox, and W. S. Saric. The Mach 6 quiet tunnel at Texas A& M: Quiet flow performance. AIAA Paper 2010-4794, Jun 2010.

[70] C. Zhang, Q. Tang, and C. Lee. Hypersonic boundary-layer transition on a flared cone. *Acta Mechanica Sinica*, 29(1):48–53, 2013.

[71] M. P. Borg. Characteristics of the contraction of the Boeing/AFOSR Mach-6 Quiet Tunnel. Master's thesis, School of Aeronautics & Astronautics, Purdue University, West Lafayette, IN, Dec 2005.

[72] C. R. Skoch. *Disturbances from Shock/Boundary-Layer Interactions Affecting Upstream Hypersonic Flow*. PhD thesis, School of Aeronautics & Astronautics, Purdue University, West Lafayette, IN, Dec 2005.

[73] Tektronix. DPO7000 series datasheet. `http://www.tek.com/datasheet/dpo7000/dpo7000-series-datasheet`, Dec 2013.

[74] B. M. Wheaton. Roughness-induced instability in a laminar boundary layer at Mach 6. Master's thesis, School of Aeronautics & Astronautics, Purdue University, West Lafayette, IN, Dec 2009.

[75] Kulite Semiconductor Products. Kulite pressure transducer handbook.

[76] M. A. Rotea, L. A. Randall, G. Song, and S. P. Schneider. Model identification of a Kulite pressure transducer. AIAA Paper 1996-2278, Jun 1996.

[77] S. J. Beresh, J. F. Henfling, R. W. Spillers, and B. O. M. Pruett. Measurement of fluctuating wall pressures beneath a supersonic turbulent boundary layer. AIAA Paper 2010-0305, Jan 2010.

[78] K. Fujii. Experiment of the two-dimensional roughness effect on hypersonic boundary-layer transition. *Journal of Spacecraft and Rockets*, 43(4):731–738, 2006.

[79] M. Estorf, R. Radespiel, S. P. Schneider, H. B. Johnson, and S. Hein. Surface-pressure measurements of second-mode instability in quiet hypersonic flow. AIAA Paper 2008-1153, Jan 2008.

[80] C. R. Alba, K. M. Casper, S. J. Beresh, and S. P. Schneider. Comparison of experimentally measured and computed second-mode disturbances in hypersonic boundary layers. AIAA Paper 2010-0897, Jan 2010.

[81] A. Abney, C. Ward, D. Berridge, R. Greenwood, and S. P. Schneider. Hypersonic boundary-layer transition experiments in the Boeing/AFOSR Mach-6 Quiet Tunnel. AIAA Paper 2013-0375, Jan 2013.

[82] M. A. Kegerise, L. R. Owen, and R. A. King. High-speed boundary-layer transition induced by an isolated roughness element. AIAA Paper 2010-4999, Jun 2010.

[83] A. J. Smits, K. Hayakawa, and K. C. Muck. Constant temperature hot-wire anemometer practice in supersonic flows. *Experiments in Fluids*, 1(2):83–92, 1983.

[84] M. R. Davis. Measurements in a subsonic turbulent jet using a quantitative schlieren technique. *Journal of Fluid Mechanics*, 46(4):631–656, Apr 1971.

[85] S. McIntyre and G. Settles. Optical experiments on axisymmetric compressible turbulent mixing layers. AIAA Paper 1991-0623, Jan 1991.

[86] R. J. Goldstein. *Fluid Mechanics Measurements*, chapter Optical Systems for Flow Measurement: Shadowgraph, Schlieren, and Interferometric Techniques, pages 377–397. Hemisphere Publishing Company, 1983.

[87] U. Kogelschatz and W. R. Schneider. Quantitative schlieren techniques applied to high current arc investigations. *Applied Optics*, 11(8):1822–1832, Aug 1972.

[88] H. Yan, R. Adelgren, M. Boguszko, G. Elliott, and D. Knight. Laser energy deposition in quiescent air. *AIAA Journal*, 41(10), Oct 2003.

[89] S. H. Collicott. Initial Mach 6 LT spot maker design summary. Technical report, Purdue University, Aug 2010. Informal design report.

[90] S. H. Collicott. Private communication, Apr 2002.

[91] T. J. Juliano. Nozzle modifications for high-Reynolds-number quiet flow in the Boeing/AFOSR Mach-6 quiet tunnel. Master's thesis, School of Aeronautics & Astronautics, Purdue University, West Lafayette, IN, Dec 2006.

[92] L. E. Steen. Characterization and development of nozzles for a hypersonic quiet wind tunnel. Master's thesis, School of Aeronautics & Astronautics, Purdue University, West Lafayette, IN, Dec 2010.

[93] A. Chou, B. M. Wheaton, C. A. C. Ward, P. L. Gilbert, L. E. Steen, and S. P. Schneider. Instability and transition research in a Mach-6 quiet tunnel. AIAA Paper 2011-0283, Jan 2011.

[94] B. M. Wheaton. *Roughness-Induced Instabilities in a Mach-6 Laminar Boundary Layer*. PhD thesis, School of Aeronautics & Astronautics, Purdue University, West Lafayette, IN, Dec 2012.

[95] T. R. Creel, Jr., I. E. Beckwith, and F. Chen. Nozzle wall roughness effects on free-stream noise and transition in the Pilot Low-Disturbance Tunnel. Technical Report NASA TM-86389, NASA Langley Research Center, Sep 1985.

[96] M. K. Kegerise. Private communication, Apr 2014.

[97] I. E. Beckwith, W. D. Harvey, J. E. Harris, and B. B. Holley. Control of supersonic wind-tunnel noise by laminarization of nozzle-wall boundary layers. NASA Technical Memorandum X-2879, National Aeronautics and Space Administration, Dec 1973.

[98] J. L. Amick. Design and performance of the University of Michigan 6.6-inch hypersonic wind tunnel. NASA Contractor Report 2569, National Aeronautics and Space Administration, Nov 1975.

[99] A. E. Blanchard, J. T. Lachowicz, and S. P. Wilkinson. NASA Langley Mach 6 Quiet Wind-Tunnel performance. *AIAA Journal*, 35(1):23–28, Jan 1997.

[100] C. A. C. Ward, B. M. Wheaton, A. Chou, D. C. Berridge, L. E. Letterman, R. P. K. Luersen, and S. P. Schneider. Hypersonic boundary-layer transition experiments in the boeing/AFOSR Mach-6 quiet tunnel. AIAA Paper 2012-0282, Jan 2012.

[101] A. Chou, S. P. Schneider, and S. H. Collicott. Measurements of the interaction of an upstream laser perturbation with a forward-facing cavity. AIAA Paper 2013-0391, Jan 2013.

[102] T. J. Juliano, R. Segura, M. P. Borg, K. Casper, Hannon, Jr., M. J., B. M. Wheaton, and S. P. Schneider. Starting issues and forward-facing cavity resonance in a hypersonic quiet tunnel. AIAA Paper 2008-3735, Jun 2008.

[103] J. Hartmann. On a new method for the generation of sound waves. *Physical Review, Second Series*, 20(6):719–727, Dec 1922.

[104] H. W. Liepmann and A. Roshko. *Elements of Gasdynamics*. Dover, Mineola, NY, 2002.

[105] L. D. Huebner and L. R. Utreja. Mach 10 bow-shock behavior of a forward-facing nose cavity. *Journal of Spacecraft and Rockets*, 30(3):291–297, May 1993.

[106] R. L. Stallings, Jr. and P. B. Burbank. Heat-transfer and pressure measurements on a concave-nose cylinder for a Mach number range of 2.49 to 4.44. Technical Report NASA TM-X-221, NASA, Oct 1959.

[107] H.Q. Yang and M. Antonison. Unsteady flowfield over a forward-looking endoatmospheric hit-to-kill interceptor. *Journal of Spacecraft and Rockets*, 32(3):440–444, 1995.

[108] K.B. Yuceil and D.S. Dolling. Nose cavity effects on blunt body pressure and temperatures at Mach 5. *Journal of Thermophysics and Heat Transfer*, 9(4):612–619, 1995.

[109] W. A. Engblom, D. B. Goldstein, D. Ladoon, and S. P. Schneider. Fluid dynamics of hypersonic forward-facing cavity flow. *Journal of Spacecraft and Rockets*, 34(4):437–444, Jul 1997.

[110] F. Seiler, J. Srulijes, M. Gimenez Pastor, and P. Mangold. Heat fluxes inside a cavity placed at the nose of a projectile measured in a shock tunnel at Mach 4.5. In Cameron Tropea, Suad Jakirlic, Hans-Joachim Heinemann, Rolf Henke, and Heinz Hönlinger, editors, *New Results in Numerical and Experimental Fluid Mechanics VI*, volume 96 of *Notes on Numerical Fluid Mechanics and Multidisciplinary Design (NNFM)*, pages 309–316. Springer Berlin Heidelberg, 2008.

[111] R. N. Hopko and H. K. Strass. Some experimental heating data on convex and concave hemispherical nose shapes and hemispherical depressions on a 30° blunted nose cone. Research Memorandum RM-L58A17a, National Advisory Committee for Aeronautics (NACA), Mar 1958. NASA Accession Number X69-76940.

[112] W. A. Engblom and D. B. Goldstein. Nose-tip surface heat reduction mechanism. *Journal of Thermophysics and Heat Transfer*, 10(4):598–606, Oct 1996.

[113] J. Levine. Additional heat-transfer measurements obtained in free flight on a hemispherical concave nose at Mach numbers up to 7.1. Technical Report NASA TM-X-466, NASA Langley Research Center, Apr 1961.

[114] Texas Instruments. Low noise, low distortion instrumentation amplifier. Specification Sheet for INA103, Mar 1998.

[115] C. W. Rowley, D. R. Williams, T. Colonius, R. M. Murray, D. G. MacMartin, and D. Fabris. Model-based control of cavity oscillations, part II: System identification and analysis. AIAA Paper 2002-0972, Jan 2002.

[116] S. P. Schneider, C. Skoch, S. Rufer, S. Matsumura, and E. Swanson. Transition research in the Boeing/AFOSR Mach-6 Quiet Tunnel. AIAA Paper 2002-0302, Jan 2002.

[117] B. M. Wheaton, T. J. Juliano, D. C. Berridge, A. Chou, P. L. Gilbert, K. M. Casper, L. E. Steen, S. P. Schneider, and H. B. Johnson. Instability and transition measurements in the Mach-6 quiet tunnel. AIAA Paper 2009-3559, Jun 2009.

[118] L. C. Salemi, H. Fasel, S. Wernz, and E. Marquardt. Numerical investigation of wave-packets in a hypersonic high-enthalpy boundary-layer on a 5° sharp cone. AIAA Paper 2014-2775, Jun 2014.

[119] D. Heitmann, R. Radespiel, and H. Knauss. Experimental study of Mach 6 boundary layer response to laser generated disturbances. AIAA Paper 2011-3875, Jun 2011.

APPENDICES

Appendix A: A Simple Heat-Conduction Model of a Thermal Disturbance

A one-dimensional heat-conduction model is used to estimate of the cooling of the freestream thermal perturbation. The heat-conduction model does not take into effect the contributions of radiative or convective heat transfer. At the very least, this estimate allows for a qualitative comparison between the expected characteristics of the perturbation and the actual measurements.

A.1 Model of the Laser Perturbation

From historical measurements, the laser perturbation is expected to be a nearly spherical thermal disturbance with a weak shockwave emanating from the core, as in Figure 2.17. The center of the thermal disturbance is estimated to be about 100 K higher than the freestream temperature [43]. The weak shock wave is expected to have dissipated by the time it reaches the measurement region of the tunnel. In the PQFLT, this measurement region was only about 30 mm downstream of the location where the perturbation was generated. In the BAM6QT, the model is expected to be at about 100 mm or more downstream of the location where the perturbation is generated, depending on the model used. Probes in the BAM6QT can be moved up to 450 mm downstream of the generation location.

A Gaussian distribution in amplitude is assumed for the thermal perturbation. The estimated radial distribution in temperature of the perturbation in the BAM6QT as shown in Figure A.1, which corresponds to an equation of

$$T = \Delta T \cdot \exp\left(-4 \ln 2 \cdot \frac{r^2}{r_p^2}\right) + T_\infty \tag{A.1}$$

where ΔT is the maximum temperature of the perturbation relative to the freestream temperature $T_\infty = 52.8$ K, r_p is the radius of the perturbation, and r is the radial distance measured from the center of the perturbation. The density distribution for a stagnation pressure of $p_0 = 621$ kPa is inferred using a perfect gas assumption. The

result of this inference is shown in Figure A.2. The corresponding equation for the density distribution is then

$$\rho = \frac{p_\infty}{RT} \tag{A.2}$$

$$\rho = \frac{p_\infty}{R} \frac{1}{\Delta T \cdot \exp\left(-4 \ln 2 \cdot \frac{r^2}{r_p^2}\right) + T_\infty} \tag{A.3}$$

where p_∞ is the freestream pressure, which is assumed to be the pressure across the thermal portion of the perturbation, and R is the gas constant for air.

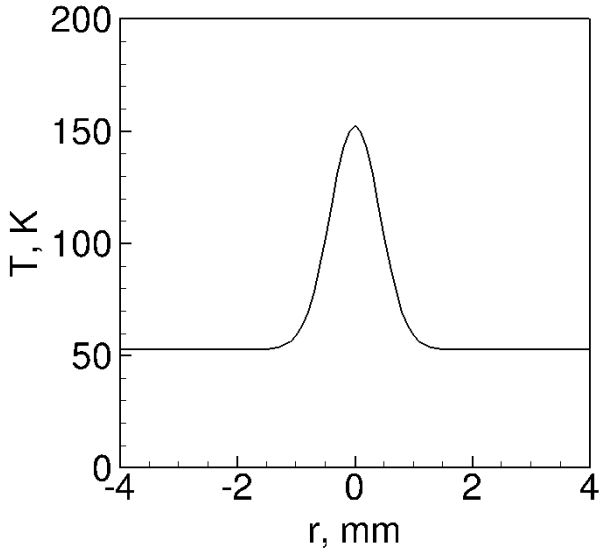

Figure A.1. Idealized model of temperature distribution in perturbation.

A one-dimensional heat transfer problem is solved to determine how much the temperature of the perturbation is expected to decay as it convects downstream in the tunnel. The assumption will be that the perturbation only undergoes conductive heat transfer and that the frame of reference is flow-fixed. Neglecting convection may be a good assumption, but since the perturbation is formed using a photoionization process, the neglect of radiative heat transfer may not be valid. Furthermore, this type of calculation does not take into account any energy which may be trapped in vibrational or rotational modes.

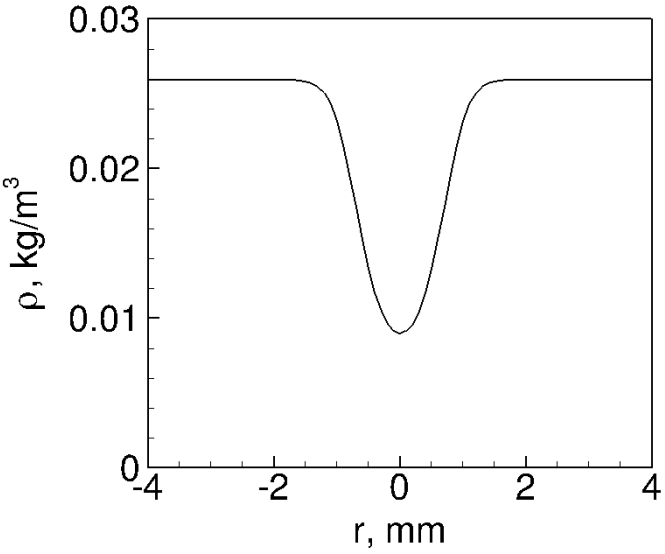

Figure A.2. Idealized model of density distribution in perturbation.

A general equation for heat conduction in spherical coordinates is

$$\rho c_p \frac{\partial T}{\partial t} = \frac{1}{r^2}\frac{\partial}{\partial r}\left(kr^2\frac{\partial T}{\partial r}\right) + \frac{1}{r^2\sin\theta}\frac{\partial}{\partial \theta}\left(k\sin\theta\frac{\partial T}{\partial \theta}\right) + \frac{1}{r\sin^2\theta}\frac{\partial}{\partial \phi}\left(k\frac{\partial T}{\partial \phi}\right) + g \quad \text{(A.4)}$$

where ρ is the density of the medium, c_p is the specific heat of the medium, t is time, r is the radial distance from the center of the perturbation, k is the heat conduction coefficient, θ and ϕ are different angles within the sphere, and g is an external heating term. Using the assumption that the heat conduction only occurs in the radial direction, terms with θ and ϕ will cancel and give

$$\rho c_p \frac{\partial T}{\partial t} = \frac{1}{r^2}\frac{\partial}{\partial r}\left(kr^2\frac{\partial T}{\partial r}\right) \quad \text{(A.5)}$$

In this model, k and c_p are assumed to be constant.

A.2 Solving the 1-D Heat Conduction Equation

First, find derivatives for Equation A.1:

$$\begin{aligned}\frac{\partial T}{\partial t} &= \frac{\partial}{\partial t}\left[\Delta T(t)\cdot\exp\left(-4\ln 2\cdot\frac{r^2}{r_p^2}\right)+T_\infty\right]\\ &= \frac{d\Delta T(t)}{dt}\exp\left(-4\ln 2\cdot\frac{r^2}{r_p^2}\right)\end{aligned}$$

$$\begin{aligned}\frac{\partial T}{\partial r} &= \frac{\partial}{\partial r}\left[\Delta T(t)\cdot\exp\left(-4\ln 2\cdot\frac{r^2}{r_p^2}\right)+T_\infty\right]\\ &= \Delta T(t)\frac{\partial}{\partial r}\exp\left(-4\ln 2\cdot\frac{r^2}{r_p^2}\right)\\ &= \Delta T\exp\left(-4\ln 2\cdot\frac{r^2}{r_p^2}\right)\cdot\frac{-8\ln 2}{r_p^2}r\\ &= -\Delta T\frac{8\ln 2}{r_p^2}\cdot r\cdot\exp\left(-4\ln 2\cdot\frac{r^2}{r_p^2}\right)\end{aligned}$$

$$\begin{aligned}r^2\frac{\partial T}{\partial r} &= r^2\left[\Delta T\frac{-8\ln 2}{r_p^2}\cdot r\cdot\exp\left(-4\ln 2\cdot\frac{r^2}{r_p^2}\right)\right]\\ &= -\Delta T\frac{8\ln 2}{r_p^2}\cdot r^3\cdot\exp\left(-4\ln 2\cdot\frac{r^2}{r_p^2}\right)\end{aligned}$$

$$\begin{aligned}\frac{\partial}{\partial r}\left(r^2\frac{\partial T}{\partial r}\right) =& \frac{\partial}{\partial r}\left[-\Delta T\frac{8\ln 2}{r_p^2}\cdot r^3\cdot\exp\left(-4\ln 2\cdot\frac{r^2}{r_p^2}\right)\right]\\ =& -\Delta T\frac{24\ln 2}{r_p^2}\cdot r^2\cdot\exp\left(-4\ln 2\cdot\frac{r^2}{r_p^2}\right)\\ &\quad -\Delta T\frac{8\ln 2}{r_p^2}\cdot r^3\cdot\exp\left(-4\ln 2\cdot\frac{r^2}{r_p^2}\right)\cdot\frac{-8\ln 2}{r_p^2}r\\ =& -\Delta T\frac{24\ln 2}{r_p^2}\cdot r^2\cdot\exp\left(-4\ln 2\cdot\frac{r^2}{r_p^2}\right)\\ &\quad +\Delta T\frac{64(\ln 2)^2}{r_p^4}\cdot r^4\cdot\exp\left(-4\ln 2\cdot\frac{r^2}{r_p^2}\right)\\ =& \frac{24\ln 2}{r_p^2}\Delta T\cdot\exp\left(-4\ln 2\cdot\frac{r^2}{r_p^2}\right)r^2\left(\frac{8}{3}\ln 2\frac{r^2}{r_p^2}-1\right)\end{aligned}$$

Then, plug this into Equation A.5:

$$\frac{c_p}{k}\frac{\partial T}{\partial t}\rho = \frac{1}{r^2}\frac{\partial}{\partial r}\left(r^2\frac{\partial T}{\partial r}\right)$$
$$\frac{c_p}{k}\frac{\partial T}{\partial t}\rho = \frac{1}{r^2}\frac{24\ln 2}{r_p^2}\Delta T\cdot\exp\left(-4\ln 2\cdot\frac{r^2}{r_p^2}\right)r^2\left(\frac{8}{3}\ln 2\frac{r^2}{r_p^2}-1\right)$$
$$\frac{c_p}{k}\frac{\partial T}{\partial t}\rho = \frac{24\ln 2}{r_p^2}\Delta T\cdot\exp\left(-4\ln 2\cdot\frac{r^2}{r_p^2}\right)\left(\frac{8}{3}\ln 2\frac{r^2}{r_p^2}-1\right)$$

$$\frac{d\Delta T(t)}{dt}\rho = \frac{d\Delta T}{dt}\exp\left(-4\ln 2\cdot\frac{r^2}{r_p^2}\right)\cdot\frac{p_\infty}{R}\frac{1}{\Delta T\cdot\exp\left(-4\ln 2\cdot\frac{r^2}{r_p^2}\right)+T_\infty}$$
$$= \frac{d\Delta T}{dt}\frac{p_\infty}{R}\frac{\exp\left(-4\ln 2\cdot\frac{r^2}{r_p^2}\right)}{\Delta T\cdot\exp\left(-4\ln 2\cdot\frac{r^2}{r_p^2}\right)+T_\infty}$$

$$\frac{c_p}{k}\frac{\partial T}{\partial t}\rho = \frac{1}{r^2}\frac{\partial}{\partial r}\left(r^2\frac{\partial T}{\partial r}\right)$$
$$\frac{c_p}{k}\frac{\partial T}{\partial t}\rho = \frac{1}{r^2}\frac{24\ln 2}{r_p^2}\Delta T\cdot\exp\left(-4\ln 2\cdot\frac{r^2}{r_p^2}\right)r^2\left(\frac{8}{3}\ln 2\frac{r^2}{r_p^2}-1\right)$$
$$\frac{c_p}{k}\frac{\partial T}{\partial t}\rho = \frac{24\ln 2}{r_p^2}\Delta T\cdot\exp\left(-4\ln 2\cdot\frac{r^2}{r_p^2}\right)\left(\frac{8}{3}\ln 2\frac{r^2}{r_p^2}-1\right)$$

$$\frac{c_p}{k}\frac{p_\infty}{R}\frac{d\Delta T}{dt}\frac{\exp\left(-4\ln 2\cdot\frac{r^2}{r_p^2}\right)}{\Delta T\cdot\exp\left(-4\ln 2\cdot\frac{r^2}{r_p^2}\right)+T_\infty}$$
$$= \frac{24\ln 2}{r_p^2}\Delta T\cdot\exp\left(-4\ln 2\cdot\frac{r^2}{r_p^2}\right)\left(\frac{8}{3}\ln 2\frac{r^2}{r_p^2}-1\right)$$

$$\frac{d\Delta T}{dt}\frac{\exp\left(-4\ln 2\cdot\frac{r^2}{r_p^2}\right)}{\Delta T\cdot\exp\left(-4\ln 2\cdot\frac{r^2}{r_p^2}\right)+T_\infty}$$
$$= \frac{k}{c_p}\frac{R}{p_\infty}\frac{24\ln 2}{r_p^2}\Delta T\cdot\exp\left(-4\ln 2\cdot\frac{r^2}{r_p^2}\right)\left(\frac{8}{3}\ln 2\frac{r^2}{r_p^2}-1\right)$$

$$\frac{d\Delta T}{dt}\frac{1}{\Delta T\cdot\exp\left(-4\ln 2\cdot\frac{r^2}{r_p^2}\right)+T_\infty} = \frac{k}{c_p}\frac{R}{p_\infty}\Delta T\cdot\frac{24\ln 2}{r_p^2}\cdot\left(\frac{8}{3}\ln 2\frac{r^2}{r_p^2}-1\right)$$
$$\frac{d\Delta T}{dt}\frac{1}{\Delta T}\frac{1}{\Delta T\cdot\exp\left(-4\ln 2\cdot\frac{r^2}{r_p^2}\right)+T_\infty} = \frac{k}{c_p}\frac{R}{p_\infty}\cdot\frac{24\ln 2}{r_p^2}\cdot\left(\frac{8}{3}\ln 2\frac{r^2}{r_p^2}-1\right)$$

Since ΔT is only a function of t, let all the r terms be constants defined as:

$$A = \exp\left(-4\ln 2\frac{r^2}{r_p^2}\right)$$

$$B = \frac{k}{c_p}\frac{R}{p_\infty}\cdot\frac{24\ln 2}{r_p^2}\cdot\left(\frac{8}{3}\ln 2\frac{r^2}{r_p^2}-1\right)$$

$$\frac{d\Delta T}{dt}\frac{1}{\Delta T}\frac{1}{A\Delta T+T_\infty} = B$$
$$\frac{d\Delta T}{dt}\frac{1}{\Delta T(T_\infty+A\Delta T)} = B$$

From an integral table, the corresponding integral is:

$$\int\frac{du}{u(a+bu)} = \frac{1}{a}\ln\left|\frac{u}{a+bu}\right|$$

where $a = T_\infty$, $b = A$ and $u = \Delta T$:

$$\int\frac{d\Delta T}{\Delta T(T_\infty+A\Delta T)} = \int B dt$$
$$\frac{1}{T_\infty}\ln\left|\frac{\Delta T}{T_\infty+A\Delta T}\right| = Bt+\mathcal{C}$$
$$\ln\left|\frac{\Delta T}{T_\infty+A\Delta T}\right| = T_\infty Bt+\mathcal{C}T_\infty$$

Since A and ΔT are always positive, can take away the absolute value signs:

$$\ln\left(\frac{\Delta T}{T_\infty+A\Delta T}\right) = T_\infty Bt+\mathcal{C}T_\infty$$
$$\exp\left[\ln\left(\frac{\Delta T}{T_\infty+A\Delta T}\right)\right] = \exp\left(T_\infty Bt+\mathcal{C}T_\infty\right)$$
$$\frac{\Delta T}{T_\infty+A\Delta T} = \exp\left(T_\infty Bt+\mathcal{C}T_\infty\right)$$
$$\Delta T = (T_\infty+A\Delta T)\exp\left(T_\infty Bt+\mathcal{C}T_\infty\right)$$
$$\Delta T = T_\infty\exp\left(T_\infty Bt+\mathcal{C}T_\infty\right)+A\Delta T\exp\left(T_\infty Bt+\mathcal{C}T_\infty\right)$$
$$\Delta T - A\Delta T\exp\left(T_\infty Bt+\mathcal{C}T_\infty\right) = T_\infty\exp\left(T_\infty Bt+\mathcal{C}T_\infty\right)$$
$$\Delta T\left[1-A\exp\left(T_\infty Bt+\mathcal{C}T_\infty\right)\right] = T_\infty\exp\left(T_\infty Bt+\mathcal{C}T_\infty\right)$$
$$\Delta T = \frac{T_\infty\exp\left(T_\infty Bt+T_\infty\mathcal{C}\right)}{1-A\exp\left(T_\infty Bt+\mathcal{C}T_\infty\right)}$$

The value of $\mathcal{C}$ can be found by using an initial condition. This initial condition is: $\Delta T(t=0) = \Delta T_0 = 100$ K for the current problem. Note that $t = 0$ here does not correspond with the tunnel start time or even the time after a laser pulse is fired t_p. Rather, in order to simplify the equations, $t = 0$ corresponds to the time after the thermal perturbation has convected downstream to the measurement location used by Schmisseur [43]. For speeds in the PQFLT, this time offset is about 44 μs. To convert this time t into one that corresponds to the time after each laser pulse, the formula $t_p = t + 44 \times 10^{-6}$ s will be used. Plugging this in:

$$\begin{aligned}
\Delta T_0 &= \frac{T_\infty \exp\left(T_\infty B \cdot 0 + T_\infty \mathcal{C}\right)}{1 - A\exp\left(T_\infty B \cdot 0 + \mathcal{C} T_\infty\right)} \\
\Delta T_0 &= \frac{T_\infty \exp\left(T_\infty \mathcal{C}\right)}{1 - A\exp\left(\mathcal{C} T_\infty\right)} \\
\Delta T_0\left[1 - A\exp\left(\mathcal{C} T_\infty\right)\right] &= T_\infty \exp\left(T_\infty \mathcal{C}\right) \\
\Delta T_0 - A\Delta T_0 \exp\left(\mathcal{C} T_\infty\right) &= T_\infty \exp\left(T_\infty \mathcal{C}\right) \\
\Delta T_0 &= T_\infty \exp\left(T_\infty \mathcal{C}\right) + A\Delta T_0 \exp\left(\mathcal{C} T_\infty\right) \\
\Delta T_0 &= \left(T_\infty + A\Delta T_0\right)\exp\left(\mathcal{C} T_\infty\right) \\
\frac{\Delta T_0}{T_\infty + A\Delta T_0} &= \exp\left(\mathcal{C} T_\infty\right) \\
\ln\left(\frac{\Delta T_0}{T_\infty + A\Delta T_0}\right) &= \ln\left[\exp\left(\mathcal{C} T_\infty\right)\right] \\
\ln\left(\frac{\Delta T_0}{T_\infty + A\Delta T_0}\right) &= \mathcal{C} T_\infty \\
\mathcal{C} &= \frac{1}{T_\infty}\ln\left(\frac{\Delta T_0}{T_\infty + A\Delta T_0}\right)
\end{aligned}$$

which gives:

$$\Delta T(t) = \frac{T_\infty \exp\left(T_\infty B t + T_\infty \cdot \frac{1}{T_\infty}\ln\left(\frac{\Delta T_0}{T_\infty + A\Delta T_0}\right)\right)}{1 - A\exp\left(T_\infty B t + T_\infty \cdot \frac{1}{T_\infty}\ln\left(\frac{\Delta T_0}{T_\infty + A\Delta T_0}\right)\right)}$$

$$\Delta T(t) = \frac{T_\infty \exp\left(T_\infty B t + \ln\left(\frac{\Delta T_0}{T_\infty + A\Delta T_0}\right)\right)}{1 - A\exp\left(T_\infty B t + \ln\left(\frac{\Delta T_0}{T_\infty + A\Delta T_0}\right)\right)}$$

$$\Delta T(t) = \frac{T_\infty \exp\left(T_\infty B t\right) \cdot \exp\left(\ln\left(\frac{\Delta T_0}{T_\infty + A\Delta T_0}\right)\right)}{1 - A\exp\left(T_\infty B t\right) \cdot \exp\left(\ln\left(\frac{\Delta T_0}{T_\infty + A\Delta T_0}\right)\right)}$$

$$\Delta T(t) = \frac{T_\infty \exp\left(T_\infty B t\right)\left(\frac{\Delta T_0}{T_\infty + A\Delta T_0}\right)}{1 - A\exp\left(T_\infty B t\right)\left(\frac{\Delta T_0}{T_\infty + A\Delta T_0}\right)}$$

$$\Delta T(t) = \frac{T_\infty \exp\left(T_\infty B t\right)\left(\frac{\Delta T_0}{T_\infty + A\Delta T_0}\right)}{1 - A\exp\left(T_\infty B t\right)\left(\frac{\Delta T_0}{T_\infty + A\Delta T_0}\right)} \cdot \frac{T_\infty + A\Delta T_0}{T_\infty + A\Delta T_0}$$

$$\Delta T(t) = \frac{T_\infty \Delta T_0 \exp\left(T_\infty B t\right)}{T_\infty + A\Delta T_0 - A\Delta T_0 \exp\left(T_\infty B t\right)}$$

Plugging in the values for A and B make the equations:

$$\Delta T(t) = \frac{T_\infty \Delta T_0 \exp\left(T_\infty B t\right)}{T_\infty + A\Delta T_0\left[1 - \exp\left(T_\infty B t\right)\right]}$$

$$\Delta T(t) = \frac{T_\infty \Delta T_0 \exp\left[T_\infty \frac{k}{c_p}\frac{R}{p_\infty} \cdot \frac{24\ln 2}{r_p^2} \cdot \left(\frac{8}{3}\ln 2 \cdot \frac{r^2}{r_p^2} - 1\right) t\right]}{T_\infty + \exp\left(-4\ln 2 \cdot \frac{r^2}{r_p^2}\right) \Delta T_0 \left[1 - \exp\left[T_\infty \frac{k}{c_p}\frac{R}{p_\infty} \cdot \frac{24\ln 2}{r_p^2} \cdot \left(\frac{8}{3}\ln 2 \cdot \frac{r^2}{r_p^2} - 1\right) t\right]\right]}$$

Using Equation A.2, the perfect gas law,

$$\Delta T(t) = \frac{T_\infty \Delta T_0 \exp\left[\frac{k}{c_p \rho_\infty} \cdot \frac{24\ln 2}{r_p^2} \cdot \left(\frac{8}{3}\ln 2 \cdot \frac{r^2}{r_p^2} - 1\right) t\right]}{T_\infty + \exp\left(-4\ln 2 \cdot \frac{r^2}{r_p^2}\right) \Delta T_0 \left[1 - \exp\left[\frac{k}{c_p \rho_\infty} \cdot \frac{24\ln 2}{r_p^2} \cdot \left(\frac{8}{3}\ln 2 \cdot \frac{r^2}{r_p^2} - 1\right) t\right]\right]}$$

$$\Delta T(t) = \frac{T_\infty \Delta T_0 \exp\left[\frac{k}{c_p \rho_\infty} \cdot \frac{24\ln 2}{r_p^2} \cdot \left(\frac{8}{3}\ln 2 \cdot \frac{r^2}{r_p^2} - 1\right) t\right]}{T_\infty + \exp\left(-4\ln 2 \cdot \frac{r^2}{r_p^2}\right) \Delta T_0 \left[1 - \exp\left[\frac{k}{c_p \rho_\infty} \cdot \frac{24\ln 2}{r_p^2} \cdot \left(\frac{8}{3}\ln 2 \cdot \frac{r^2}{r_p^2} - 1\right) t\right]\right]}$$

and that the thermal diffusivity is defined as $\alpha = \frac{k}{\rho c_p}$

$$\Delta T(t) = \frac{T_\infty \Delta T_0 \exp\left[\alpha \cdot \frac{24\ln 2}{r_p^2} \cdot \left(\frac{8}{3}\ln 2 \cdot \frac{r^2}{r_p^2} - 1\right) t\right]}{T_\infty + \exp\left(-4\ln 2 \cdot \frac{r^2}{r_p^2}\right) \Delta T_0 \left[1 - \exp\left[\alpha \cdot \frac{24\ln 2}{r_p^2} \cdot \left(\frac{8}{3}\ln 2 \cdot \frac{r^2}{r_p^2} - 1\right) t\right]\right]} \quad \text{(A.6)}$$

Plugging equation A.6 into equation A.1, the temperature distribution for time then becomes

$$T = \frac{T_\infty \Delta T_0 \exp\left[\alpha \cdot \frac{24\ln 2}{r_p^2} \cdot \left(\frac{8}{3}\ln 2 \cdot \frac{r^2}{r_p^2} - 1\right) t\right] \exp\left(-4\ln 2 \cdot \frac{r^2}{r_p^2}\right)}{T_\infty + \exp\left(-4\ln 2 \cdot \frac{r^2}{r_p^2}\right) \Delta T_0 \left[1 - \exp\left[\alpha \cdot \frac{24\ln 2}{r_p^2} \cdot \left(\frac{8}{3}\ln 2 \cdot \frac{r^2}{r_p^2} - 1\right) t\right]\right]} + T_\infty$$

$$T = \frac{T_\infty \Delta T_0 \exp\left[\alpha \cdot \frac{24\ln 2}{r_p^2} \cdot \left(\frac{8}{3}\ln 2 \cdot \frac{r^2}{r_p^2} - 1\right) t - 4\ln 2 \cdot \frac{r^2}{r_p^2}\right]}{T_\infty + \exp\left(-4\ln 2 \cdot \frac{r^2}{r_p^2}\right) \Delta T_0 \left[1 - \exp\left[\alpha \cdot \frac{24\ln 2}{r_p^2} \cdot \left(\frac{8}{3}\ln 2 \cdot \frac{r^2}{r_p^2} - 1\right) t\right]\right]} + T_\infty$$

Using these two equations and Equation A.5, the temperature distribution over time and space can be represented by the equation:

$$\begin{aligned} T = T_\infty + & \\ & \left(T_\infty \Delta T_0 \exp\left[\alpha \cdot \frac{24 \ln 2}{r_p^2} \cdot \left(\frac{8}{3} \ln 2 \cdot \frac{r^2}{r_p^2} - 1 \right) t - 4 \ln 2 \cdot \frac{r^2}{r_p^2} \right] \right) / \\ & \left(T_\infty + \Delta T_0 \exp\left(-4 \ln 2 \cdot \frac{r^2}{r_p^2} \right) \right. \\ & \left. - \Delta T_0 \exp\left[\alpha \cdot \frac{24 \ln 2}{r_p^2} \cdot \left(\frac{8}{3} \ln 2 \cdot \frac{r^2}{r_p^2} - 1 \right) t - 4 \ln 2 \cdot \frac{r^2}{r_p^2} \right] \right) \end{aligned} \tag{A.7}$$

where ΔT_0 is the initial temperature at the center of the perturbation and α is the thermal diffusivity coefficient for air in the freestream.

A.3 Plots of the Results

Two scenarios are shown in this section: using values measured in the PQFLT [43] and using estimates from the PQFLT measurements applied to the BAM6QT conditions. The values used for the parameters in Equation A.7 are shown in Table A.1. The temperature distribution over time is shown in Figure A.3. These plots show that the temperature of the perturbation decays over time, by about as much as 67 K in 47 μs.

Table A.1 Table with parameters used for 1-D heat transfer calculation.

Parameter	**PQFLT**	**BAM6QT**
T_∞, K	71.0	52.8
ΔT_0, K	100	100
r_p, mm	1	1
α, m^2/s	5.07×10^{-4}	4.36×10^{-4}
p_0, kPa	68.9	621

The rate at which this temperature decay occurs can be seen by plotting the maximum temperature at the center of the perturbation versus the time elapsed.

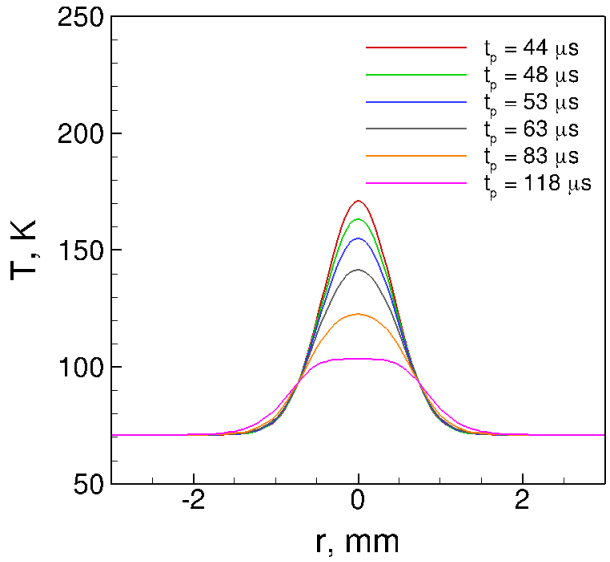

(a) PQFLT Conditions.

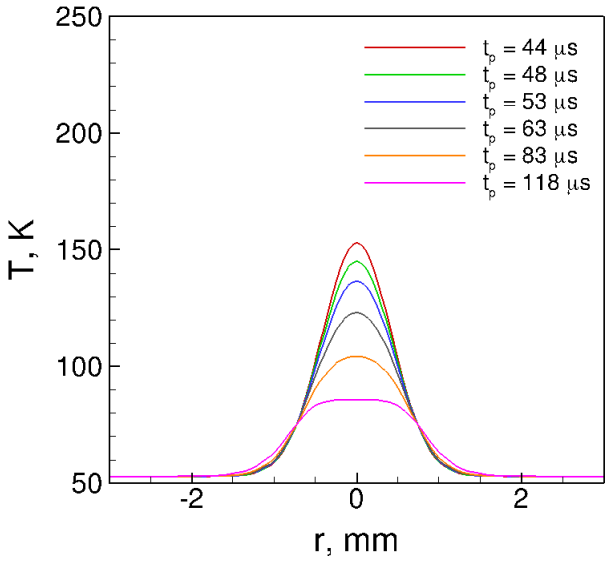

(b) BAM6QT Conditions.

Figure A.3. Evolution of the temperature distribution for an ideal laser-generated disturbance over time.

This temperature decay seems to level out after about 180 μs. This could be due to the numerical assumptions required for the calculations. The change maximum temperature at the center of the perturbation over time for both the PQFLT and BAM6QT is shown in Figure A.4.

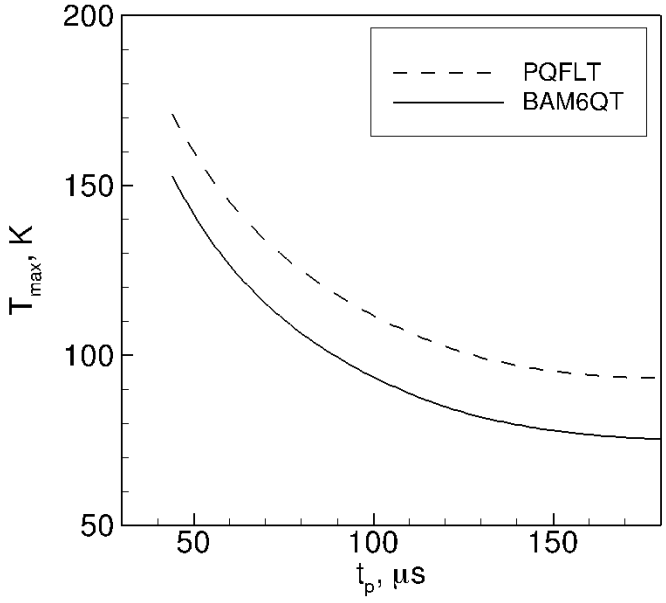

Figure A.4. A comparison of the calculated maximum temperature of the perturbation over time.

Appendix B: Run Conditions for Kulite Probe Measurements

These runs were all conducted in the BAM6QT. When the diaphragms burst and the run starts, $t = 0$. The flat laser window insert was installed in the 3×10-inch insert. The porthole windows were installed in the 7×14-inch insert. Bleed valves were open for all of the runs here. Laser energy was about 290 mJ/pulse for the runs starting with "14-" and 280 mJ/pulse for the runs starting with "15-." For reference, in the text, laser shot numbers start at 0 when $t = 0$.

Table B.1: Run conditions for Kulite probe measurements of freestream perturbation.

Run	$p_{0,i}$, **psia**	$T_{0,i}$, **°C**	z_{probe}, **m**	Δz_i, **mm**	y_i, **mm**	**Traverse Direction, Distance (mm)**
14-01	164.0	161.1	1.954	42.5	10.0	down, 8.0
14-02	164.0	160.8	1.954	42.5	10.0	down, 8.0
14-03	164.7	160.7	1.965	50.0	5.0	down, 10.0
14-04	164.5	161.3	1.965	50.0	−5.0	up, 10.0
14-05	164.5	164.5	1.965	50.0	−1.0	no movement
14-06	164.0	163.0	1.965	50.0	−2.0	no movement
14-07	164.5	163.2	1.965	50.0	+2.0	no movement
14-08	164.5	162.6	1.965	50.0	+1.0	no movement
14-09	164.4	162.5	1.965	50.0	0.0	no movement
14-10	164.2	165.5	1.965	50.0	+4.0	no movement
14-11	164.2	163.6	1.965	50.0	−4.0	no movement
14-12	164.7	162.7	1.965	50.0	−6.0	no movement
14-13	164.3	161.5	1.965	50.0	+4.0	no movement
14-14	122.3	162.5	1.965	50.0	−4.0	up, 10.0
14-15	121.9	162.1	1.965	50.0	+4.0	down, 10.0
14-16	93.6	163.6	1.965	50.0	+4.0	down, 10.0
14-17	93.5	163.8	1.965	50.0	−4.0	up, 10.0
14-18	165.1	163.8	1.978	63.0	0.0	no movement
14-19	164.5	162.5	1.978	63.0	+4.0	down, 10.0
14-20	94.1	163.6	1.978	63.0	+4.0	down, 10.0
14-21	93.3	163.8	1.978	63.0	−5.0	up, 10.0
14-22	122.4	161.8	1.978	63.0	−5.0	up, 10.0

Continued on next page...

Run	$p_{0,i}$, **psia**	$T_{0,i}$, **°C**	z_{probe}, **m**	Δz_i, **mm**	y_i, **mm**	**Traverse Direction, Distance (mm)**
14-23	123.1	162.5	1.978	63.0	+4.0	down, 10.0
14-24	165.6	165.9	1.978	63.0	+3.0	down, 10.0
14-25	163.9	162.1	2.015	103.5	−5.0	up, 10.0
14-26	164.3	159.6	2.015	103.5	+5.0	down, 10.0
14-27	163.9	158.1	2.015	103.5	0.0	no movement
14-28	93.2	157.0	2.015	103.5	+4.0	down, 9.0
14-29	92.8	156.4	2.015	103.5	−5.0	up, 10.0
14-30	122.6	164.7	2.015	103.5	−5.0	up, 10.0
14-31	121.8	162.4	2.015	103.5	−6.0	up, 10.0
14-32	122.8	161.5	2.015	103.5	+5.0	down, 9.0
14-33	163.9	163.2	2.015	103.5	+1.0	no movement
14-34	164.8	162.0	2.015	103.5	−1.0	no movement
14-35	164.6	162.2	2.015	103.5	+2.0	no movement
14-36	164.5	162.7	2.015	103.5	−2.0	no movement
14-37	164.2	162.6	2.015	103.5	−4.0	no movement
14-38	164.4	164.7	2.015	103.5	+4.0	no movement
14-39	164.1	162.4	2.015	103.5	+6.0	no movement
14-40	164.7	162.2	2.015	103.5	−6.0	no movement
14-41	164.4	162.5	2.015	103.5	−3.0	no movement
14-42	164.5	162.4	2.015	103.5	0.0	no movement
14-43	164.2	163.7	2.015	103.5	+3.0	no movement
15-01	164.8	163.7	2.195	250.5	−3.0	up, 4.0
15-02	164.8	162.7	2.195	250.5	+3.0	down, 4.0
15-03	165.5	161.6	2.195	250.5	+1.0	no movement
15-04	164.2	163.6	2.195	250.5	−6.0	up, 4.0
15-05	164.9	161.6	2.195	250.5	+6.0	down, 4.0
15-06	165.3	165.8	2.256	312.0	−6.0	down, 4.0
15-07	164.7	162.7	2.256	312.0	+1.0	down, 4.0
15-08	165.5	160.8	2.256	312.0	−6.0	up, 4.0
15-09	164.4	160.4	2.256	312.0	0	no movement
15-10	164.6	162.6	2.256	312.0	−1.0	up, 4.0
15-11	164.7	162.5	2.377	433.0	−1.0	up, 4.0
15-12	167.8	162.4	2.388	444.0	+1.0	down, 4.0
15-13	164.9	163.8	2.388	444.0	−1.0	up, 4.0
15-14	165.2	161.7	2.388	444.0	0	no movement
15-15	164.4	160.5	2.388	444.0	−6.0	up, 4.0
15-16	164.7	162.8	2.388	444.0	+6.0	down, 4.0

Continued on next page...

Run	$p_{0,i}$, **psia**	$T_{0,i}$, **°C**	z_{probe}, **m**	Δz_i, **mm**	y_i, **mm**	**Traverse Direction, Distance (mm)**
15-17	165.0	162.8	2.309	364.5	+1.0	down, 4.0
15-18	164.1	164.7	2.313	368.5	+1.0	down, 4.0
15-19	165.0	162.1	2.313	368.5	−1.0	up, 4.0
15-20	165.0	161.4	2.313	368.5	0	no movement
15-21	163.9	161.0	2.204	260.0	−1.0	up, 4.0
15-22	165.5	160.8	2.204	260.0	+1.0	down, 4.0
15-23	164.5	164.7	2.204	260.0	0	no movement
15-24	164.3	163.3	2.204	260.0	+6.0	down, 4.0
15-25	165.9	162.5	2.204	260.0	−6.0	up, 4.0
15-26	164.8	161.7	2.313	368.5	−6.0	up, 4.0
15-27	164.1	160.4	2.313	368.5	+6.0	down, 4.0
15-28	164.6	160.2	2.152	208.0	+1.0	down, 4.0
15-29	165.0	160.4	2.152	208.0	−1.0	up, 4.0
15-30	164.2	164.6	2.152	208.0	0	no movement
15-31	164.9	162.2	2.152	208.0	−6.0	up, 4.0
15-32	164.6	159.7	2.152	208.0	+6.0	down, 4.0
15-33	162.8	158.7	2.152	208.0	0	no movement
15-34	163.8	158.0	2.388	444.0	0	no movement

Appendix C: Run Conditions for PCB Probe Measurements

These runs were all conducted in the BAM6QT. The flat laser window insert was installed in the 3×10-inch insert. The porthole window was installed in the 7×14-inch insert. Bleed valves were open for all of the runs here. Laser energy was about 280 mJ/pulse. For reference, in the text, laser shot numbers start at 0 when $t = 0$.

Table C.1: Run conditions for PCB probe measurements of freestream perturbation.

Run	$p_{0,i}$, **psia**	$T_{0,i}$, **°C**	z_{probe}, **m**	Δz_i, **mm**	y_i, **mm**	**Traverse Direction, Distance (mm)**
16-17	163.3	162.9	2.137	210.5	−4.0	up, 10.0
16-18	163.0	158.9	2.137	210.5	−1.0	down, 6.0
16-19	163.2	157.6	2.137	210.5	0	no movement
16-20	162.5	157.0	2.137	210.5	0	no movement
16-21	161.6	156.5	2.145	219.0	−1.0	no movement
16-22	162.3	153.9	2.145	219.0	−2.0	no movement
16-23	164.9	162.6	2.145	219.0	0	no movement
16-24	163.1	158.8	2.145	219.0	+1.0	no movement
16-25	163.1	156.6	2.145	219.0	−3.0	no movement
16-26	162.8	155.9	2.145	219.0	+2.0	no movement
16-27	162.8	158.9	2.145	219.0	+3.0	no movement
16-28	163.2	157.6	2.145	219.0	−4.0	no movement
16-29	165.0	156.4	2.145	219.0	+4.0	no movement
16-30	163.2	161.8	2.145	219.0	+6.0	no movement
16-31	163.2	159.2	2.145	219.0	−6.0	no movement
16-32	163.1	158.1	2.145	219.0	−8.0	no movement
16-33	162.6	157.2	2.145	219.0	+8.0	no movement
16-34	164.4	156.7	2.145	219.0	+10.0	no movement
16-35	163.5	159.1	2.145	219.0	−10.0	no movement
16-36	162.1	156.6	2.145	219.0	0	no movement
16-37	161.7	154.2	2.145	219.0	0	no movement
16-38	163.1	163.5	2.145	219.0	0	no movement
16-39	164.4	162.0	2.145	219.0	0	no movement
16-40	163.8	160.4	2.145	219.0	0	no movement

Appendix D: Run Conditions for the Forward-Facing Cavity Experiment

These runs were all conducted in the BAM6QT. When the diaphragms burst and the run starts, $t = 0$. The contoured stainless steel blank was installed in the 3×10-inch insert for runs with a "9-" or a "11-" prefix. The flat laser window insert was installed in the 3×10-inch insert for runs with a "12-" or a "13-" prefix. For reference, in the text, laser shot numbers start at 0 when $t = 0$.

Table D.1: Run numbers and conditions for forward-facing cavity measurements.

Run	$p_{0,i}$, **psia**	$T_{0,i}$, **°C**	**Bleed Valve Position**	L/D	E_{pulse}, **mJ**	Δz_i, **mm**
9-01	161.9	161.0	open	0.00	0.00	
9-02	160.9	158.8	closed	0.00	0.00	
9-03	161.6	157.5	open	1.00	0.00	
9-04	161.2	156.5	open	1.00	0.00	
9-05	161.1	155.9	closed	1.00	0.00	
9-06	161.6	163.7	open	2.00	0.00	
9-07	161.8	160.8	open	2.00	0.00	
9-08	161.9	159.2	closed	2.00	0.00	
9-09	161.6	157.0	closed	2.00	0.00	
9-10	161.2	156.1	open	3.00	0.00	
9-11	162.2	154.8	closed	3.00	0.00	
9-12	162.1	166.7	open	4.00	0.00	
9-13	161.3	162.4	closed	4.00	0.00	
9-14	161.5	160.9	open	5.00	0.00	
9-15	161.4	158.1	closed	5.00	0.00	
9-16	161.5	157.2	open	0.00	0.00	
9-17	161.3	156.4	closed	0.00	0.00	
9-18	162.0	162.1	open	0.50	0.00	
9-19	161.1	160.1	closed	0.50	0.00	
9-20	161.9	159.6	open	0.75	0.00	
9-21	161.7	163.3	closed	0.75	0.00	
9-22	161.7	160.8	open	1.50	0.00	
9-23	161.7	161.4	open	1.50	0.00	
9-24	161.8	159.6	closed	1.50	0.00	
9-25	161.6	160.2	open	1.30	0.00	
9-26	161.4	158.3	closed	1.30	0.00	

Continued on next page...

Run	$p_{0,i}$, **psia**	$T_{0,i}$, **°C**	**Bleed Valve Position**	L/D	E_{pulse}, **mJ**	Δz_i, **mm**
9-27	161.8	163.5	open	1.20	0.00	
9-28	161.5	162.8	closed	1.20	0.00	
9-29	161.8	161.2	open	1.10	0.00	
9-30	161.6	157.4	closed	1.10	0.00	
9-31	161.8	156.7	closed	1.10	0.00	
9-32	161.3	157.1	open	1.15	0.00	
9-33	161.6	156.8	closed	1.15	0.00	
9-34	161.8	158.2	open	0.25	0.00	
9-35	161.2	157.4	closed	0.25	0.00	
9-36	161.5	157.3	open	1.20	0.00	
9-37	161.9	163.0	open	1.40	0.00	
9-38	161.9	162.0	open	1.75	0.00	
9-39	161.7	161.4	open	1.15	0.00	
9-40	161.5	161.4	open	1.25	0.00	
9-41	160.7	157.8	open	1.25	0.00	
9-42	149.9	159.3	open	1.25	0.00	
11-01	161.8	166.0	open	1.50	0.00	
11-02	171.3	162.6	open	1.50	0.00	
11-03	143.1	160.9	open	1.50	0.00	
11-04	122.9	158.5	open	1.50	0.00	
11-05	95.7	164.6	open	1.50	0.00	
11-06	152.8	161.7	open	1.50	0.00	
11-07	105.0	159.0	open	1.50	0.00	
11-08	114.0	160.3	open	1.50	0.00	
11-09	168.8	157.9	open	1.50	0.00	
11-10	128.9	155.2	open	1.50	0.00	
12-01	162.6	162.9	open	1.00	0.00	
12-02	163.8	161.2	open	1.00	297.5	476.0
12-03	163.9	161.2	open	1.00	297.5	28.6
12-04	163.9	162.3	open	.00	297.5	28.6
12-05	163.5	159.5	open	1.00	238.2	28.6
12-06	145.5	159.3	open	1.00	297.5	28.6
12-07	107.0	157.2	open	1.00	297.5	28.6
12-08	79.8	157.1	open	1.00	297.5	28.6
12-09	55.3	158.9	open	1.00	297.5	28.6
12-10	42.0	156.8	open	1.00	297.5	28.6
12-11	165.3	159.1	open	0.80	238.2	28.6
12-12	164.3	160.3	open	0.75	238.2	28.6
12-13	164.1	158.3	open	0.50	238.2	28.6

Continued on next page...

Run	$p_{0,i}$, **psia**	$T_{0,i}$, **°C**	**Bleed Valve Position**	L/D	E_{pulse}, **mJ**	Δz_i, **mm**
12-14	164.1	157.1	open	0.50	238.2	28.6
12-15	163.9	159.7	open	0.25	238.2	28.6
12-16	162.2	158.2	open	0.00	238.2	28.6
12-17	164.3	157.6	open	0.50	238.2	28.6
12-18	165.0	161.4	open	0.60	238.2	28.6
12-19	164.7	159.3	open	0.40	238.2	28.6
12-20	164.4	157.2	open	0.20	238.2	28.6
12-21	95.5	161.3	open	0.90	238.2	28.6
12-22	164.1	159.6	open	0.90	238.2	28.6
12-23	164.7	158.7	open	0.10	238.2	28.6
13-01	163.1	163.1	open	1.00	234.0	93.5
13-02	164.5	160.5	open	1.00	234.0	103.5
13-03	165.4	163.9	open	1.00	234.0	90.0
13-04	164.8	160.6	open	1.00	234.0	130.0
13-05	165.2	159.5	open	1.00	234.0	191.0
13-06	165.1	157.7	open	1.00	234.0	206.0
13-07	165.5	161.6	open	1.00	234.0	260.0
13-08	165.2	159.5	open	1.00	234.0	315.0
13-09	165.4	158.3	open	1.00	234.0	374.0
13-10	166.1	157.7	open	1.00	234.0	456.0
13-11	165.3	156.6	open	1.00	234.0	512.6
13-12	165.1	161.8	open	1.00	234.0	470.0
13-13	165.5	159.1	open	1.00	0.00	
13-14	125.7	158.4	open	1.00	234.0	470.0
13-15	124.9	158.0	open	1.00	0.00	
13-16	165.3	157.4	open	0.80	234.0	470.0
13-17	123.8	161.7	open	0.80	234.0	470.0
13-18	164.4	159.8	open	0.80	0.00	
13-19	125.5	159.4	open	0.80	0.00	
13-20	165.6	158.0	open	0.60	234.0	470.0
13-21	125.0	158.0	open	0.60	234.0	470.0
13-22	165.4	160.4	open	0.60	0.00	
13-23	125.1	159.8	open	0.60	0.00	
13-24	164.5	160.9	open	0.50	234.0	470.0
13-25	126.7	161.4	open	0.50	234.0	470.0
13-26	165.2	162.2	open	0.40	234.0	470.0
13-27	124.5	162.5	open	0.401	234.0	470.0
13-28	165.4	162.7	open	0.40	0.00	
13-29	124.4	162.0	open	0.40	0.00	

Continued on next page...

Run	$p_{0,i}$, **psia**	$T_{0,i}$, **°C**	**Bleed Valve Position**	L/D	E_{pulse}, **mJ**	Δz_i, **mm**
13-30	164.8	159.7	open	0.00	234.0	470.0
13-31	165.0	158.1	open	0.00	0.00	
13-32	124.8	156.9	open	0.00	234.0	470.0
13-33	124.6	156.3	open	0.00	0.00	470.0
13-34	40.6	154.6	open	1.00	312.5	470.0
13-35	40.8	154.2	open	1.00	312.5	470.0
13-36	163.5	159.8	open	1.50	234.0	470.0
13-37	125.6	159.3	open	1.50	234.0	470.0
13-38	165.9	158.3	open	0.90	234.0	470.0
13-39	122.8	156.0	open	0.90	234.0	470.0
13-40	165.7	156.5	open	0.90	0.00	
13-41	126.2	156.7	open	0.90	0.00	
13-42	165.9	160.2	open	0.70	234.0	470.0
13-43	126.6	159.2	open	0.70	234.0	470.0
13-44	165.6	158.4	open	0.70	0.00	
13-45	126.0	157.7	open	0.70	0.00	
13-46	165.9	158.5	open	0.50	0.00	
13-47	125.4	157.9	open	0.50	0.00	

Appendix E: Run Conditions for the Flared Cone Experiment

These runs were all conducted in the BAM6QT. The flat laser window insert was installed in the 3×10-inch insert, except where indicated. For reference, in the text, laser shot numbers start at 0 when $t = 0$. Run numbers preceded by "17-" were conducted in August 2013 and used primarily to determine possible test conditions and model modifications. After the "17-" tests, sensor rays at $\pm 120°$ were added to simultaneously measure around the azimuth of the cone. Run numbers preceded by "18-" were conducted in September 2013 and used primarily to determine the usable stagnation pressures and model positioning.

Table E.1: Run conditions for boundary-layer measurements of the interaction between freestream laser perturbations and the flared cone boundary layer.

Run	$p_{0,i}$, **psia**	$T_{0,i}$, **°C**	r_n, **mm**	Δz_i, **mm**	**Offset, mm**	**Toward Ray**	E_{pulse}, **mJ**
18-01	137.9	161.2	1	No laser perturbation used			
18-02	138.5	157.9	1	No laser perturbation used			
18-03	137.0	156.4	1	No laser perturbation used			
18-04	137.2	162.1	1	No laser perturbation used			
18-05	136.6	161.2	1	No laser perturbation used			
18-06	136.9	161.1	1	No laser perturbation used			
18-07	125.7	159.9	1	No laser perturbation used			
18-08	125.5	160.3	1	118.0	No offset		262.2
18-09	113.1	157.6	1	118.0	No offset		262.2
18-10	95.0	157.6	1	118.0	No offset		262.2
18-11	85.8	157.4	1	118.0	No offset		262.2
18-12	84.4	156.2	1	118.0	No offset		262.2
18-13	76.6	155.4	1	118.0	No offset		262.2
18-14	103.9	154.1	1	118.0	No offset		262.2
18-15	136.9	155.3	1	118.0	No offset		262.2
18-16	125.8	158.4	0.16	87.5	No offset		262.2
18-17	116.1	157.3	0.16	87.5	No offset		262.2
18-18	105.4	156.4	0.16	87.5	No offset		262.2
18-19	94.3	155.2	0.16	87.5	No offset		262.2
18-20	85.6	155.3	0.16	87.5	No offset		262.2
18-21	85.7	155.9	0.16	87.5	No offset		262.2

Continued on next page...

Run	$p_{0,i}$, **psia**	$T_{0,i}$, **°C**	r_n, **mm**	Δz_i, **mm**	**Offset, mm**	**Toward Ray**	E_{pulse}, **mJ**
18-22	84.9	157.3	0.16	87.5	No offset		262.2
18-23	77.4	154.9	0.16	87.5	No offset		262.2
18-24	77.2	155.0	0.16	87.5	No offset		262.2
18-25	70.4	155.3	0.16	87.5	No offset		262.2
18-26	74.8	155.1	0.16	87.5	No offset		262.2
18-27	74.5	160.5	0.16	87.5	No offset		262.2
18-28	76.9	157.9	0.16	87.5	No offset		262.2
18-29	88?	155.6?	0.16	87.5	No offset		262.2
18-30	87.2	155.8	1	118.0	No offset		262.2
18-31	117.2	156.9	1	118.0	No offset		262.2
18-32	106.8	154.5	1	118.0	No offset		262.2
18-33	125.8	155.0	1	118.0	No offset		262.2
18-34	107.4	158.7	1	111.5	No offset		262.2
18-35	90.2	155.4	1	111.5	No offset		262.2
18-36	119.8	155.9	1	111.5	No offset		262.2
18-37	74.4	160.7	0.16	81.0	No offset		262.2
18-38	85.9	161.6	0.16	81.0	No offset		262.2
18-39	75.4	161.7	0.16	81.0	No offset		262.2
18-40	83.5	161.6	0.16	81.0	No offset		262.2
18-41	93.8	161.3	0.16	81.0	No offset		262.2
18-42	94.9	160.1	0.16	81.0	No offset		262.2
18-43	106.4	161.5	1	111.3	No offset		262.2
18-44	116.2	162.7	1	111.3	No offset		262.2
18-45	116.4	162.1	1	111.3	No offset		262.2
18-46	125.6	162.9	1	111.3	No offset		262.2
18-47	94.1	160.4	0.16	80.8	No offset		262.2
18-48	86.8	158.2	0.16	80.8	No offset		262.2
18-49	78.9	157.8	0.16	80.8	No offset		262.2
18-50	116.8	156.2	1	114.3	No offset		262.2
18-51	116.3	161.8	1	114.3	No offset		262.2
18-52	113.6	163.0	1	114.3	No offset		262.2
18-53	86.2	162.2	0.16	83.8	No offset		262.2
18-54	85.5	161.5	0.16	83.8	No offset		262.2
18-55	81.2	159.6	0.16	83.8	No offset		262.2
18-56	81.0	157.5	0.16	83.8	No offset		262.2
18-57	95.0	162.5	0.16	No laser perturbation used			
18-58	86.3	163.2	0.16	No laser perturbation used			
18-59	80.8	161.9	0.16	No laser perturbation used			
18-60	75.2	163.6	0.16	No laser perturbation used			

Continued on next page...

Run	$p_{0,i}$, **psia**	$T_{0,i}$, **°C**	r_n, **mm**	Δz_i, **mm**	**Offset, mm**	**Toward Ray**	E_{pulse}, **mJ**
18-61	116.4	161.1	1	No laser perturbation used			
18-62	116.4	159.4	1	No laser perturbation used			
18-63	105.8	156.6	1	No laser perturbation used			
18-64	95.7	156.5	1	No laser perturbation used			
19-01	118.6	165.2	1	No laser perturbation used			
19-02	114.9	166.6	1	No laser perturbation used			
19-03	115.4	165.8	1	134.2	No offset		273.0
19-04	106.3	163.8	1	134.2	No offset		273.0
19-05	106.2	164.1	1	134.2	No offset		273.0
19-06	90.9	161.2	0.16	106.0	No offset		273.0
19-07	84.5	160.5	0.16	106.0	No offset		273.0
19-08	106.6	168.1	1	134.2	No offset		273.0
19-09	92.4	163.8	0.16	104.7	1.5	0	273.0
19-10	84.1	164.1	0.16	104.7	1.5	0	273.0
19-11	113.4	163.9	1	132.9	1.5	0	273.0
19-12	105.1	161.7	1	132.9	1.5	0	273.0
19-13	91.9	160.3	0.16	92.4	1.5	+120	273.0
19-14	84.6	166.8	0.16	92.4	1.5	+120	273.0
19-15	115.7	164.6	1	120.6	1.5	+120	273.0
19-16	106.2	163.3	1	120.6	1.5	+120	273.0
19-17	115.6	165.5	1	132.9	1.5	−120	273.0
19-18	104.9	164.4	1	132.9	1.5	−120	273.0
19-19	93.0	162.5	0.16	104.7	1.5	−120	273.0
19-20	83.8	161.7	0.16	104.7	1.5	−120	273.0
19-21	84.7	166.6	0.16	108.8	No offset		273.0
19-22	91.7	163.6	0.16	108.8	No offset		273.0
19-23	115.7	161.3	1	137.0	No offset		273.0
19-24	106.1	161.6	1	137.0	No offset		273.0
19-25	105.6	164.9	1	134.4	3.0	+120	273.0
19-26	115.1	163.8	1	134.4	3.0	+120	273.0
19-27	106.4	163.8	1	134.4	3.0	+120	273.0
19-28	92.3	160.2	0.16	106.2	3.0	+120	273.0
19-29	84.4	160.8	0.16	106.2	3.0	+120	273.0
19-30	84.3	162.7	0.16	106.2	3.0	0	273.0
19-31	93.4	163.8	0.16	106.2	3.0	0	273.0
19-32	115.7	163.9	1	134.3	3.0	0	273.0
19-33	106.3	162.6	1	134.3	3.0	0	273.0
19-34	105.9	162.5	1	134.3	3.0	0	273.0
19-35	115.9	165.8	1	133.8	3.0	0	273.0

Continued on next page...

Run	$p_{0,i}$, **psia**	$T_{0,i}$, **°C**	r_n, **mm**	Δz_i, **mm**	**Offset, mm**	**Toward Ray**	E_{pulse}, **mJ**
19-36	105.9	165.0	1	133.8	3.0	0	273.0
19-37	93.0	163.8	0.16	105.7	3.0	0	273.0
19-38	84.2	163.9	0.16	105.7	3.0	0	273.0
19-39	84.5	163.0	0.16	108.5	3.0	−120	273.0
19-40	93.3	164.5	0.16	108.5	3.0	−120	273.0
19-41	115.9	163.9	1	136.7	3.0	−120	273.0
19-42	106.1	166.2	1	136.7	3.0	−120	273.0
19-43	106.3	164.4	1	141.8	No offset		273.0
19-44	115.4	162.9	1	141.8	No offset		273.0
19-45	106.3	161.7	1	141.8	No offset		273.0
19-46	93.5	163.6	0.16	113.6	No offset		273.0
19-47	84.3	164.7	0.16	113.6	No offset		273.0

Appendix F: Part Drawings

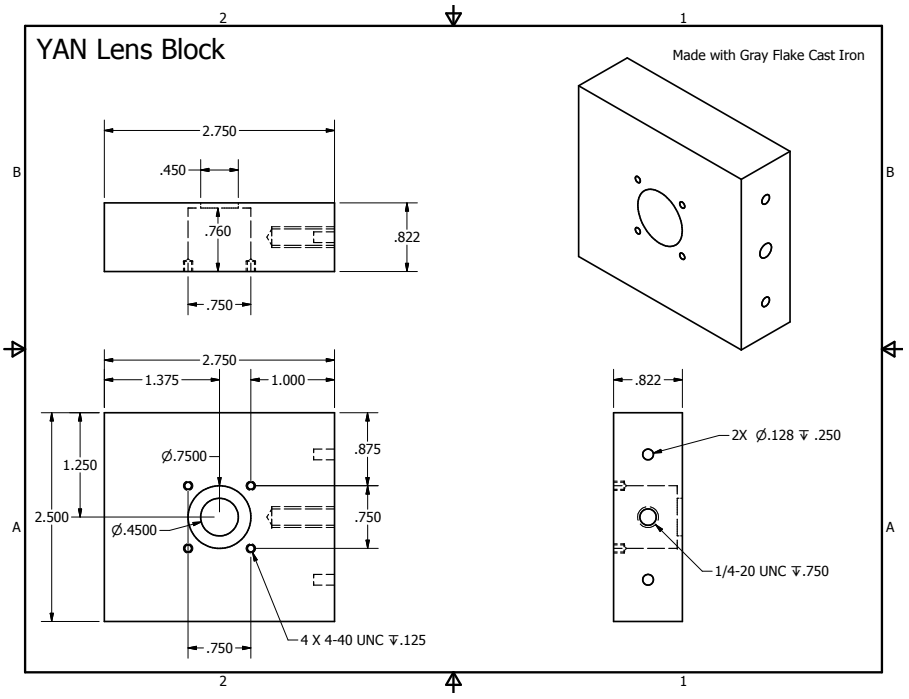

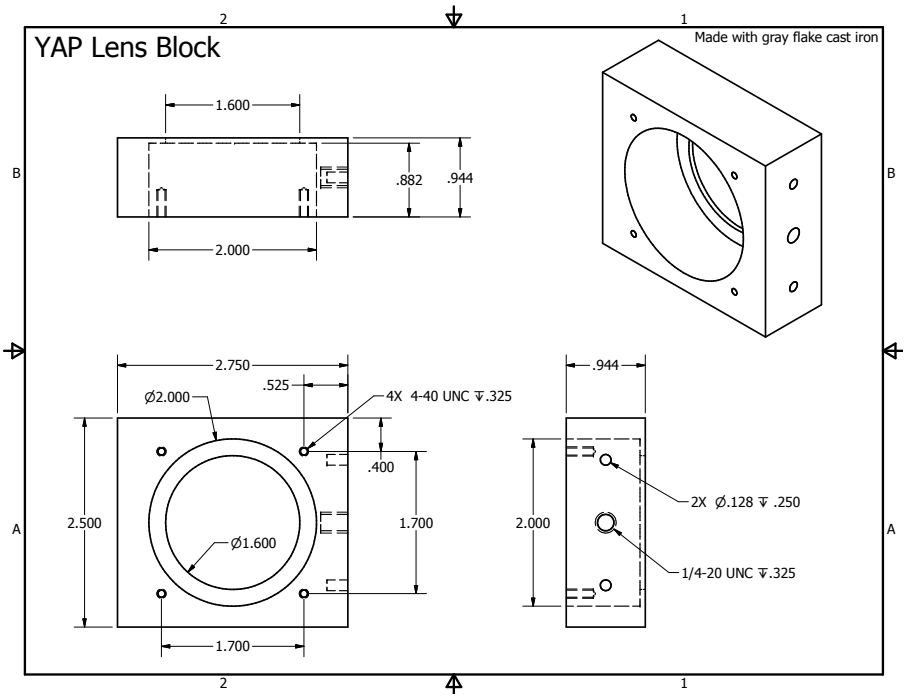

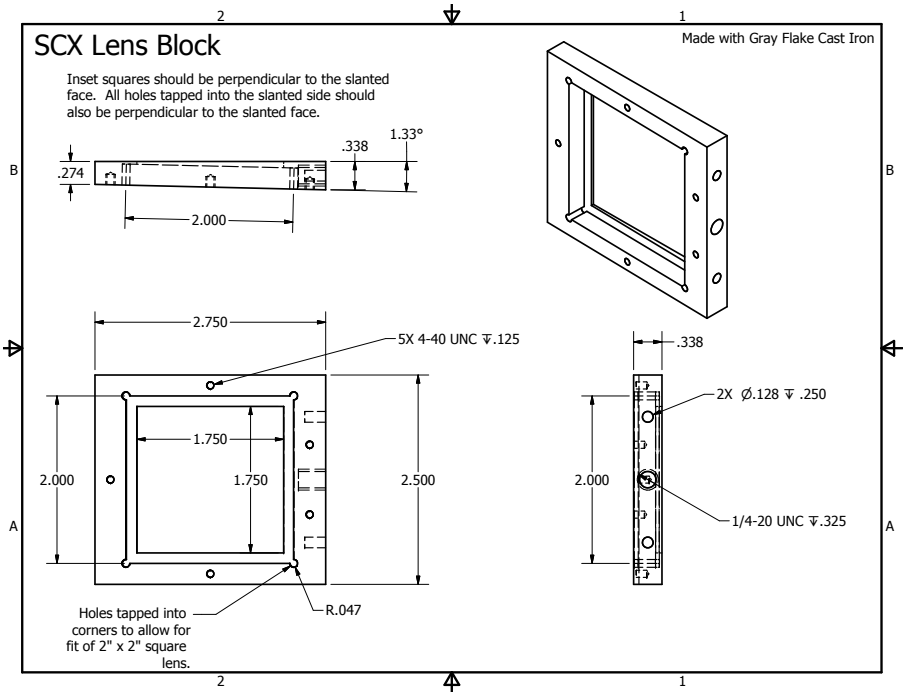
SCX Lens Block
Made with Gray Flake Cast Iron
Inset squares should be perpendicular to the slanted face. All holes tapped into the slanted side should also be perpendicular to the slanted face.
1.33°
.338
.274
2.000
2.750
5X 4-40 UNC ↧.125
.338
2X Ø.128 ↧ .250
1.750
2.000
1.750
2.500
2.000
1/4-20 UNC ↧.325
Holes tapped into corners to allow for fit of 2" x 2" square lens.
R.047

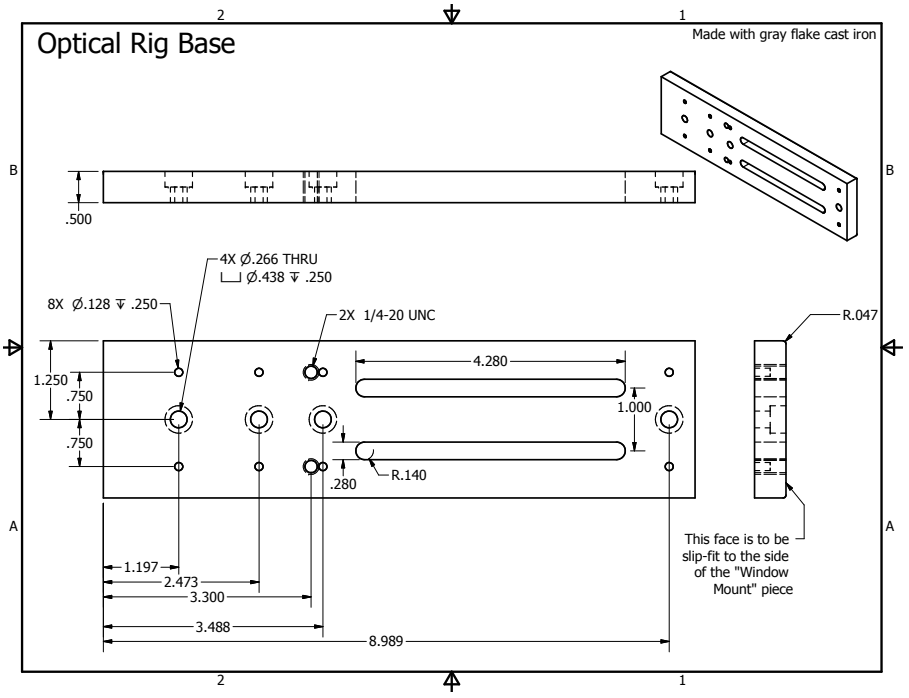
Optical Rig Base
Made with gray flake cast iron
.500
4X Ø.266 THRU
⌴ Ø.438 ↧ .250
8X Ø.128 ↧ .250
2X 1/4-20 UNC
R.047
4.280
1.250
.750
.750
1.000
.280
R.140
This face is to be slip-fit to the side of the "Window Mount" piece
1.197
2.473
3.300
3.488
8.989

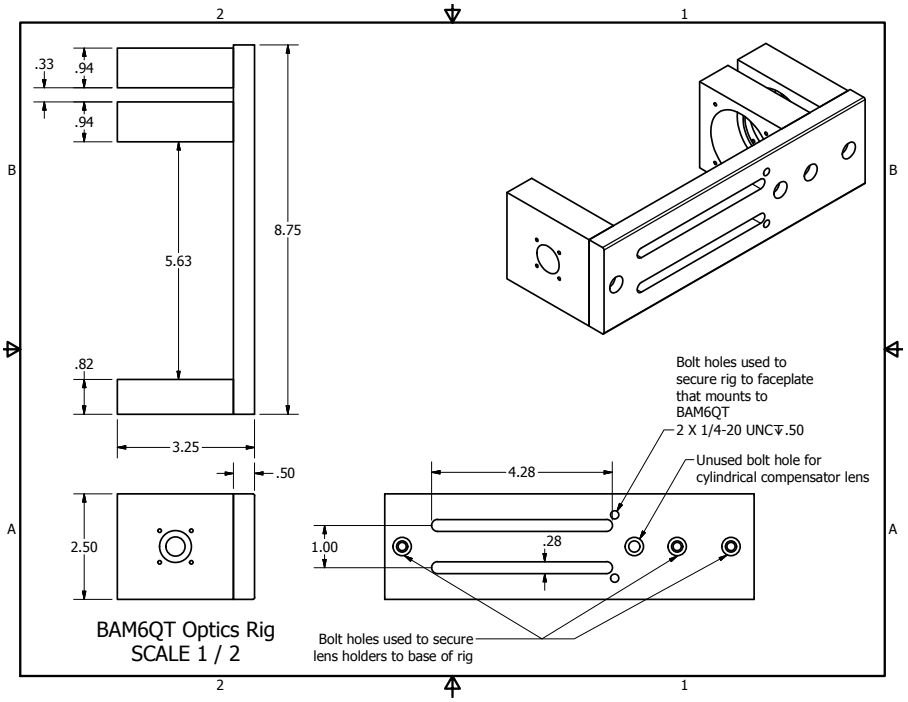
.33
.94
.94
8.75
5.63
.82
3.25
.50
2.50
BAM6QT Optics Rig
SCALE 1 / 2
Bolt holes used to
secure rig to faceplate
that mounts to
BAM6QT
2 X 1/4-20 UNC↧.50
Unused bolt hole for
cylindrical compensator lens
4.28
1.00
.28
Bolt holes used to secure
lens holders to base of rig

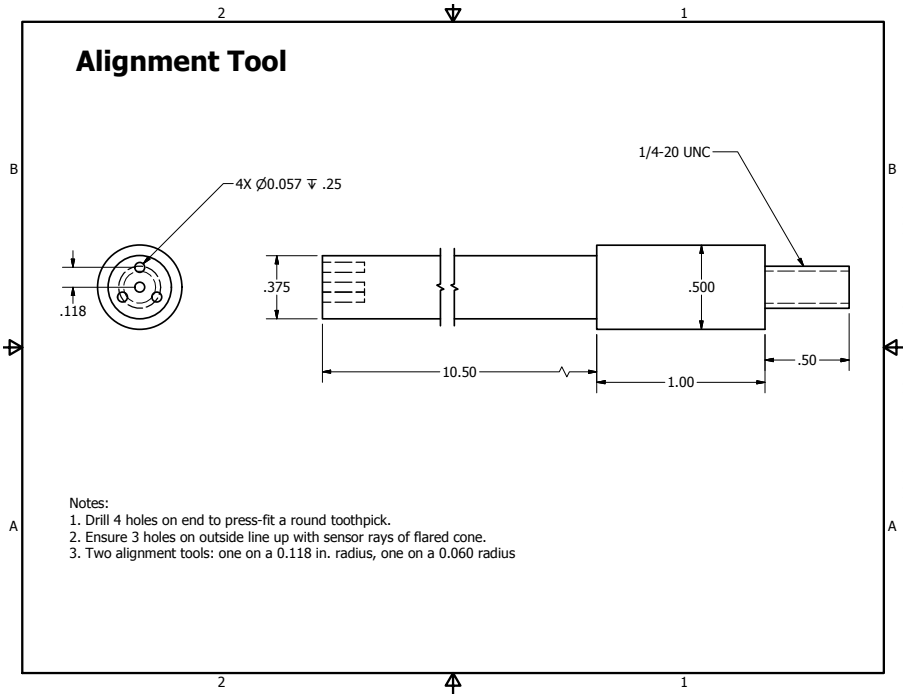
Alignment Tool
1/4-20 UNC
4X Ø0.057 ↧ .25
.118
.375
.500
10.50
1.00
.50
Notes:
1. Drill 4 holes on end to press-fit a round toothpick.
2. Ensure 3 holes on outside line up with sensor rays of flared cone.
3. Two alignment tools: one on a 0.118 in. radius, one on a 0.060 radius

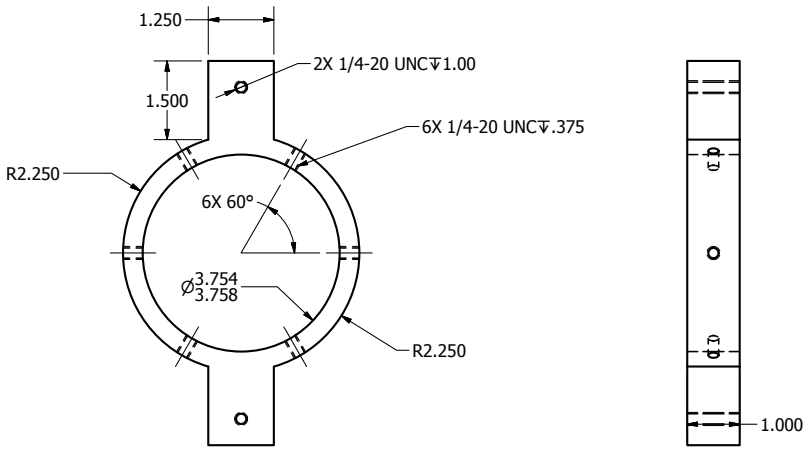

PCT Nozzle Collar
SCALE 1 / 2

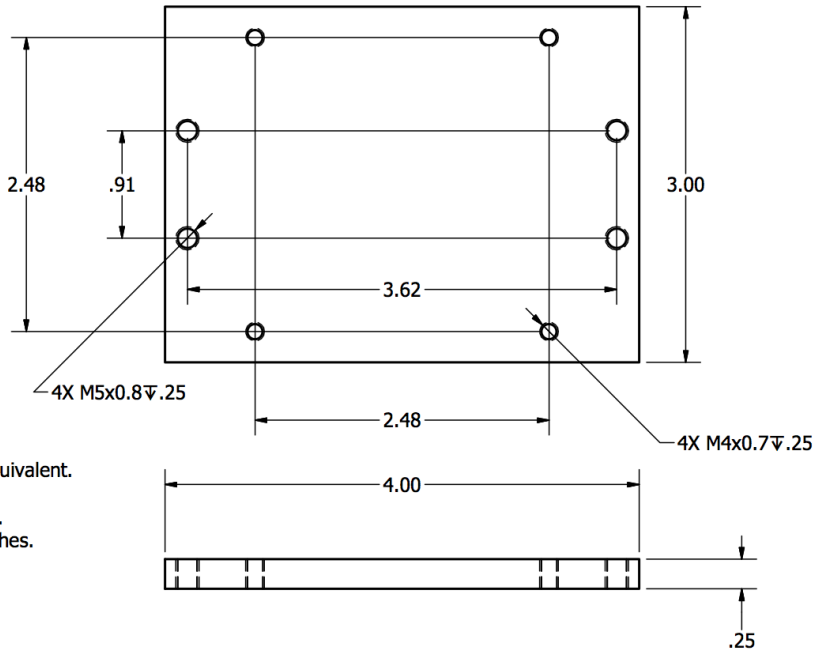

Notes:
1. Material: Aluminum 2024-T4 or equivalent.
2. All dimensions in inches.
3. Remove all sharp edges and burrs.
4. Surface roughness of 63 micro-inches.

Test Plate Adapter
SCALE 1 : 1

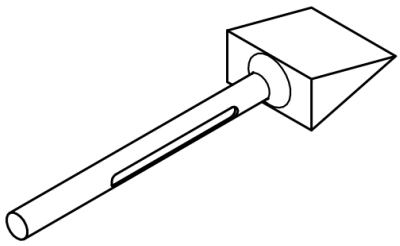

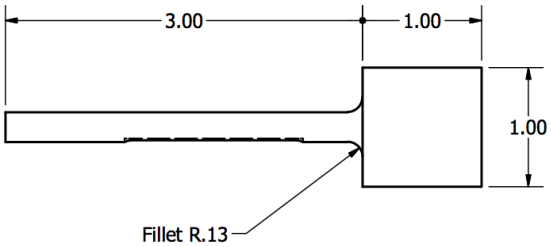

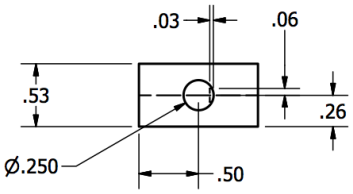

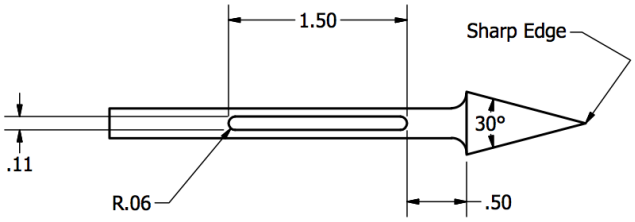

15 deg Wedge
SCALE 1 : 1

Notes:
1. All dimensions in inches.
2. Material: Aluminum 6061 or equivalent
3. Remove sharp edges and burrs, EXCEPT where specified.
4. Surface finish on wedge needs to be at most 32 microinches.

VITA

VITA

Amanda Chou was born in Rockville, MD. She graduated from Thomas Jefferson High School for Science and Technology, Governor's Magnet School for Science and Technology in Alexandria, VA in 2004. For her undergraduate education, she attended Virginia Polytechnic Institute and State University (Virginia Tech). During her undergraduate education, Amanda had an Alumni Presidential Scholarship and a Virginia Space Grant Consortium (VSGC) Undergraduate Research Scholarship. She held summer internships at the Taiwanese National Space Organization in Hsinchu, Taiwan in 2005, Pratt & Whitney in Hartford, CT in 2006, Lockheed Martin Aeronautics in Palmdale, CA in 2007, and Lockheed Martin Aeronautics in Fort Worth, TX in 2008. She graduated in 2008 with a B.S. in Aerospace Engineering *in Honors*.

For graduate school, Amanda attended Purdue University for degrees in Aeronautics & Astronautics. She received her M.S. in Aeronautics & Astronautics in 2010 and her Ph.D. in 2014. During her graduate education, Amanda was a David M. Knox Fellow, a National Defense Science and Engineering Graduate (NDSEG) Fellow, and an Amelia Earhart fellow. She was also a graduate co-op at NASA Langley in Hampton, VA from 2012–2014 with the Flow Physics & Control Branch in the Research Directorate.